SYNTHESIS AND CHARACTERIZATION OF DOWN-SHIFTING LN3+ DOPED LANTHANUM-BASED NANOPARTICLES FOR PHOTOVOLTAIC APPLICATIONS

Maria Méndez Málaga

Dipòsit Legal: T.186-2013

Maria Méndez Màlaga

SYNTHESIS AND CHARACTERIZATION OF DOWN-SHIFTING Ln^{3+} DOPED LANTHANUM-BASED NANOPARTICLES FOR PHOTOVOLTAIC APPLICATIONS

Doctoral thesis

Supervised by
Dr. Yolanda Cesteros Fernández
Dr. Joan Josep Carvajal Martí
Dr. Lluís F. Marsal Garví

Departament de Química Física i Inorgànica
Engineering of Materials and Micro/Nanosystems (EMaS)

UNIVERSITAT ROVIRA I VIRGILI

Tarragona
2013

UNIVERSITAT ROVIRA I VIRGILI
DEPARTAMENT DE QUÍMICA FÍSICA I INORGÀNICA
Campus Sescelades
Marcel·lí Domingo, s/n
43007 Tarragona
Tel. +34 977 55 81 37
Fax +34 977 55 95 63
www.quimica.urv.es

I STATE that the present study, entitled **"Synthesis and characterization of down-shifting Ln^{3+} doped lanthanum-based nanoparticles for photovoltaic applications"**, presented by Maria Méndez Màlaga for the award of the degree Doctor, has been carried out under my supervision at the Department of Physical and Inorganic Chemistry of this university, and that it fulfils all the requirements to be eligible for the International Doctorate Award.

Tarragona, 21th November 2012

Doctoral Thesis Supervisors

Dr. Yolanda Cesteros Fernández

Dr. Lluís F. Marsal Garví

Dr. Joan Josep Carvajal Martí

Acknowledgements

First of all, I would like to express my gratitude to my three advisors Dr. Lluís F. Marsal, Dr. Yolanda Cesteros and Dr. Joan Josep Carvajal, for giving me the opportunity to work in their respective groups, and for their guidance, support and encouragement. The three of them have been very valuable in the development of my PhD investigation and they made this interdisciplinary project an exciting adventure.

I would like to thank Dr. Lluís F. Marsal for making me feel from the beginning part of his group and also for introducing me to the field of electronic devices. I would also give my special gratitude to Dr. Pilar Formentín for always being so near and for her unconditional interest in the progress of my work. Also special thanks to Dr. Pep Ferré for his help in the 234 laboratory on many occasions. All the Nephos group members (María, Víctor, Ely, Mahbub, Peiling, Laura, Gerard, Pedro) that make the laboratory work easier, especially to Dr. Raquel Palacios, who had an important role in the first years of this thesis. I also want to give my special gratitude to Ghader Darbandy for always being there and also to the rest of the members of the 235 laboratory (Muthu, Alejandra, Francois).

I would like to thank Dr. Yolanda Cesteros for her support and her help on many occasions, and also for teaching me a lot of things about the synthesis of materials. I want to give my special gratitude to Dr. Pilar Salagre, for the interesting conversations in the uncountable trips by car and for all the good moments we shared. All the members of Greencat (Dolores, Isa, Tatiana, Helen, Xavi, Judit, Fiseha) and also to Susana for her help in the laboratory.

I would like to thank Dr. Joan Josep Carvajal for transmitting to me all his enthusiasm and motivation in the research world, and also for teaching me the interesting field of lanthanide spectroscopy and crystallography. I also want to thank Dr. Francesc Díaz, Dr. Magdalena Aguiló, Dr. Cinta Pujol and Dr. Montse Galceran for having time for me on many occasions. Thanks also to all the members of the FiCMA-FiCNA group (Jaume, William, Marta, Western, Oleksandr, Raj, Venkat, Qadri) and the technicians of the laboratory for their invaluable help (Agustí, Laura and Nicole).

My special gratitude goes also to Dr. Anke Krüger for giving me the opportunity to do my stay in a foreign country and for letting me work under her supervision. Thanks to all the members of the Nanocarbon group, especially to Susanne, Simone, and Sabine. There are not words to express my enormous gratitude to you. Also thanks to Gustavo, Ana, María José and Ángel to make also my stay in Germany more comfortable.

Finally, I give my thanks to the technicians of the Servei de Recursos Científico-Tècnics of the University Rovira i Virgili (Francesc, Mariana, Rita, Mercè, Núria, Lucas), to Dr. Jordi Llorca of Polytechnic University of Catalunya for the XPS measurements, to Dr. Adolfo

Speghini for the photoluminescence measurements, to Dr. Dominique Drouin and Dr. Alexandre Giguère for the cathodoluminescence measurements and to Dr. Emilio Palomares and Dr. Eugenia Martínez-Ferrero for the photoluminescence measurements and the fabrication of solar cell devices (Núria, Josep, Toni).

Thanks also to the people who have been there sharing special moments during these four years, talking about this project or not, but also giving important support. I want to specially thank my family, Sergi and also his family for being there and making this project possible.

Tarragona, 21th November 2012

This project has been supported by the Spanish Government under projects MAT2008-06729-C02-02/NAN, MAT 2010-114 2-E, MAT2011-29255-C02-02, TEC2009-09551, TEC2010-21574-C02-02, HOPE CSD2007-00007 (Consolider-Ingenio 2010), AECID-A/016246/08, , by the Catalan Authority under project 2009SGR549, and 2009SGR235; by the European Union under project CLEANSPACE FP7-SPA-2010-263011, by the Research Center on Engineering of Materials and Systems (EMaS) of the URV, by the Research and Innovation Ministry of Spain and European Social Fund under the Ramón y Cajal, RYC2006-858.

Publications related to this thesis

Journal articles

M. Méndez, J.J. Carvajal, L.F. Marsal, P. Salagre, M. Aguiló, F. Díaz, P. Formentín, J. Pallarès, Y. Cesteros, "Effect of the $La(OH)_3$ preparation method on the surface and rehydroxylation properties of resulting La_2O_3 nanoparticles" *J. Nanopart. Res.* (Accepted).

Maria Méndez, Yolanda Cesteros, Lluís Francesc Marsal, Alexandre Giguère, Dominique Drouin, Pilar Salagre, Pilar Formentín, Josep Pallarès, Magdalena Aguiló, Francesc Díaz, Joan Josep Carvajal, "Effect of thermal annealing on the kinetics of rehydroxylation of Eu^{3+}:La_2O_3 nanocrystals" *Inorg. Chem.* 51 **2012** 6139.

M. Méndez, Y. Cesteros, L.F. Marsal, E. Martínez-Ferrero, P. Salagre, P. Formentín, J. Pallarès, M. Aguiló, F. Díaz, J.J. Carvajal, "Polymer composite P3HT:Eu^{3+} doped La_2O_3 nanoparticles as a down-converter material to improve the solar spectrum energy" *Opt. Mater.* 33 **2011** 1120.

M. Méndez, J.J. Carvajal, Y. Cesteros, M. Aguiló, F. Díaz, A. Giguère, D. Drouin, E. Martínez-Ferrero, P. Salagre, P. Formentín, J. Pallarès, L. F. Marsal, "Sol–gel Pechini synthesis and optical spectroscopy of nanocrystalline La_2O_3 doped with Eu^{3+}" *Opt. Mater.* 32 **2010** 1686.

M. Méndez, J.J. Carvajal, Y. Cesteros, L.F. Marsal, E. Martínez-Ferrero, A. Giguère; D. Drouin, P. Salagre, P. Formentín, J. Pallarès, M. Aguiló, F. Díaz, "Photoluminescence and cathodoluminescence of Eu: La_2O_3 nanoparticles synthesized by several methods" *Phys. Proc.* 8 **2010** 114.

Electronic articles

M. Méndez, Y. Cesteros, L. F. Marsal, P. Salagre, P. Formentín, J. Pallarès, M. Aguiló, F. Díaz, J. J. Carvajal, "Strategies to tailor the UV absorption band of Eu^{3+}:La_2O_3 down-shifting nanocrystals" *Photonics for Solar Energy Systems IV* 8438 **2012** 843804.

M. Méndez, J. J. Carvajal, Y.Cesteros, L. F Marsal, E. Martínez-Ferrero, , P. Salagre, P. Formentín, J. Pallarès, M. Aguiló, F. Díaz, "Exploring the possibilities of Eu^{3+}:La_2O_3 nanoparticles as an approach for down conversion processes in solar energy systems" *Photonics for Solar Energy Systems III* 7725 **2010** 77250V.

The important thing in science is not so much to obtain new facts as to discover new ways of thinking about them.

William Lawrence Bragg

To my Family and Sergi,

Contents

Chapter 1

General introduction and aims of the thesis

Chapter 1 is mainly focused in explaining the reasons of our interest in the research topic of this thesis. First, we will explain the motivations that made us to study the solar spectrum modification by using down-shifting materials. Then, we will expose the aims of this thesis.

Motivation of this thesis

The fast increasing energy demand in the World together with the higher global climate change consciousness has made researchers attention to focus on renewable and clean energy sources. Since the Sun provides Earth with as much energy per hour as human civilization uses every year, the photovoltaic energy plays a very promising challenge. If a small fraction of sunlight could be captured by photovoltaic (PV) cells that turn it straight into electricity, there would be no need to emit any greenhouse gases from any power plant [1].

The major issue in the PV cells lies in their efficiencies. A conventional PV cell effectively converts only photons of energy close to the semiconductor band gap (E_g) as a result of the mismatch between the incident solar spectrum and the spectral absorption properties of the material that constitutes the solar cell [2]. Thus, one of the major problems in the PV devices is related to the spectral mismatch. Figure 1.1 shows the standard air mass 1.5 global (AM 1.5G) terrestrial solar spectrum [3]. The AM 1.5G simulates the terrestrial solar spectrum on the ground when the Sun is at 48.2º zenith angle [4].

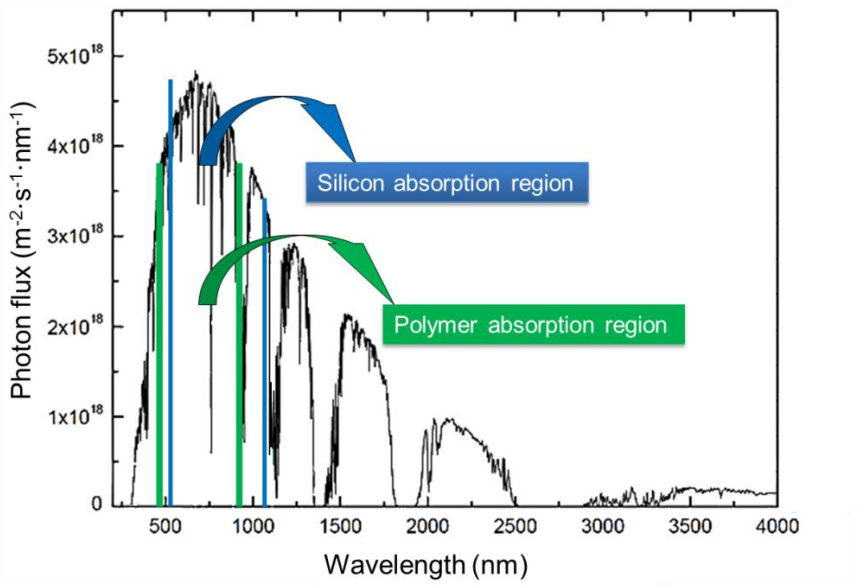

Figure 1.1. The standard AM 1.5G terrestrial solar spectrum together with the regions absorbed by the silicon and the semiconducting polymers in general.

In general terms, there are three different types of PV devices: the inorganic (Si-based) ones, the organic (normally conjugated polymers) ones and the organic-inorganic hybrids (combination of the conjugated polymer and inorganic nanoparticles). As none of these kind of PV cells completely matches the solar spectrum (see Fig. 1.1), the solar spectrum modification is one of the Third Generation concepts suggested to overcome the classical efficiency limit of the existing solar cells [5]. This concept is also an important research topic

in physics and chemistry and has been applied in other fields, for example to infrared quantum counters [6] or efficient lamp phosphors [7].

Therefore, an approach that can be used to increase the efficiencies of PV devices can be the use of materials able to extend the overlap of the semiconductor material with which the PV cell is made of, with the solar spectrum to gain a broader coverage. Here is where the lanthanide (Ln^{3+}) ions play an important role. The motivation for using Ln^{3+} ions is that this family of elements absorb and emit light over a wide spectral range, from the near-infrared (NIR), through the visible (vis) to the ultraviolet (UV). They are able to absorb in a region of the electromagnetic spectrum and emit in another different region very efficiently. Thus, they are considered excellent materials for down-shifting (DS), down-conversion (DC) and up-conversion (UC) processes [8]. Figure 1.2 shows a representation of the mechanisms involving these three different processes. By using DS and DC materials, one can take advantage of the high energy part of the solar spectrum more efficiently (UV-vis). DS and DC involve similar mechanisms, but in DS only one photon is emitted and part of the energy is lost due to non-radiative relaxation while in DC two photons of longer wavelengths are emitted after only one photon of shorter wavelength is absorbed. However, DS mechanisms avoid thermalization of solar cells due to the absorption of high energy photons that produce hot electron-hole pairs that relax to the band edges, allowing also enhancing the efficiency of solar cells and extending the lifetimes of these devices. By using UC, photons with lower energies than that of the band gap can be harvest.

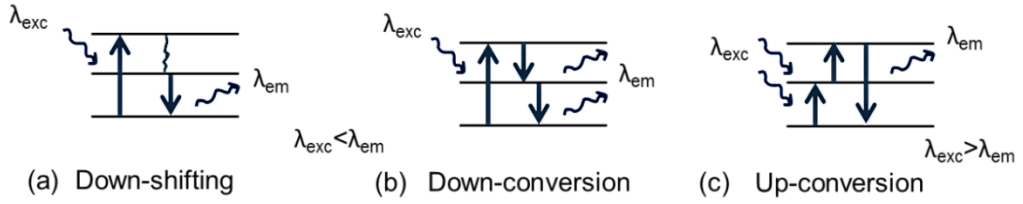

Figure 1.2. A representation of **(a)** down-shifting, **(b)** down-conversion and **(c)** up-conversion mechanisms [19].

Another motivation of using materials containing Ln^{3+} ions is that their optical transitions involve electrons in 4f orbitals, which are well shielded from their local environment by the outer completely-filled $5s^2$ and $5p^6$ shells [8]. This leads them to be largely insensitive to the environment in which they are placed.

The first application of spectrum modification for PV cell applications involving Ln^{3+} materials was reported by Gibart et al. in 1995 [9]. They applied an UC layer on the back of a solar cell formed by an ultra thin (3 μm) GaAs cell placed on a 100 μm thick vitroceramic co-doped with trivalent erbium (Er^{3+}) and trivalent ytterbium (Yb^{3+}). It showed 2.5% efficiency upon excitation of 256 $kW \cdot m^{-2}$ monochromatic sub-band-gap (1.391) laser light (1 W on 0.039 cm^2 cell area). The first application of an up-converter in a Si-based cell was reported by Shalav et al. in 2003 [10]. They used an up-converter consisting of $NaYF_4$ doped with 20

mol% Er^{3+} and demonstrated a 2.5% increase of external quantum efficiency. Finally, for the case of organic solar cells, Wang et al. [11] employed Yb^{3+}:Er^{3+} co-doped yttrium fluoride phosphors as a UC material for the P3HT:PCBM (poly(3-hexylthiophene):[6,6]-phenyl-C61-butyricacidmethylester) system. Though no efficiencies were reported for this system, they observed, under laser illumination, that the photocurrent density measured for the sample with UC phosphor was 16.5 $\mu m.cm^{-2}$ (roughly 14 times the power density yielded by the AM 1.5G solar spectrum between 960 and 1000 nm). They concluded that the UC mechanism might also work for organic solar cells.

For Si-based solar cells, an approach that "squeezes" the wide solar spectrum (300-2500 nm) to a single band spectrum without too many losses would greatly enhance the efficiency over 80% [12]. The efficiency of the organic solar cells, made for instance of P3HT, which is one of the polymers most used in organic cells, is calculated to be able to absorb about 46% of the available solar photons [13] but only in the wavelength range between 350 and 650 nm. In the case of developing a polymer that could capture all of the solar photons down to 1.1 eV would allow an absorption of almost 77% of all the solar photons [14].

In this thesis, we focus our attention on the use of down-shifting Ln^{3+} doped lanthanide compounds nanoparticles. We want to test them in polymer-based solar cells with the aim to increase the polymer absorption power of the sunlight.

Down-Shifting using Ln^{3+} ions

Down-shifting by using Ln^{3+} activators can convert one higher energy photon into a lower energy one that is more efficiently absorbed by the solar cells avoiding the thermalization effects that direct absorption of UV photons can have in conventional PV devices. DS materials containing Ln^{3+} ions have been developed by doping and co-doping nanoparticle hosts, which act as broadband sensitizers, with these ions, forming Dy^{3+}:$LaVO_4$ [15], Bi^{3+}:Ln^{3+}:YVO_4 (Ln= Dy, Er, Ho, Eu, Sm, and Yb) [16] and Eu^{3+}:TiO_2 [17] among others. These materials have been found to be well suited for applications in Si-based cells [18] and dye-sensitized solar cells [15]. However, the literature regarding the use of DS Ln^{3+} doped lanthanide compounds nanoparticles in polymer-based solar cells is rather scarce [11]. With this we face to a new way to improve the efficiencies of organic photovoltaic (OPV) devices by using DS Ln^{3+} doped lanthanide compounds nanoparticles.

In most of the systems having DS properties, the absorption takes place either via the host-material (band-to-band absorption, broad band in the absorption spectrum) or within the active ions (sharp lines in the absorption spectrum) [19]. The broad absorption band via host-material is located usually at the UV part of the electromagnetic spectrum, e.g. the Eu^{3+} doped Gd_2O_3 and Y_2O_3 show this band at around 260 nm [20,21]. Thus, using DS one can take benefit from the highest energy photons arriving on Earth from the Sun.

The basis of Organic Photovoltaic (OPV) devices

The devices made from semiconducting polymers have shown promise for future commercialization due to their low cost, easy fabrication from a simple solution, and small environmental impact relative to silicon and heavy metal based semiconductor solar cells [22-24].

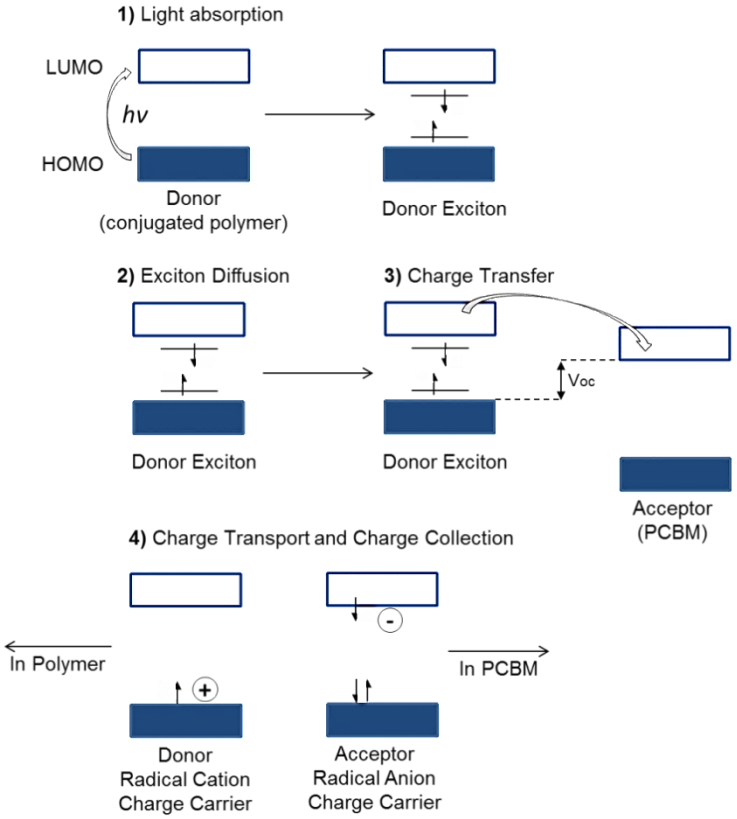

Figure 1.3. General mechanism for energy conversion in polymer-fullerene solar cells [29].

With the effort to increase the power conversion efficiency of the organic photovoltaic (OPV) cells, which is very low in comparison with the silicon counterparts, many different organic solar cell structures are currently being studied worldwide [25]. Among the different parts of a typical OPV device, the active layer is one of the most studied because is considered as the most promising approach to increase the efficiencies of such devices [26,27]. The active layer is formed by both p- and n-type semiconductors (also known as donor and acceptor, respectively), and is where the mechanism by which light is converted to electric power takes place (see Figure 1.3). The energy conversion has four fundamental steps in the most commonly accepted mechanism [28]: 1) a photon is absorbed by the active material which promotes the electron from the highest occupied molecular orbital (HOMO) to the lowest unoccupied molecular orbital (LUMO) of the p-type semiconductor. The excited electron-

hole pair is still bound by Coulomb attraction forces forming an exciton, 2) the exciton diffuses to the interface between the donor and the acceptor, 3) the exciton is dissociated into free carriers at the interface of the donor and the acceptor, and 4) the free carriers are transported and collected at the opposite electrodes.

In this thesis we based our studies in solar cells where the p-type semiconductor is a polymer and the n-type semiconductor is a fullerene. At present, one of the most studied OPVs is formed by P3HT acting as the donor material and PCBM acting as the acceptor [29]. This is because P3HT presents an absorption edge at ~ 650 nm matching well with the strongest solar spectrum and it has the best charge transport properties among the conjugated polymers [30]. Regarding the acceptor, fullerenes are in general currently considered to be the ideal acceptors because they have an energetically deep-lying LUMO [31]. Since the active layer is very important, it has been developed in three different ways: single layer, double layer, and bulk heterojunction [25]. However, since the best charges separation has been observed to be more efficient in bulk heterojunction (BHJ) cells, they have been the most studied. Figure 1.4 depicts a scheme of a typical BHJ organic solar cell. In this figure ITO stands for indium tin oxide and acts as anode in the final device. PEDOT:PSS stand for poly(3,4-ethylenedioxythiophene)-polystyrene sulfonate and it acts as the intermediate layer. PEDOT:PSS provides a well-defined work function which is higher than that of ITO, it smoothes the rough ITO surface and so avoids short-circuits, and it protects the active layer from entrance of indium or oxygen, leading to longer device lifetimes [32-34].

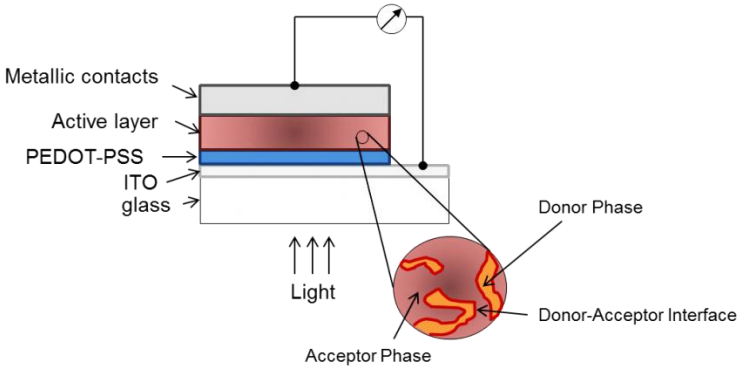

Figure 1.4. Schematic structure of a typical bulk heterojunction organic solar cell.

As we mentioned previously, the major issue in PV in general lies in their low efficiencies. Since the OPV can only harvest the photons of the visible region, a large fraction of sunlight is not being absorbed. We suggest embedding DS Ln^{3+} doped lanthanide compounds nanoparticles in the active layer in order to take benefit of the higher energy of the electromagnetic spectrum region. The DS Ln^{3+} ions can absorb light in the UV part and emit that light in the visible very efficiently, where most of the polymers used in PV can absorb light and consequently with that we would be able to transform the UV light in electricity. Howver, it is important to remark that most of the light absorbed by these Ln^{3+} ions, covers a

large fraction of the solar spectrum that, although being already absorbed by the materials used to fabricate the existing solar cells we can avoid the thermalization processes they generate allowing for higher efficiencies and longer lifetimes.

1.1. Aims of this thesis

The main objective of this thesis was to improve the efficiency of bulk heterojuntion solar cells by using Ln^{3+} doped lanthanum compound nanoparticles for spectrum modification. The spectrum modification using these nanoparticles consists of taking benefit from the higher energy part of the solar spectrum by absorbing in the UV and emitting in the visible region. To take advantage of this mechanism we propose to focus our research on the charge-transfer (CT) energy mechanism with the ligand of the host, instead of focusing our attention on the lanthanide f-f absorption bands, which are several order of magnitude lower, and their spectral positions can not be tailored. Therefore, using different synthesis methods, different hosts, or co-doping with other sensitizer ions, we propose to tailor the position of the CT band in order to match as better as possible with the AM 1.5G solar spectrum and harvest more efficiently the sunlight that arrives to the earth.

Other objectives related to this thesis are exposed as follows:

- Synthesis of the Eu^{3+} and Pr^{3+} doped and co-doped lanthanum compound nanoparticles by using different methods.
- Characterization of the synthesized nanoparticles by using different techniques in order to find the most suitable method (minimum reaction time and temperature, homogeneity, dispersion, etc.) which provides us the best nanoparticles to use them in photovoltaic applications.
- Study of the spectroscopic properties in order to shift and expand the charge transfer absorption bands (Eu^{3+}-O^{2-} and Eu^{3+}-S^{2-}) towards the red part of the electromagnetic spectrum.
- Study of the chemical stability of several lanthanum compound hosts.
- Use of mechanical and chemical techniques to de-agglomerate luminescent nanoparticles.
- Synthesis of semiconductor polymer-based films by using the spin-coating technique and their characterization by different techniques.
- Fabrication and characterization of composites formed by Ln^{3+} doped and co-doped lanthanum compound nanoparticles embedded in polymeric matrices.
- Study of the application of these organic-inorganic composites in a real device by fabricating a bulk heterojunction organic/hybrid solar cell.

Chapter 2

Characterization techniques

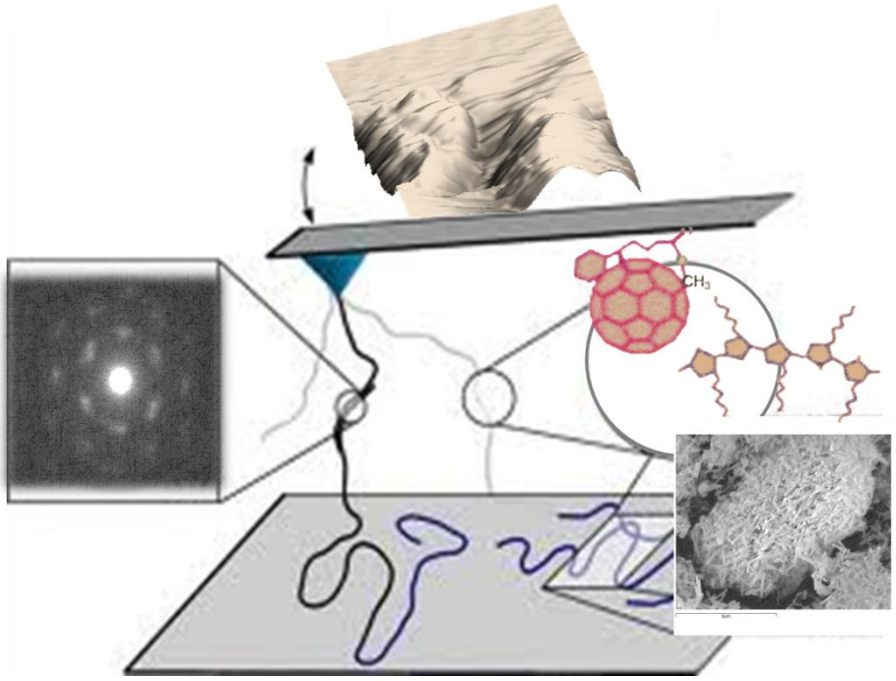

In this chapter we present the fundamentals of the characterization techniques used in this thesis. Furthermore, we give the features of the instruments used for each technique, the sample preparation process (if necessary), and the measurement conditions. The instruments were available at the research groups of the *EMaS* (*FiCMA-FiCNA*, *GreenCat* and *Nephos*) and at the *Servei de Recursos Científico-Tècnics*, at University Rovira i Virgili of Tarragona (Spain). Some other equipment were available in collaboration with the *Institute of Chemical Research of Catalonia* (ICIQ) and the *Polytechnic University of Catalunya* (UPC), in Spain, and also through foreign collaborations with the *Department of Electrical and Computer Engineering* at the University of Sherbrooke (Canada), the *Institute of Organic Chemistry* (*Nanocarbon* group) at the University of Würzburg (Germany), and the *Laboratory of Solid State Chemistry* at the University of Verona (Italy).

2.1. X-Ray Powder Diffraction (XRD)

X-rays were discovered by W.C. Rötgen's in 1895 at the University of Würzburg. The fundaments of this technique consist in the interaction between an incident beam and a crystalline material. X-rays are electromagnetic radiation of the same nature that light but as it has much shorter wavelength (typically ranging 0.7-2 Å) are energetic enough to penetrate solid materials and inform us about their internal crystalline structure.

In this thesis, we used the X-ray powder diffraction technique because the materials that we synthesized are not single crystals but are composed of multitude of tiny crystallites. This type of material is referred to as a powder or a polycrystalline aggregate [35]. When a beam of X-rays interacts with a material, it is diffracted by the crystalline phases of the material according to the Bragg's law:

$$\lambda = 2d\sin\theta \qquad \textbf{(Eq. 2.1)}$$

where d_{hkl} is the spacing between atomic planes in the crystalline phase and λ is the X-ray wavelength. The basic geometry of diffraction is shown in Figure 2.1. The waves incoming under an angle θ against the surface are "reflected" at the same angle. Between two consecutive lattice planes, the "reflected" waves have a phase difference of 2θ. In general terms, the intensity of the diffracted rays provides information about atomic positions and consequently, about the structure of a crystal.

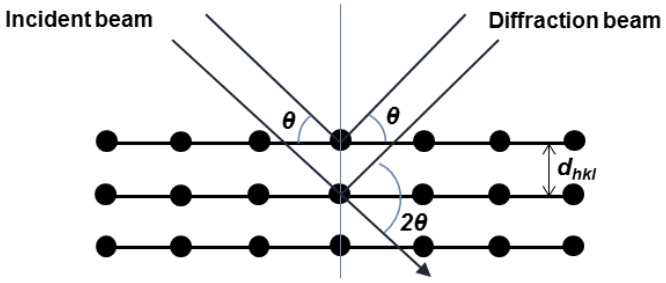

Figure 2.1. Schematic description of the diffraction of two consecutive lattice planes.

When the peak width is caused by homogeneous or uniform elastic strain and that it is not contributed in part by the crystallite size and inhomogeneous strain, the crystallite size, D (nm), can be estimated from the peak width using the Scherrer's equation [36]:

$$D = \frac{K\lambda}{\beta\cos\theta_B} \qquad \textbf{(Eq. 2.2)}$$

where λ is the X-ray wavelength used, β is the full width at half maximum (FWHM) of a diffraction peak, θ_B is the Bragg angle, and K is a constant value equal to 0.9 for D taken as

the volume-averaged crystallite dimension perpendicular to the *hkl* diffraction plane. The validity of this formula has been widely discussed in the literature and it might be considered valid only for small particles <500 nm. As in this work, the particle sizes obtained were below this value we used the Scherrer's equation to estimate the crystallite size. It is also worth to distinguish between grain size, crystal size and crystallite size. Fig 2.2 shows schematic images representing with a dotted line what is considered when one refers to these different sizes. The *grain size*, is the size of a group of crystals, the *crystal size* is the size of one crystal and the *crystallite size*, measured by the Scherrer's equation, is the size of a coherent scattering domain (perfect arrangement of unit cells or perfect crystals).

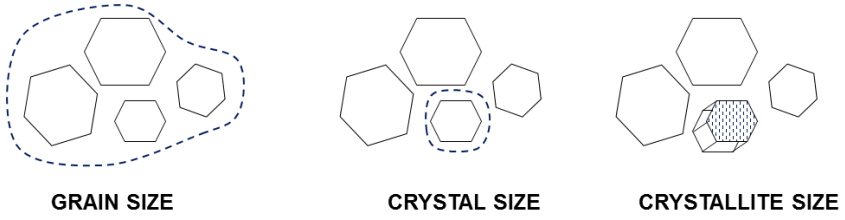

Figure 2.2. Schematic representations of the grain size, crystal size and crystallite size.

X-ray powder diffraction is a non-destructive technique so that is widely used to characterize crystalline materials. The patterns obtained act like a digital prints and are characteristic of every material. These patterns are analysed by the files of the Joint Committee for Powder Diffraction Standards (JCPDS) which identify what phases are present in the sample. Most of the XRD patterns reported in this thesis were collected at the *Serveis de Recursos Científico-Tècnics* of University Rovira i Virgili, using a Bruker-AXS D8-Discover diffractometer with parallel incident beam (Göble mirror) and vertical goniometer, a 0.02^{o} receiving slit and a scintillation counter as detector. Cu Kα radiation was obtained from a copper X-ray tube operated at 40 kV and 40 mA. The angular 2θ diffraction range was set between 5 to 70^{o}. Data were collected with an angular step of 0.05^{o} at 3 s per step and at slower conditions in the case of the patterns recorded for the cell-parameters calculation, with an angular step of 0.02^{o} at 16 s per step. For the thermal evolution and re-hydroxylation studies, the XRD patterns were carried out using a Siemens D5000 diffractometer and Ni-filtered Cu Kα radiation (30 mA, 40 kV), with a Braun position sensitive detector PSD. The angular 2θ diffraction range was from 10 to 70^{o} for thermal evolution, and the measuring time was 10 s per degree in the heating and cooling cycles. The angular 2θ diffraction range was from 25 to 35^{o} for re-hydroxylation studies.

By this technique, we will analyse the crystalline structures of several samples in order to identify the phase or phases that constitute such nanoparticles, to determine the crystallite size by using the Scherrer's equation (Eq. 2.2) and to determine the unit cell parameters by refining the XRD patterns by using the Fullprof software based on Rietveld method [37-39].

2.2. X-Ray Photoelectron Spectroscopy (XPS)

X-ray Photoelectron Spectroscopy (XPS) allows us to identify and quantify the atoms located at surface levels in a sample. In XPS, relatively low-energy X-rays are used to eject the electrons from an atom via a photoelectric effect. The energy of the ejected electron, E_E, is determined by both the energy of the incident photon, $h\nu$, and the bound electron state, E_B:

$$E_E = h\nu - E_B \qquad \textbf{(Eq. 2.3)}$$

Since values of the binding energy are element-specific, atomic identification is possible through measurement of photoelectron energies [40]. The range of detection is 0.2-1.5 keV of E_E. XPS provides information of value for many industrial applications such as polymer surface modification, catalysis, corrosion, adhesion, thin film coatings, etc. XP spectra were obtained by a SPECS system available in the *Polytechnic University of Catalunya* (UPC) laboratories. This system is equipped with an Al XR50 anodic source working at 150 W, and with a Phoibos 150 MCD-9 detector. The energy used was between 25-0.1 eV with a pressure below $6 \cdot 10^{-9}$ mbars.

In this thesis, XPS technique was used to obtain information about the concentration of europium at the surface of the synthesized sample and evaluate the surface Eu/La ratio in several samples.

2.3. Nitrogen physical adsorption

Nitrogen physical adsorption is a powerful technique and is particularly useful in the determination of specific surface area and pore volume in mesopores (~2 - 50 nm) or micropores (< 2 nm) materials. Basically, when nitrogen comes in contact with a solid surface, under 77 K and suitable pressure, nitrogen molecules will adsorb onto the surface so as to reduce the imbalanced attractive force on surface atoms, and thus to reduce the surface energy. Then, the amount of gas needed to form a monolayer or to fill pores in various sizes can be measured as a function of the gas pressure.

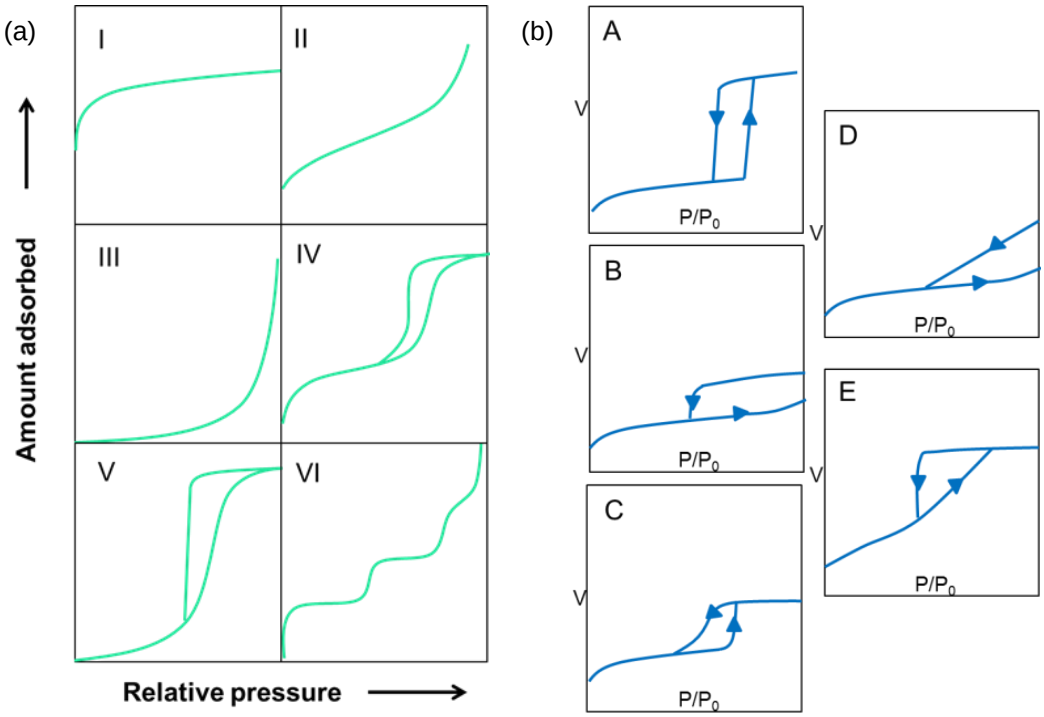

Figure 2.3. Illustrations of different types of **(a)** gas adsorption isotherms (I-VI) and **(b)** hysteresis (A-E).

An isotherm is considered as the curve obtained from the amount of gas adsorbed as a function of pressure at constant temperature. Figure 2.3(a) shows different types of isotherms:

- Isotherm I is typical of microporous solids with very low external surface (molecular sieves and activated carbons).
- Isotherm II represents multilayer physisorption on a flat surface (nonporous or macroporous solids).
- Isotherm III is characteristic of weak gas solid interactions.
- Isotherm IV is characteristic of multilayer adsorption accompanied by capillary condensation in mesopores.
- Isotherm V is similar to that of isotherm III but it reflects the existence of mesoporous in the sample.
- Isotherm VI occurs when the surface of a nonporous adsorbent is energetically uniform and the isotherm may have a step-like shape.

For isotherms IV and V the hysteresis phenomena between adsorption and desorption is very common. There are five different types of hysteresis and it depends on the pore shape (see Figure 2.3(b)):

- Hysteresis A is related to, open on both sides, tubular pores.
- Hysteresis B is related to pores formed by parallel crystalline layers separated by small particles or by crystalline defects.
- Hysteresis C and D come from type A and B, respectively. Type C is related to conic pores and type D is related to pores formed by non-parallel layers. Both are quite difficult to be found.
- Hysteresis E indicated the presence the neck bottle shaped pores. This means that pores are wide but with a narrow neck.

The Brunauer-Emmett-Teller (BET) is the main method used to determine the surface area in porous materials. BET value is calculated by the following equation:

$$\mathrm{A\ (BET)} = \frac{\mathrm{V_m \cdot L \cdot A_m}}{\mathrm{M}} \qquad \textbf{(Eq. 2.4)}$$

where L is the Avogadro number, V_m is the volume of nitrogen adsorbed on the monolayer, A_m is the occupied area per each adsorbed nitrogen molecule (0.162 nm^2 at 77 K) and M is the mass of adsorbed gas.

The measurements were performed in *GreenCat* (*EMaS*) laboratories by using a Quadrasorb surface analyser apparatus of Quantrachrome. The BET specific surface areas were calculated using adsorption data in the relative pressure range $0<P/P_0<0.3$. All samples were outgassed in vacuum at 393 K for 20 h and the amount of sample analysed was enough to obtain an absolute area >10 m^2.

The nitrogen adsorption technique gave us information about the porosity and the surface area of several samples. This information was useful to compare the surface area of the nanoparticles synthesized by the different synthesis methods.

2.4. Thermal analysis

The definition of thermal analysis by IUPAC is "a group of techniques in which a physical property of a substance, or its reaction products, is measured as a function of temperature whilst the substance is subjected to a controlled temperature program". Among the different techniques involved in this definition, we used thermogravimetric analysis (TGA) and the combination of differential thermal and thermogravimetric analysis (DTA-TGA).

2.4.1. Thermogravimetric analysis (TGA)

Thermogravimetric analysis is used to determine the thermal stability of a sample. The mass of the sample is monitored while it is subjected to a thermal treatment in a particular

environment (air, O_2, N_2). TGA determines the weight gain or loss of a phase due to gas absorption or release as a function of temperature under a controlled atmosphere. The decomposition steps of the sample can be observed throughout the graphic representation of weight variation vs. temperature. The first derivative of this curve permits to better differentiate these steps [41].

TGA measurements were carried out in a Perkin Elmer TGA 7 microbalance at the *GreenCat* group and in a Perkin Elmer STA 6000 instrument at the *Institute of Organic Chemistry* at the University of Würzburg. The thermograms were carried out heating at 10 $K \cdot min^{-1}$, in a synthetic air flow with a rate of 80 $cm^3 \cdot min^{-1}$. All measurements were recorded from room temperature to 1273 K.

In general, these tests helped to analyse dehydration processes as well as the decomposition of every sample according to their weight loss. Additionally, by the TGA technique it was possible to study the sample surface loading. This parameter indicates the capability of the organic compound, which is used to functionalize the nanoparticles [42], to react with their surface. This value is calculated from the weight loss of the organic compound.

2.4.2. Differential thermal analysis (DTA)

Differential thermal analysis consists in following the temperature of a substance as a function of time and comparing its evolution with that of an inert reference material. This methodology presents several advantages because both, the sample and the reference material react similarly cancelling the potential effect and leaving the baseline unperturbed. The temperatures changes due to transformations occurred, such as glass transitions, crystallization, melting and sublimation, are shown as exothermic peaks (positive ΔT) or endothermic peaks (negative ΔT) on DTA curves. Ideally, the area under the DTA peak should be proportional to the enthalpy of the process that gave rise to the peak.

In this thesis, the combination of DTA-TGA analysis was employed to simultaneously measure thermal behaviour and mass changes using a SDT 2960 analysis system from TA Instruments at *FiCMA-FiCNA* group. The experiments were carried out in Pt crucibles using calcined Al_2O_3 as reference material (provided by TA Instruments). The sample was heated at 10 $K \cdot min^{-1}$ in the 300-1273 K range. Synthetic air was used as the purge gas at a flow rate of 90 $cm^3 \cdot min^{-1}$. The storage rate of data was 0.5 s per data point.

These measurements make possible to differentiate between endothermic/exothermic transitions with (e.g. degradation) and without weight change (e.g. fusion or crystallization). Therefore, the DTA-TGA measurements give an approximation of the minimum temperature of calcination necessary to obtain the oxide phase.

2.5. Electron microscopy

Electron microscopy is the best-suited technique in order to study the shape, size and structure of nanoparticles. What mainly distinguished an electron microscope from an optical one is the length of the applied waves that interact with the sample to be imaged, and according to Abbe [43], it is impossible resolving structural details smaller than half of the wavelength due to the diffraction barrier. The diffraction barrier restricts the ability of optical instruments to distinguish between two objects separated by a lateral distance less than approximately half of the wavelength of light used to image the specimen.

The electron microscopy techniques that we used in this thesis were the scanning electron microscopy (SEM), environmental scanning electron microscopy (ESEM) and transmission electron microscopy (TEM).

2.5.1. Scanning electron microscopy (SEM)

The scanning electron microscope is the most widely used technique of electron microscopy in the field of materials sciences. In a typical SEM, a source of electrons is focused into a beam, with a very fine spot size of ~5 nm and having energy ranging from a few hundred eV to 50 keV. This spot size determines the resolution of the image, which is obtained by scanning. Several types of signals are produced when the focussed electron beam impinges on the specimen surface, and they can be used to form an SEM image. Some of the quanta are secondary electrons, backscattered electrons, X-rays, and cathodoluminescence generated by the impinging electrons (see Fig. 2.4).

Because the SEM beam can be focused on samples which are rough or irregularly shaped, the preparation of the samples for SEM examination is relatively easy. However, if the sample is not a good electrical conductor then it is often desirable to provide some conductivity by evaporating a thin metal layer (typically 3 to 10 nm of gold) on the surface of the sample. We used a SEM JEOL JSM 6400 microscope to record images of the samples, which were coated with gold using a Bal-Tec SCD004. This equipment is available at the *Servei de Recursos Científico-Tècnics* of the University Rovira i Virgili. The SEM was operated at an accelerating voltage of 20 kV, using a work distance of 8 mm, and magnifications in the range 5000-50000×.

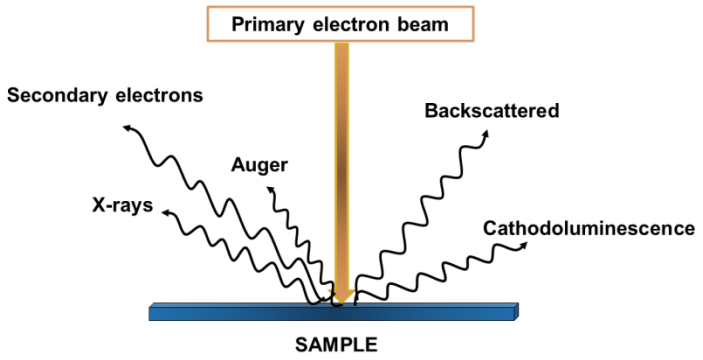

Figure 2.4. The different interactions occurred when a beam of electrons collide and penetrate the surface of a sample.

The SEM images were obtained for several nanopowder samples in order to study their morphology and agglomeration degree.

2.5.2. Environmental scanning electron microscopy (ESEM)

The environmental scanning electron is based on the same principle than SEM. However, because it removes the high vacuum constraint on the sample environment, samples can be examined in their natural state without preparation. An ESEM contains gas at low pressure in the sample chamber, where the primary electrons travel across the gas phase and interact with the surface of the sample, which releases secondary electrons that interact with the phase gas to produce additional secondary electrons. The primary electrons interact with the gas molecules to produce ions and additional electrons. Thus, the phase gas functions as an amplifier of the electron signal from the sample. Therefore, wet, oily, dirty and non-conductive samples can be examined without having to coat them with a conductor media such as gold and their original characteristics can be observed for further manipulation.

A FEI QUANTA 600 environmental scanning electron microscope at low vacuum was used to acquire the images. This microscope is also available at the *Servei de Recursos Científico-Tècnics* of the University Rovira i Virgili.

By observing ESEM images, we studied the morphology of several nanopowder samples, the distribution of the nanoparticles in several polymer-based nanocomposites, and the porous sizes of the porous silicon templates.

2.5.3. Transmission electron microscopy (TEM)

The transmission electron microscope (TEM) is an electronic analogue to the conventional optical light microscope but the electrons are accelerated to 100 keV or higher voltages (up to a MeV). The greatest advantages that TEM offers are the high magnification ranging from 50

to $10^6\times$ and its ability to provide both image and diffraction information from a single sample.

We used a TEM JEOL JEM-1011 located at the *Servei de Recursos Científico-Tècnics* of the University Rovira i Virgili. The preparation of the samples consist in placing a drop of the nanopowder, previously mixed in a volatile solvent such as ethanol or acetone, on a cooper grid covered by a holey carbon film (HD200 Cooper Form-var/carbon). Since, the key requirement for using TEM is that the sample must be very thin, a special previous preparation was necessary to observe the structured P3HT-based nanocomposite sample. First, a mixture of the nanocomposite in a low viscosity resin was introduced into a silicone template. After an annealing treatment at 333 K for 48 h in a furnace, the sample was separated from the template and cut with an ultramicrotome that allowed preparing thin sample layers of around 60 nm in thickness. TEM was used operating at an accelerating voltage of 80-100 kV and magnification in the range 25000-150000×.

From TEM images, we obtained information of the size and morphology of the nanoparticles. In addition, structured polymer-based nanocomposites were also observed under TEM in order to study the distribution of the particles into the polymeric matrix.

Electron diffraction

By transmission electron microscopy and by adjusting the electron lenses, one also can obtain the diffraction pattern of the same region of the sample observed in the electron microscope images. This is observed on a fluorescence screen and recorded on photographic film. For crystalline materials, electron diffraction only occurs at specific angles, which are characteristic of the crystal structure of the sample. In the case of polycrystalline materials, the electron diffraction produces a pattern of concentric rings from many spots very close together whereas in amorphous materials, that do not consist of atoms arranged in ordered lattices, the electron beam is diffracted in multiple directions and consist of fuzzy rings of light on the fluorescent screen.

When comparing X-ray diffraction and electron diffraction, there is one essential difference. X-rays applied for structural analyses usually are in the wavelength range between 0.05 and 0.22 nm (the most common is the Cu Kα radiation with a wavelength of 0.154 nm). In the case of electron diffraction, the energy of the electrons is selected to be in a range from 100 to 200 keV which is equivalent to a wavelength range from 2.5×10^{-3} to 3.7×10^{-3} nm.

By using this technique we observed the crystalline and non-crystalline behaviour of different nanopowder samples.

2.6. Atomic force microscopy (AFM)

Atomic force microscopy (AFM) was developed in 1986 by Binnig, Quate, and Gerber, for dielectric materials as a modification of scanning tunnelling microscopy (STM) since this last technique was limited to electrical conductive surfaces [40]. AFM is a scanned-proximity probe microscopy, which measures the local attractive/repulsive forces with a tip (or in a more general way, with a probe) placed very close to the sample. Figure 2.5 shows how the AFM works. The equipment consists of a cantilever with a nanoscale tip, a laser pointing at the end of the cantilever, a mirror and a photodiode collecting the reflected laser beam.

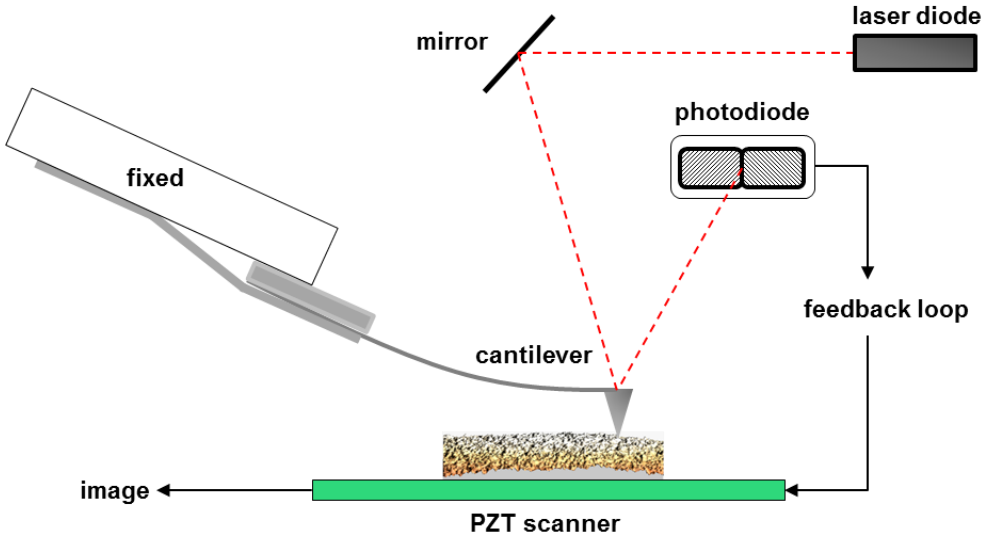

Figure 2.5. Simplified diagram showing how the AFM works and the different parts of the equipment.

There are two different ways to acquire the AFM images: in contact mode and in tapping mode. In the contact mode (or repulsive mode), the piezoelectric scanners maintain the tip at a constant force and the microscope measures the vertical deflection of the cantilever that indicates the local height of the sample. In the tapping mode (or attractive mode), the tip is kept at a fixed height from the sample surface and the microscope derives topographic images from measurements of attractive forces.

As the sample does not need to be coated, AFM provides extraordinary topographic contrast and direct height measurements. The AFM images were collected in tapping mode from 4 to 7 V of peak amplitude, depending on the roughness of the sample, at a speed of 1 line/s. These images were acquired in air under ambient conditions using a Molecular Imaging model Pico SPM II (Pico +) available at the *Serveis de Recursos Científico-Tècnics* of the University Rovira i Virgili.

We used this technique mainly to study the roughness of the polymeric films and the polymer-based nanocomposite films. Additionally, by scrapping off part of the sample we determined the thickness of several films.

2.6.1. Current sensing atomic force microscopy (CS-AFM)

Current sensing AFM (CS-AFM) is a powerful technique for electrical characterization of conductivity variations in resistive samples. It allows a direct and simultaneous visualization of the topography and current distribution on a sample. The CS-AFM technique needs a cantilever coated with a conducting film (see Figure 2.6). Applying a voltage bias between the substrate and the conducting cantilever generates a current flow. Thus, current-voltage (I-V) characteristics can be measured by using this technique.

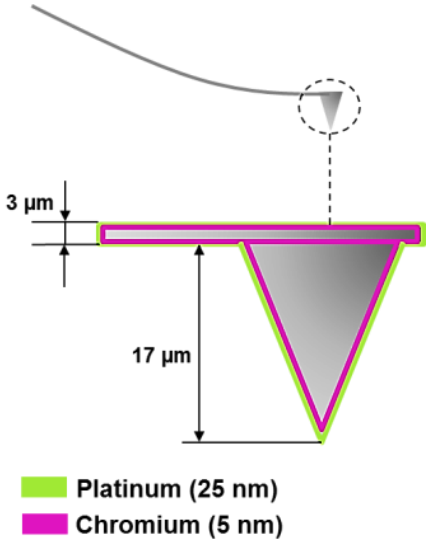

Figure 2.6. Some of the features of the electrical tip used to record current measurements.

The CS-AFM studies were performed in contact mode in dark conditions in air under ambient conditions. For CS-AFM measurements, electrically conductive platinum-chromium coated cantilevers (Multi75E-G with a resonant frequency of 75 kHz and a force constant of 3N/m from Budgetsensors) were used to scan the samples while the current was measured between the tip and the ITO substrate. CS-AFM measurements were carried out using a Molecular Imaging model Pico SPM II (Pico +) available at the *Serveis de Recursos Científico-Tècnics* of the University Rovira i Virgili.

We used current sensing mode to study the I-V curves of the polymeric and nanocomposites samples.

2.7. Dynamic Light Scattering (DLS)

The Dynamic Light Scattering (DLS) technique, also known as photon correlation spectroscopy, is one of the most popular methods used to determine the size of the particles. Shining a monochromatic light beam, such as a laser, onto a solution with spherical particles in Brownian motion causes a Doppler shift when the light hits the moving particle, changing the wavelength of the incoming light. This change in the wavelength is related to the size of the particle.

Figure 2.7 shows a schematic diagram of a conventional, 90º dynamic light scattering instrument. Light is scattered by the particles at all angles. However, a dynamic light scattering instrument with one detector only detects the scattered light at one angle and this, historically has usually been at 90º [44]. The intensity fluctuations of the scattered light are converted into electrical pulses, which are fed into a digital correlator.

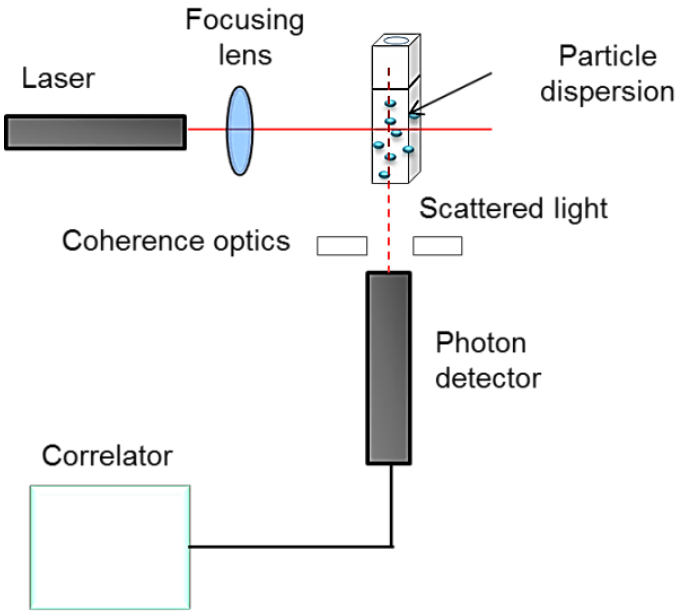

Figure 2.7. Simplified scheme of the dynamic light scattering set-up.

In this thesis, DLS technique had an important role on the determination of the particle sizes. The measurements were carried out in a Malvern Zetasizer (Nano-ZS) instrument in the laboratories of the *Institute of Organic Chemistry* of the University of Würzburg. The experiment duration is short and a previous preparation is not needed, thus it makes possible to measure the size of the samples immediately after every test.

2.7.1. Capillary Viscometer Analysis

Since the viscosity is considered an important data to determine the particle size by the DLS technique, the viscosity of all the solvents where the particles were dispersed has to be analysed. The viscosity of Newtonian fluids can be determined using capillary viscometers. This method measures the time taken for a known quantity of fluid to flow through a capillary with a known diameter and length.

These analyses were carried out by using a AVS 20, made by SCHOTT Instruments and using two different capillaries with different diameters (see Table 2.1 and Figure 2.8). This system was available at the laboratories of the *Institute of Organic Chemistry* of the University of Würzburg. These viscometers were designed with a suspended ball, according to the principle of the Ubbelohde viscometer for determination of the limit viscosity number of polymers [45].

Thus, by capillary viscometer analysis, we determined the viscosity of the (3-acryl-oxypropyl)trimethoxysilane (APTMS) compound which was used to functionalize the nanoparticles and also as a medium to disperse them.

Table 2.1. Specifications about the different types of capillary visometer used to determine the viscosity parameter.

Type	Capillary viscometer Ø (mm)	Constant k (approx.)	Measuring range ($mm^2 \cdot s^{-1}$) (approx.)
531.03	0.47	0.003	0.5-2
531.13	0.84	0.03	3-20

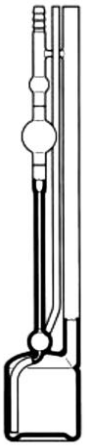

Figure 2.8. Image of the AVS 20 viscometer used in this thesis.

2.8. Spectroscopic Techniques

Spectroscopic characterization has been widely used for the characterization of nanomaterials, and the techniques can be generally categorized into two groups:

- Vibrational spectroscopy (infrared and Raman spectroscopy).
- Absorption and emission spectroscopy (absorption and transmission, photoluminescence and cathodoluminescence).

The vibrational techniques include those techniques involving the interactions of photons with species in a sample that results in energy transfer to or from the sample via vibrational excitation or de-excitation. The vibrational frequencies provide the information of chemical bonds in the samples characterized.

The second group of techniques, determine the electronic structures of atoms, ions, molecules or crystals through exciting electrons from the ground to excited states (absorption) and relaxing them from the excited to ground states (emission).

2.8.1. Fourier Transformed Infrared spectroscopy (FT-IR)

Infrared spectroscopy was measured by a Fourier transformed infrared spectroscopy (FT-IR) technique. Infrared spectra wavelengths range from 10 to 14000 cm^{-1}. However FTIR spectroscopy has been mainly used in the middle infrared region (MIR) where the main vibrational models appear and corresponds to wavelengths between 400 and 4000 cm^{-1}. This technique may be used to identify the type of bond between two or more atoms and consequently identify functional groups.

A sample preparation process was required to use the FT-IR technique, and consisted in mixing a small amount of nanopowder with potassium bromide (KBr has no infrared absorption in this region) and subsequently preparing a pellet. It is important to dry properly both sample and KBr to avoid broad bands signals in the spectrum coming from water. The transmission infrared spectra of all these samples were recorded on a Bruker-Equinox-55 FTIR spectrometer by accumulating 32 scan with a resolution of 4 cm^{-1} in the range of 400-4000 cm^{-1}. The FT-IR equipment was available at the *GreenCat* laboratories.

Within this thesis, FT-IR was used in order to observe phase transformations versus temperature, to confirm the presence of europium in the samples and also to analyse the functionalized samples.

2.8.2. Raman spectroscopy

Raman spectroscopy is also a vibrational technique but differs from the IR spectroscopy, by an indirect coupling of high-frequency radiation, such as visible light, with vibration of chemical bonds. Thus, when the incident photon interacts with the chemical bond, the chemical bond is excited to a higher energy state. Most of the energy would be reradiated at the same frequency as that of the incident exciting light, which is known as the Rayleigh scattering (elastically scattered). However, Raman scattering relies on inelastic scattering of monochromatic light resulting in the energy of the scattered photons being shifted down or up for the Stokes or anti-Stokes lines, respectively. The shift in energy gives information about the photon modes in the system because it is related to the vibrational energy spacing at the ground level. A Raman spectrum is very sensitive to the lengths, strengths, and arrangements of chemical bonds in the material. Thus it is more a structural technique than a chemical analysis technique.

The experimental set-up comprised a Renishaw confocal InVia Reflex spectrometer, a confocal Leica 2500 adapted microscope and an argon laser with excitation in the visible region (λ = 514 nm and 25 mW). The Raman spectroscopy technique was available at the *Serveis de Recursos Científico-Tècnics* of the University Rovira i Virgili.

Raman scattering was used to characterize the dispersion of nanocrystals into polymeric films.

2.8.3. Absorption and transmission spectroscopy

Absorption is the fraction of incident electromagnetic radiation absorbed by electron, ions or molecules in the material over spectral ranges of light. It results from the transformation of the incident wave energy into other types of energy (mostly heat). Particular wavelengths usually excite electrons of the outer shells of an atom (optical electrons) and as a result the absorbing material appears coloured and the intensity of the incident beam is weakened. The Beer-Lambert law relates the absorption of light with the properties of the material through which the light is travelling:

$$I = I_0 e^{-\alpha d} \qquad \textbf{(Eq. 2.5)}$$

where I is the intensity of the emerging radiation, I_0 is the incident light intensity, α is the absorption coefficient and d is the thickness of the sample.

The absorption was measured using a PerkinElmer-Lambda 950 (UV/Vis/IR) spectrophotometer available at the *Nephos* laboratories. The experimental spectra were recorded with a slit width of 2 nm, using a tungsten lamp. The spectral range was between 350 and 800 nm and the signal was recorded every 1nm with an integration time of 0.20 s.

This technique was used in this thesis to obtain information about the absorption range of several polymers, small molecules such as fullerenes, and the corresponding blends of these materials.

2.8.4. Luminescence techniques

Luminescence refers to the emission of light by a material through any process other than blackbody radiation. The emission of that light can be the result of a variety of stimulations. When it results from photon stimulation it is referred to as photoluminescence (PL), and when it results from electron stimulations it is referred to as cathodoluminescence (CL). Both techniques have been used in this work.

2.8.4.1. Photoluminescence (PL)

In photoluminescence, physical and chemical properties of materials are measured by using photons toexcite electrons towards excited electronics states in the material and analysing the optical emission as these electrons relax. Typically, light is directed onto the sample for excitation, and the emitted luminescence is collected by a lens and passed through an optical spectrometer onto a photodetector. The time between the start of the emission and the time when its intensity decreases to 1/e of its initial value is called the radiative lifetime (τ). This is an important parameter which characterizes not only the depopulation of an electronic level but also the thermal excitation mechanism of these processes.

The photoluminescence measurements were carried out by using a fluorescence spectrophotometer from Photon Technology International Inc. with a 150 W Xenon lamp used as the excitation light source at room temperature. Both the excitation and emission spectra were recorded from 220 to 550 nm and from 550 to 725 nm, respectively, in a 90º geometry and taking measurements every 1 nm at a scanning rate of 1 $nm \cdot s^{-1}$. The excitation spectrum is the measurement of the fluorescence intensity at a fixed wavelength (for instance at the wavelength of maximum emission fluorescence) as a function of the excitation wavelength. This spectrum is useful to measure how fluorescence intensity depends on the excitation wavelength. In our case, since the excitation spectrum is essentially an absorption spectrum, we observed the absorption region of the nanoparticles. The emission spectrum represents the intensity of fluorescence light emitted by the sample as a function of emission wavelength.

Figure 2.9 shows an scheme of the fluorescence spectrophotometer which is available in the laboratories of the *Nephos* group of the University Rovira i Virgili. The lifetime of the calcined sample was obtained by steady-state fluorescence at room temperature. It was recorded in an Aminco-Bowman Series 2 fluorimeter equipped with a 7 W pulsed Xenon lamp, in the laboratories of *ICIQ* of Tarragona.

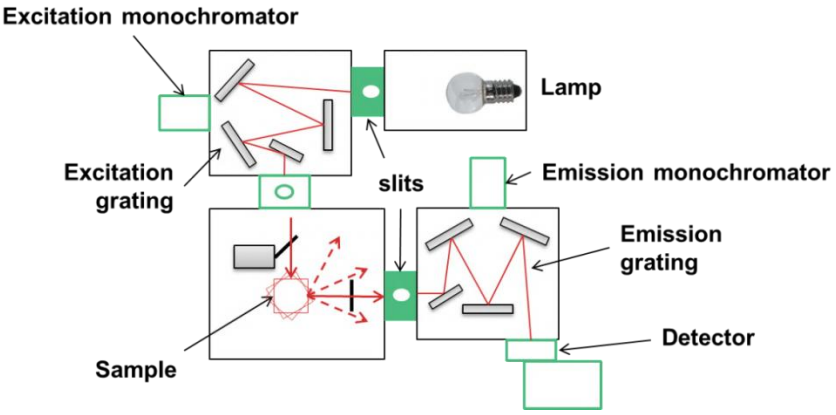

Figure 2.9. Set-up of the fluorescence spectrophotometer equipment from Photon Technology International Inc.

Emission spectra were also performed by using a OPOTEK Inc. Vibrant (HE) 355II + UV, with a pump laser Nd^{3+}:YAG (Q-switched). For detection, the emission was collected at a 90º geometry to minimize the influence of the laser pump on the collected spectra and was dispersed by a JOBIN YVON-SPEX HR 460 double monochromator with a focal length of 460 mm and a spectral resolution of 0.05 nm. The detector used was a Hamamatsu PMTR928 which was connected to a lock-in amplifier Perkin Elmer DSP-7265. Figure 2.8 shows the experimental set-up used to measure the luminescence at the *FiCMA-FiCNA* group of the University Rovira i Virgili. The lifetime of the rehydroxilated sample was measured by using this set-up shown in Fig. 2.10 and with a computer-controlled Tektronik TDS-714 digital oscilloscope.

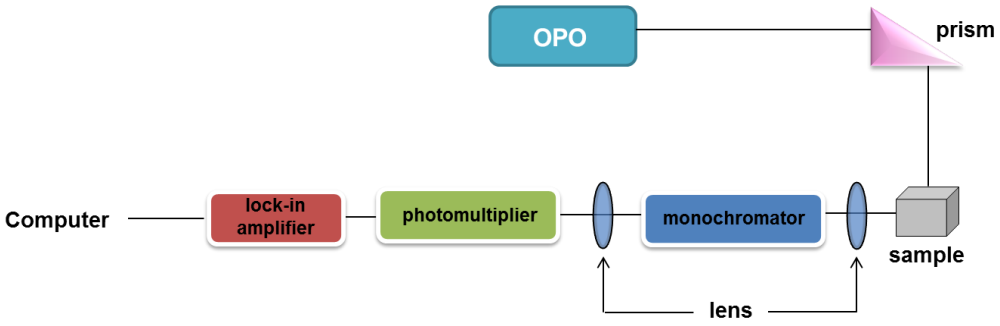

Figure 2.10. Experimental set-up used to measure the luminescence emission spectra at the *FiCMA-FiCNA* group.

By using the PL technique we have measured several samples to get information about their luminescence capabilities, their structural and chemical changes, and their emission life-times. Furthermore, the polymeric samples and the polymer-based nanocomposites were also characterized by this technique.

2.8.4.2. Cathodoluminescence (CL)

The basis of cathodoluminescence (CL) is the same of PL but using electrons instead of photons to excite the sample. CL is the emission of a photon (light) when excited by an electron beam. The energy of those emitted photons is typically in the 0.3 to 6 eV covering the range of wavelengths from the UV to the near-infrared. In the last decades, CL has developed into a powerful method for a lot of investigations in geosciences, for instance, because it allows not only a rapid identification and sometime quantification of the different mineral constituents. An important advantage of this technique is that the multimode imaging capability of the scanning electron microscope (SEM) enables the correlation of optical properties (via CL) with surface morphology (secondary electron beam) at the nanometre scale.

CL measurements were recorded at room and low (6 K) temperatures in a field emission scanning electron microscope (LEO Supra 55VP) using a Gatan Mono CL 2 system. The spectra and images were acquired using a Hamamatsu photomultiplier tube (R2228). The spectra were acquired in the 3-10 keV range using a probe current of 4-7 nA over a scanned area of 10^4 μm^2. For this characterization, the nanopowder was dispersed in an ethanol solution, and several drops of these solutions were deposited on Si substrates. For the case of polymer-based nanocomposites, the nanopowder and the polymer were dispersed in tetrahydrofuran solution and several drops were deposited also on Si substrates. The CL equipment was available at the *Department of Electrical and Computer Engineering* of the University of Sherbrooke (Canada).

By this technique we obtained information about the introduction of the active ion into the lanthanide compound and its homogeneity into the corresponding host. We followed the phase transition changes in the samples by observing the different signals, coming from the active ions, in the CL spectra.

2.9. Device Performance techniques

The final devices fabricated in this thesis were characterized by measuring both power conversion and the incident photon-to-current conversion efficiencies by Solar Simulator equipment.

2.9.1. Power conversion efficiency (η)

The power conversion efficiency (η) is calculated by the following equation:

$$\eta = FF\ \frac{(J_{sc})(V_{oc})}{P_{in}} = \frac{P_{out}}{P_{in}} \qquad \textbf{(Eq. 2.6)}$$

where J_{sc} is the short-circuit current density, V_{oc} is the open circuit voltage and *FF* is the filling factor. η is defined also simplistically as the ratio of power out (P_{out}) to power in (P_{in}). *FF* is a more sensitive parameter in comparison to J_{sc} and V_{oc}, and depends on the thickness of the active layer, and on the morphology of the interface between the cathode and the active layer. It defines the square-shaped part of the curve and can be calculated by using the following equation:

$$FF = \frac{(J_m)(V_m)}{(J_{sc})(V_{oc})} \qquad \textbf{(Eq. 2.7)}$$

where J_m and V_m are the current and voltage at maximum power. Figure 2.11 shows the typical current-voltage characteristics for dark and light current in a solar cell and illustrates the important parameters studied in the above equations.

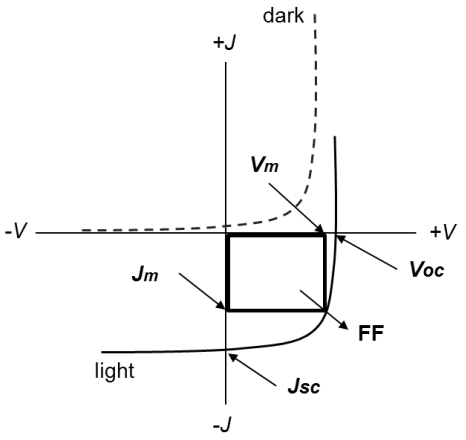

Figure 2.11. Typical current-voltage characteristics for dark and light current in solar cells.

The photovoltaic measurements were carried in a 150 W Solar Simulator from ABET© Technologies with the appropriate set of filters for the correct simulation of the AM 1.5G (AM: air mass coefficient) solar spectrum. The incident light power was adjusted at 100 $mW \cdot cm^{-2}$ with a calibrated silicon photodiode. On a clear sunny day in Florida the total power of the Sun is 100 $mW \cdot cm^{-2}$ (~ 1000 $W \cdot m^{-2}$). This has become the standard intensity at which the efficiencies of solar cells are reported and is often referred to as 1 Sun conditions. The applied potential and cell current were measured with a Keithley model 2400 digital source meter at the *ICIQ* laboratories and with a Keithley model 2420 at the *Nephos* group. The current-voltage (I-V) curve was measured automatically with a home built Labview© program.

2.9.2. Incident photon-to-current conversion efficiency (IPCE)

The incident photon-to-current conversion efficiency (IPCE (%)) or external quantum efficiency (EQE (%)) measures the spectral response of the photoelectric conversion device. Its spectrum is a plot of the ratio between the number of output electrons (current) and the input photons (irradiance) against wavelengths. IPCE is calculated by the following equation:

$$\mathrm{IPCE} = \frac{1240\ \mathrm{J_{sc}}}{\lambda\ \mathrm{P_{light}}} \qquad \textbf{(Eq. 2.8)}$$

where J_{sc} (mA·cm^{-2}) is the short-circuit current density, P_{light} (mW·cm^{-2}) is the number of incident photons, λ (nm) is the measured wavelength, and 1240 is a conversion factor. This measurement includes the losses due to external factors like the substrate absorption and reflection. The shape of the curve usually follows the absorbance spectrum of the molecules implied in the photovoltaic process.

The measurements of incident photon-to-current conversion efficiency (IPCE) were carried out with a homemade system consisting of a 150 W Xenon lamp as the light source, a motorized monochromator which changes the wavelength to be measured and a Keithley 2400 digital source meter for acquiring the current generated. An integrated sphere was employed in order to provide homogeneous monochromatic light distribution over the whole active area of the devices. These measurements were carried out at the *ICIQ* laboratories.

Chapter 3

Synthesis and characterization of doped and un-doped lanthanum compound nanoparticles

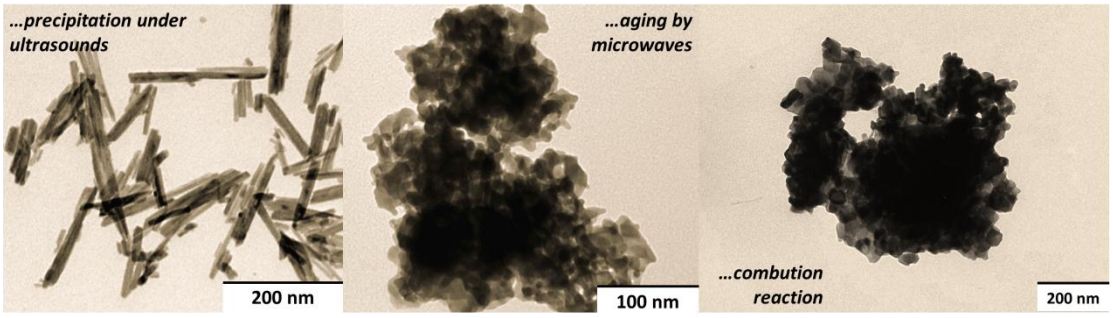

Nowadays, there are a lot of methods to synthesize nanocrystals with different sizes and morphologies, which could affect their properties. In this chapter, first we will do a brief overview about the strategies reported in the literature for preparing several doped and un-doped lanthanum compounds. After that, we will present the experimental methods that we used to synthesize un-doped lanthanum hydroxide and lanthanum oxide nanoparticles, and to prepare lanthanum oxide and lanthanum oxysulfide samples doped with Eu^{3+}, Pr^{3+} or Eu^{3+}:Bi^{3+} by different procedures. Finally, we will discuss the characterization results of the synthesized nanoparticles, obtained by different techniques (XRD, DTA-TG, N_2 physisorption, ESEM, SEM and TEM, IR, XPS).

3.1. Overview

Lanthanum compounds are of great research interest because of their prospect as catalytic materials and for optical, electrical, magnetic and ceramic applications [46-51]. The morphology and size of the nanostructures of these compounds might be different by changing their preparation procedures. Thus, using different synthesis methods one can obtain structures with shapes of nanobelts, nanowires, nanorods, etc., which can be of interest for different applications [52,53].

Rare earth hydroxides are mainly prepared by precipitation, which is based on an acid-base reaction, or by hydrothermal treatment of a reagents mixture in an autoclave. These procedures are simple, highly efficient, and with a low cost. According to the precipitation method, lanthanum hydroxide ($La(OH)_3$) is usually obtained by increasing the pH of a La^{3+}-containing solution with the addition of a base (NH_3, NaOH, KOH) at room temperature under magnetic stirring [54-56]. In the hydrothermal method, a lanthanum hydroxide gel, previously synthesized by precipitation or by the direct mixture of a lanthanum salt with base solutions, is placed in a Teflon autoclave and heated at 453-513 K for 12-48 h without stirring [57-59]. Recently, Wang et al. [60] reported the synthesis of lanthanum hydroxide by hydrothermal treatment of a mixture of lanthanum chloride and hexamethylenetetramine solutions with microwaves at 150 W and 2450 MHz at atmospheric pressure for 15 min. Microwaves heating has been shown to be an efficient, energy saving and clean synthesis method [60-63]. Lanthanum hydroxides have been also synthesized by sol-gel [64], gel combustion [65] and sonochemical [66] methods. In the sol-gel procedure, the starting solution is prepared by dissolving La_2O_3 in an aqueous solution of nitric acid and after stirring at 363 K, a gel is formed by adding polyethylene glycol (PEG). Based on the same idea, in the gel combustion method the gel formed is continuously heated until it self-ignited. When lanthanum hydroxide is precipitated with the addition of a base while using a multiwave ultrasonic generator, the method is called sonochemical.

Lanthanum oxide (La_2O_3) is often synthesized by thermal decomposition of nitrates, hydroxides or other thermally degradable lanthanum compounds [67,68]. Dehydration of lanthanum hydroxide to lanthanum oxide is the most common technique used [69,70].

Dopant materials, better known as activators ions in luminescent materials, can be introduced in lanthanum compounds, which act as hosts. Lanthanide doped lanthanum oxide nanocrystals (Ln^{3+}:La_2O_3), also called nanophosphors due to their luminescence properties, have been usually prepared by the combustion as well as the sol-gel Pechini methods. The combustion method, also known as propellant synthesis, is a highly promising way for obtaining the desired phase in a very short time, at low cost and using simple equipment. It consists in the exothermic reaction between metal nitrates and an organic fuel [71]. For example, in the case of preparing lanthanum oxide nanocrystals by using glycine, the synthesis reaction could be expressed as:

$6M(NO_3)_3 + 10NH_2CH_2COOH + 18O_2 \rightarrow 3La_2O_3 + 5N_2 + 18NO_2 + 20CO_2 + 25H_2O$

where M = La, Eu. Different organic fuels, such as citric acid, urea, glycine, carbohydrazide, oxalyl dihydrazide, etc. have been used as reducers for combustion synthesis [72] and apart from Eu^{3+}:La_2O_3 nanoparticles [71,73], Yb^{3+}:Er^{3+}:La_2O_3 and Er^{3+}:La_2O_3 [74] nanoparticles have been also obtained by this method.

Regarding sol-gel methods, first, a mixture of cations is formed in citric acid as an organic complexing agent and ethylene glycol solution. Second, the cations become a chelate. Third, the polymeric resin forms, and finally it decomposes at 573 K. Galceran et al. [75], based on the sol-gel Pechini [76], adapted the sol-gel modified Pechini method by using ethylenediaminetetraacetic acid (EDTA) as a complexing agent during the synthesis for preparing $KGd(WO_4)_2$ and $KYb(WO_4)_2$ nanocrystals. Nowadays, other nanocrystals such as Eu^{3+}:GdOF [77], Ce^{3+}:$Y_3Al_5O_{12}$ [78] and $Mn^{2+/4+}$:$YAlO_3$ [79] have been prepared by the sol-gel Pechini method. Pr^{3+} has been also introduced by sol-gel methods in several hosts such as yttrium aluminium garnet (YAG) [75], $LaAlO_3$ [81] and Y_2O_3 [82]. In general, sol-gel methods allow a molecular mixing of constituents, leading to good chemical homogeneity, an increase in the reaction rate and a decrease of the crystallization temperature [83]. More recently, Ln^{3+}:La_2O_3 materials have been synthesized by hydrothermal treatment of a mixture of doping agent (Ln^{3+}) and lanthanum salts in basic medium followed by calcination using a furnace [58,84] or a microwave oven [55].

Lanthanide doped rare earth oxides can be also prepared by co-precipitation and spray deposition methods. Eu^{3+}:Y_2O_3 and Eu^{3+}:Lu_2O_3 nanopowders have been obtained by the co-precipitation procedure, which consists of adding basic medium to a mixture of doping agent and lanthanide salts to precipitate the hydroxides, which are transformed to oxides after calcination [85,86]. Pr^{3+} doped La_2O_3 nanocrystals have been synthesized by the co-precipitation method [87] or thermal decomposition of co-precipitate oxalates followed by firing at 1250 ºC for 10 h under a N_2:H_2 (3:1) atmosphere [88]. From the best of our knowledge, the co-precipitation method has not been used for the synthesis of Eu^{3+}:La_2O_3 nanoparticles. The spray deposition method, which is especially useful for preparation of films with large areas, consists basically in spraying a $LaCl_3$ solution through a nozzle onto the preheated substrates [89].

Finally, another well-established technique to dope materials is the wetness impregnation method where a doping salt is added drop by drop to a material until filling its pore volume, followed by drying and calcination processes. This method has been widely used for preparing catalysts, such as Ir/La_2O_3 [90], or lanthanide-loaded Ag_3VO_4 catalysts (Ln^{3+}-Ag_3VO_4, Ln=Nd, Sm, and Eu) [91]. However, there are not references about the use of the wetness impregnation method to synthesize lanthanide doped lanthanum oxides for luminescence purposes.

Other lanthanum compounds of interest as nanophosphor hosts are lanthanum oxysulfides. On the whole, the traditional method to prepare lanthanide oxysulfide samples is the solid-state reaction of the lanthanide oxide with elemental sulphur and by refluxing $Na_2CO_3/K_3PO_4/Na_2S_2O_3$ at high temperatures [92]. Peng et al. [93] reported that working with Eu^{3+}:La_2O_2S in the nanoscale size becomes troublesome. This explains the few references found about the synthesis of these materials. For instance, Dhanaraj et al. [94] used a two-step solution-gel polymer thermolysis method to prepare Eu^{3+}:Y_2O_2S. The use of sodium thiosulfate ($Na_2S_2O_3$) as a sulfur source led to the introduction of sodium impurities, which might influence the luminescent properties of Eu^{3+}. Bang et al. [95] reported in 2004 the fabrication of Eu^{3+}:La_2O_2S by the combustion method using dithiooxamide ($CSNH_2)_2$) as the sulfur source. Thus, the corresponding nitrates were dissolved in water and the $CSNH_2$ was added, mixed and ground together with the nitrates. After 24 h dehydrating in a desiccator, the mixture was heated in an air tube furnace at 573-623 K and the decomposition reaction, forming the precursor, occurs. This method is an efficient route to synthesize nanocrystals because of its advantage with direct crystallization of nanoscaled particles, low process temperature, and reduced time consumption. However, $(CSNH_2)_2$ is expensive and the size of the nanocrystals obtained was large (100-200 nm). Thus, a good approach was the novel combustion method developed by Luo et al. in 2005 [96] to overcome the shortcoming of the above solid combustion method. That novel method is called ethanol-assisted solution combustion (EASC) and uses ethanol as the preignition fuel and inexpensive thioacetamide as the sulphur-containing organic fuel. These reagents are mixed with the corresponding nitrates in an ethanol solution and a small amount of distilled water in a crucible. In order to obtain the precursor powders, the crucible is introduced into a furnace pre-heated at 673 K for 20 min. Nanoparticles such as Yb^{3+}:Pr^{3+}:La_2O_2S [97] and Eu^{3+}:Y_2O_2S [98] have been prepared by the EASC method.

Recently, the blue emissions originating from the transition in Bi^{3+} observed from Bi-activated oxide phosphors (activated by ions with ns^2 configuration) have attracted much attention for phosphor applications [99-102]. However, the usable host materials of Bi-activated oxide phosphors are severely limited because the Bi^{3+} ion radius of 0.102 nm is relatively large. Bi^{3+} is mainly introduced as doping or co-doping agent by deposition or EASC methods. There are no references about the use of the Pechini method to incorporate Bi^{3+} in La_2O_3 or La_2O_2S hosts.

3.2. Synthesis of doped and un-doped lanthanum compounds nanoparticles

First of all, we will explain the methods that we used to prepare different un-doped and doped lanthanum compound nanoparticles: un-doped lanthanum hydroxide, un-doped lanthanum oxide and doped and co-doped lanthanum compounds (lanthanum oxide and lanthanum oxysulfide).

3.2.1. Synthesis of lanthanum hydroxide ($La(OH)_3$) and lanthanum oxide (La_2O_3)

Synthesis of $La(OH)_3$ samples

Five samples were prepared by the precipitation method using a 0.04 M $La(NO_3)_3 \cdot 6H_2O$ (Fluka, ≥ 99 %) aqueous solution and ammonia (VWR, 28 %) as the precipitation agent. The first (sample *Pc*) was precipitated at constant pH (pH=10 ± 0.1) and room temperature by adding simultaneously drop by drop, under magnetic stirring, the lanthanum nitrate aqueous solution and a 2 M ammonia solution to an aqueous solution of NH_4NO_3 (Fluka, > 99 %), which acted as buffer (see Figure 3.1).

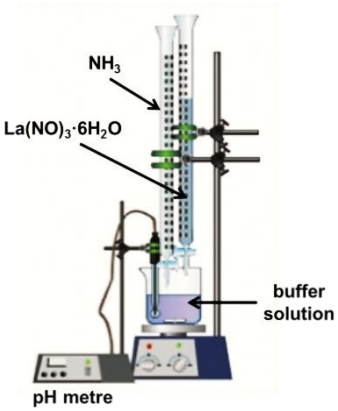

Figure 3.1. Scheme of the process to synthesize nanoparticles by the precipitation method at constant pH.

Other three samples were precipitated at variable pH by adding a 2 M ammonia solution drop by drop to the lanthanum nitrate aqueous solution until achieving pH=10 at room temperature under magnetic stirring (sample *Pv*), at 348 K under magnetic stirring (sample *Pvt*) and at room temperature but using ultrasounds instead of magnetic stirring (sample *Pvu*). Lastly, one more sample was precipitated by bubbling NH_3 gas (Carburos Metálicos, 1% NH_3: 99 % N_2) through the lanthanum nitrate aqueous solution until achieving pH= 10 (sample *Pvb*). After precipitation, all samples were filtered, washed with deionised water several times, and dried in an oven overnight.

Another series of samples were prepared by the conventional hydrothermal method as follows: 1 g of $La(NO_3)_3 \cdot 6H_2O$ was dissolved into 120 mL of deionised water. After 10 min under magnetic stirring, 4 g of KOH (Sigma-Aldrich, > 85 %) was added, thus leading to a white precipitate (sample *H-0*), which was transferred into a Teflon autoclave in a furnace (see Fig. 3.2(a)) and heated at 393 K for 1, 3, 6, 12, 24, and 48 h (samples *H-1*, *H-3*, *H-6*, *H-12*, *H-24* and *H-48*, respectively). Four more samples were synthesized by the hydrothermal method but using a laboratory microwave oven (Milestone Ethos-Touch Control) for heating. The initial white precipitate obtained (sample *H-0*) was autoclaved inside the microwave

oven (see Fig. 3.2(b)) at 323 K for 5 min, 15 min and 60 min (samples *MwH-323-5*, *MwH-323-15* and *MwH-323-60*, respectively), and at 353 K for 60 min (sample *MwH-353-60*). All samples were filtered, washed with deionised water several times, and dried in an oven overnight.

Table 3.1. Preparation conditions of un-doped lanthanum hydroxide samples synthesized by the precipitation and hydrothermal methods.

Sample	Method	Precipitating agent	Precipitation temperature	Aging	
				Heating method	Temperature/ time
Pc	Precipitation at constant pH	NH_3 (aq)	RT	---	
Pv	Precipitation at variable pH	NH_3 (aq)	RT	---	
Pvu	Precipitation at variable pH with ultrasounds	NH_3 (aq)	RT	---	
Pvt	Precipitation at variable pH with temperature	NH_3 (aq)	348 K	---	
Pvb	Precipitation at variable pH	NH_3 (g)	RT	---	
H-0	Instantaneous precipitation	KOH (aq)	RT	---	
H-1	Hydrothermal	KOH (aq)	RT	Oven	393 K/ 1 h
H-3	Hydrothermal	KOH (aq)	RT	Oven	393 K/ 3 h
H-6	Hydrothermal	KOH (aq)	RT	Oven	393 K/ 6 h
H-12	Hydrothermal	KOH (aq)	RT	Oven	393 K/ 12 h
H-24	Hydrothermal	KOH (aq)	RT	Oven	393 K/ 24 h
H-48	Hydrothermal	KOH (aq)	RT	Oven	393 K/ 48 h
MwH-323-5	Hydrothermal	KOH (aq)	RT	Microwaves	323 K/ 5 min
MwH-323-15	Hydrothermal	KOH (aq)	RT	Microwaves	323 K/ 15 min
MwH-323-60	Hydrothermal	KOH (aq)	RT	Microwaves	323 K/ 60 min
MwH-353-60	Hydrothermal	KOH (aq)	RT	Microwaves	353 K/ 60 min

RT: room temperature.

Table 3.1 summarizes the preparation conditions of samples synthesized by the precipitation and hydrothermal methods.

Figure 3.2. Pictures showing the different hydrothermal methods: (a) conventional and (b) microwaves.

Synthesis of La_2O_3 samples

Lanthanum oxides were obtained by calcining several representative synthesized $La(OH)_3$ samples (*Pv*, *Pvu*, *H-0*, *H-1*, *H-48* and *MwH-323-5*) at 1173 K for 2 h. La_2O_3 samples were named as *C* followed by the name of the lanthanum hydroxide sample, e.g. *CH-1* was the sample obtained by calcining *H-1*.

3.2.2. Synthesis of europium doped lanthanum oxide (Eu^{3+}:La_2O_3)

All the Eu^{3+}:La_2O_3 samples contained 5 mol% Eu^{3+} because this percentage was that one shown by Park et al. [103] to be the optimum one to obtain less quenching concentration effects and consequently better luminescence efficiency.

Wetness impregnation method

First, we prepared $La(OH)_3$ nanoparticles by the conventional hydrothermal method at 393 K for 24 h (sample *H-24*). To dope by the impregnation method, it was necessary to know the pore volume of this $La(OH)_3$ sample. To do that, deionised water was added drop by drop until the sample was not able to absorb more water. The pore volume obtained experimentally for *H-24* was 0.65 $ml \cdot g^{-1}$. The relation coefficient between $La(OH)_3$ and $Eu(NO_3)_3$ was 0.118 and was obtained taking into account that the mol % in the final product must be 0.95 and 0.05 for La^{3+} and Eu^{3+}, respectively. To calculate the amount in grams of $Eu(NO_3)_3 \cdot 5H_2O$ needed to prepare the aqueous solution in the volumetric flask, we used the following equation:

$$\text{flask volume (ml)} * \frac{\text{relation coefficient}}{\text{pore volume } (\frac{\text{ml}}{\text{g}})} \qquad \textbf{(Eq. 3.1)}$$

0.65 ml of the europium nitrate solution were added drop by drop to 1 g of sample *H-24*. After impregnation, the sample was dried in an oven at 353 K for 8 h. This impregnated sample was named as *Eu^{3+}-H-24-IMP*. The sample obtained by calcination of *Eu^{3+}-H-24-IMP* at 1173 K for 2 h, was named *Eu^{3+}-CH-24-IMP*.

Co-precipitation and hydrothermal methods

Several 5 mol % of Eu^{3+} doped $La(OH)_3$ samples were synthesized by the co-precipitation and hydrothermal methods following the same procedure used to prepare several un-doped $La(OH)_3$ samples but starting with a mixture or europium and lanthanum nitrate salts. To distinguish these doped samples from the un-doped ones, we added the symbol of *Eu^{3+}* ion in the identification name. Therefore, whether sample *H-24* was un-doped, *Eu^{3+}-H-24* is the corresponding doped one.

Table 3.2 summarizes the preparation conditions of the Eu^{3+}:$La(OH)_3$ samples synthesized by these two methods.

Table 3.2. Preparation conditions of Eu^{3+}-doped lanthanum hydroxide samples synthesized by co-precipitation and hydrothermal methods.

Sample	Method	Precipitating agent	Precipitation temperature	Aging	
				Heating method	Temperature/ time
Eu^{3+}-Pv	Co-precipitation at variable pH	NH_3 (aq)	RT	---	
Eu^{3+}-Pvu	Co-precipitation at variable pH with ultrasounds	NH_3 (aq)	RT	---	
Eu^{3+}-H-0	Instantaneous co-precipitation	KOH (aq)	RT	---	
Eu^{3+}-H-1	Hydrothermal	KOH (aq)	RT	Oven	393 K/ 1 h
Eu^{3+}-H-24	Hydrothermal	KOH (aq)	RT	Oven	393 K/ 24 h
Eu^{3+}-H-48	Hydrothermal	KOH (aq)	RT	Oven	393 K/ 48 h
Eu^{3+}-MwH-323-5	Hydrothermal	KOH (aq)	RT	Microwaves	323 K/ 5 min
Eu^{3+}-MwH-323-15	Hydrothermal	KOH (aq)	RT	Microwaves	323 K/ 15 min

RT: room temperature.

In order to obtain the oxide phases, all these samples were calcined at 1173 K for 2 h. Thus, following the same rules, the samples were named with a *C* when they were calcined (e.g. *Eu^{3+}-CH-24*).

Sol-gel Pechini method

Other Eu^{3+}:La_2O_3 samples were synthesized by the sol-gel Pechini method (see Fig. 3.3). First, La_2O_3 and Eu_2O_3 were dissolved in hot acid. The acids used were either HNO_3 (Merck, 65%) or HCl (VWR, 35%). The solution were let, under stirring, to generate the corresponding nitrate ($La(NO_3)_3$ and $Eu(NO_3)_3$) or chloride ($LaCl_3$ and $EuCl_3$) reagents. After the solution was dried at 358 K to remove the excess amount of acid, the salts were dissolved in deionised water. We added an organic acid (OA) to this solution with a molar ratio [OA]/[Metal] = 1 where [Metal] is the concentration of lanthanum and europium in the solution. The OAs used were either ethilenediaminetetracetic (EDTA, Aldrich, 99%) or citric (CA, Fluka, 99.5%) acids. Then a esterification agent (EA) was added with a molar ratio [OA]/[EA] equal to 2 or equal to 1 depending on the OA used, while stirring and heating the solution. The EAs used were either ethylene glycol (EG, Sigma-Aldrich, 99.8%) or polyethylene glycol (PEG, Sigma-Aldrich, M.W. 400).

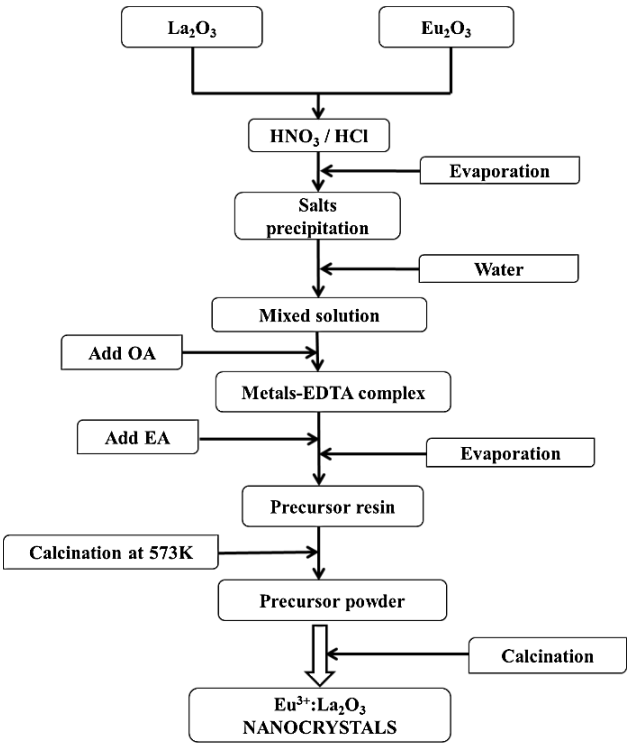

Figure 3.3. Flow scheme of the synthesis of Eu^{3+}:La_2O_3 nanoparticles by the sol-gel Pechini method.

In previous works, Galceran et al. [75] found that the use of molar ratios [OA]/[Metal] < 1 affects the homogeneity in the chelation of metals by the OA due to an insufficient number of molecules to chelate metal cations. For molar ratios [OA]/[Metal] > 1 the amount of organics to be removed in the final calcination process was excessive. Then, the molar ratio [OA]/[EA] was determined according to the esterification reaction: since EDTA has four carboxylic acids groups and EG has two alcohol groups we need 2 molecules of EG to react with 1 molecule of EDTA. In the case of using CA as organic acid and PEG as esterification agent, we worked with a molar ratio [OA]/[EA] equal to 1 because CA has only two carboxylic acids groups and PEG has also two alcohol groups.

Thus, four different samples were synthesized by the sol-gel Pechini method and were named depending on the starting reagents and the organic acid and esterification agents used: *Eu^{3+}-Pech1*, *Eu^{3+}-Pech2*, *Eu^{3+}-Pech1B* and *Eu^{3+}-Pech2B*. The preparation conditions of these precursor powders are summarized in Table 3.3. All these precursor powders were obtained after calcining the initial precursor resin at 573 K for 3 h.

Table 3.3. Preparation conditions of Eu^{3+}doped precursor powders by the sol-gel Pechini method.

Sample name	Method	Starting reagents	Organic acid	Esterification agent
Eu^{3+}-Pech1	Sol-gel Pechini	HNO_3 (aq)	EDTA	EG
Eu^{3+}-Pech2	Sol-gel Pechini	HNO_3 (aq)	CA	PEG
Eu^{3+}-Pech1B	Sol-gel Pechini	HCl (aq)	EDTA	EG
Eu^{3+}-Pech2B	Sol-gel Pechini	HCl (aq)	CA	PEG

EDTA: ethilenediaminetetracetic; CA: citric acid; EG: ethylene glycol; PEG: polyethylene glycol

Finally, the precursor powders were calcined at different temperatures, between 573 K and 1273 K, in air atmosphere for 2 h to obtain nanoparticles of Eu^{3+}:La_2O_3. After calcination, samples were named by adding *C* to the name of the precursor powder and by indicating the temperature of calcination at the end of the nomenclature, e.g. *Eu^{3+}-CPech1*-573 was the sample obtained by calcining *Eu^{3+}-Pech1* at 573 K for 2 h.

3.2.3. Synthesis of praseodymium doped lanthanum oxide (Pr^{3+}:La_2O_3)

Lanthanum oxide doped with 0.5, 1, 3, 5 mol % of Pr^{3+} samples were synthesized by the sol-gel Pechini method. Here, lanthanum oxide and praseodymium oxide (Aldrich, 99.9%) were dissolved in HNO_3 and the reagents used for preparing these samples were EDTA as organic acid and EG as esterification agent. The next steps were exactly the same explained above to synthesize Eu^{3+}:La_2O_3 samples.

Pr^{3+} doped La_2O_3 nanoparticles were named as *(x%)Pr^{+3}-Pech1* indicating the molar amount *x* of Pr^{3+} in each case. The calcined samples were distinguished by adding *C* to the name of

the precursor powder, e.g. (*x%*)Pr^{3+}*-CPech1* was the sample obtained by calcining (*x%*)Pr^{3+}*-Pech1* at 1273 K for 2 h.

3.2.4. Synthesis of europium doped lanthanum oxysulfide (Eu^{3+}:La_2O_2S)

La_2O_2S doped with 5 mol% of Eu^{3+} nanoparticles were obtained by the ethanol-assisted solution combustion method (EASC). In a small zirconia crucible, 1.2 g of $La(NO_3)_3 \cdot 6H_2O$ (Fluka, ≥ 99.9%), 0.062 g of $Eu(NO_3)_3 \cdot 5H_2O$ (Sigma-Aldrich, ≥ 99.9%) and 0.9 g of thioacetamide (CH_3CSNH_2, Sigma-Aldrich, ≥ 99.0 %) were added and dissolved using a small amount of ethanol and distilled water (0.0025 M). The solution was let 1 h stirring under 353 K. Then, the zirconia crucible was introduced into a tubular furnace pre-heated at 673 K for 20 min and the combustion reaction was immediately carried out as confirmed by observing the yellow-brown fumes, coming from the by-products. Figure 3.4 shows the zirconia crucible containing the porous powder after the combustion reaction. The sample obtained was named as *Eu^{3+}:La_2O_2S*.

Figure 3.4. Photograph showing the zirconia crucible containing the final product.

3.2.5. Synthesis of europium and bismuth co-doped lanthanum oxide and lanthanum oxysulfide (Eu^{3+}:Bi^{3+}:La_2O_3, Eu^{3+}:Bi^{3+}:La_2O_2S)

Samples Eu^{3+}:Bi^{3+}:La_2O_3 co-doped with 5% of Eu^{3+} (as for all doped samples) and either 1% or 3% of Bi^{3+}, were prepared following the sol-gel Pechini method explained above but now adding also the $Bi(NO_3)_3$ (Aldrich, 99.9%) reagent while the other nitrates were already formed by HNO_3. Samples were named as *Eu^{3+}:(1%)Bi^{3+}-Pech1* and *Eu^{3+}:(3%)Bi^{3+}-Pech1* and adding a *C* in the case of calcined samples, e.g. *Eu^{3+}:(1%)Bi^{3+}-CPech1* was the sample obtained by calcining *Eu^{3+}:(1%)Bi^{3+}-Pech1* at 1173 K for 2 h.

Eu^{3+}:Bi^{3+}:La_2O_2S co-doped with 5% of Eu^{3+} and 1% of Bi^{3+} nanoparticles were prepared by the EASC method explained above and adding also the $Bi(NO_3)_3$ reagent in the starting mixture with ethanol. This sample was named as *Eu^{3+}:Bi^{3+}:La_2O_2S*.

3.3. Characterization of the synthesized nanoparticles

In the next part of this chapter we will expose and discuss the results obtained from the characterization of the un-doped and doped lanthanum compound samples synthesized by different methods. The techniques used were: X-Ray diffraction (XRD) mainly to identify the crystalline phases but also to calculate the crystallite size of the samples, X-ray photoelectron spectroscopy (XPS) to obtain information about the surface and Eu/La ratio for doped samples, nitrogen physisorption to obtain the pore size and BET area of the hosts, differential thermal and thermogravimetric analysis (DTA-TGA) to characterize the thermal evolution of the precursors, infrared spectroscopy (IR) to study the presence of europium for doped samples, and microscopy techniques (ESEM, SEM and TEM) to observe the morphology and the aggregation level of the synthesized nanoparticles.

3.3.1. Characterization of lanthanum hydroxide ($La(OH)_3$) and lanthanum oxide (La_2O_3)

Lanthanum hydroxide samples

XRD patterns of the samples obtained by precipitation, conventional hydrothermal aging, and by microwaves hydrothermal aging (see preparation conditions in Table 3.1) are shown in Fig. 3.5, 3.6 and 3.7, respectively.

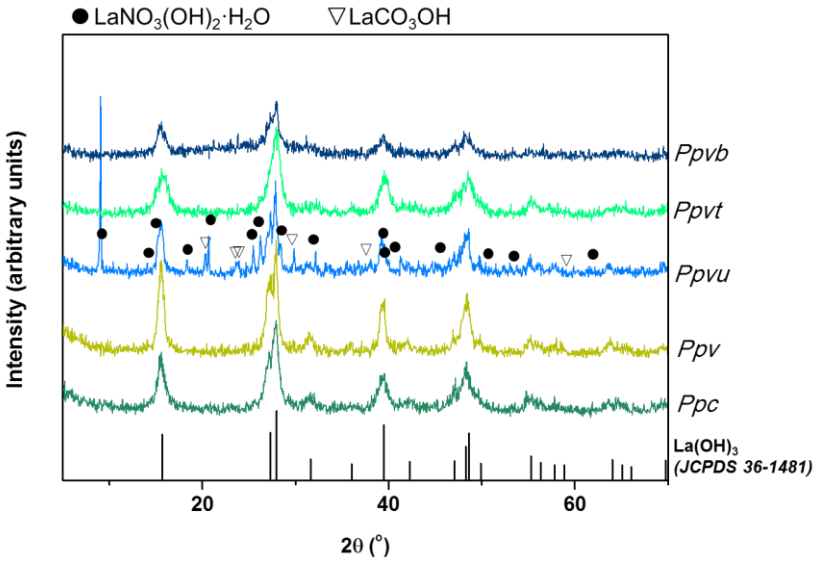

Figure 3.5. X-ray diffraction patterns of the samples prepared by the precipitation method.

The lanthanum hydroxide phase was observed for all samples with different crystallinity degree. Additionally, sample *Pvu*, precipitated at variable pH under ultrasounds, also presented two additional crystalline phases which were identified as $LaNO_3(OH)_2 \cdot H_2O$ and

$LaCO_3(OH)$ (Fig 3.5) according to the JCPDS files 37-1190 [104] and 49-0981 [105], respectively. Cavitation waves movement can favour the solubilisation of atmospheric CO_2, which reacts with lanthanum nitrate resulting in a carbonate/hydroxyl phase while hindering the complete hydroxylation of lanthanum nitrate.

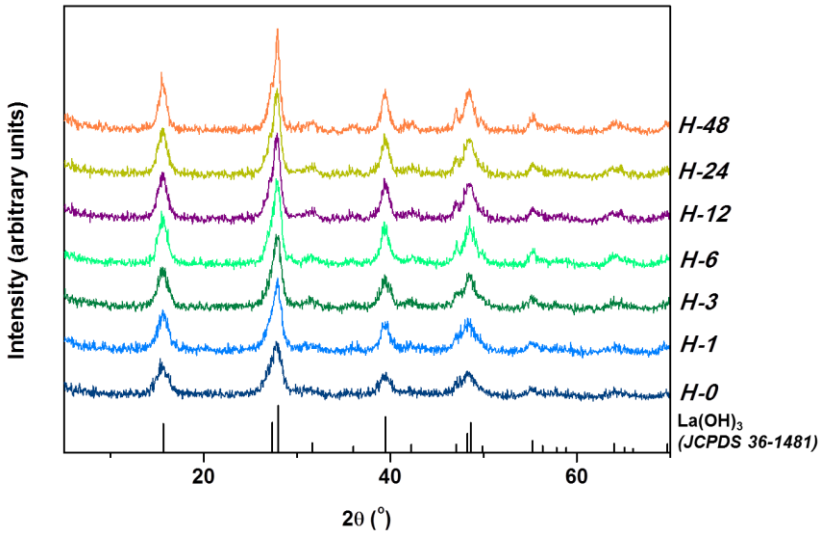

Figure 3.6. X-ray diffraction patterns of the samples aged by conventional hydrothermal heating.

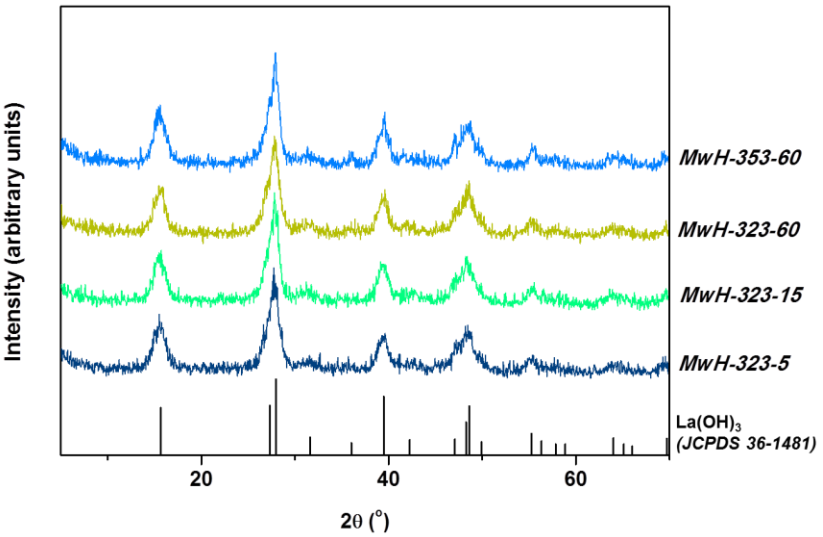

Figure 3.7. X-ray diffraction patterns of the samples aged by microwaves hydrothermal heating.

Crystallite size of the samples was calculated from the (100) and (201) peaks of the XRD patterns, using the Scherrer's equation (Table 3.4).

Regarding the crystallite size of the samples obtained by precipitation (*Pc*, *Pv*, *Pvu*, *Pvt* and *Pvb*), the gel precipitated at 348 K showed the lowest crystallite size. This could be related to

a lower polycondensation of the colloidal particles initially formed in agreement with the less water loss observed by TGA for this gel compared with the rest of precipitated samples (later shown in Table 3.5). At higher precipitation temperature, a higher solubilisation of the hydroxylated species should be expected, and therefore, a higher difficulty for polycondensating the insoluble colloidal species initially formed can be expected. The resulting gel contains less water, and consequently, has smaller crystallite sizes. Sample *H-0*, obtained by direct precipitation with KOH and used as the starting powders for conventional and microwaves aging, had a lower crystallite size than the samples obtained by precipitation with ammonia except for the *Pvt* sample. This can be explained by the slower precipitation rate of the samples precipitated with ammonia, which were precipitated drop by drop, allowing for a higher crystallization degree of the sample than that obtained for the *H-0* sample, which was obtained by instantaneous precipitation.

Table 3.4. Crystallite sizes of several samples.

Sample	$La(OH)_3$ crystallite size (nm)[a]	Sample	$La(OH)_3$ crystallite size (nm)[a]
Pc	10.6	*H-6*	9.6
Pv	13.5	*H-12*	9.3
Pvu	13.7	*H-24*	10.4
Pvt	8.1	*H-48*	11.7
Pvb	11.6	*MwH-323-5*	8.0
H-0	8.2	*MwH-323-15*	8.1
H-1	8.2	*MwH-323-60*	8.3
H-3	8.7	*MwH-353-60*	10.0

[a] Calculated from the (100) and (201) peaks of the XRD patterns.

Aging is the spontaneous evolution of a gel structure, which results from an ordering of its crystalline state. For the samples aged by the conventional hydrothermal method, the crystallite size of $La(OH)_3$ increased with the aging time. For the samples aged by the hydrothermal method under microwave irradiation, an increase in the temperature of aging from 323 to 353 K led to the a higher crystallite size (10 nm). Therefore, an increase of aging temperature and aging time favoured crystallization of lanthanum hydroxide, as expected.

In order to study the thermal decomposition of the lanthanum hydroxides prepared by different methods, TGA analyses of all samples were performed. Figure 3.8 shows the TGA curves obtained for several representative lanthanum hydroxide samples whereas Table 3.5 depicts the maximum temperature for each weight loss (WL) for all of them. Thermograms of the samples obtained by precipitation (*Pc*, *Pv*, *Pvu*, *Pvt* and *Pvb*) showed similar profiles (e.g. *Pc* and *Pvu* in Fig. 3.8) with three temperature intervals corresponding to three significant weight losses (defined as I, II and III in Table 3.5): the first between 573 K and 773 K, the second between 773 K and 1000 K and the third between 1000 K and 1200 K. The TGA curve of the *H-0* sample, prepared by instantaneous precipitation, also exhibited three main

weight losses (Fig. 3.8) but the temperature maximum of the second and third weight loss shifted to lower and higher temperature values¸ respectively, than those of the precipitated samples previously commented (Table 3.5).

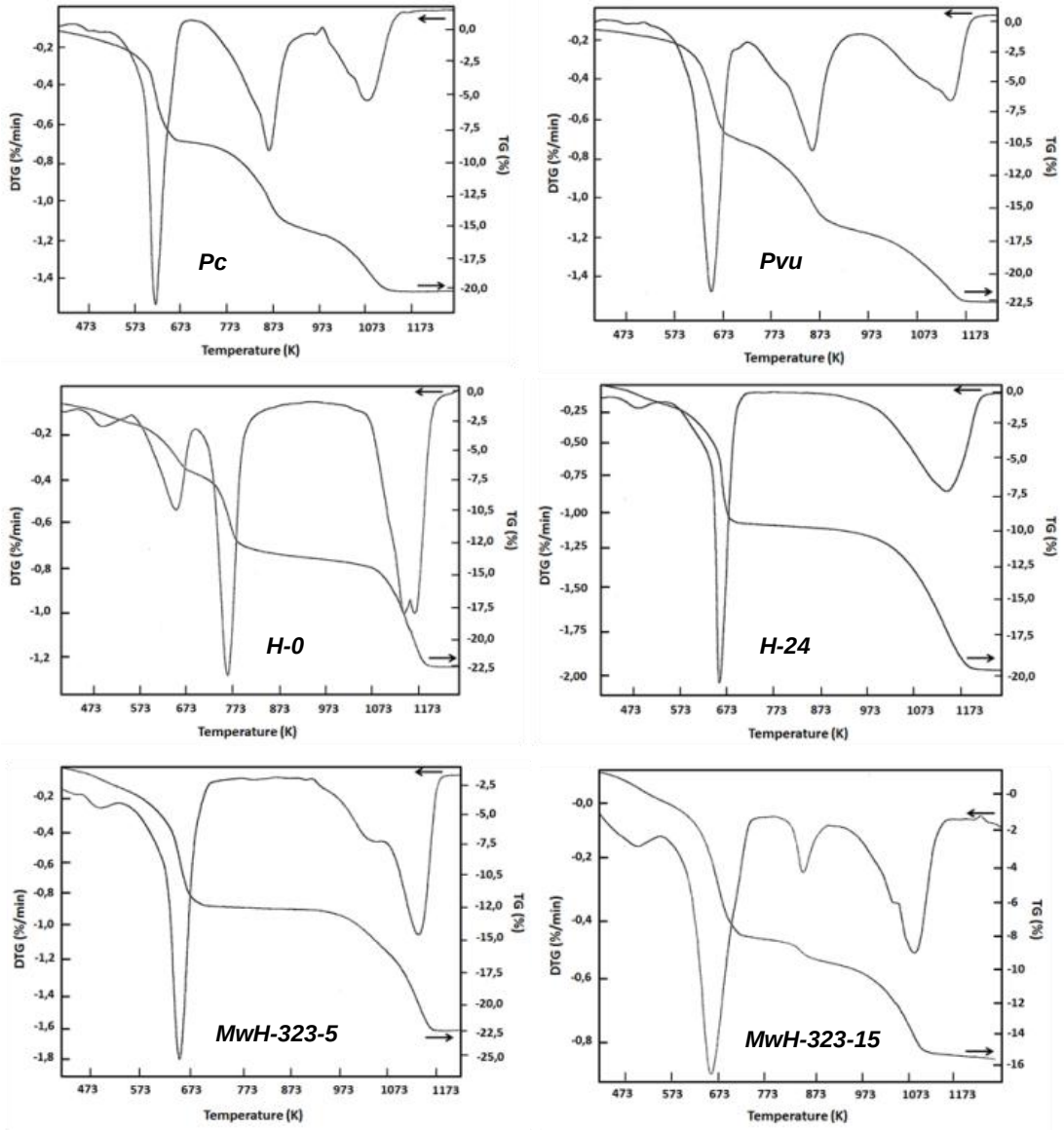

Figure 3.8. TGA curves of several $La(OH)_3$ representative samples.

Interestingly, samples obtained by aging *H-0* by conventional heating at 393 K at different time intervals only showed two weight losses at similar temperature intervals than those of the weight losses I and III of the rest of samples (e.g. *H-24* in Fig. 3.8, Table 3.5). Additionally, the TG curve of the sample obtained by aging the *H-0* sample with microwaves at 323 K for 5 min also had two weight losses (Fig. 3.8, Table 3.5) but when a higher preparation temperature (353 K) and/or time are used, again three main weight losses were detected (e.g. *MwH-323-15* in Fig. 3.8, Table 3.5).

Table 3.5. Characterization of some $La(OH)_3$ precursors by TGA technique.

Sample	Tg (K)[a]			Total weight loss (%)[b]
	WL I	WL II	WL III	
Pc	613	868	1073	21.0
Pv	614	863	1063	22.7
Pvu	658	873	1153	23.0
Pvt	658	798	1133	18.5
Pvb	618	863	1043	22.5
H-0	658	763	1158	22.5
H-1	668	-	1128	18.0
H-3	668	-	1148	20.0
H-6	668	-	1128	18.5
H-12	668	-	1138	19.5
H-24	668	-	1173	19.0
H-48	668	-	1153	17.5
MwH-323-5	658	-	1043/1128	22.5
MwH-323-15	663	848	1088	15.5
MwH-323-60	658	813	1098	15.0
MwH-353-60	673	833	1073	12.0

[a] Tg is the maximum temperature for each weight loss obtained from TGA curves.
WL: weight loss; [b] This value includes the initial loss of adsorbed water of the sample.

In the literature, the thermal decomposition of $La(OH)_3$ was divided in three stages [106,107]. The first one was related to the dehydration of free and physically adsorbed molecular water associated with the powder, the second one was attributed to the $La(OH)_3 \rightarrow LaOOH + H_2O$ reaction and the third one was owed to the $LaOOH \rightarrow La_2O_3 \cdot 1/2\ H_2O \rightarrow La_2O_3$ reaction.

In order to identify the intermediate phase or phases for our samples, we analysed the thermal evolution of several representative samples from room temperature to 1073 K by XRD. Fig. 3.9 shows the XRD patterns of several representative samples after calcination at 873 K (temperature related to the second weight loss). The most significant result is that in any case we observed the formation of LaOOH but the formation of peaks corresponding to the lanthanum carbonate phase: $La_2O_2CO_3$. For calcined *Pvu*, this $La_2O_2CO_3$ phase proceeded

from the three phases present in the starting gel: $La(OH)_3$, $LaCO_3(OH)$ and $LaNO_3(OH)_2 \cdot H_2O$ (see Fig. 3.5). It is well known that the decomposition of $LaNO_3(OH)_2 \cdot H_2O$ in air occurs through the formation of $LaONO_3$, which transforms to $La_2O_2CO_3$ at temperatures above 773 K [108]. The presence of these additional phases in the initial gel could justify the higher temperature maximum of the weight loss II observed in the TG of the *Pvu* sample when compared with the other precipitated samples (see Table 3.5).

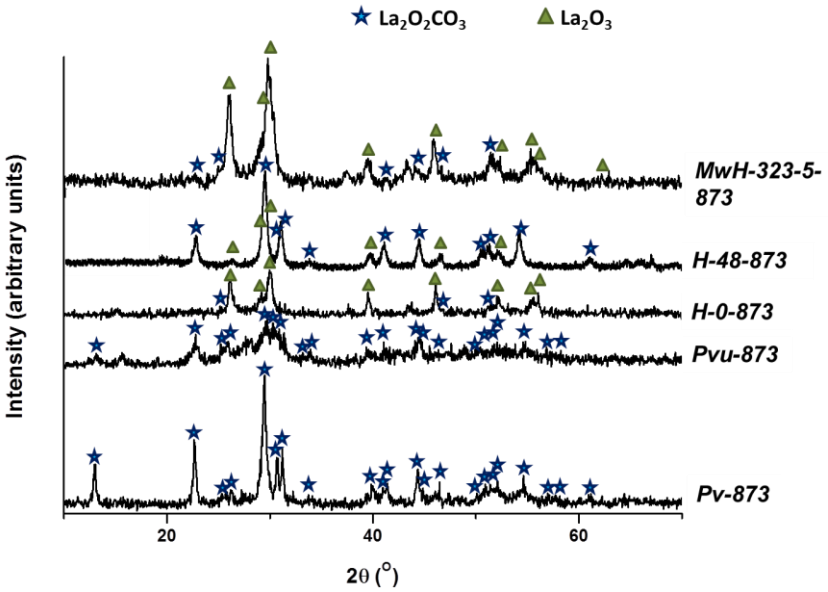

Figure 3.9. XRD patterns of several lanthanum hydroxide samples calcined at 873 K for 2h.

For the samples prepared by hydrothermal aging (e.g. *H-24*, *MwH-323-15*, Fig. 3.9) several peaks corresponding to $La(OH)_3$ were detected in the XRD pattern obtained after calcination at 873 K. Therefore, the calcination process of lanthanum hydroxide proceeds through two steps, assuming that the first weight loss is due to the dehydration of free and physically adsorbed molecular water:

$$2\ La(OH)_3 + CO_2 \xrightarrow{T = 723\ K} La_2O_2CO_3 + 3H_2O \text{ (Weight loss II)}$$

$$La_2O_2CO_3 \xrightarrow{T = 938\ K} La_2O_3 + CO_2 \text{ (Weight loss III)}$$

The presence of this intermediate carbonate phase was also reported by Zhu et al. [109] who obtained lanthanum hydroxide nanorods by precipitation with hydrazine and later aging.
Interestingly, the samples aged hydrothermally with microwaves showed a lower maximum temperature at the WL III than those aged by conventional heating (see Table 3.5). This could be attributed to the higher surface area and lower crystallite size of these samples, which could favour a faster formation of the lanthanum oxide phase. For the samples aged by conventional heating, and increased in the aging time led to a slight higher maximum

temperature for the WL III (see Table 3.5). This can be associated to the slight higher crystallite sizes obtained for longer aging times (see Table 3.5).

N_2 adsorption-desorption isotherms of all the lanthanum hydroxide samples were identified as type IV, corresponding to mesoporous materials (see Fig. 3.10). Longer aging time of the gel led to a decrease in the slope of the isotherm.

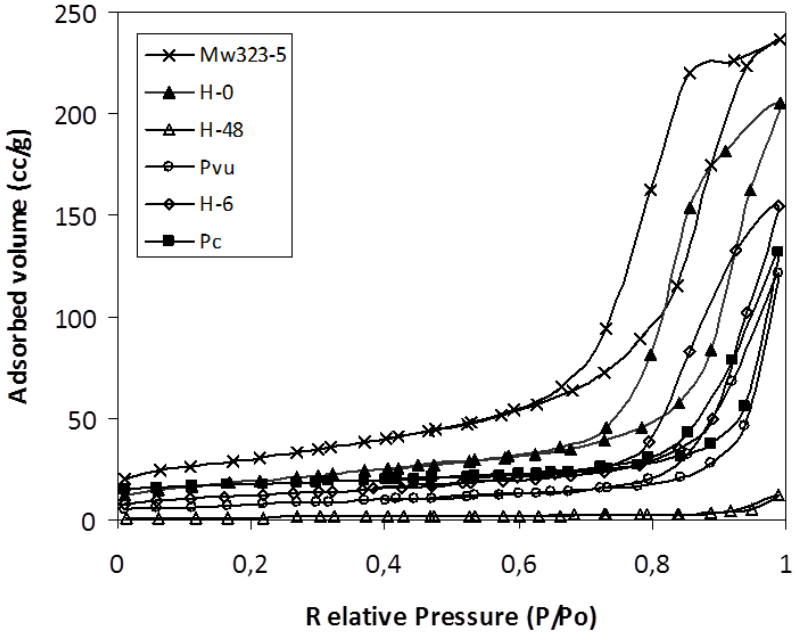

Figure 3.10. N_2 adsorption-desorption isotherms of several representative lanthanum hydroxide samples.

Table 3.6. Surface areas of some $La(OH)_3$ representative samples.

Sample	BET area ($m^2 \cdot g^{-1}$)[a]	Sample	BET area ($m^2 \cdot g^{-1}$)[a]
Pc	35	*H-6*	42
Pv	35	*H-12*	65
Pvu	28	*H-24*	100
Pvt	62	*H-48*	113
Pvb	66	*MwH-323-5*	146
H-0	134	*MwH-323-15*	114
H-1	82	*MwH-323-60*	109
H-3	33	*MwH-353-60*	94

[a] Calculated from nitrogen physisorption.

Regarding BET surface areas of the precipitated gels (see Table 3.6), *Pvu* showed the lowest surface area probably due to the presence of other crystalline phases in addition to lanthanum

hydroxide, as observed by XRD. In contrast, *Pvt* and *Pvb* had higher surface areas than *Pv* (also precipitated at variable pH) because of their lower crystallinity. When *H-0*, which exhibited the highest surface area of all the precipitated gels, was aged by conventional heating, we observed an initial lowering of surface areas until 3 h of aging (see Table 3.6). A similar behaviour was observed for samples aged under microwaves. However, after longer aging times, the surface area of the samples aged conventionally increased (see Table 3.6). We believe that some amorphous species formed initially during aging at short times occupy the pores of the most crystallized phase resulting in a more compact material, which consequently has a lower surface area. However, at longer aging times, these amorphous species are incorporated progressively into the crystalline structure, liberating the pores. This explains the increase in the crystallite size and surface area observed. Samples aged with microwaves showed higher surface areas than those aged by conventional heating. This can be related to the lower temperature and time used during aging with microwaves.
Both SEM and TEM techniques were used to monitor the morphology of the $La(OH)_3$ samples. Some representative SEM and TEM micrographs are presented in Figures 3.11 and 3.12, respectively.

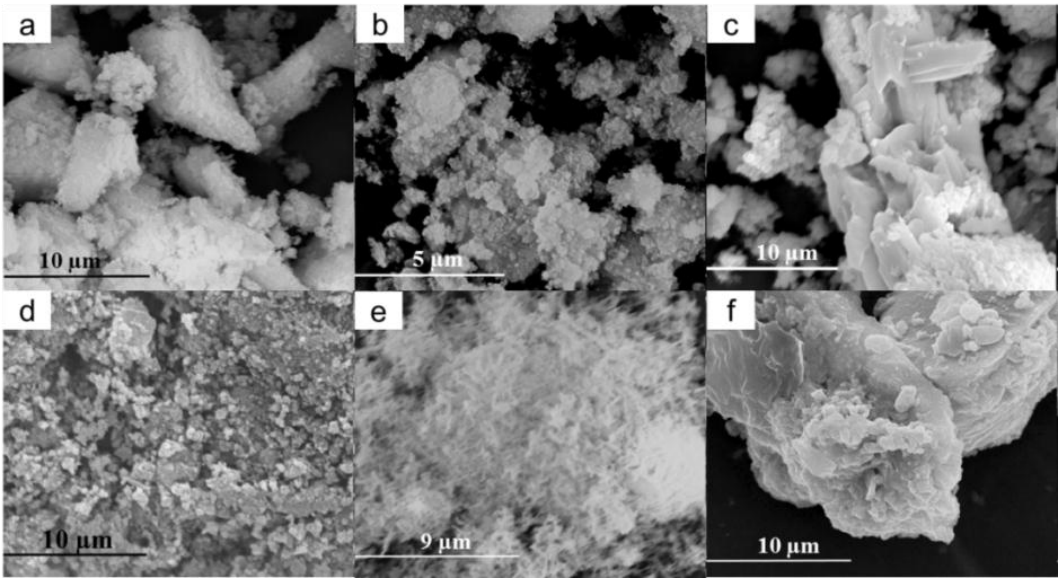

Figure 3.11. SEM images of the lanthanum hydroxide gels synthesized by different methods: **(a)** *Pc*, **(b)** *Pvb*, **(c)** *Pvt*, **(d)** *H-0*, **(e)** *H-48* and **(f)** *MwH-353-60*.

SEM images of *Pc* and *Pvb* (see Fig. 3.11(a) and (b)), as representative samples of those obtained by precipitation, exhibited particles with sizes around 5-10 µm, formed by much smaller aggregated particles with sizes around 10 nm. In contrast, two different particle shapes were clearly distinguished for *Pvu* (see Fig. 3.11(c)). This could be associated with the two crystalline phases detected for this sample by XRD. On the other hand, *H-0*, obtained by instantaneous precipitation, showed smaller particles with a more homogeneous size

distribution between 1-3 μm (see Fig. 3.11(d)). When this gel was aged in an autoclave by conventional heating for 48 h (see Fig. 3.11(e)), small homogeneous needle-shape particles were obtained. Lastly, the gels aged in an autoclave under microwave irradiation appeared agglomerated forming big particles (see Fig. 3.11(f)).

TEM images allowed us to observe with more definition the shape and size of the particles. Thus, precipitated gels showed nanorods between 30 × 8 nm and 110 × 8 nm (see Fig. 3.12(a), (b), (c) and (d)). Nanorods were less agglomerated for *Pvu*, probably due to the use of ultrasounds during precipitation. The *H-0* sample (see Fig. 3.12(e)) and those obtained by aging in autoclave by conventional heating (see Fig. 3.12(f), (g)) or under microwave irradiation (see Fig. 3.12(h), (i)) showed a higher homogeneity in size distribution and lower nanorod sizes (from 20 × 5 to 50 × 15 nm) than the precipitated samples but with a higher agglomeration degree.

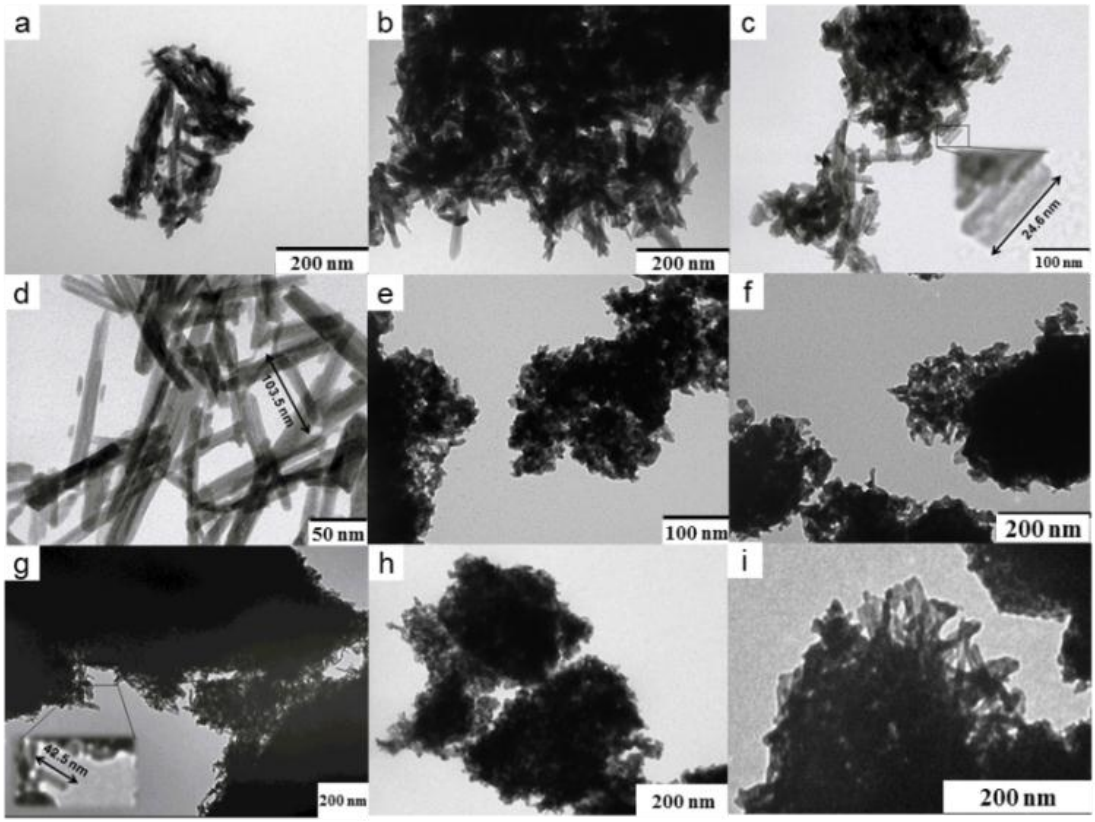

Figure 3.12. TEM images of the lanthanum hydroxide gels synthesized by different methods: **(a)** *Pc*, **(b)** *Pvb*, **(c)** *Pvt*, **(d)** *Pvu*, **(e)** *H-0*, **(f)** *H-6*, **(g)** *H-48*, **(h)** *MwH-323-5* and **(i)** *MwH-353-60*.

Lanthanum oxide samples

Several representative lanthanum hydroxide samples (*Pv*, *Pvu*, *H-0*, *H-1*, *H-48* and *MwH-323-5*) were calcined at 1173 K for 2 h. We chose these calcination conditions to be sure that

all the lanthanum hydroxylated phases were converted to lanthanum oxide. XRD patterns of the calcined samples only showed the presence of the La_2O_3 phase with similar crystallite sizes for all samples ranging from 48 to 61 nm (see Fig. 3.13 and Table 3.7).

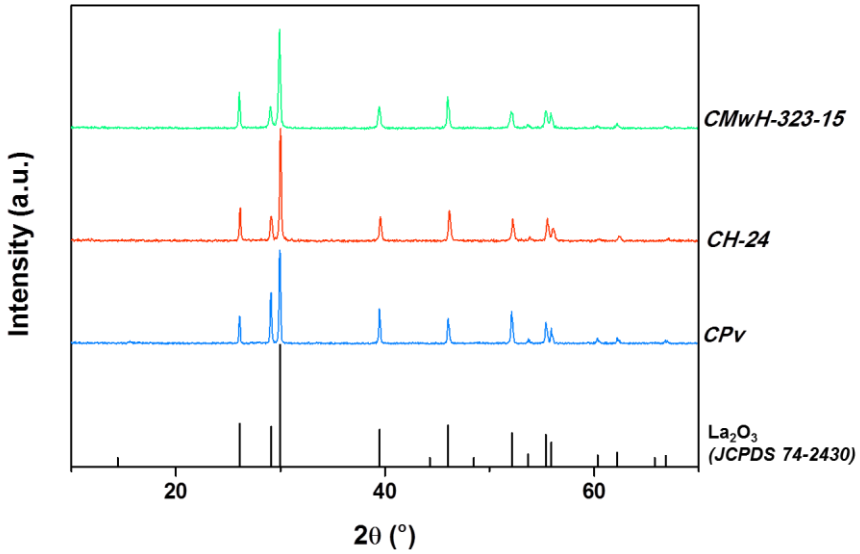

Figure 3.13. XRD patterns of some representative La_2O_3 samples prepared by precipitation and hydrothermal methods.

Table 3.7. Crystalline phases and crystallite sizes of some calcined samples.

Sample	Crystalline phases (XRD)	La_2O_3 crystallite size (nm)[a]
CPv	La_2O_3	61.5
CPvu	La_2O_3	60.1
CH-0	La_2O_3	50.1
CH-1	La_2O_3	65.8
CH-48	La_2O_3	48.3
CMwH-323-5	La_2O_3	61.4

[a] Calculated from the (100), (002) and (011) peaks of the XRD patterns.

Nitrogen adsorption-desorption isotherms of calcined samples were identified as Type IV, corresponding to mesoporous materials. After calcination, the surface areas significantly decreased until 3-5 $m^2 \cdot g^{-1}$ (see Table 3.8), as expected due to the formation of a more compact oxide phase. Therefore, there are not great differences between the calcined samples, just some slight lower surface areas were observed for the samples obtained from the lanthanum hydroxide prepared by direct precipitation (*CH-0*) and those obtained from the samples aged at shorter times (*CH-1*, *CMwH-323-5*).

Once the samples were calcined at high temperatures in order to obtain the corresponding oxide phase, the particles became more agglomerated. Figure 3.14 shows some TEM images of some calcined gels synthesized by the precipitation method.

Table 3.8. Surface areas of some representative La_2O_3 samples.

Sample	BET area ($m^2 \cdot g^{-1}$)[a]
CPv	4.6
CPvu	4.9
CH-0	1.8
CH-1	2.9
CH-48	4.6
CMwH-323-5	2.8

[a] Calculated from nitrogen physisorption.

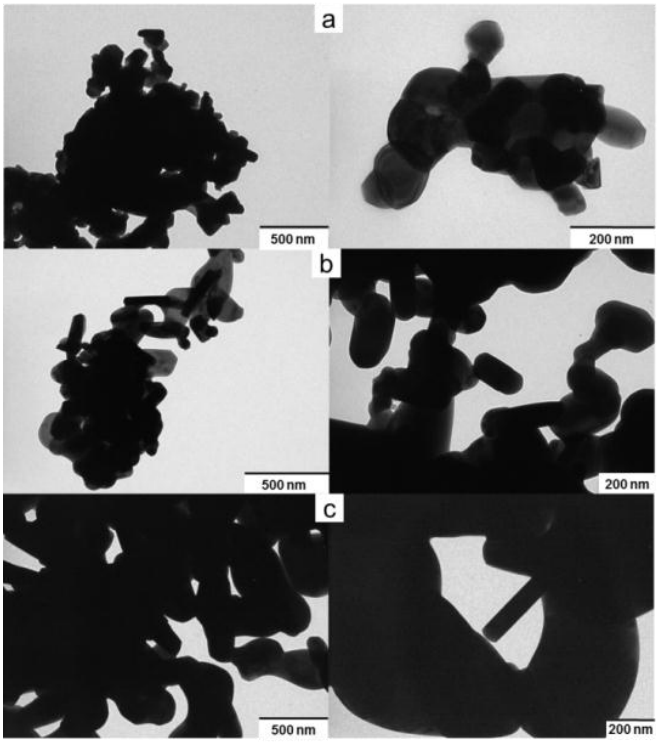

Figure 3.14. TEM images of several La_2O_3 samples: **(a)** *CPv*, **(b)** *CH-48* and **(c)***CMwH-323-5*.

While calcined samples did not show significant difference in the surface area values obtained, there were significant differences with respect to the particle sizes and the agglomeration degree. Thus, despite of the nanorod morphology of some precipitated gels, these tend to be more agglomerated. For example, calcined samples obtained from $La(OH)_3$ synthesized by precipitation without later aging (e.g. *CPv*) showed particles with lower

particle sizes (around 150-200 nm) than calcined samples obtained from aged lanthanum hydroxides (e.g. *CH-48*, *C-MwH-323-5*) which exhibited bigger particles (200-250 and 500-600 nm, respectively).

3.3.2. Characterization of europium doped lanthanum oxide (Eu^{3+}:La_2O_3) and praseodymium doped lanthanum oxide (Pr^{3+}:La_2O_3)

Eu^{3+}:La_2O_3 precursors

Figure 3.15 shows the XRD patterns of several Eu^{3+}:La_2O_3 precursor powders representing the different synthesis methods.

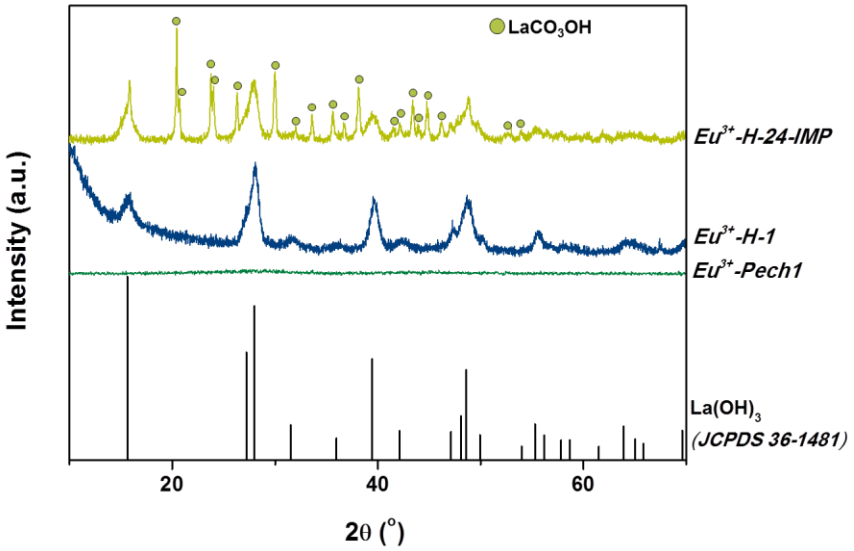

Figure 3.15. XRD patterns of the *Eu^{3+}-Pech1*, *Eu^{3+}-H-1* and *Eu^{3+}-H-24-IMP* samples.

The XRD pattern of *Eu^{3+}-H-1,* as a representative sample of europium doped lanthanum hydroxide synthesized by co-precipitation or hydrothermal methods, only showed the presence of the lanthanum hydroxide crystalline phase, as for their corresponding un-doped samples. However, the XRD pattern of *Eu^{3+}-H-24-IMP*, showed a mixture of lanthanum hydroxide and lanthanum hydroxyl carbonate ($LaCO_3OH$) due to the fact to dope in atmospheric conditions, and as was confirmed by the JCPDS pattern 49-0981 [107]. A decrease of the cell parameters corresponding to the $La(OH)_3$ phase was observed for all samples when compared with the same un-doped samples. This can be explained by the introduction of the Eu^{3+} in the structure, since the ionic radius of La^{3+} is 1.06 Å whereas Eu^{3+} has an ionic radius of 0.95 Å. On the other hand, the XRD pattern of the sample synthesized by the sol-gel Pechini method, *Eu^{3+}-Pech1,* presented an amorphous phase, as expected, due to the organic template used during its synthesis.

A thorough study was carried out taking one XRD pattern every 50 degrees under non-controlled atmosphere for several europium doped lanthanum hydroxide samples prepared by different methods in order to study the evolution of the crystalline phases with the temperature. Figure 3.16(a) shows the XRD patterns of the *Eu^{3+}-H-24* sample from room temperature to 1073 K. Four different crystalline phases were observed.

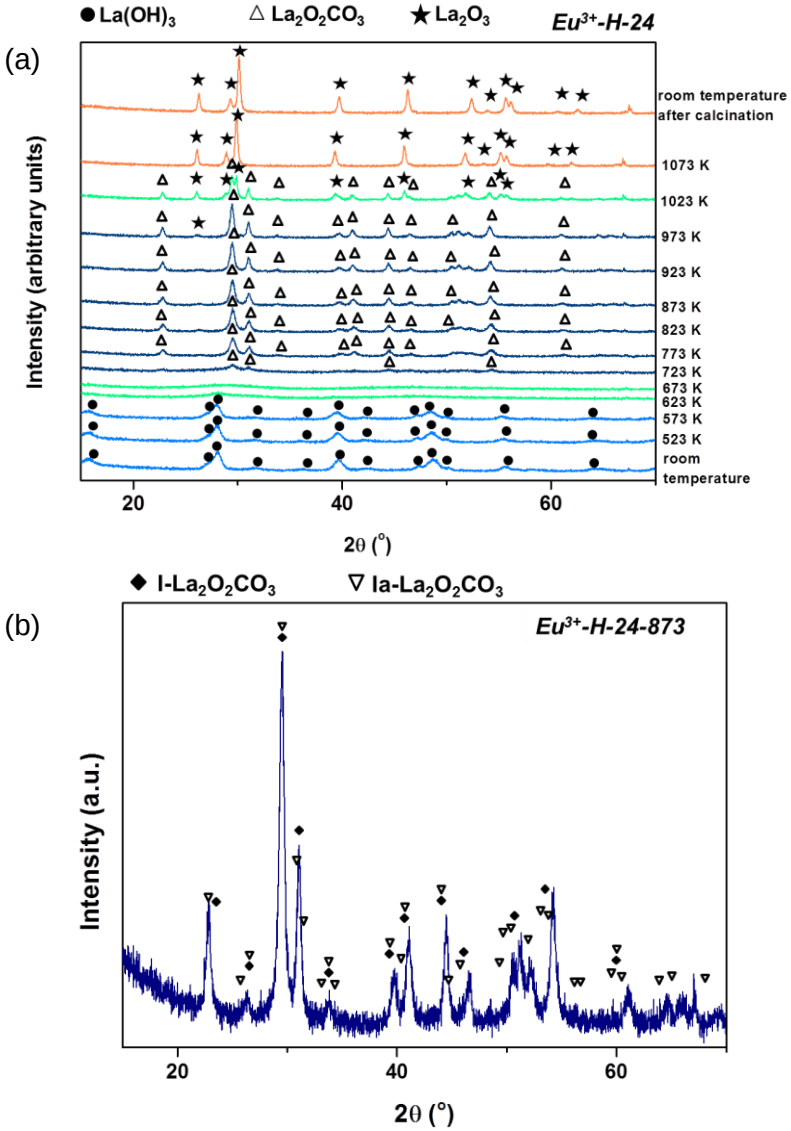

Figure 3.16. XRD patterns at different calcination temperatures of the **(a)** *Eu^{3+}-H-24* sample, **(b)** zoom of the *Eu^{3+}-H-24* sample calcined at 873 K

The crystalline peaks of the precursor at room temperature were identified as $La(OH)_3$ according to the JCPDS file 36-1481 [110]. This phase lasted up to 623 K when the crystalline peaks led to an amorphous phase between 623 and 673 K. This amorphous phase evolved with temperature to a carbonated crystalline phase $La_2O_2CO_3$ [111-113], due to the

absorption of atmospheric CO_2, since the sample was heated in air atmosphere. Turcotte et al. [114] reported the appearance of three different polymorphic forms of $La_2O_2CO_3$ during its decomposition process. According to them, the tetragonal I-$La_2O_2CO_3$ phase (JCPDS file 23-0320) [111], which can be derived from the tetragonal C-form of lanthana sesquioxides, formed first. Then, it transformed into an intermediate monoclinic Ia-$La_2O_2CO_3$ phase (JCPDS file 48-1113) [112], and finally, the hexagonal II-$La_2O_2CO_3$ was formed (JCPDS file 37-0804) [113], the structure of which is related to trigonal La_2O_3 (JCPDS file 74-2430) [115]. In our case, we obtained a mixture of tetragonal and monoclinic phases of $La_2O_2CO_3$ (see Figure 3.16(b)). We did not detect the hexagonal phase of $La_2O_2CO_3$. The La_2O_3 phase began to appear at 973 K, coexisting with the $La_2O_2CO_3$ phase, but at 1073 K, La_2O_3 was the only crystalline phase observed in the diffraction pattern. After cooling at room temperature, the same crystalline phase was observed: La_2O_3.

For the *Eu^{3+}-Pech1* and *Eu^{3+}-Pech2* samples the thermal evolution was different until removing utterly the organic molecule (EG or PEG) at around 673 K (see e.g. Fig. 3.17).

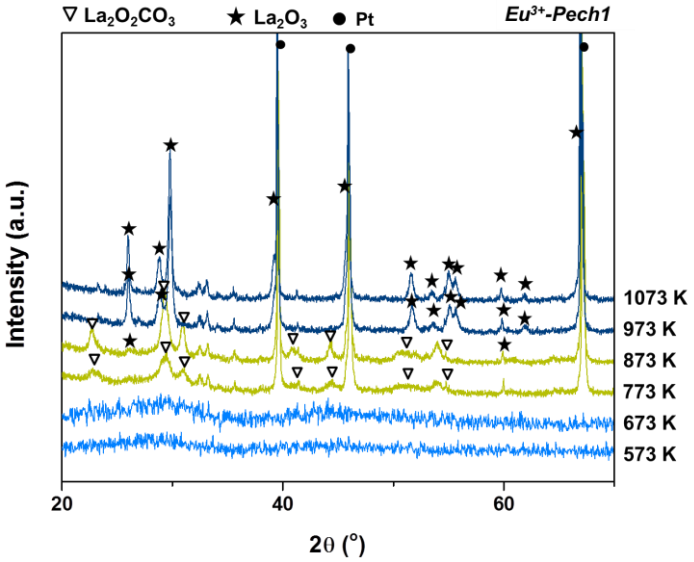

Figure 3.17. XRD patterns at different calcination temperatures of the *Eu^{3+}-Pech1* sample.

Apart from that, lanthanum carbonate phases were also formed at 773 K due to the calcination under ambient conditions and finally at 873 K, we observed the lanthanum oxide as the only phase present. At 973 K and above, only this phase remained and the lanthanum carbonate phases disappeared completely, as expected. The Pt crystalline peaks observed in these diffraction patterns were not coming from the sample but from the support used to record these patterns.

DTA-TG curves of these two precursors (*Eu^{3+}-H-24* and *Eu^{3+}-Pech1*) were taken to study deeply their thermal decomposition (see Figs. 3.18 and 3.19, respectively).

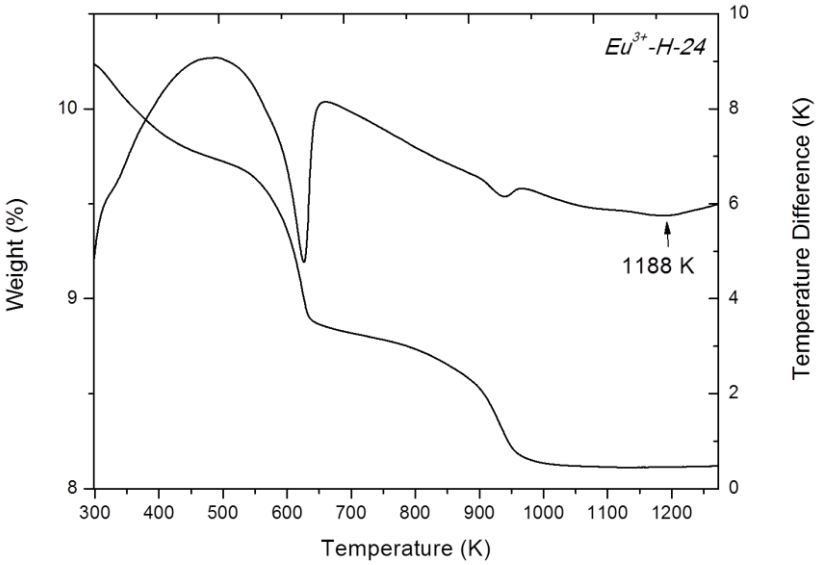

Figure 3.18. DTA-TG curve of the *Eu*$^{3+}$*-H-24* sample.

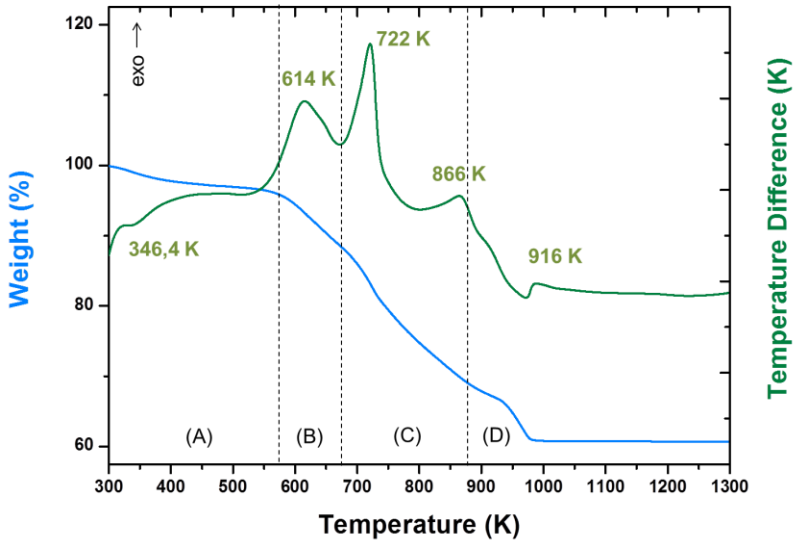

Figure 3.19. DTA-TG of the *Eu*$^{3+}$*-Pech1* sample.

The thermogram of *Eu*$^{3+}$*-Pech1* showed four different regions (A, B, C and D) associated to different weight losses. The first region, marked as A in Figure 3.19 is associated with the evaporation of water formed during the esterification reaction between the organic acid (OA) and the esterification agent (EA). This water evaporation is produced in the temperature interval from 300 K to 680 K with a weight loss of 3%. The second region, marked as B, corresponds to the evaporation of the organic molecule, OA, whose boiling point is 573 K [116,117]. The DTA curve also exhibits an exothermic peak at 614 K in this region. In the third region, C in the figure, between 700 and 900 K, the DTA curve shows two exothermic

peaks at 722 K and 866 K that are attributed to the oxidation of the residual organic compounds, with a weight loss of 22%. Finally, the last region, marked as D in the figure, between 873 and 1200 K, corresponds to the crystallization of the two crystalline phases that we observed by X-ray diffraction (see Fig. 3.17): $La_2O_2CO_3$ and La_2O_3, observed as two endothermic peaks in the DTA curve at 873 and 916 K, respectively. The weight loss associated to this interval is around 7%. From these results, we concluded that the minimum calcination temperature of the precursor powders to obtain Eu^{3+}:La_2O_3 nanoparticles must be higher than 916 K when the sol-gel Pechini is the method used. Interestingly, the crystallization temperature was lower when compared to the crystallization temperatures of samples synthesized by co-precipitation and hydrothermal methods (see e.g. Fig. 3.18). These results were in agreement with those reported in the literature and might be attributed to the good chemical homogeneity of the samples prepared by this method.

Eu^{3+}:La_2O_3 samples

XRD patterns of the samples calcined at 1273 K for 2 h showed the presence of lanthanum oxide phase for all samples, as expected (see Table 3.9, Fig. 3.20(a-b) and Fig. 3.21).

Table 3.9. Crystalline phases and crystallite size of some doped lanthanum oxide samples.

Sample	Crystalline phases (XRD)	La_2O_3 crystallite size (nm)[a]
Eu^{3+}-CH-1	La_2O_3	52.5
Eu^{3+}-CH-24-IMP	La_2O_3	57.4
Eu^{3+}-CPech1	La_2O_3	50.0
Eu^{3+}-CPech2	La_2O_3	52.1
Eu^{3+}-CPech1B	La_2O_3 + LaOCl	37.2
Eu^{3+}-CPech2B	La_2O_3 + LaOCl	51.0

[a] Calculated from the (100), (002) and (011) peaks of the XRD patterns.

However, calcined samples whose precursors were synthesized by the sol-gel Pechini method using chlorides as starting materials (*Eu^{3+}-CPech1B* and *Eu^{3+}-CPech2B*) exhibited, additionally, an other crystalline phase identified as LaOCl, JCPDS file 73-2063 [118] (see Fig. 3.20(a-b)). This indicates that the use of chloride reagents favours the formation of LaOCl, and this phase cannot transform completely to La_2O_3 at the temperature and time of calcination used.

By comparing the intensity of the most important diffraction peak of both phases, it was possible to calculate the percentage of each phase. For the *Eu^{3+}-CPech1B* sample, the proportion of phases was 42% La_2O_3 and 58% LaOCl whereas for the *Eu^{3+}-Pech2B* sample, the proportion was 62% La_2O_3 and 38% LaOCl.

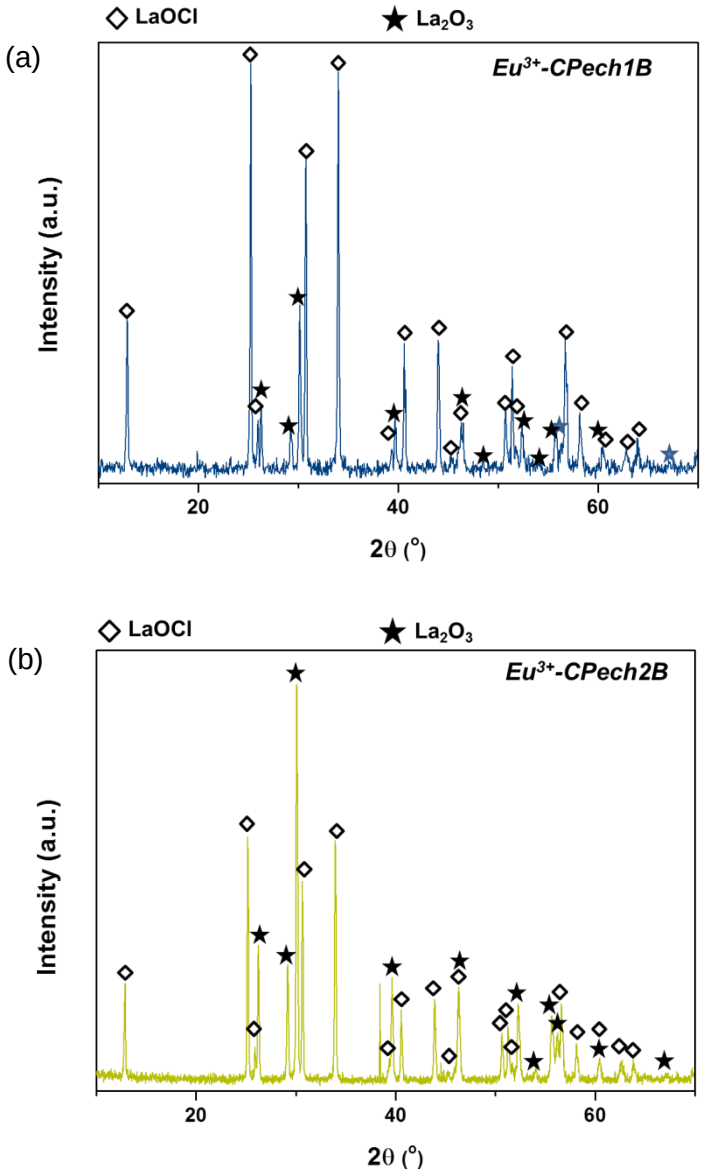

Figure 3.20. XRD patterns of the: **(a)** *Eu^{3+}-CPech1B* and **(b)** *Eu^{3+}-CPech2B* samples.

Fig. 3.21 shows the XRD patterns of several calcined Eu^{3+} doped lanthanum oxide samples synthesized by using different methods. All the samples comprised the La_2O_3 phase and only the *Eu^{3+}-CH-24-IMP* sample had a few traces of the $La(OH)_3$ phase. This could be attributed to the time passed between the preparation and the XRD measurement, as we will further explain in Chapter 5.

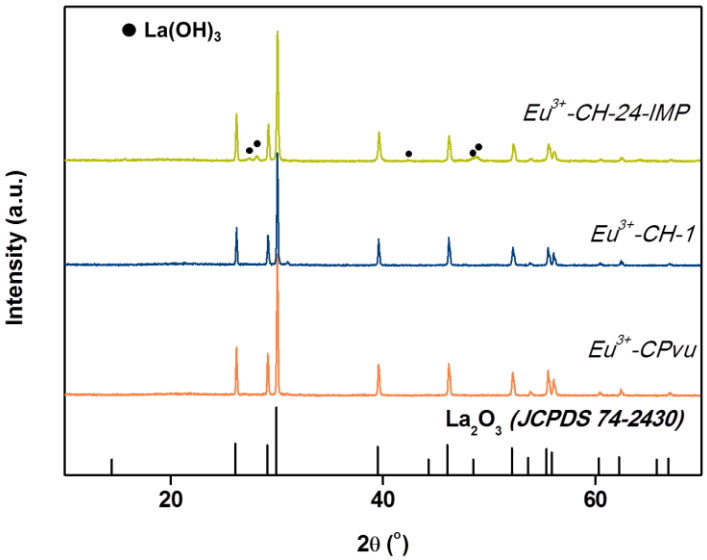

Figure 3.21. XRD patterns of several Eu^{3+}-doped lanthanum oxide samples prepared by the wetness impregnation method (*Eu^{3+}-CH-24-IMP*), the hydrothermal method (*Eu^{3+}-CH-1*) and the co-precipitation method (*Eu^{3+}-CPvu*).

Table 3.9 also summarizes the crystallite sizes of the La_2O_3 phase for the different samples. Regarding to the crystallite sizes of calcined samples they were ranging from 37.2 to 65.1 nm. In comparison to the values obtained for the un-doped samples, there were no significant differences apart from the lowest value, which was obtained for the *Eu^{3+}-CPech1B* sample. Curiously, that sample was mainly formed by the LaOCl phase (58%) and this makes difficult the correct use of Scherrer's equation. For the case of the *Eu^{3+}-CPech2B* sample, where there was also the presence of LaOCl (38%) but in less proportion compared to the La_2O_3 phase, the crystallite size was 51 nm.

The cell parameters, corresponding to the La_2O_3 phase, were also calculated from the XRD patterns for the *Eu^{3+}-CH-1*, *Eu^{3+}-CPech1* and *Eu^{3+}-CPech2* samples. The cell parameters of these samples were lower than those corresponding to the un-doped samples. This could be attributed to the incorporation of Eu^{3+} in the La_2O_3 structure.

Another technique, very useful to check whether europium is succesfully inside the lanthanum oxide host matrix or not, is infrared spectroscopy. First of all, we studied where the absorption bands of our corresponding commercial compounds appear (La_2O_3 (Aldrich, 99.9%) and Eu_2O_3 (Aldrich, 99.9%)). *Eu^{3+}-Pech1* was the sample used to study the infrared spectra of this material. From the data reported in the literature [119], we can identify the peaks. The theoretical values were confirmed experimentally, by taking the IR spectra of commercial La_2O_3 and Eu_2O_3 (see Fig. 3.22). As we can see, the ν(Eu-O) band appears at 753.25 cm^{-1} [120] and the ν(La-O) band appears at 644 cm^{-1} [121].

When we calcined the precursor powders of our samples to 1073 K or over for 2 h, a similar band appeared at 649 cm^{-1}. Taking into account the different atomic weight of La^{3+} (138.91 a.u.) and Eu^{3+} (151.96 a.u.), if Eu^{3+} is substituting La^{3+} in the structure, as we expect, this characteristic vibration band should shift towards larger energies, as we observed. Although the shift observed is small and may appear negligible, it constitutes a probe that we succeeded in the incorporation of Eu^{3+} in the structure of La_2O_3. If we compare the position of the ν(La-O) band in La_2O_3 at 644 cm^{-1} with the position of the ν(Eu-O) band in Eu_2O_3, that appears at 753 cm^{-1} [115], and if we suppose, making a very rough approximation, that the position of this band will change linearly with the concentration of Eu^{3+} in La_2O_3, the shift of 5 cm^{-1} we observed would correspond to a sample of La_2O_3 doped with 5 mol% of Eu^{3+}. This corresponds exactly to the concentration of Eu^{3+} we introduced in our synthesis process.

Other peaks corresponding to different O-H and CO_3^{2-} modes were also observed in all the samples studied. However, the absorption peaks responsible of the presence of carbonates (1636-652 cm^{-1}) were more intense for the *Eu^{3+}-Pech1* sample calcined at 973 K in comparison to the intensity peaks for samples calcined over 973 K. In the thermal evolution study, the presence of these peaks were analysed in more detail.

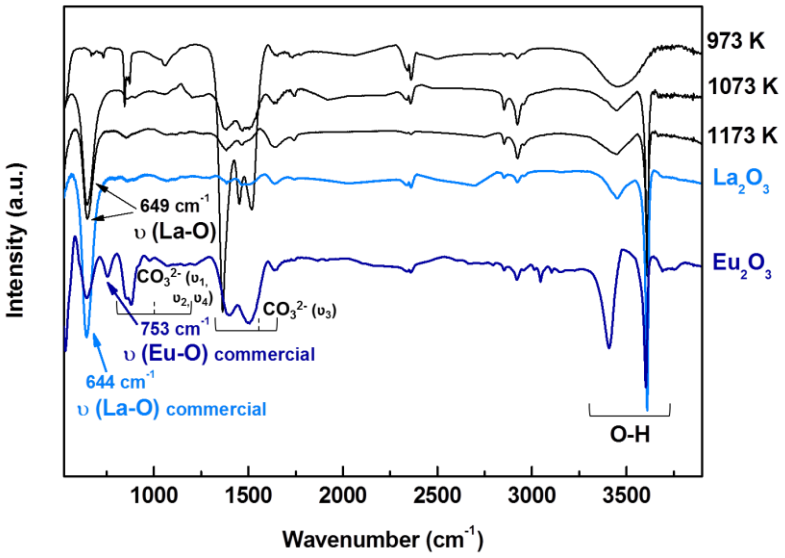

Figure 3.22. Infrared spectra of Eu^{3+} doped La_2O_3 (*Eu^{3+}-Pech1*) nanoparticles at different temperatures of calcination and un-doped commercial La_2O_3 and Eu_2O_3 nanoparticles.

Figure 3.23 shows the thermal evolution of the Eu^{3+}:$La(OH)_3$ nanoparticles followed by infrared (IR) spectroscopy. *Eu^{3+}-H-24* and its corresponding calcined counterparts were the samples used for this study. The absorption peaks at 3614 cm^{-1} and 3439 cm^{-1} were attributed to the stretching vibration mode of the O-H bond and the bending vibration of H-O-H, respectively. Thus, the peak at 3614 cm^{-1} was indicative of the presence of $La(OH)_3$ whereas the wide band at 3493 cm^{-1} can be associated with water formed during the handling process

of the samples to record the spectra. In the same way, the absorption of carbon dioxide from the atmosphere was confirmed by the appearance of several peaks corresponding to the υ_3 and υ_1, and υ_2 and υ_4 modes of the CO_3^{2-} (1636-652 cm^{-1}). This corroborates the presence of $La_2O_2CO_3$, detected by XRD (see Figure 3.16). At higher annealing temperatures, the peaks corresponding to $La_2O_2CO_3$ decreased in intensity, whereas the intensity of the broad absorption peaks observed at low wavenumbers (434, 498 cm^{-1}) increased, as expected, due to the formation of the La_2O_3 phase, in agreement with XRD results (see Figure 3.16).

The IR spectra observed for the samples synthesized by the precipitation method showed similar results than those obtained for the samples synthesized by the sol-gel and the hydrothermal methods.

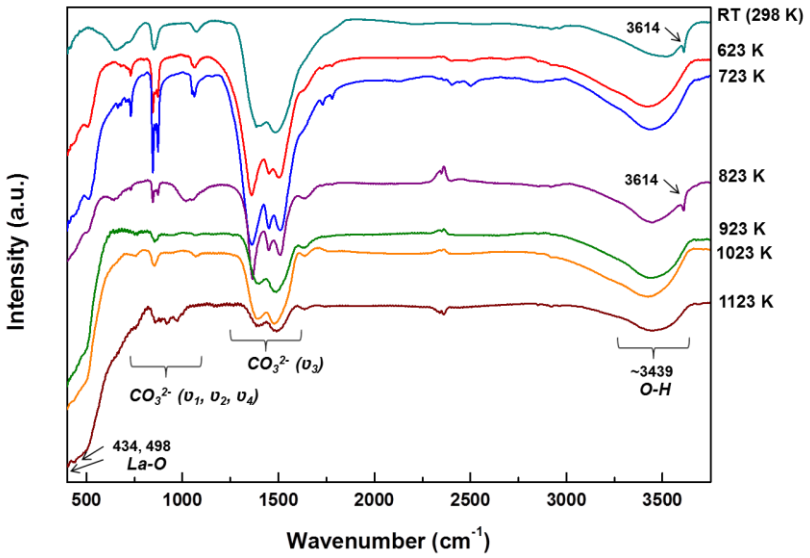

Figure 3.23. Infrared spectra of the thermal evolution of Eu^{3+}:$La(OH)_3$ towards Eu^{3+}:La_2O_3 nanoparticles synthesized by the hydrothermal method.

The XPS technique was used to confirm the presence of europium and evaluate the Eu/La ratio on the surface of several representative samples (*Eu^{3+}-CH-24-IMP* and *Eu^{3+}-CH-1*, Fig. 3.24).

The literature of X-ray photoelectron spectra of Eu and its compounds is rather scarce [122, 123]. The main difficulty on the evaluation of Eu spectra is their complex nature due to the appearance of shake up and/or shakes down satellites. The presence of satellite lines on the spectra are due to the final state effect which itself is in connection with the density of states in the 4f orbital. The Eu 3d5/2 peak corresponding to Eu^{3+} was detected at 1134.89 eV and 1135.19 eV for the *Eu^{3+}-CH-24-IMP* and *Eu^{3+}-CH-1* samples, respectively (see Fig. 3.24). These values are located at slightly higher energies than those published in the literature for Eu_2O_3 samples (1133.7 eV) but it is well known that different environments of Eu^{3+} can shift

slightly the position of the maximum of this peak [122]. In our samples, the slight higher binding energy observed for the sample prepared by the Pechini method could be related to a higher incorporation of the Eu^{3+} in the lanthanum oxide structure. Therefore, by XPS we confirmed the presence of europium in our samples prepared by different methods. Additionally, we calculated the Eu/La ratio for both samples which was of 0.098 and 0.045 for the *Eu^{3+}-CH-24-IMP* and *Eu^{3+}-CH-1* samples, respectively. Taking into account that the theoretical value used during preparation was Eu/La= 0.05 and XPS is a surface characterization technique, these results allowed us to conclude that at the surface of the sample obtained by impregnation with europium (III) nitrate and later calcination, there is more concentration of Eu^{3+}, whereas for the sample prepared by the Pechini method, the distribution of Eu^{3+} should be more homogeneous. This agrees with the results obtained by other characterization techniques for both samples.

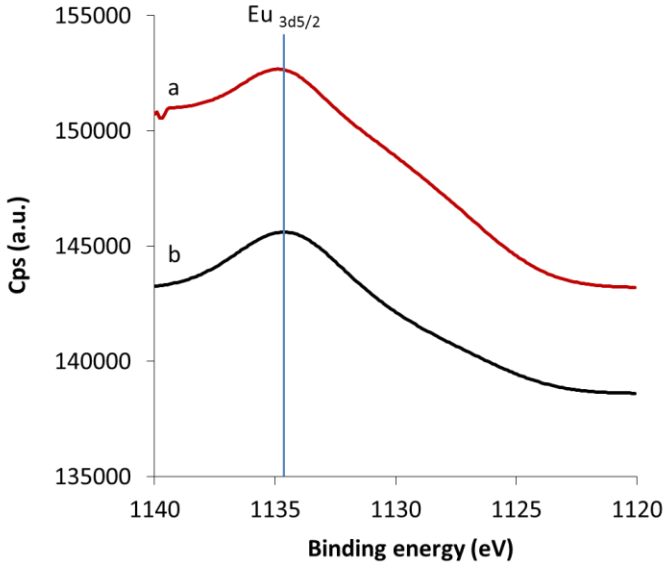

Figure 3.24. $Eu_{3d5/2}$ XPS spectra of the a) *Eu^{3+}-CH-1* and b) *Eu^{3+}-CH-24-IMP* samples.

For Eu^{3+} doped La_2O_3 samples synthesized by co-precipitation and hydrothermal methods, no differences, in terms of shape of the nanoparticles obtained, were observed by electron microscopy (see Figs. 3.25 and 3.26) with respect to the un-doped samples (see Fig. 3.12).

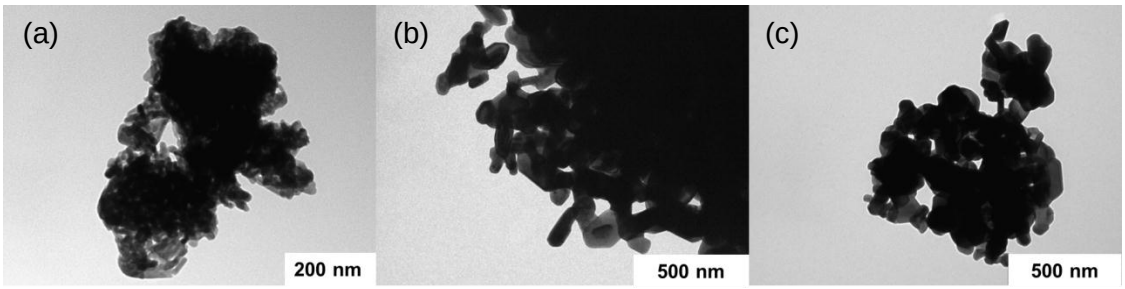

Figure 3.25. TEM images of some representative Eu^{3+}-doped La_2O_3 nanoparticles synthesized by the co-precipitation and hydrothermal methods: **(a)** *Eu^{3+}-CPvu* **(b)** *Eu^{3+}-CH-48* and **(c)** *Eu^{3+}-CMwH-353-60*.

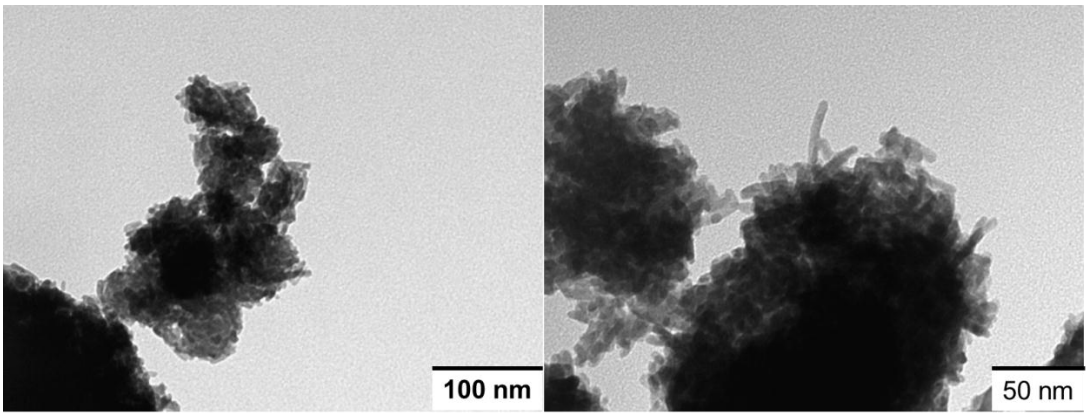

Figure 3.26. TEM images of the *Eu^{3+}-CH-24-IMP* sample obtained by wetness impregnation method.

However, samples synthesized by the sol-gel Pechini method showed significant differences. Thus, Figure 3.27 (a), (b) and (c) shows the ESEM micrographs of the *Eu^{3+}-Pech1* sample calcined at 973, 1073 and 1273 K for 2 h, respectively.

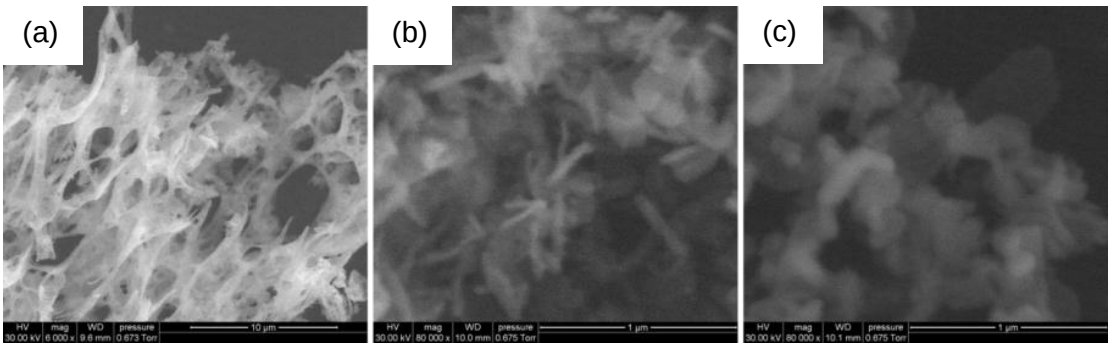

Figure 3.27. ESEM images of the *Eu^{3+}-Pech1* sample at different temperature of calcination: **(a)** 973 K, **(b)** 1073 K and **(c)** 1273 K.

In Figure 3.27(a) we can see still a porous matrix due to the resin precursor but after calcining at 1073 K, the sample appearance changed significantly. It is important to remind that the last peak observed in the DTA-TG thermogram for this sample, corresponds to the

crystallization temperature at 916 K (see Fig. 3.19). Thus, according to the thermogram results, we should observe some powders of lanthanum oxide at 973 K instead of a matrix. However, since measurements were taken at different calcination conditions, there is a discrepancy between the crystallization temperature obtained by themogravimetry and the morphology observed in ESEM images. By DTA-TG the measurements were taken at the same time the samples were calcined at a rate of 10 $K \cdot min^{-1}$, whereas in the ESEM images, the samples were calcined at 973 K for 2 h and studied later. Some differences were also observed when increasing the calcination temperature since nanoparticles became more and more round-shaped and forming bigger aggregates (see Fig. 3.27(c)). This sample was observed at higher magnification by SEM (see Figure 3.28(a), (b) and (c)). The images of the nanoparticles obtained after calcination at 1073, 1173 and 1273 K for 2 h indicated that the size of the nanoparticles were larger as the calcination temperature increased, as expected.

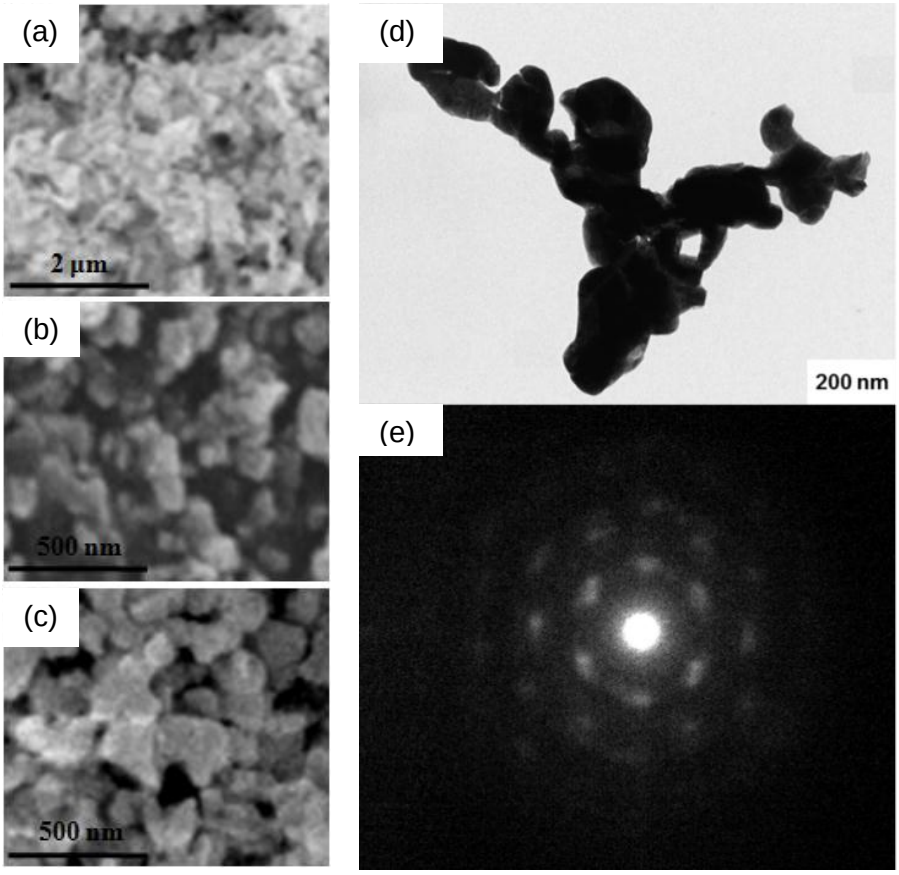

Figure 3.28. In the left, SEM images of the *Eu^{3+}-Pech1* sample at different calcination temperatures: **(a)** 1073 K, **(b)** 1173 K and **(c)** 1273 K. In the right: **(d)** TEM image of the *Eu^{3+}-Pech1* sample at 1273 K and **(e)** image of the electron diffraction of the *Eu^{3+}-CPech1* sample.

Figure 3.28(d) shows a TEM image of the *Eu^{3+}-Pech1* sample calcined at 1273 K for 2 h. The nanoparticles appeared agglomerated with sizes between 50 and 200 nm. By electron

diffraction we were able to confirm that each of these nanoparticles were a single crystal and corroborated that the structure of these nanoparticles was trigonal, as can be observed in Figure 3.28(e).

Regarding to other samples synthesized by the sol-gel Pechini method, we can say that, nanoparticles had sizes around 50 and 200 nm, with irregular shapes and with a high agglomeration degree (see Fig. 3.29).

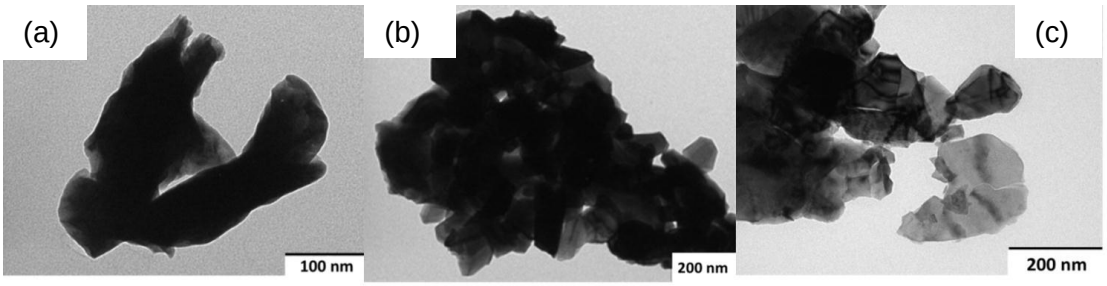

Figure 3.29. TEM images of the **(a)** *Eu^{3+}-CPech2*, **(b)** *Eu^{3+}-CPech1B* and **(c)** *Eu^{3+}-CPech2B* samples.

Pr^{3+}:La_2O_3 samples

The XRD pattern of the *(5%)Pr^{3+}-Pech1* sample shows an amorphous phase, as expected. After calcining at 1273 K during 2 h, the XRD pattern exhibits crystalline peaks corresponding to the La_2O_3, which was the only present crystalline phase (see Fig. 3.30). The La_2O_3 crystallite size, calculated from the (100), (002) and (011) peaks of the XRD pattern for this sample, was 65.1 nm.

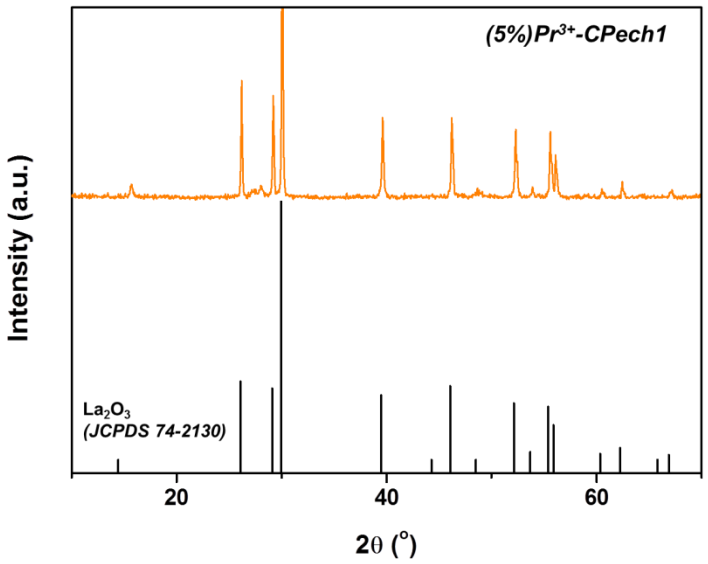

Figure 3.30. XRD pattern of the *(5%)Pr^{3+}-CPech1* sample.

TEM images of this sample shown in Fig. 3.31 give information about the distribution and morphology of the (*(5%)Pr^{3+}-CPech1* sample at different magnifications. The particles were quite agglomerated with a non-defined shape and with a high variety of sizes ranging from 250 to 500 nm (see Fig. 3.31(a) and (b)). In Figure 3.31(c) and (d), it was possible to observe the smaller particles, which were forming those big aggregates, with sizes between 100-200 nm.

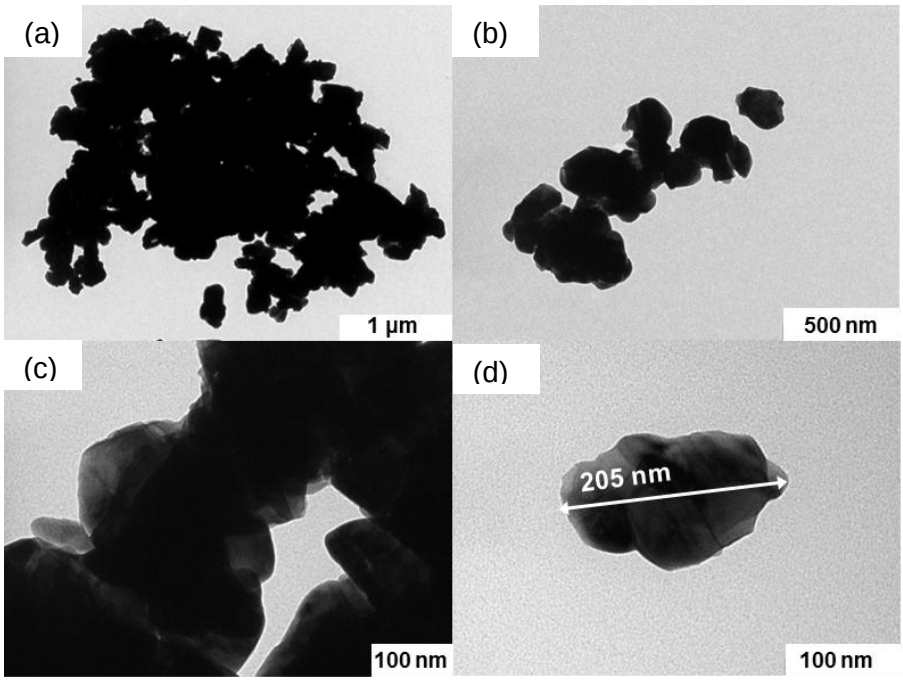

Figure 3.31. (a-d) TEM images of the *(5%)Pr^{3+}-CPech1* sample.

3.3.3. Characterization of europium doped lanthanum oxysulfide (Eu^{3+}:La_2O_2S) and europium and bismuth co-doped lanthanum oxide and lanthanum oxysulfide (Eu^{3+}:Bi^{3+}:La_2O_3, Eu^{3+}:Bi^{3+}:La_2O_2S)

Eu^{3+}:La_2O_2S sample

The crystalline peaks observed in the XRD pattern of the *Eu^{3+}:La_2O_2S* sample, which was obtained by the EASC method, were identified as La_2O_2S according to the JCPDS file 71-2098 [124]. However, traces of $La_2O_2SO_4$ [125] and La_2O_3 [115] were also detected (see Figure 3.32). Both La_2O_3 and La_2O_2S crystallize in the trigonal system structure with space group $P\bar{3}m1$. The formation of $La_2O_2SO_4$ and La_2O_3 can be attributed to some oxidative processes occurred during the combustion reaction. Thus, the reaction for the formation of Eu^{3+}:La_2O_2S nanoparticles using thioacetamide as sulfur-containing fuel can be represented as:

$La(NO_3)_3 \cdot H_2O + Eu(NO_3)_3 \cdot 5H_2O + CH_3CSNH_2 \rightarrow Eu^{3+}:La_2O_2S$ (major) + $Eu^{3+}:La_2O_2SO_4$ (minor) + $Eu^{3+}:La_2O_3$ (minor) + by-products (gases) ↑

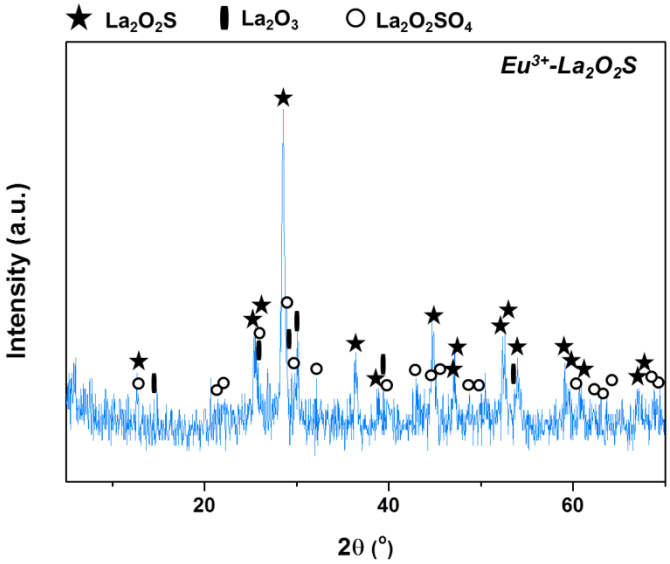

Figure 3.32. XRD pattern of the $Eu^{3+}:La_2O_2S$ sample.

The crystallite size of the $Eu^{3+}:La_2O_2S$ sample was 30.0 nm and was calculated from the (101) and (012) peaks of the XRD pattern, using Scherrer's equation.

Figure 3.33(a), (b) and (c) shows the TEM images of the $Eu^{3+}:La_2O_2S$ sample. Figure 3.33(a) shows aggregates with different sizes, which were formed by nanoparticles with rod shapes. Figure 3.33(b) exhibits an image at higher magnification where it was easier to distinguish each nanocrystal and a zoom of a smaller part was taken to show that nanocrystal sizes were ranging 20-50 nm.

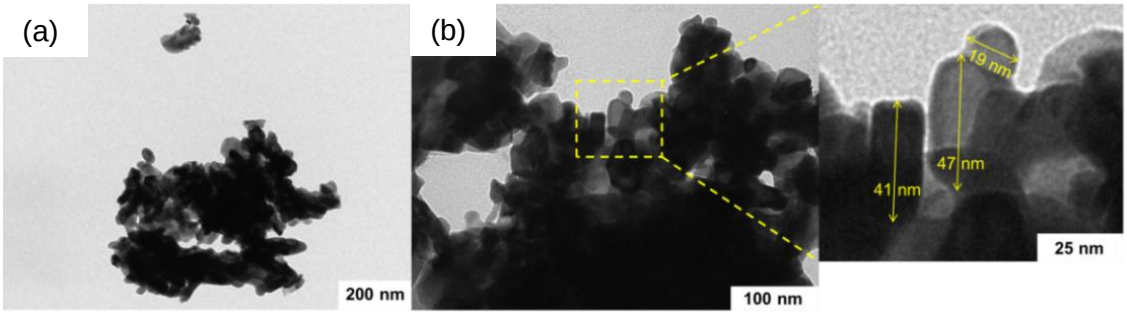

Figure 3.33. TEM images of the $Eu^{3+}:La_2O_2S$ sample.

Eu^{3+}: Bi^{3+}:La_2O_3 samples

The XRD pattern of the *Eu^{3+}:(1%)Bi^{3+}-CPech1* sample showed the presence of the lanthanum oxide as the only crystalline phase (see Fig 3.34), as expected. The crystallite size obtained from the (100), (002) and (011) peaks for this sample was 67.9 nm.

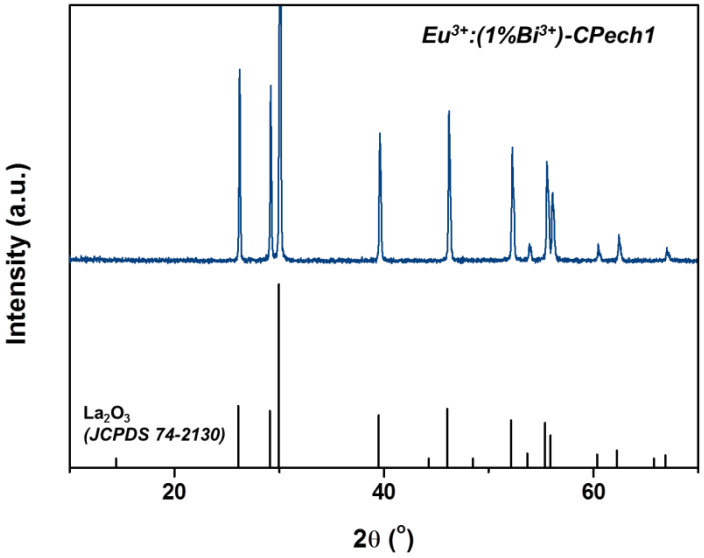

Figure 3.34. XRD pattern of the *Eu^{3+}:(1%)Bi^{3+}-CPech1* sample.

Figure 3.35(a-b) shows several TEM images of the *Eu^{3+}:(1%)Bi^{3+}-CPech1* sample. The size and shape of the particles were similar to those of the other samples obtained by the sol-gel Pechini method: large particle sizes and non-defined shapes.

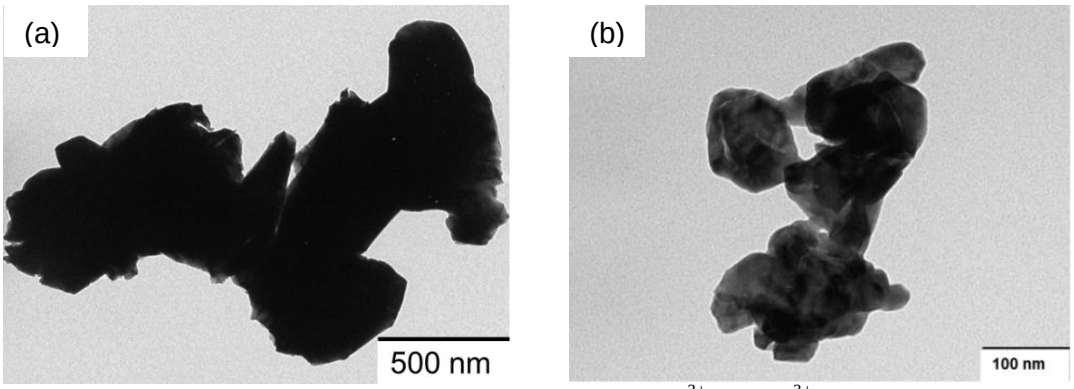

Figure 3.35. (a-b) TEM images of sample *Eu^{3+}:(1%)Bi^{3+}-CPech1*.

Eu^{3+}: Bi^{3+}:La_2O_2S samples

Regarding to the *Eu^{3+}:(1%)Bi^{3+}:La_2O_2S* sample, the XRD pattern showed similar results as those obtained for the *Eu^{3+}:La_2O_2S* sample (see Fig. 3.32), and the morphology of the nanoparticles was also very similar (see Fig. 3.33).

Chapter 4

Spectroscopic characterization of doped lanthanum compound nanoparticles

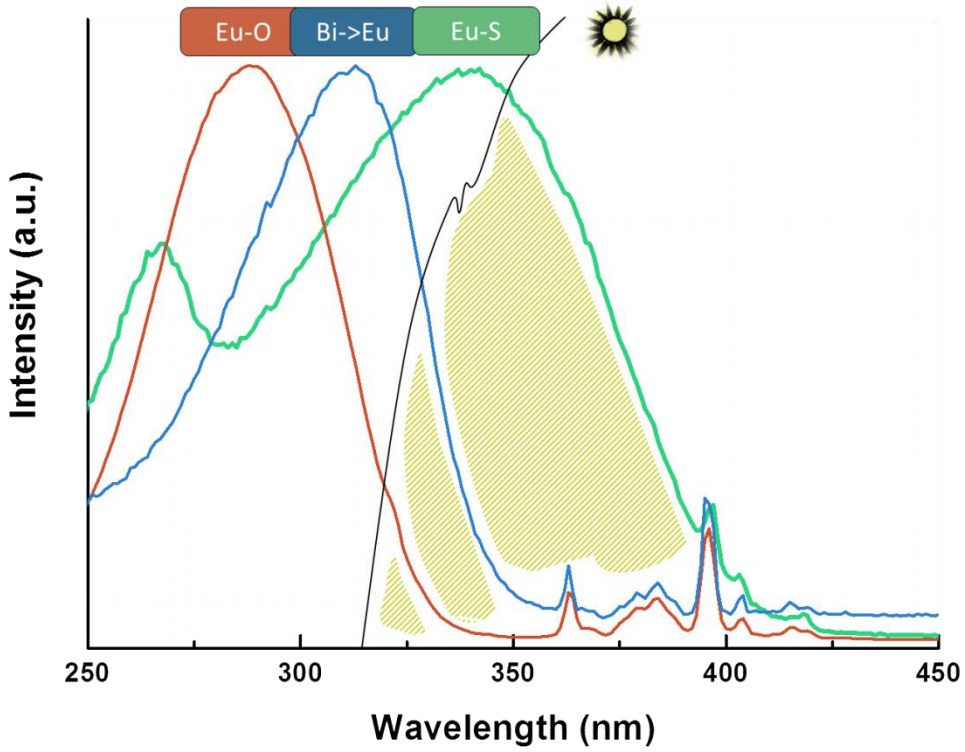

Chapter 4 is focused in the spectroscopic characterization of the lanthanide doped lanthanum compounds synthesized by the different methods exposed in Chapter 3. Photoluminescence and cathodoluminescence were the techniques used to analyse the luminescence properties of the active ions in the different hosts. Additionally, by these techniques we have studied if the incorporation of the active ions into their respective hosts was successfully achieved. We have also analysed how the different methods and techniques used to synthesize these nanoparticles influence on their spectroscopic properties.

4.1. Overview

Lanthanide (Ln^{3+}) doped lanthanum compounds have been extensively investigated due to their luminescence properties [55,58,103,126,127]. Understanding the spectroscopic properties of these materials is important for optimizing their emission capability for technological applications such as solid-state lasers [128], luminescent lamps[129], flat displays [89], optical fiber communication systems [130], and other photonic devices [131]. Moreover, when the size of the luminescence compounds decreases to the nanoscale, the materials exhibit a series of novel structural, electronic, and optical properties which are not present in the corresponding bulk materials [126]. Some important size effects regarding the luminescence properties are the emission lifetime, the luminescence quantum efficiency, and the concentration quenching [132].

Photoluminescence materials generally require a host crystal structure, which is doped with a small amount of an active ion and sometimes, a second type of ion is added to act as a sensitizer [133]. All these kind of materials used in this work are presented below.

La_2O_3 host for Ln^{3+} active ions

Rare earth (RE) sesquioxides (La_2O_3, Y_2O_3, Lu_2O_3, etc) are known as excellent optical host materials for Ln^{3+} active ions [134]. They hold the properties a good matrix must have for the applications we explore: they are transparent for visible and infrared light; they do not have effect on the spectroscopic properties of the lanthanide ions shifting significantly the position of their emission bands because they are due to optical transitions within the f-manifold (well shielded electrons), and the Ln^{3+} luminescence can be efficiently sensitized by means of optical pumping [135,136]. Even though the optical host does not have a significant effect on the position of the Ln^{3+} ions emission bands, host determines the position of their charge transfer band by host sensitized luminescence. Charge transfer (CT) is a significant type of excitation for Ln^{3+} doped phosphors. In CT excitation, an electron is transferred from the ligand of the optical centre to the central ion (e.g. $O^{2-} \rightarrow Ln^{3+}$) [137]. When lanthanum oxide is doped with Eu^{3+} active ion, it presents the most red-shifted position of the CT band among other rare earth sesquioxides [138]. This feature makes the La_2O_3 a good host in photovoltaic applications since the solar energy that arrives at the Earth comprises only a small part of the UV region of the electromagnetic spectrum. Another advantage that La_2O_3 presents as a host for Ln^{3+} ions is that compared with other RE host materials (Y_2O_3, Gd_2O_3, etc.), inorganic compounds containing lanthanum are relatively low-cost host materials [139].

La_2O_3 is a semiconductor material [89] with a band bap of 4.3 eV [140]. It has the lowest lattice energy and the La^{3+} has the largest ionic radius among Ln^{3+} in sesquioxides [141]. La_2O_3 crystallizes in the trigonal system and belongs to the $P\bar{3}m1$ space group [142]. La^{3+} ions in the La_2O_3 structure can be easily substituted by any other trivalent lanthanide ion in its symmetry site, C_{3v} [143]. Another important issue regarding the La_2O_3 host is that it can react relatively fast with carbon dioxide and water in the atmosphere to form new stable

carbonated and hydroxylated phases [144]. This feature is related to the large ionic radius of La^{3+} in La_2O_3. This issue will be further discussed in Chapter 5.

Several Ln^{3+} active ions (Eu^{3+}, Nd^{3+}, Er^{3+}, Yb^{3+}, etc.) have been introduced in the La_2O_3 host [74]. In particular, La_2O_3 is an excellent sesquioxide for the active ions studied in this thesis because La^{3+} has a similar ionic radius (1.10 Å) than that for Eu^{3+} (1.01 Å) and Pr^{3+} (1.08 Å) [145] in a seven-fold coordination structure like that corresponding to La_2O_3.

Eu^{3+} active ion

Trivalent europium (Eu^{3+}) ion has been extensively investigated due to its applications as a red phosphor [146-149]. In general, this interest has increased recently because lanthanide ions bear unique electronic and optical characteristics arising from their 4f electrons. The electronic configuration of europium is [Xe] $6s^2$ $4f^7$ and for trivalent europium is [Xe] $4f^6$. This means that the optical transitions of Eu^{3+} ion, involve electrons in 4f orbitals, which are well shielded from their local environment by the outer completely-filled $5s^2$ and $5p^6$ shells. Therefore, emissions of Eu^{3+} in any matrix are almost similar to those of the free ion and consequently the f-f emission spectrum consists of sharp lines. Apart from that, Eu^{3+} doped phosphors can be efficiently excited by CT excitation, increasing greatly its luminescence efficiency. For this reason, Eu^{3+} is very popular and extensively applied in fluorescent lighting and displays [103]. Furthermore, Eu^{3+} is often used as a structural probe [150], because of the relative simplicity of its energy-level structure. It possesses ground ^7F_J (J = 0-6) and excited $^5D_{J'}$ (J' = 0-3) states well separated and as these states are non-degenerated, the $^5D_0 \rightarrow {}^7F_0$ transition usually appears as a single peak in the photoluminescence spectra when the Eu^{3+} ions occupy identical site symmetries [151]. Figure 4.1 shows the energy level diagram for Eu^{3+} [152]. The $^5D_0 \rightarrow {}^7F_1$ transition is usually taken as a reference since it is allowed by magnetic dipole and its intensity is not considerably altered by the perturbing crystal field [153,154]. For instance, Szuszkiewicz et al. [155] analysed the structure of an alkali metal lanthanide double phosphate of the type $M_3Ln(PO_4)_2$ which crystallizes mainly in three phases: hexagonal, orthorhombic and monoclinic. By doping this material with Eu^{3+}, they observed absorption and emission spectra with a different number of peaks and with different relative intensities among them. That indicated higher or lower symmetry Eu^{3+} sites and consequently they could elucidate the structure in which the $M_3Ln(PO_4)_2$ crystallized.

Eu^{3+} has been previously introduced in several hosts, including sesquioxides such as La_2O_3, Lu_2O_3, Y_2O_3, etc. [103,132,156] but also into other host materials such as vanadates (YVO_4) [157], tungstates (MWO_4, M=Ca^{2+}, Ba^{2+}) [158] and all kind of optical glasses [159,160].

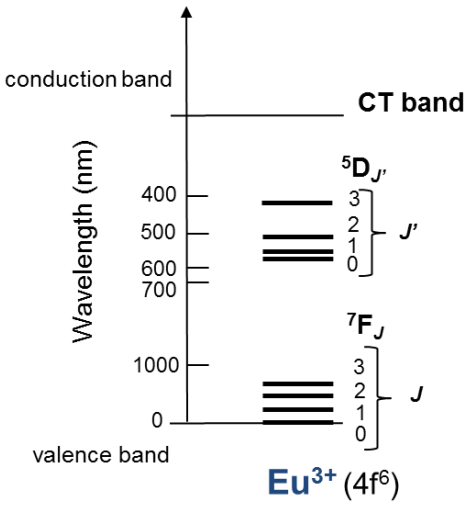

Figure 4.1. Simplified energy level diagram for the trivalent europium ion doped into LaF_3 [152].

Eu^{3+} doped La_2O_3 nanoparticles

The optical and spectroscopic characterization of Eu^{3+}:La_2O_3 nanoparticles has been already studied in detail by other authors [103,126,161]. The typical excitation spectrum shows a broad band at low wavelengths (~290 nm) which is attributed to the charge transfer (CT) band between Eu^{3+}-O^{2-} ions [103]. This band usually has a weak shoulder at lower wavelengths (~230 nm) related to the La_2O_3 excitation and attributed to electronic transitions from the O 2p valence band to the La (5d6s) conduction band [71]. The position of the maximum of the CT band on Eu^{3+} doped La_2O_3 [126,161], but also that of other Eu^{3+} doped materials such as Gd_2O_3[162], Lu_2O_3[163], Y_2O_2S [164] or LaOCl [165] among others, depends mainly on the Eu-O distance. The shorter the Eu-O distance, the larger the energy difference between the 4f and O 2p electrons and consequently the CT band is found at shorter and more energetic wavelengths [166]. Due to that, since La^{3+} has the highest ionic radius in comparison with other Ln^{3+} in RE_2O_3 structures [141], when Eu^{3+} is replacing the La^{3+} in Eu^{3+}:La_2O_3 nanoparticles, the Eu-O distance is also the largest among this family of materials. This explains why this material presents the most red-shifted position of the CT band among other rare earth sesquioxides [167]. Apart from that, characteristic Eu^{3+} f-f transitions: $^7F_0 \rightarrow {}^5D_J$ (J = 1-4), $^7F_0 \rightarrow {}^5G_J$ and $^7F_0 \rightarrow {}^5L_6$ are also observed in the excitation spectrum of Eu^{3+}:La_2O_3 nanoparticles in the 350-500 nm region.

The typical emission spectrum of Eu^{3+} in La_2O_3 corresponds to ^5D_J (J = 0, 1, 2) $\rightarrow {}^7F_{J'}$ (J'= 0, 1, 2, 3) transitions [103]. Some authors observed that the photoluminescence behaviour of Eu^{3+}:La_2O_3 phosphors depends on the Eu^{3+} concentration [76]. For example, Park et al. [103] observed that the spectra of samples doped with 1 mol% Eu^{3+} were dominated by the $^5D_0 \rightarrow {}^7F_1$ transition, while the spectra of samples doped with a larger concentration of Eu^{3+} were dominated by the $^5D_0 \rightarrow {}^7F_2$ transition. Since the maximum emission intensity of this last

transition was observed for samples doped with 5 mol% Eu^{3+} we used this doping concentration for all the Eu^{3+}:La_2O_3 samples synthesized in Chapter 3. Very recently, other authors have also studied the emission intensity as a function of the Eu^{3+} concentration and have confirmed a decrease for concentrations of Eu^{3+} higher than 5 mol% [168]. Hoefdraad et al. [166] attributed this effect to an increase of the degree of covalency (nephelauxetic effect or "cloud-expanding") when the concentration of Eu^{3+} ions increased, and to the interaction between Eu^{3+} ions at long distances in this structure. When the covalency increases, the interaction between the electrons is reduced, so that they spread out over wider orbitals. Consequently, electronic transitions between energy levels with an energy difference, which is determined by electron interaction, shift to lower energies for increasing covalency. Loitongbam et al. [168] mentioned that when the Eu^{3+} concentration increases above 1 mol% the intensities of the transitions arising from the $^5D_1$ or $^5D_2$ levels decrease significantly, whereas the intensity of the transitions arising from the $^5D_0$ level increases. Then, cross-relaxation among excited states of Eu^{3+} (i.e. $^5D_{J=1-3}$) is higher and thus excited electrons relax to the $^5D_0$ level causing high emission intensity from that level. Another parameter that leads to observe changes in the emission spectrum is the local symmetry of the Eu^{3+} site. Eu^{3+} ions substitute La^{3+} at the C_{3v} symmetry site [143] of this structure and the emission spectrum of the Eu^{3+} ions near the centre of the nanoparticles is similar to that of the bulk [126]. However, Chang et al [73] observed that the emission spectrum of the Eu^{3+} ions showed gradually changes when the site occupied by Eu^{3+} ions varies from the centre toward the surface of the nanoparticles.

Pr^{3+} active ion

The electronic configuration of praseodymium is [Xe] $6s^2$ $4f^2$ and for the trivalent praseodymium is [Xe] $4f^1$. Among various activators, praseodymium ion is particularly interesting due to its specific energy level scheme enabling, among others, several optical transitions in the blue, green and red spectral range originating from excited $^3P_0$ (emitting in blue, green and red) and $^1D_2$ (emitting in red) manifolds [169]. The energy levels diagram of Pr^{3+} is shown in Figure 4.2 [170]. As Pr^{3+} shows a variety of emissions, Pr^{3+} doped active materials can be used as visible lasing media [171], phosphors [172], scintillators [173] and even 3-D displays [174]. In particular, it has been shown that in several sesquioxides, Pr^{3+} ions exhibit efficient red luminescence arising from the $^1D_2$ level, while the $^3P_0$ emission is totally quenched (e.g. in Y_2O_3, Gd_2O_3) [175]. The opposite behaviour has also been reported about the excellent blue-green luminescence arising from the ^3P_J manifold with partial or total quenching of the $^1D_2$ emission (e.g. in La_2O_3) [176].

Pr^{3+} ion has been previously introduced in several sesquioxides such as La_2O_3, Gd_2O_3, Y_2O_3, etc. [81], in LaOF [88], in tungstates [177], in yttrium aluminum garnet (YAG) [80], and in many other hosts.

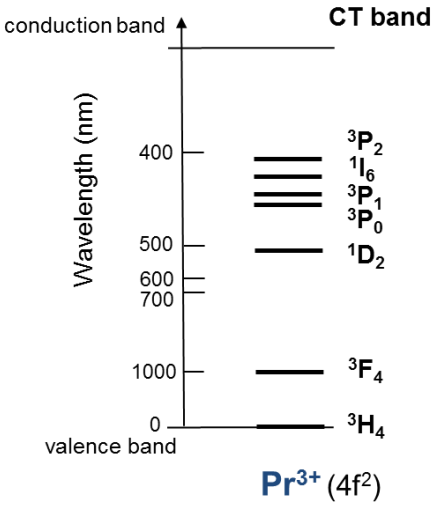

Figure 4.2. Simplified energy level diagram for the trivalent praseodymium ion doped into LaF_3 [170].

Pr^{3+} doped La_2O_3 nanoparticles

Several authors have characterized the luminescent properties of Pr^{3+} doped La_2O_3 nanoparticles [88,178]. The excitation spectrum of Pr^{3+}:La_2O_3 consist of several lines in the 440-550 nm region, corresponding to transitions within the $4f^2$ configuration ($^3H_4 \rightarrow {}^3P_{0,1,2}$ and $^1I_6$), and two broad bands with maxima at ~294 nm and ~240 nm. These bands are ascribed to the CT band and to the excitation via host lattice absorption, respectively [88]. It has been studied that the CT band shifts to lower energies as the Pr^{3+} concentration increases in the La_2O_3 host and an unchanging CT band position seems to be reached at about 5 mol% Pr^{3+} [88].

In the emission spectrum of Pr^{3+}:La_2O_3 nanoparticles, the typical emission peaks from the $^3P_0$ levels are observed when the emission is recorded at room temperature ($^3P_0 \rightarrow {}^3H_{4,5,6}$, $^3F_{2,3,4}$) [84]. However, other works [178] showed the $^1D_2 \rightarrow {}^3H_4$ transition in the emission spectrum recorded at low temperature (4.2 K), but only observed for concentrations of Pr^{3+} below 1 mol% due to concentration quenching effects. This quenching effect has also been observed for the $^3P_0$ emission for concentrations equal to or higher than 2 mol% Pr^{3+}. Although multipole-multipole interactions in Pr^{3+}:La_2O_3 cannot be excluded, Donegá et al. [88] ascribed this intense quenching effect to cross relaxation via super exchange interaction between Pr^{3+} ions.

La_2O_2S host for Ln^{3+} active ions

RE oxysulfide compounds (RE_2O_2S) have also been known as good host materials for a long time and possess favourable physical properties such as excellent chemical and thermal stability, insolubility in water and high luminescence efficiency [97]. All the elements of the lanthanide series, along with yttrium, can form compounds with the composition RE_2O_2S.

The name usually used is oxysulfide but alternative names are thio-oxide, sulfoxide, or oxide sulfide. The oxysulfides can be considered as intermediates between the oxides and the sulfides. However, optically speaking, compared to rare earth oxides, rare earth oxysulfides are more efficient phosphors with a wider excitation band [179]. RE oxysulfides are known as wide-gap (4.6-4.8 eV) materials suitable for doping with Ln^{3+} active ions [180]. Thus, these features make them very useful as catalysts, laser crystals, and luminescent host materials of several commercially available phosphors, such as red emitting phosphors for colour television picture tubes, up-conversion phosphors, etc.

Lanthanum oxysulfide (La_2O_2S) crystallizes in the trigonal system with the $P\bar{3}m1$ space group [93]. Its structure is closely related to the A-type rare-earth oxide structure, with the difference that in La_2O_2S one of the three oxygen sites is occupied by a sulfur atom. La^{3+}, which is found in C_{3v} symmetry sites in La_2O_2S, can be easily replaced by any active lanthanide ion. Thus, several Ln^{3+} such as Eu^{3+} [93], Tb^{3+} [95], or Tm^{3+} [95], have been introduced in La_2O_2S phosphors. It has been assumed that Ln^{3+} ions occupy the lanthanum site because of the slight difference of ionic radius between the cations. Ln^{3+} ions in La_2O_2S are coordinated to three sulfur and four oxygen ions.

<u>Eu^{3+} doped La_2O_2S nanoparticles</u>

Eu^{3+} activated lanthanum oxysulfide has been extensively investigated because it is a very efficient red phosphor used in television picture tubes [181].

The excitation spectrum of Eu^{3+} doped La_2O_2S nanoparticles presents a broad excitation band corresponding to two different CT bands. The first one, located at around 250 nm is attributed to the $O^{2-} \rightarrow Eu^{3+}$ transition whereas the other, located at around 320 nm, is attributed to the $S^{2-} \rightarrow Eu^{3+}$ transition [93]. Moreover, it is suggested that the quenching effect produced by the Eu^{3+} concentration is greater for the Eu-O CT band than for the Eu-S CTS band [179]. Therefore, the relative intensity of these two bands is affected by the Eu^{3+} doping concentration. At lower Eu^{3+} concentrations, the Eu-O band is dominant whereas above 2 mol% Eu^{3+} the excitation spectrum is dominated by the Eu-S band. In addition, the sharp lines due to f-f Eu^{3+} transitions, in some cases semi-overlapped by the Eu-S band, are also observed [179].

In the emission spectra, the typical transitions from the excited $^5D_0$ state to ^7F_J (J = 1-4) states are observed. The $^5D_0 \rightarrow {}^7F_2$ band is the most intense and is peaking at 625 nm.

<u>Eu^{3+} and Bi^{3+} energy transfer</u>

Activation of luminescent materials by various lanthanide ions has drawn much attention in the last few decades. The basis of co-doping or double activation of luminescent materials is to create an energy transfer mechanism between both ions, where one acts as a sensitizer (Bi^{3+}, Sb^{3+}, Ce^{3+}, etc.) and the other is the activator ion (Eu^{3+}, Sm^{3+}, Tb^{3+}, etc) [182]. This process is successfully achieved after strong interactions and movement of charge carriers

[183]. The physical process is schematically presented in Figure 4.3 [183], where *nx* indicates the occurrence of multiple Bi^{3+}-Bi^{3+} interactions.

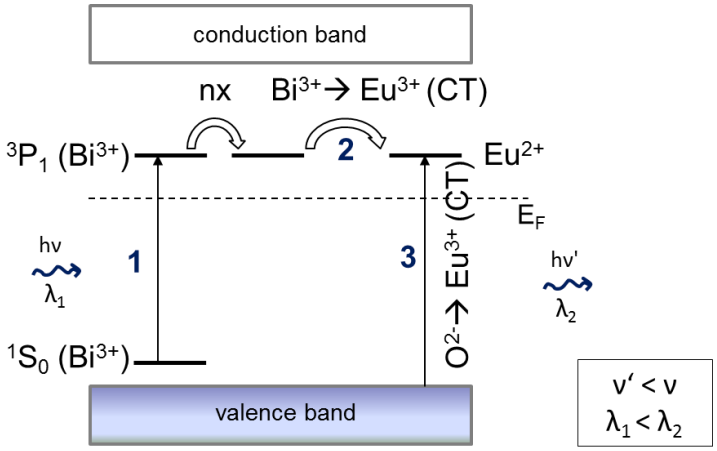

Figure 4.3. Schematic energy level model of Bi^{3+} sensitization of Eu^{3+} in Eu^{3+}:Bi^{3+}:La_2O_3 phosphors.

Although most of the Ln^{3+} ions are efficiently excited under cathode ray and short UV wavelength (210-250 nm) conditions, these phosphors have very poor response when excited at long UV wavelength (330-400 nm) radiation. On the other hand, Bi^{3+} has strong absorption ability in the UV and Vis region [184]. So that, by the energy transfer from Bi^{3+} to Ln^{3+} ions, the near UV efficiency can be greatly enhanced [185]. Moreover, the f-f typical transitions of Ln^{3+} also enhance their intensities through this energy transfer [186].

Other authors have already introduced Bi^{3+} and Eu^{3+} ions into different RE sesquioxides such as Y_2O_3 [183] and Gd_2O_3 [185], but also in tungstates, vanadates and into other materials [186,187]. From the best of our knowledge, no works about Eu^{3+} and Bi^{3+} co-doped RE oxysulfides have been found in the literature. Furthermore, only few were related with Eu^{3+} and Bi^{3+} co-doped La_2O_3 phosphors [188].

The relation with this thesis:

Since the spectral mismatch between the incident solar photon spectrum and the band gap of semiconductor based on which the photovoltaic device is fabricated is one of the major issues concerning the solar cells efficiency, Ln^{3+} ions has attracted much interest. The search for suitable and efficient Ln^{3+} doped materials for modifying the solar spectrum has been continuously intensified [19]. The Eu^{3+} doped compound nanoparticles have the ability to absorb in the ultraviolet-visible region of the electromagnetic spectrum and emit in the visible. However, since the absorption cross section of f-f transitions are very small, additional excitation mechanisms have to be explored to achieve efficient solar spectrum modification using Eu^{3+} or other lanthanide ions doped compounds. Tailoring the Eu-O CT band by following different strategies can be one of the solutions to increase the efficiency of solar spectrum modification, and then increase the efficiency of the existing solar cells.

4.2. Photoluminescence of doped lanthanum compounds

In the next part of this chapter we will show and discuss the luminescence properties of all the samples prepared, first by showing the luminescence properties of a representative sample and then, we will compare the luminescence results obtained as a function of the different synthesis methods used. The main reason for the preparation of those samples exposed in Chapter 3 was to tailor the position of the CT state band towards longer wavelengths. Thus, an important emphasis about the characterization of the CT band is developped in this section.

4.2.1. Excitation spectrum of europium doped lanthanum oxide (Eu^{3+}:La_2O_3) nanoparticles

Figure 4.4 shows the excitation spectrum of Eu^{3+}:La_2O_3 nanoparticles (*Eu^{3+}-CPech1*). In general, the excitation spectra were obtained by monitoring the emission at 626 nm corresponding to the $^5D_0 \rightarrow {}^7F_2$ transition that shows the most intense peak in the emission spectra [103]. That spectrum was recorded from 220 to 550 nm in a 90º geometry and taking the measurements every 1 nm at a scanning rate of 1 nm·s^{-1}.

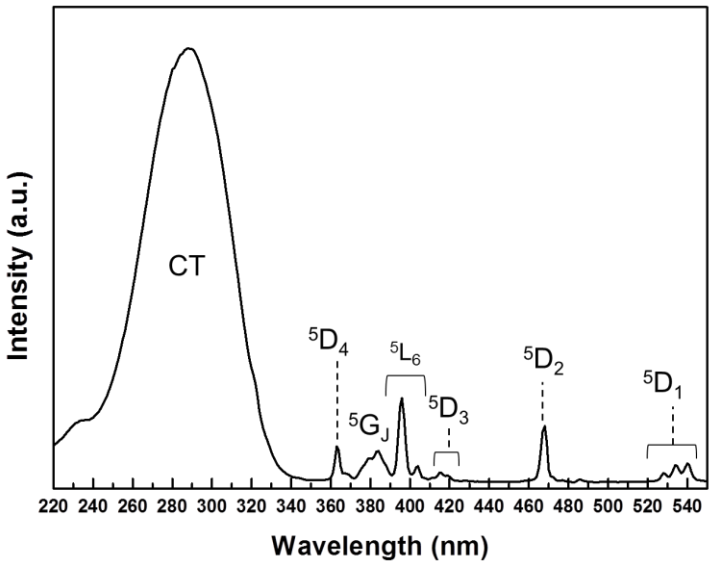

Figure 4.4. Excitation spectrum of Eu^{3+}:La_2O_3 nanoparticles monitored at λ_{emi} = 626 nm.

The band peaking at around 290 nm in the UV region spectra was attributed to the CT band. In the charge transfer excitation, oxygen 2p electrons are excited into 4f levels, and the position of the charge transfer excitation band is determined by the energy difference between the O 2p valence band and the 4f levels of Eu^{3+} [166]. According to Liu et al. [71], together with the CT band we also observed a weak shoulder at about 230 nm which was attributed to the band related to the host excitation, i.e., electronic transitions from the O 2p

valence band to the La (5d6s) conduction band (La_2O_3 host lattice absorption) [189]. Furthermore, the excitation spectrum also showed the typical Eu^{3+} f-f transitions: $^7F_J \rightarrow {}^5D_J$ (J = 1-4), $^7F_0 \rightarrow {}^5G_J$ and $^7F_0 \rightarrow {}^5L_6$ with low intensity compared to the CT band of the Eu^{3+}-O^{2-} transition. Such Eu^{3+} f-f transitions were also observed for this material by other authors [103,139,190]. Depending on the method used to synthesize the Eu^{3+}:La_2O_3 nanoparticles, the f-f transitions can show different relative intensities. For instance, Liu et al. [139] obtained much stronger excitation properties of Eu^{3+} f-f transitions when using CA and PEG in the sol-gel method. The CT band position at about 290 nm was also in agreement with the ones reported in the literature by other authors [72,103,139,190]. However, the position of the CT band is further discussed throughout this chapter.

4.2.2. Emission spectrum of europium doped lanthanum oxide (Eu^{3+}:La_2O_3) nanoparticles

The emission spectrum of Eu^{3+}:La_2O_3 nanoparticles (*Eu^{3+}-CPech1*) was recorded from 550 to 720 nm at room temperature, after pumping into the CT band at 290 nm (see Figure 4.5). The measurements were taken every 1 nm at a scanning rate of 1 nm·s^{-1}. By pumping into the CT band, O 2p electrons are excited into 4f levels and consequently the CT relaxes to the 4f levels of Eu^{3+}.

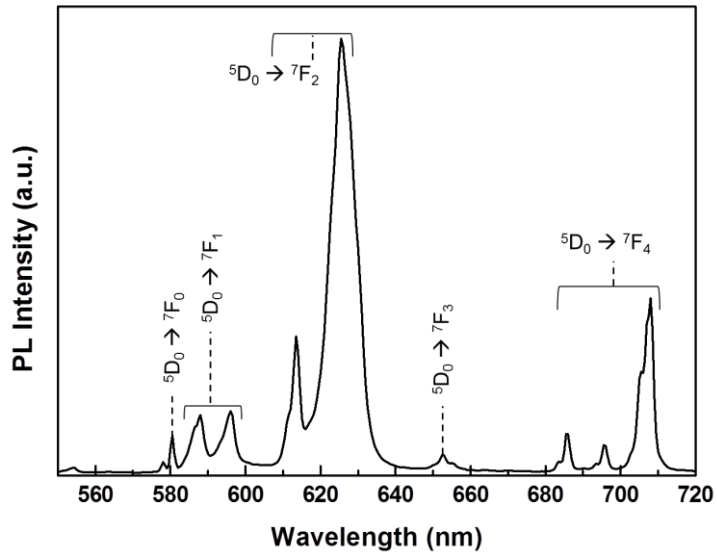

Figure 4.5. Emission spectrum of Eu^{3+}:La_2O_3 nanoparticles monitored at λ_{exc} = 290 nm.

In this figure, the typical emission spectrum of Eu^{3+} due to the $^5D_0 \rightarrow {}^7F_J$ (J = 0-4) transitions was observed. This indicates that Eu^{3+} can be efficiently excited in La_2O_3 nanoparticles through the energy transfer between oxygen and europium ions. The spectrum is dominated by the $^5D_0 \rightarrow {}^7F_2$ transition which consists of two peaks at 613 and 626 nm, respectively. The fact that the spectrum is dominated by this transition confirms the results obtained by Park et

al. [103] for a sample doped with 5 mol% Eu^{3+}. It also indicated that europium is located in a structural site without an inversion centre [143], such as the crystallographic site occupied by La^{3+} in this structure (C_{3v}).

The $^5D_0 \rightarrow {}^7F_1$ transition was seen as two peaks located at 587 and 595 nm, respectively. It is well known that the electric dipolar $^5D_0 \rightarrow {}^7F_2$ transition (hypersensitive) is very sensitive to the ligand field, and it is sensitive to small changes in the chemical environment around Eu^{3+} ions and the coupling strength of the host. Instead, due to the magnetic dipole transition, the $^5D_0 \rightarrow {}^7F_1$ transition is independent of the local environment of europium, it does not depend strongly on coordination, and it hardly varies with the crystal field strength introduced by the matrix around the Eu^{3+} ion. So, it can be taken as a reference for different materials. Therefore, because of their different mechanism, the intensity ratio between the intensity of the $^5D_0 \rightarrow {}^7F_2$ transition at 626 nm and the intensity of the $^5D_0 \rightarrow {}^7F_1$ transition at 595 nm, can be used as a spectroscopic probe for evaluating the asymmetry of the coordination polyhedron of the Eu^{3+} ions, and gives a measure of the degree of distortion from the inversion symmetry of the local environment of the Eu^{3+} ion in the matrix [103]. This parameter is known as the I_2 ratio or asymmetry ratio. A large value of this ratio, means that the electric dipole interaction is enhanced, associated to a stronger crystal field in the short range, that can be related to an increase of the covalency of the structure or to a distortion of the bonds surrounding the active ion. This ratio was 6.7 for the *Eu^{3+}-CPech1* sample. In order to compare this ratio with other ratios, we calculated by ourselves other I_2 ratios from emission spectra of the Eu^{3+}:La_2O_3 nanoparticles reported by other authors [72,103,139]. The emission spectra we use to calculate these I_2 ratios are shown in Figure 4.6. We can say that the I_2 we obtained was within the maximum values reported indicating that europium in the host lattice is located in a low symmetry site, as was expected after observing the high intensity of the peak corresponding to the $^5D_0 \rightarrow {}^7F_2$ transition.

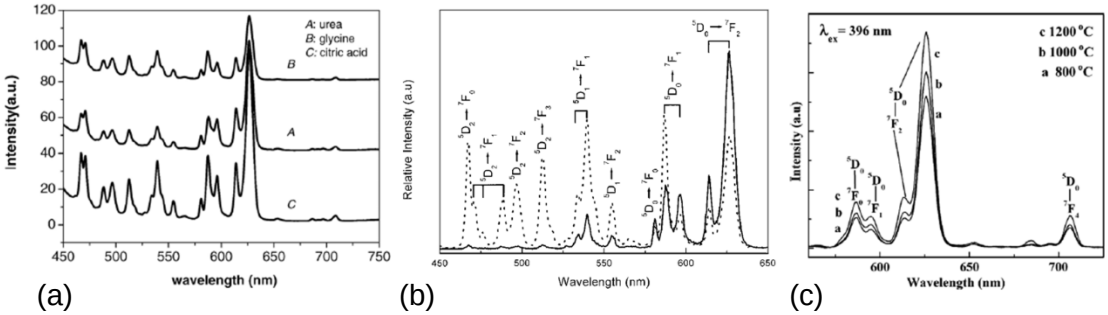

Figure 4.6. Emission spectra of Eu^{3+}:La_2O_3 nanoparticles reported in the literature and used to calculate the I_2 ratios **(a)** [72], **(b)** [103] and **(c)** [139].

Another parameter less studied by the authors, but also giving valuable information in the luminescence spectra analysis, is the I_1 or fluorescence intensity ratio. It is calculated from the relative intensities of the two peaks of the $^5D_0 \rightarrow {}^7F_2$ transition and located at around 626

nm and 615 nm. Liu et al. [71] have used this parameter to observe differences as a function of the annealing temperature used during the calcination process but also as a function of the Eu^{3+} doping concentration. On one hand, Liu et al. [71] observed that the I_1 ratio decreases when increasing the Eu^{3+} concentration from 1 mol% to 3 mol% but when the concentration of Eu^{3+} increases up to 10 mol%, the I_1 increases gradually. On the other hand, the I_1 ratio decreases gradually when increasing the calcination temperature from 1073 to 1373 K. That fact might be attributed to strong agglomeration effects [71]. The I_1 ratio obtained for the *Eu^{3+}-CPech1* sample was 3.2. In comparison with other values reported [71] and calculated by ourselves from the emission spectra reported by other authors [72,84], this I_1 ratio would correspond to a Eu^{3+} concentration between 5-10 mol% in the La_2O_3 sample. The emission spectra reported by other authors for Eu^{3+}:La_2O_3 and that we used to calculate the I_1 ratio, are shown in Fig. 4.7.

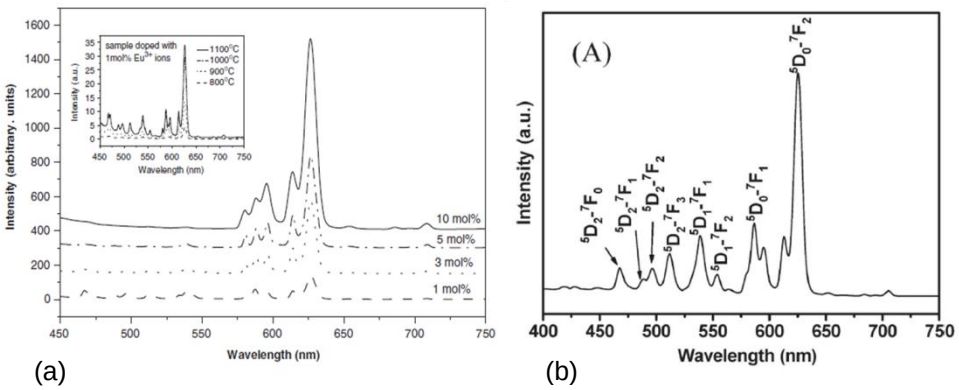

Figure 4.7. Emission spectra of Eu^{3+}:La_2O_3 nanoparticles reported in the literature to compare the I_1 and I_2 values reported by other authors **(a)** [71], and used to calculate the I_1 and I_2 from the spectra **(b)** [84].

The $^5D_0 \rightarrow {}^7F_0$ transition, that should have been completely forbidden since the transition probability between $J = 0$ and $J' = 0$ is zero at first order, was seen as a small peak at 580 nm. Nieupoort and Blasse [154] reported that the 0-0 transition might be partially allowed due to the presence of a linear crystal field term in some lattice site symmetries such as C_s, or C_{nv}. So, the observation of the 0-0 transition agrees with the substitution of Eu^{3+} in the regular La^{3+} site in the structure of these nanoparticles with symmetry C_{3v}.

In conclusion, we can say that the PL spectrum shown in Figure 4.5 was in agreement with the PL spectra of Eu^{3+}:La_2O_3 phosphors synthesized by other techniques [66-68,129]. In this case, however, the intensity ratios (I_1 and I_2) changed slightly. As I_1 and I_2 depend on many factors, usually these ratios change for the same compund ((5 mol%)Eu^{3+}:La_2O_3) if it is prepared by different synthesis methods. Finally, we were also able to identify the bands corresponding to the $^5D_0 \rightarrow {}^7F_3$ and $^5D_0 \rightarrow {}^7F_4$ transitions that appeared at longer wavelengths. The apparent broadness of the emission bands of Eu^{3+} in our sample is due to the large spectral bandwidth (1 nm) used to record this spectrum.

4.2.3. Fluorescence lifetime of nanoparticles

The fluorescence lifetime of Eu^{3+}:La_2O_3 nanoparticles was measured. Figure 4.8 shows the fluorescence lifetime at room temperature of the *Eu^{3+}-CPech1* sample. Decay curves monitored at 626 nm were measured and the lifetime derived from single exponential fitting was 1.05 ms. This lifetime was in concordance with other Eu^{3+}:La_2O_3 samples found in the literature [126], which were formed by particles with sizes around 9 nm (1.02 ms) while samples formed by larger particles (20-90 nm) showed higher lifetimes (1.25-1.96 ms).

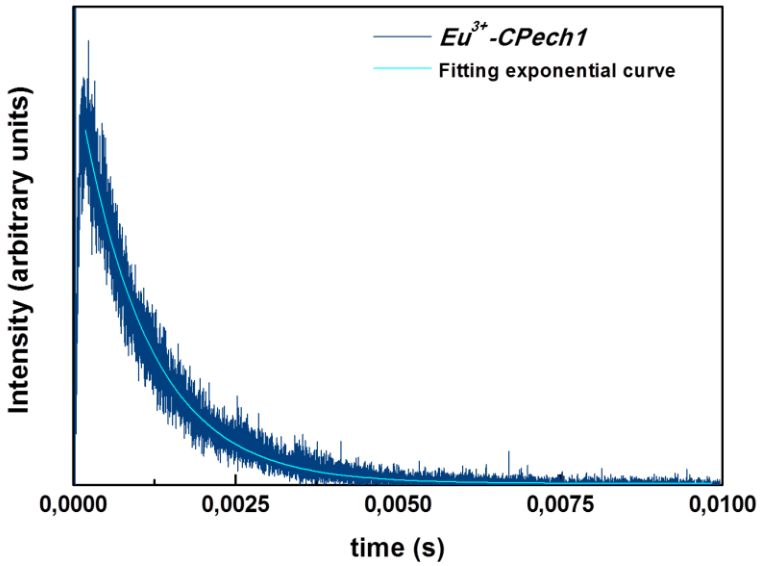

Figure 4.8. Lifetime decay of the *Eu^{3+}-CPech1* sample recorded at room temperature.

4.2.4. Excitation and emission spectra of europium doped lanthanum oxide (Eu^{3+}:La_2O_3) nanoparticles as a function of the synthesis method used

The excitation and emission spectra were studied also for the rest of the doped samples prepared by the different synthesis methods. The spectra were normalized in intensity at around 290 nm and 626 nm for the excitation and emission spectra, respectively, to avoid differences in terms of quantity of sample and power of the pumping lamp. Figure 4.9(a) shows the excitation spectra with the characteristic CT bands and the f-f Eu^{3+} transitions. The position corresponding to the maximum intensity of the CT bands was found within the range 288-293 nm, as observed in more detail in Figure 4.9(b). Table 4.1 lists the position of the maximum intensity of the CT band for each of these samples.

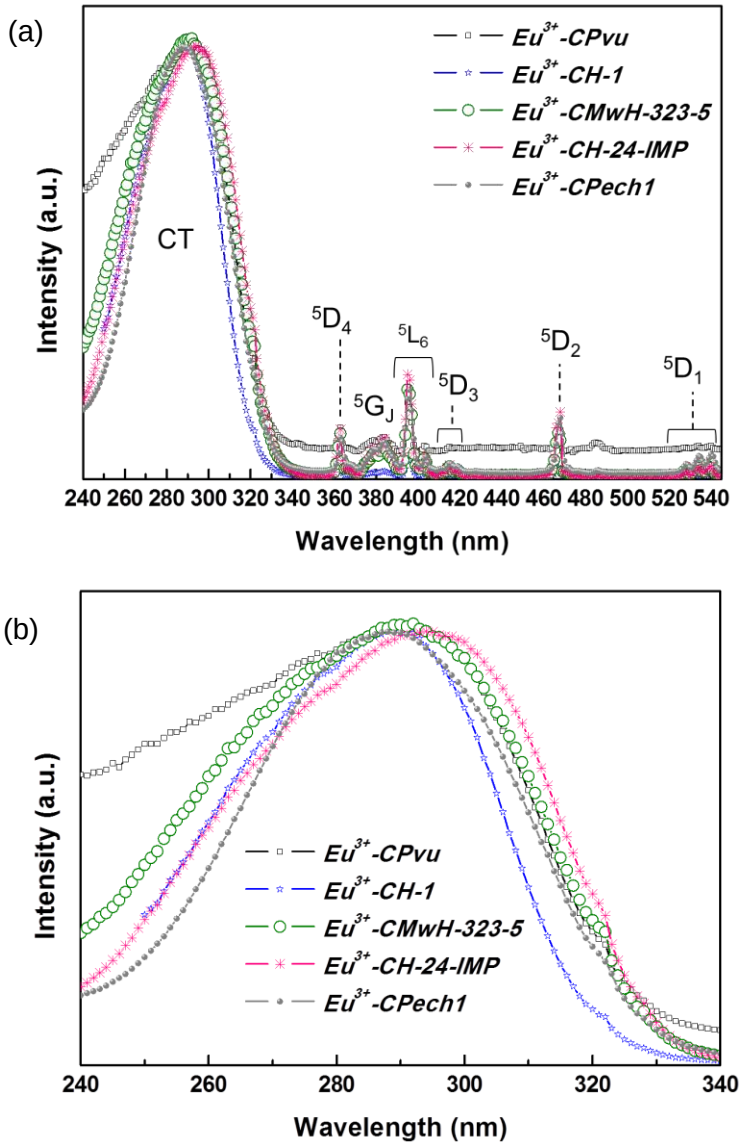

Figure 4.9. (a) Excitation spectra of Eu^{3+}:La_2O_3 samples synthesized by different methods. **(b)** Detailed view of the position of the CT band.

This slight difference in the position of the maximum of the CT band might be attributed to the different synthesis methods used because it is well known from other authors [66], that the CT band shifts with dopant concentration changes. In theory, all samples must contain 5 mol% Eu^{3+}, but at the same time, they were prepared by different methods. Consequently, different preparation conditions might affect the real Eu^{3+} concentration in La_2O_3 and it could be a factor important enough to be responsible for the shift on the position of the CT band. A good technique and widely used by other authors [191] for determining the concentration of doping ions into the matrix host is the Electron probe microanalysis (EPMA) technique.

However, for Eu^{3+}:La_2O_3 samples, it was not possible to measure the concentration of Eu^{3+} by this technique due to the fast re-hydroxylation of this material. Basically, the EPMA technique is based on the X-rays detected at particular wavelength associated at one element. However, this technique requires having a flat surface to conduct quantitative analysis. The re-hydroxylation of this material induced a roughness in the samples that did not allow using the EPMA technique. The shift observed in the CT band might also be associated to the appearance of Eu^{3+}-Eu^{3+} pairs in the system associated to a decrease in the average distance between Eu^{3+} ions. Nevertheless, from these results we could only say that synthesizing Eu^{3+}:La_2O_3 nanoparticles by different synthesis methods, using the experimental conditions we used did not lead to significant differences in the position of the CT band.

Figure 4.10 shows the emission spectra for all the samples recorded from 550 to 725 nm under different excitation wavelengths, since the CT had different maximum position. So that, the excitation wavelengths were 289, 289, 292, 293 and 288 nm for the *Eu^{3+}-CPvu*, *Eu^{3+}-CH-1*, *Eu^{3+}-CMwH-323-5*, *Eu^{3+}-CH-24-IMP* and *Eu^{3+}-CPech1* samples, respectively (see Table 4.1). The typical peaks corresponding to transitions from different ^5D_J (J = 0, 1, 2) states to the $^7F_{J'}$ (J' = 0, 1, 2, 3, 4) fundamental state were identified in all cases and the most intense peak was centred at 626 nm for all the samples and corresponded to the $^5D_0 \rightarrow {}^7F_2$ transition. Apparently the results did not show differences depending on the method used to prepare the sample. However, by analysing the values obtained for the asymmetry ratio (I_2) some differences were observed. I_2 were calculated by comparing the intensities of the $^5D_0 \rightarrow {}^7F_2$ transition, located at 626 nm, and the $^5D_0 \rightarrow {}^7F_1$ transition, located at 595 nm.

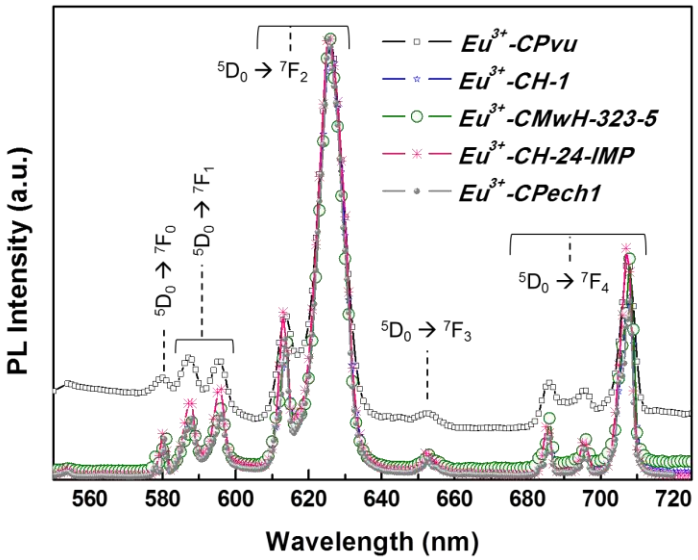

Figure 4.10. Emission spectra of Eu^{3+}:La_2O_3 samples synthesized by different methods.

Table 4.1 also shows the I_2 values obtained for the samples synthesized by the different methods. The I_2 values were found ranging 3.7-6.7. The lower values 3.7 and 4.9 were

observed for the *Eu^{3+}-CPvu* and *Eu^{3+}-CH-24-IMP* samples, respectively, whereas the higher values, 6.2, 6.6 and 6.7, were observed for the *Eu^{3+}-CMwH-323-5*, *Eu^{3+}-CH-1* and *Eu^{3+}-CPech1* samples, respectively. These differences observed for I_2 values could be attributed to the different synthesis methods used to prepare the samples. As commented above in the studies of the CT band shift, the use of different synthesis methods can cause differences in the active ion concentration, but also differences in the morphology of the nanoparticles. For instance, the lower I_2 value, observed for the *Eu^{3+}-CPvu* sample, was obtained for nanoparticles with a nanorod-shape, which was quite different to respect to the other samples. In agreement to this, other authors that prepared ultra-long Eu^{3+}:La_2O_3 nanowires obtained spectra from which we calculated I_2 values of 3.5 [84] and others that prepared round-shaped particles obtained spectra from which we calculated I_2 values of 6.5 [72] (see Figs. 4.7(b) and 4.6(a), respectively). In the nanowire/nanorod particles, the number of surface defects should increase due to the large surface-to-volume ratio. Consequently there are larger amount of atoms located at the surface causing higher disorder than the inside atoms and producing a lot of quenching centres [127]. It is attributed to the stronger non-radiative relaxation for the $^5D_0 \rightarrow {}^5D_1$ and $^5D_1 \rightarrow {}^5D_0$ levels which causes the decrease of the I_2 intensity ratio. The same reason can be used to explain also the low I_2 ratio observed for the *Eu^{3+}-CH-24-IMP* sample (Table 4.1), since as it was doped by the wetness impregnation method, the amount of Eu^{3+} ions in the surface was supposed to be higher than that one would expect for the rest of the samples.

Table 4.1. CT band position, asymmetry ratio (I_2) and fluorescence ratio (I_1) values obtained from the emission spectra of the Eu^{3+}:La_2O_3 samples synthesized by different methods.

Sample	CT band position (nm)	I_2 (asymmetry ratio)	I_1 (fluorescence ratio)
Eu^{3+}-CPvu	289	3.7	2.7
Eu^{3+}-CH-1	289	6.6	3.9
Eu^{3+}-CMwH-323-5	292	6.2	3.3
Eu^{3+}-CH-24-IMP	293	4.9	2.7
Eu^{3+}-CPech1	288	6.7	3.2

From the emission of the $^5D_0 \rightarrow {}^7F_2$ transition which consists of two bands, at 614 and 626 nm, one can obtain the fluorescence intensity ratio I_1. Although all the samples were calcined under the same conditions (at 1273 K for 2 h) and doped with 5 mol% Eu^{3+}, but using different synthesis methods, consequently the amount of Eu^{3+} in the samples can be different. Since it was not possible to measure the exact amount of Eu^{3+} in the samples due to their hygroscopic nature, this is an approach that we can use to know if there exist significant differences on the concentration of Eu^{3+} depending on the synthesis method used. In previous

studies, Liu et al. [71] prepared La_2O_3 nanoparticles with 1, 3, 5 and 10 mol% Eu^{3+} by the combustion synthesis method and the I_1 parameter was 6.6, 1.45, 2.5 and 3.5, respectively. The I_1 parameter for our samples was 2.73, 3.85, 3.30, 2.70, and 3.15 for *Eu^{3+}-CPvu*, *Eu^{3+}-CH-1*, *Eu^{3+}-CMwH-323-5*, *Eu^{3+}-CH-24-IMP* and *Eu^{3+}-CPech1* samples, respectively (see Table 4.1). We could say that the difference obtained for the I_1 values was significant because the minimum (2.70) and the maximum (3.85) values differed from more than one unit, which would correspond to samples doped with Eu^{3+} concentrations between 5 mol% and 10 mol% [71]. Thus, we can conclude that it seems that our samples contain different concentrations of Eu^{3+} ranging from 5 mol% to above 10 mol%.

Once we observed no significant differences in the CT band position among the La_2O_3 nanoparticles produced by different synthesis methods used, we tried to optimize one of the routes of synthesis we explored, the sol-gel Pechini method, by changing the initial reagents used. This was the reason for synthesizing the rest of samples through this method: *Eu^{3+}-CPech2*, *Eu^{3+}-CPech1B*, and *Eu^{3+}-CPech2B*.

The *Eu^{3+}-CPech2* sample, which was the one synthesized by using citric acid and polyethylene glycol, substituting EDTA and EG, respectively, presented significant differences in its spectroscopic characterization when compared to the rest of the samples presented up to now. Figures 4.11(a) and 4.11(b) show the comparison of the excitation and emission spectra of *Eu^{3+}-CPech2* and *Eu^{3+}-CPech1* samples. The excitation spectra were recorded by monitoring the emission at 626 nm. Figure 4.11(a) shows that the position of the CT band of the *Eu^{3+}-CPech2* sample was shifted by 9 nm towards higher wavelengths in comparison to the position of the CT band of the *Eu^{3+}-CPech1* sample, with the maximum intensity located at 297 nm. This could be attributed to a certain distortion of the Eu-O coordination polyhedron which affects the Eu-O bond distance and thus, the position of the CT band, or to a different Eu^{3+} concentration in the samples. However, despite the shift obtained, both bands still comprised the same range of the electromagnetic spectrum (within the range of 240-330 nm). Therefore, we can say that by changing the reagents used to prepare the polymeric network in the sol-gel method, we only changed the position of the CT band maximum and did not extended the absorption capacity towards the red part of the electromagnetic spectrum.

Regarding the emission spectrum of the *Eu^{3+}-CPech2* sample (Fig. 4.11(b)), it exactly coincides with that recorded previously for the *Eu^{3+}-CPech1* sample. The I_2 and I_1 values for the *Eu^{3+}-CPech2* sample were 6.6 and 3.8, respectively. These ratios obtained were within the range found in the samples studied up to now (see Table 4.2). The I_2 value is similar to that obtained for the *Eu^{3+}-CPech1* sample. The higher I_1 value observed for the *Eu^{3+}-CPech2* sample (3.8) compared to the one observed for the *Eu^{3+}-CPech1* sample (3.2) might be attributed to the fact that PEG allows obtaining samples with higher Eu^{3+} concentration [139]. Liu et al. [139] observed that, by using PEG, the networks of the polymeric chain were formed steadily. Moreover, it increases the potentials heat of combustion which is favourable

for crystal growth, reducing the number of defects on the surface of the particle. From the emission spectrum that Liu et al. [139] showed (see Fig. 4.6(c)) we calculated the I_2 and I_1 with 7.2 and 4.5 values, respectively, for a sample of La_2O_3 containing 8 mol% Eu^{3+} and which had been synthesized using the same methodology we used to synthesize the *Eu^{3+}-CPech2* sample.

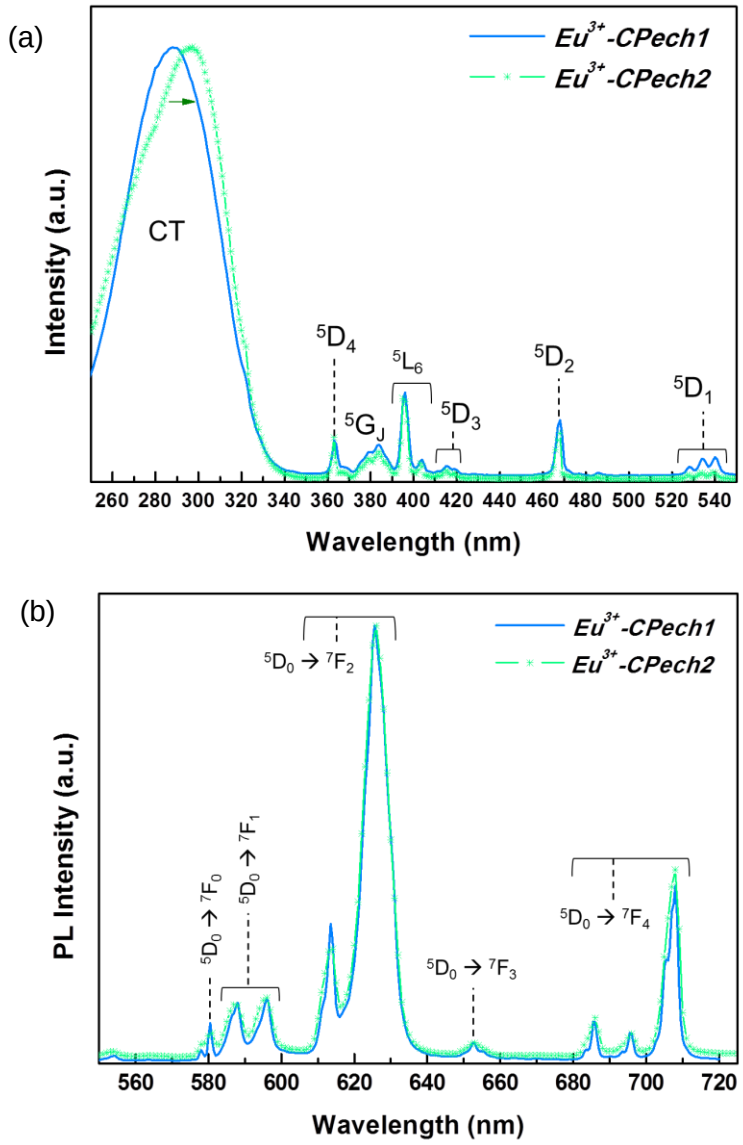

Figure 4.11. (a) Excitation and **(b)** emission spectra of the *Eu^{3+}-CPech2* sample compared to that of the *Eu^{3+}-CPech1* sample.

Figures 4.12(a) and 4.12(b) show the excitation and emission spectra of two samples prepared by the sol-gel method but using chlorides as starting reagents (*Eu^{3+}-CPech1B* and *Eu^{3+}-CPech2B*). In order to easily compare the changes with the samples synthesized with

the nitrate reagents, the excitation and emission spectra of the *Eu^{3+}-CPech1* sample are also shown in these two graphs.

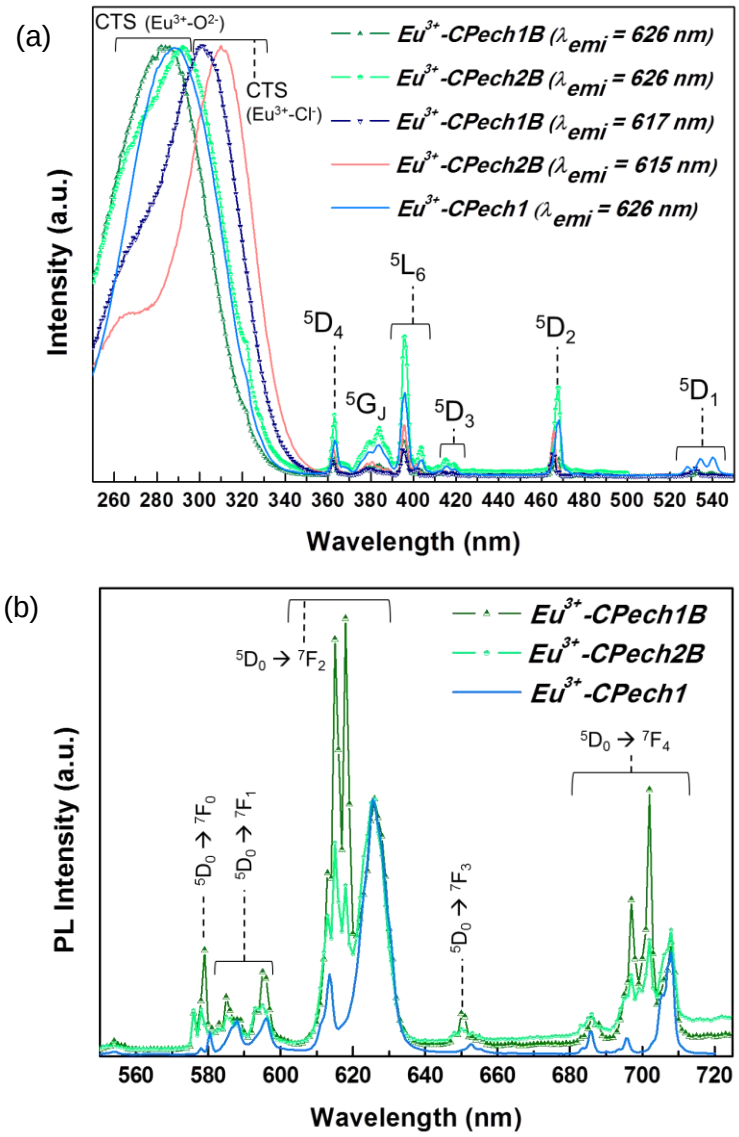

Figure 4.12. (a) Excitation and **(b)** emission spectra of Eu^{3+}:La_2O_3 samples synthesized using chlorides reagents in the sol-gel modified Pechini method.

As usually, the excitation spectra were recorded by monitoring the emission at 626 nm and the results were normalized to the maximum intensity of the CT band. The *Eu^{3+}-CPech1B* sample shows a CT band with a maximum located at 284 nm, while the *Eu^{3+}-CPech2B* sample shows the maximum of this band at 292 nm, both at similar positions than the CT band observed for the *Eu^{3+}-CPech1* sample. However, when we recorded the emission spectra of the *Eu^{3+}-CPech1B* and *Eu^{3+}-CPech2B* samples (see Fig. 4.12(b)), new emission

peaks appeared with their maxima located at 617 and 615 nm, respectively, due to the presence of the LaOCl phase [192], as identified from their XRD patterns in Chapter 3 (Fig. 3.20(a-b)).

Thus, the PL spectra corroborated the presence of both phases containing Eu^{3+}, La_2O_3 and LaOCl. Oxychlorides crystallize in the tetragonal system with the space group P4/*nmm*. In this structure, La^{3+} ions are coordinated to four oxygen ions and four chloride ions in a C_{4v} symmetry site. That means that when La^{3+} are replaced by Eu^{3+}, Eu^{3+} is located in two different symmetry sites, C_{3v} and C_{4v}, with different environment surrounding it. Therefore, differences in the number of peaks and in the relative intensity between the peaks were expected in the emission spectrum. When we used the 617 and 615 emission wavelengths to monitor the excitation spectra of the *Eu^{3+}-CPech1B* and *Eu^{3+}-CPech2B* samples, respectively, the results obtained were significantly different (see Fig. 4.9(a)). The position of the maximum of the CT band was now shifted towards longer wavelengths and a weak shoulder at lower wavelengths was formed. We attributed this fact to the coexistence of the two phases, La_2O_3 and LaOCl, and so that each phase could be the responsible for one CT band. The weak shoulder at ~ 275 nm would correspond to the Eu-O CT band and the intense band at longer wavelengths would correspond to the Eu-Cl CT band [165]. Similar to the La_2O_3 structure, in the LaOX (X = F, Cl, Br) the charge transfer band is also determined by the interaction between the ligand halogen anions and the 4f levels of Eu^{3+}.

As a preliminar conclusion, it is clear that the samples prepared using the chloride reagents showed the reddest-shift CT band position up to now, although it is due to the presence of a new compound.

Since the *Eu^{3+}-CPech1B* and *Eu^{3+}-CPech2B* samples showed distinguished emission peaks coming from the two different phases we used the peaks corresponding to the La_2O_3 phase to calculate the I_2 and I_1 ratios (see Table 4.2). Then those ratios could be compared with the ratios studied up to now for the samples synthesized by using different methods. The I_1 ratio obtained for the *Eu^{3+}-CPech2B* sample, synthesized using PEG, was slightly higher than that obtained for the *Eu^{3+}-CPech1B* sample. Since we observed a similar tendency when we compared the I_1 ratio for the *Eu^{3+}-CPech1* and *Eu^{3+}-CPech2* samples (see Table 4.2), we believe that this would confirm that by using PEG, the Eu^{3+} concentration in the resulting La_2O_3 nanoparticles was higher than when using EG in the synthesis process. However, it is worth to notice that the *Eu^{3+}-CPech1B* sample was formed of 42 % of La_2O_3 and 58% of LaOCl whereas the *Eu^{3+}-CPech2B* sample was formed of 62 % of La_2O_3 and 38% of LaOCl. In other words, for the *Eu^{3+}-CPech2B* sample, the number of Eu^{3+} ions localized in the C_{3v} position (the one responsible of the emission peaks used to calculate these I_1 ratios) was higher the number of Eu^{3+} ions localized in the same position for the *Eu^{3+}-CPech1B* sample. The fact of having a lower amount of La_2O_3 than in the samples prepared from nitrates, which presented the La_2O_3 as the only crystalline phase, is also responsible for the low I_1 values obtained for these samples. Regarding the asymmetry ratio, the one calculated for the

Eu^{3+}*-CPech2B* sample was considerably higher than that for the *Eu*$^{3+}$*-CPech1B* sample (see Table 4.2). Here, the fact of having different percentage of La_2O_3 and LaOCl in the two samples seemed to be the best reason to explain these differences between the I_2 ratios obtained.

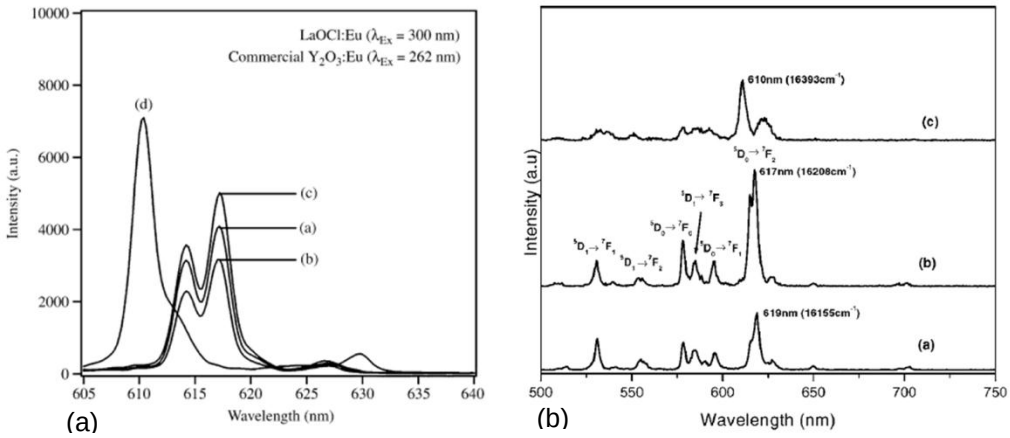

Figure 4.13. Excitation spectra of Eu^{3+}:LaOCl nanoparticles reported in the literature taken to calculate the I_1 and I_2 values from the spectra reported by other authors **(a)** [192] **(b)** [165].

Table 4.2. CT band position, asymmetry ratio (I_2) and fluorescence ratio (I_1) values obtained from the emission spectra of the Eu^{3+}:La_2O_3 samples synthesized by using different reagents in the Pechini method.

Sample	CT band position (nm)	I_2 (asymmetry ratio)	I_1 (fluorescence ratio)
Eu^{3+}*-CPech1*	288	6.7	3.2
Eu^{3+}*-CPech2*	297	6.6	3.8
Eu^{3+}*-CPech1B* (La_2O_3)	284	3.3	1.4
Eu^{3+}*-CPech2B* (La_2O_3)	292	5.8	1.8
Eu^{3+}*-CPech1B* (LaOCl)	301	5.2	1.1
Eu^{3+}*-CPech2B* (LaOCl)	310	3.3	0.8

Furthermore, the different wavelengths of La_2O_3 and LaOCl phases corresponding to each transition are listed in Table 4.3 and the I_1 and I_2 ratios were also calculated by using the emission peaks from the LaOCl phase (see Table 4.2) for the *Eu*$^{3+}$*-CPech1B* and *Eu*$^{3+}$*-CPech2B* samples. The values obtained had the opposite behaviour than the ratios calculated from the emission peaks of the La_2O_3 phase. In other words, the *Eu*$^{3+}$*-CPech1B* sample showed now higher I_2 and I_1 ratios than those obtained for the *Eu*$^{3+}$*-CPech2B* sample, as expected since the *Eu*$^{3+}$*-CPech1B* sample was constituted by a larger concentration of the

LaOCl phase (58 %) than the *Eu^{3+}-CPech2B* sample (38%). The I_1 and I_2 ratios obtained for the LaOCl phase were in good agreement with those calculated by ourselves from the emission spectra reported by other authors [165,192] and which are shown in Figure 4.13.

Table 4.3. Wavelength values of the photoluminescence peaks of Eu^{3+} in La_2O_3 and LaOCl phases.

Transition	Eu^{3+}:La_2O_3 peak position (nm)	Eu^{3+}:LaOCl peak position (nm)
$^5D_0 \rightarrow {}^7F_0$	580	579
$^5D_0 \rightarrow {}^7F_1$	587, 596	585, 595
$^5D_0 \rightarrow {}^7F_2$	613, 625	615, 617
$^5D_0 \rightarrow {}^7F_3$	652	650
$^5D_0 \rightarrow {}^7F_4$	685, 695, 708	679, 702

4.2.5. Excitation and emission spectra of europium and bismuth co-doped lanthanum oxide (Eu^{3+}:Bi^{3+}:La_2O_3) nanoparticles

The excitation and emission spectra of the *Eu^{3+}:(1%)Bi^{3+}-CPech1*, *Eu^{3+}:(3%)Bi^{3+}-CPech1* and *Eu^{3+}-CPech1* samples are shown in Figures 4.14(a) and 4.14(b), respectively. The excitation spectrum of *Eu^{3+}:(1%)Bi^{3+}-CPech1* and *Eu^{3+}:(3%)Bi^{3+}-CPech1* samples showed a CT band with a maximum centred at 313 nm. The shift of the CT band corresponding to the *Eu^{3+}-CPech1* sample to that corresponding to the *Eu^{3+}:(1%)Bi^{3+}-CPech1* and *Eu^{3+}:(3%)Bi^{3+}-CPech1* samples was about 25 nm. The Eu^{3+} f-f transitions were, however, seen at the same position (within the range 360-550 nm) as in the other samples studied previously. However, the intensity of the 4f-4f transitions of Eu^{3+} also increased when co-doping with Bi^{3+} ions, which was more noticeable when the Bi^{3+} concentration was increased from 1 mol% to 3 mol% in Eu^{3+}:La_2O_3 nanoparticles. The shift of the CT bands to higher wavelengths can be attributed to an efficient energy-transfer process from Bi^{3+} to Eu^{3+} as other authors have already observed between both ions in other matrices (Bi^{3+}:Eu^{3+}:Gd_2O_3 and Bi^{3+}:Eu^{3+}:Y_2O_3) [185,193]. Bi^{3+} ions have a $6s^2$ electronic configuration with the $^1S_0$ level as the ground state and a 6s6p configuration with the excited states that split into $^3P_0$, $^3P_1$, $^3P_2$, and $^1P_1$ states in the sequence of increasing energy. As no other configurations are taken into account, the transitions from the $^1S_0$ level to the $^3P_0$ and $^3P_2$ levels are completely spin forbidden. The other two excited levels $^3P_1$ and $^1P_1$ are mixed by spin-orbit coupling. Thus, the broad absorption centred at 313 nm might correspond to the overlap of the Eu^{3+}-O^{2-} CT band and the Bi^{3+} transitions from the $^1S_0$ level towards the $^3P_1$ and $^1P_1$ levels. No extra peaks from Bi^{3+} appeared in the excitation spectrum. We attributed this fact to two different causes: one was due to the overlapping or combination of any possible band from Bi^{3+} with the strong band of Eu^{3+}-O^{2-} from 250 to 350 nm. The other reason was that the Bi^{3+} ions play a role not only as a

luminescence activator but also as a sensitizer for Eu^{3+} ion, which would confirm that a significant and efficient energy-transfer happened between both ions.

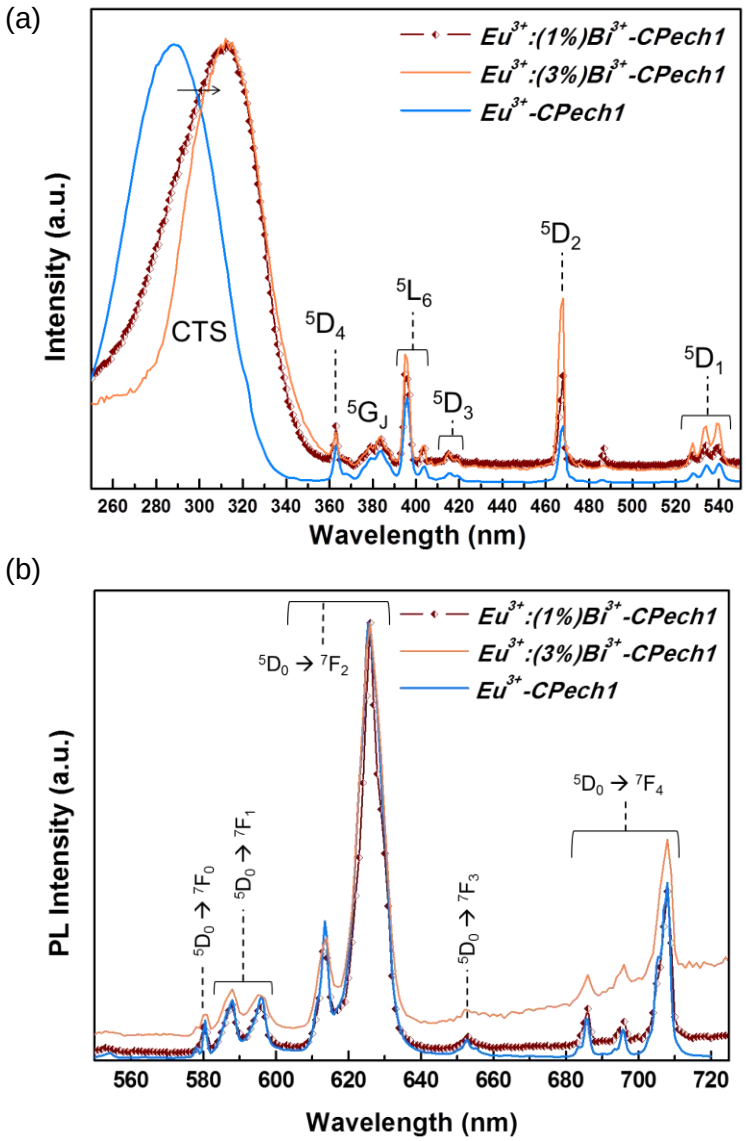

Figure 4.14. (a) Excitation and **(b)** emission spectra of *Eu^{3+}:(1%)Bi^{3+}-CPech1*, *Eu^{3+}:(3%)Bi^{3+}-CPech1* and *Eu^{3+}-CPech1* samples.

Figure 4.14(b) shows the emission spectra of the *Eu^{3+}:(1%)Bi^{3+}-CPech1*, *Eu^{3+}:(3%)Bi^{3+}-CPech1* and *Eu^{3+}-CPech1* samples which are very similar among them. Thus, as already described by other authors [193], the introduction of Bi^{3+} ions in the La_2O_3 structure does not alter the sublattice structure around the luminescence centre that constitute the Eu^{3+} ions and confirms the successful energy transfer between these active ions.

The I_2 ratios calculated from these emission spectra were 8.2 and 6.3 for the *Eu^{3+}:(1%)Bi^{3+}-CPech1* and *Eu^{3+}:(3%)Bi^{3+}-CPech1* samples, respectively. The *Eu^{3+}:(1%)Bi^{3+}-CPech1* showed the highest value in comparison with the other samples studied up to now (see Tables 4.1 and 4.2). Since the Bi^{3+} ion has a different ionic radius than Eu^{3+} and La^{3+} and it is supposed to occupy the same position of these ions, a higher distortion in the coordination polyhedra is expected when it is introduced in the host. Consequently, the I_2 ratio increases. According to this, one would expect to observe a higher distortion, and thus, a higher I_2 ratio, when the Bi^{3+} concentration in the sample increased. However, the sample containing 3 mol% Bi^{3+} showed a lower I_2 ratio than that for the sample containing 1 mol% Bi^{3+}. Park et al. [187] observed that for substitutions exceeding 3 mol% Bi^{3+} in Eu^{3+}:YVO_4 nanoparticles, the intensity of the red emission decreased. This was attributed to the formation of Bi_n^{3+} aggregates which can act as trapping centres and dissipate absorbed energy non-radiatively, instead of transferring it to the Eu^{3+} activator ion. Thus, a similar effect might also happen in our case.

The I_1 ratios obtained were 4.0 and 3.6 for the *Eu^{3+}:(1%)Bi^{3+}-CPech1* and *Eu^{3+}:(3%)Bi^{3+}-CPech1* samples, respectively. These values were among the highest calculated up to now in comparison to the rest of the samples (see Tables 4.1 and 4.2). This would be in good agreement with the fact that the I_1 ratio increases when the sample contains a higher amount of active ion (within 5-10 mol% Eu^{3+}). The I_1 ratio was also lower for the sample containing a higher Bi^{3+} concentration which would be in good agreement with the results observed by Park et al. [187], and would be due to the effects of non-transferred energy from Bi^{3+} to Eu^{3+} ions.

4.2.6. Experimental lattice parameters and Eu^{3+}-O^{2-} distances of Eu^{3+}:La_2O_3 and Eu^{3+}:Bi^{3+}:La_2O_3 nanoparticles

In order try to understand the reason for the CT band shifting, the Eu-O bond distances were calculated for the samples seen up to now. The X-ray diffraction patterns of all samples studied up to now by the PL technique, were recorded at slow conditions (an angular step of 0.02º at 16 s per step) to calculate their lattice parameters. The experimental lattice parameters were calculated using the Full-Prof software based on the Rietveld method [38] (see Fig. 4.15). We refined 10 different parameters (one overall scale factor, six background parameters, five shape parameters and three cell parameters). The lattice parameters for un-doped La_2O_3 were taken as a reference, listed in the 74-2430 reference pattern of the JCPDS database, that are a=b= 3.9373 Å, c= 6.1299 Å [115]. We observed smaller lattice parameters for La_2O_3 doped with Eu^{3+} and co-doped with Eu^{3+} and Bi^{3+} in comparison with pure La_2O_3 (see Table 4.4). This decrease in the unit cell parameter could be attributed to the introduction of europium in the structure of the crystals, since the ionic radius of europium is smaller than that of lanthanum in a 7-fold coordination [145]. Also, when samples were co-doped with Bi^{3+}, the lattice parameters were also smaller, despite that the ionic radius of Bi^{3+} is larger

than the ionic radius of La^{3+}. Since the concentration of Eu^{3+} in the samples is higher than the concentration of Bi^{3+}, the effect of Eu^{3+} in the structure seems to be more important than the effect of Bi^{3+}. However, if we compare the cell parameters of the *Eu^{3+}:(1%)Bi^{3+}-CPech1* with those of the *Eu^{3+}-CPech1* sample, we observe a slight increase in the cell parameters, that might be due to the introduction of Bi^{3+} in the structure. The average Eu^{3+}-O distance was calculated using the ATOMS software [194] which allowed also representing the La_2O_3 structure (see Fig. 4.16), introducing the experimental lattice information we obtained from the refined XRD patterns and calculating the average of the La^{3+}-O distance. The La_2O_3 structure was first investigated by Zachariasen in 1926 [195,196], but it was later revised by Pauling in 1928 [197]. For the La_2O_3 representation we used the atomic positions predicted by the Pauling's model which can be represented in the $P\bar{3}m1$ space group. The atomic coordinates for the La_2O_3 structure are listed in Table 4.5. Figure 4.16 shows three projections of the structure of La_2O_3 along the three crystallographic axes, showing the linked sevenfold LnO_7 polyhedra. The average Eu^{3+}-O distance was considered to be the same than that calculated for La^{3+}-O since we consider that they should be in the same structural position (C_{3v}) after observing the $^5D_0 \rightarrow {}^7F_0$ transition in the emission spectra. Table 4.4 shows the average Eu^{3+}-O distance of the calcined samples prepared using different methods. The average Eu^{3+}-O distances were similar for all the samples prepared. From these results, it is clear that another parameter apart from the Eu-O distance must be taken into account to explain the shift in the position of the CT band we observed in our samples. This parameter could be the real concentration of Eu^{3+} in the samples, as we already pointed up before. In this analysis we did not consider the *Eu^{3+}-Pech1B* and *Eu^{3+}-Pech2B* samples since they were formed by a mixture of La_2O_3 and LaOCl.

Table 4.4. Experimental lattice parameters and average Eu^{3+}-O distances of the calcined samples prepared by different synthesis methods.

Sample	Lattice parameters (Å)		Average Eu^{3+}-O distance (Å)	Maximum of the CT band (nm)
	a=b	c		
Eu^{3+}-CPvu	3.9371(9)	6.1298(1)	2.5342	289
Eu^{3+}-CH-1	3.9372(1)	6.1298(2)	2.5342	289
Eu^{3+}-CMwH-323-5	3.9372(1)	6.1297(8)	2.5342	292
Eu^{3+}-CH-24-IMP	3.9372(4)	6.1298(2)	2.5342	293
Eu^{3+}-CPech1	3.9370(8)	6.1296(7)	2.5341	288
Eu^{3+}-CPech2	3.9371(6)	6.1297(5)	2.5342	297
Eu^{3+}:(1%)Bi^{3+}-CPech1	3.9371(5)	6.1297(2)	2.5342	313

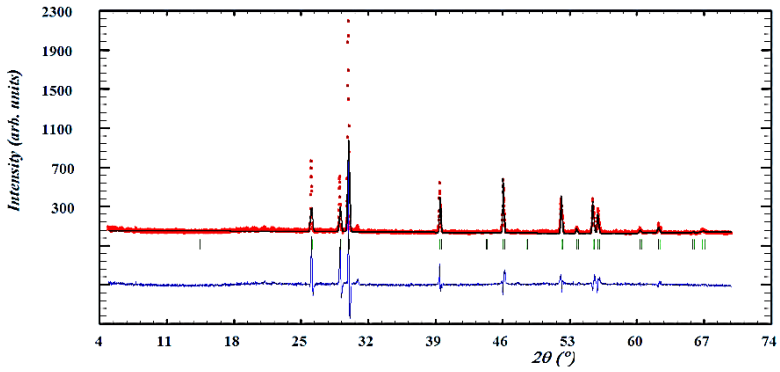

Figure 4.15. Experimental (black line), calculated (red line), and difference (bottom) results of XRD refinement for the *Eu*$^{3+}$*-CH-1* sample by the Full-Prof software.

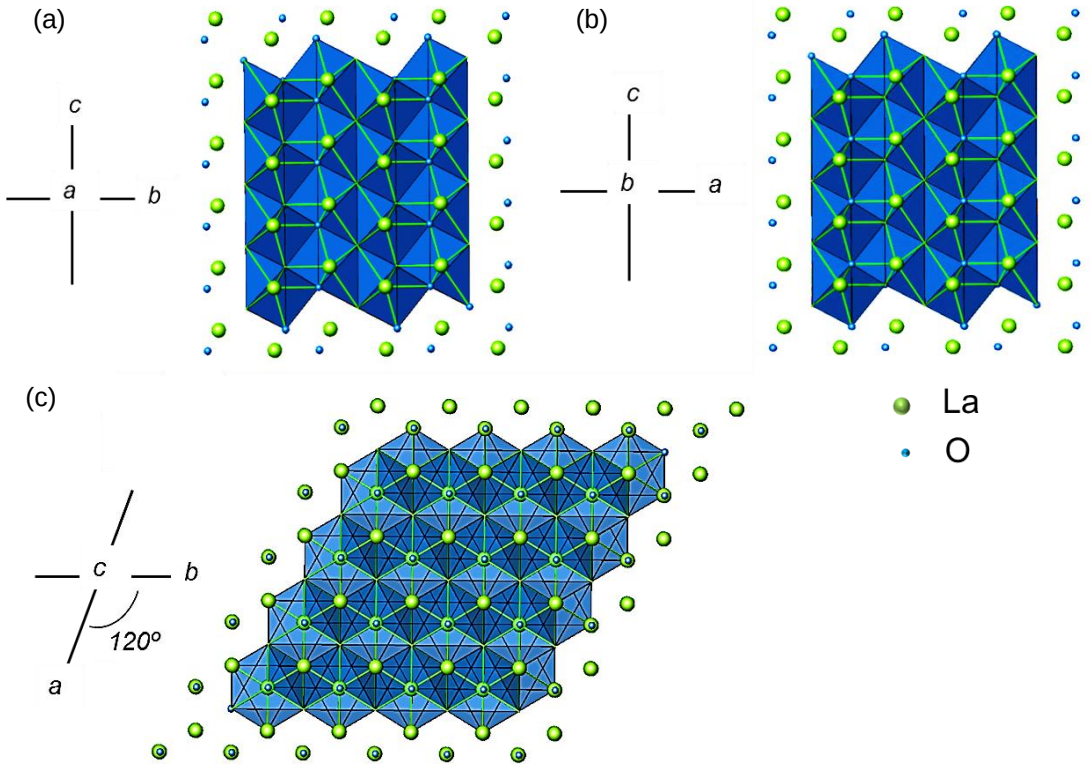

Figure 4.16. Schematic representations depicting the three projections of the La_2O_3 structure crystallizing in the P$\bar{3}$m1 space group along the **(a)** *a* **(b)** *b* and **(c)** *c* crystallographic axes.

Table 4.5. Coordinates of the La and O atoms in the La_2O_3 structure crystallizing in the trigonal system with space group $P\bar{3}m1$.

	x	y	z
La	1/3	2/3	0.25
O(1)	0	0	0
O(2)	1/3	2/3	0.65

4.2.7. Excitation and emission spectra of europium doped lanthanum oxysulfides

Changing from La_2O_3 as a host to the La_2O_2S host was carried out in order to shift the position of the CT band still towards the red region of the electromagnetic spectrum. The Eu^{3+}:La_2O_2S sample showed a red-shifted CT band with its maximum centered at 340 nm. It was also the broadest band observed for all these samples analysed extending from 250 to 400 nm, approximately (see Fig 4.17(a)). In order to compare the shifting observed in the position of the CT band in the Eu^{3+}:La_2O_2S sample with that of the Eu^{3+}:La_2O_3 samples, Fig. 4.17 shows the excitation and emission spectra of the Eu^{3+}:La_2O_2S and Eu^{3+}-*CPech1* samples. In agreement with other authors, we also observed an additional band at 266 nm in the excitation spectrum of the Eu^{3+}:La_2O_2S sample. In recent studies, this band has been attributed to the charge transfer for the Eu^{3+}-O^{2-} pairs, which form a band at lower wavelengths (266 nm). The broad band with the maximum intensity centered at 340 nm has been attributed to the charge transfer for the Eu^{3+}-S^{2-} pairs [93,179]. La_2O_2S is isostructural to La_2O_3, and thus, it also crystallizes in the trigonal system with the $P\bar{3}m1$ space group. In La_2O_2S, La^{3+} is coordinated to three sulphur and four oxygen ions and is located in a C_{3v} symmetry site, as for the La_2O_3 structure. The interatomic distances are as follows: La-S, 3.07 Å; La-O, 2.38 Å; La-O', 2.41 Å. According to these bond distances, the probability to observe the Eu^{3+}-O^{2-} charge transfer state band should be larger than the probability to observe the Eu^{3+}-S^{2-}charge transfer state band. Despite this, we observed that the CT band for the Eu^{3+}-S^{2-} interaction was more intense than that for the Eu^{3+}-O^{2-} interaction. Other authors [179] found similar results when preparing nanoparticles with a high Eu^{3+} concentration (5-20 mol%). In that case, more Eu^{3+} ions are expected to be located nearby the defect states, which can then capture the excitation energy and quench both charge transfer transitions. However, it is suggested that the quenching probability by defect states on the Eu^{3+}-O^{2-} CT band is greater than that on the Eu^{3+}-S^{2-} one [179]. The fact of observing the maximum of the Eu^{3+}-O^{2-} CT band at lower wavelengths in the Eu^{3+}:La_2O_2S sample, where the Eu-O distance is ~2.39 Å, than in the Eu^{3+}:La_2O_3 nanoparticles, where the Eu-O distance is ~2.53 Å, corroborated that at shorter Eu-O bond distances, the Eu^{3+}-O^{2-} CT band appears at lower wavelengths. The same hypothesis can be used to explain the fact of observing the Eu^{3+}-S^{2-} CT band at longer wavelengths, since the Eu-S distance is 3.07 Å. The Eu^{3+} f-f transitions

were also observed in the Eu^{3+}*:*La_2O_2S sample, at the same positions than those observed for the rest of the samples.

The Eu^{3+}*:*La_2O_2S sample showed all the emission peaks, both when using λ_{exc} = 266 nm and 340 nm, that we observed for the rest of the samples analysed in this work, but with a slight difference for the $^5D_0 \rightarrow {}^7F_0$ transition (see zoom of Fig. 4.17(b)). The $^5D_0 \rightarrow {}^7F_0$ peak, which was located at around 580 nm in the Eu^{3+}:La_2O_3 samples, appeared weaker in this sample. Reddy et al. [164] already observed a very weak emission peak for the $^5D_0 \rightarrow {}^7F_0$ transition in Eu^{3+} doped La_2O_2S powder phosphors, and Peng et al. [93] attributed this fact to the nephelauxetic effect, which directly depends on the crystal field strength of the host. Thus, according to this, the crystal field strength should be lower in Eu^{3+}:La_2O_2S nanoparticles than in Eu^{3+}:La_2O_3 samples. Furthermore, the position of the emission peaks corresponding to the Eu^{3+}*:*La_2O_2S sample were slightly shifted towards shorter wavelengths due to the different crystallographic parameters and nature of ligands surrounding Eu^{3+} in this sample.

The I_2 ratio for the Eu^{3+}*:*La_2O_2S sample was calculated from the emission spectrum obtained after pumping the sample at 266 nm (Eu^{3+}-O^{2-} CT band), and the I_2 obtained was 3.8. If we compare this low 3.8 value of I_2 with the I_2 values obtained up to now for the other samples (see Tables 4.1 and 4.2), we could say that the Eu^{3+} is located in a weaker crystal field in La_2O_2S than when it is in La_2O_3, as it was already observed when studying the low intensity of the $^5D_0 \rightarrow {}^7F_0$ peak. Additionally, as we mentioned above, the I_2 parameter is related with the covalency of the Eu-O bond, and means that with higher values of the I_2, the covalency should be lower. This suspicion was confirmed by Mikami et al. [198]. They observed that the La-O covalency in La_2O_2S is lower than the La-O covalency in the La_2O_3 compound.

Furthermore, in order to confirm this, the intensity ratio between the $^5D_0 \rightarrow {}^7F_4$ transition, located at 702 nm, and the $^5D_0 \rightarrow {}^7F_1$ transition, located at 585 nm, was also calculated. This ratio gives us information about the crystal field strength at long distances and is known as the I_4 parameter [199,200]. The I_4 values obtained were 0.5 for the Eu^{3+}*:*La_2O_2S sample (exciting at 266 nm) and 2.8 for the Eu^{3+}*-CPech1* sample. Thus, we can say that the crystal field strength of La_2O_2S is also weaker at long distances than that of the La_2O_3. The fact of having a weaker crystal field strength might also explain the slight shift towards lower wavelengths of the emission peaks (see Fig. 4.17(b)).

The I_1 ratio obtained when using λ_{exc} = 266 nm was 3.2. This ratio was within the range of I_1 obtained for the rest of the Eu^{3+}:La_2O_3 samples synthesized by using different methods (I_1 = 2.7-3.9, see Tables 4.1 and 4.2). This would confirm that the concentration of Eu^{3+} in the Eu^{3+}*:*La_2O_2S sample is similar to that obtained in the Eu^{3+}:La_2O_3 samples.

The parameters calculated by taking the peaks from the emission spectra of the Eu^{3+}:La_2O_2S sample but exciting at 340 nm (in the Eu^{3+}-S^{2-} CT band) were: 8.2, 1 and 3.3, for the I_2, I_4 and I_1 ratios, respectively. The similarity of the I_1 ratios when pumping at 266 nm (3.2) and

pumping at 340 nm (3.3) would corroborate the use of this parameter to calculate the Eu^{3+} ion concentration in the samples.

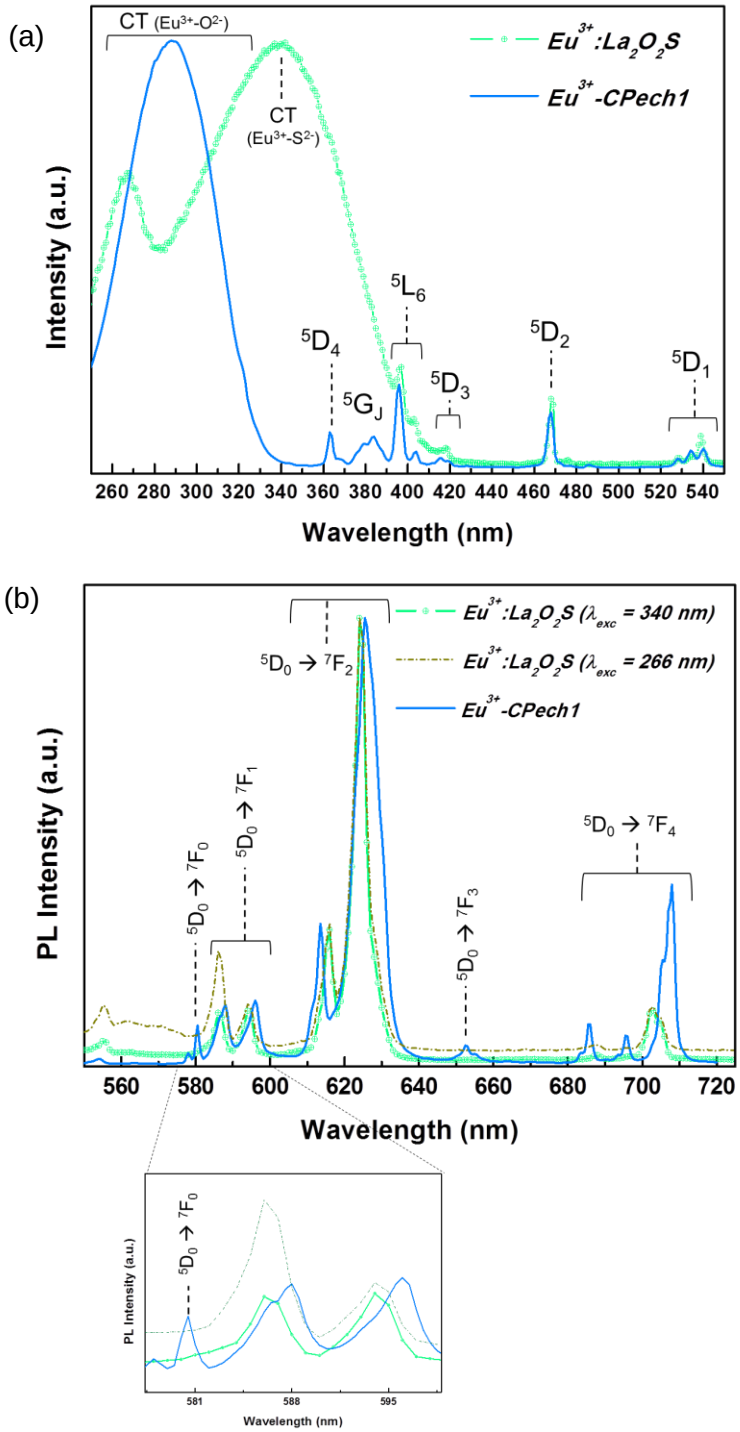

Figure 4.17.(a) Excitation and **(b)** emission spectra of the *Eu^{3+}-CPech1* and *Eu^{3+}:La_2O_2S* samples.

The Eu^{3+}:Bi^{3+}:La_2O_2S sample was studied in order to check if both improvements together (the addition of Bi^{3+} and the use of La_2O_2S as a host) were even better to shift the position of the CT band towards longer wavelengths. Figures 4.18(a-b) show the excitation and emission spectra of the Eu^{3+}:La_2O_2S, Eu^{3+}:(1%)Bi^{3+}-*CPech1* and Eu^{3+}:Bi^{3+}:La_2O_2S samples, respectively.

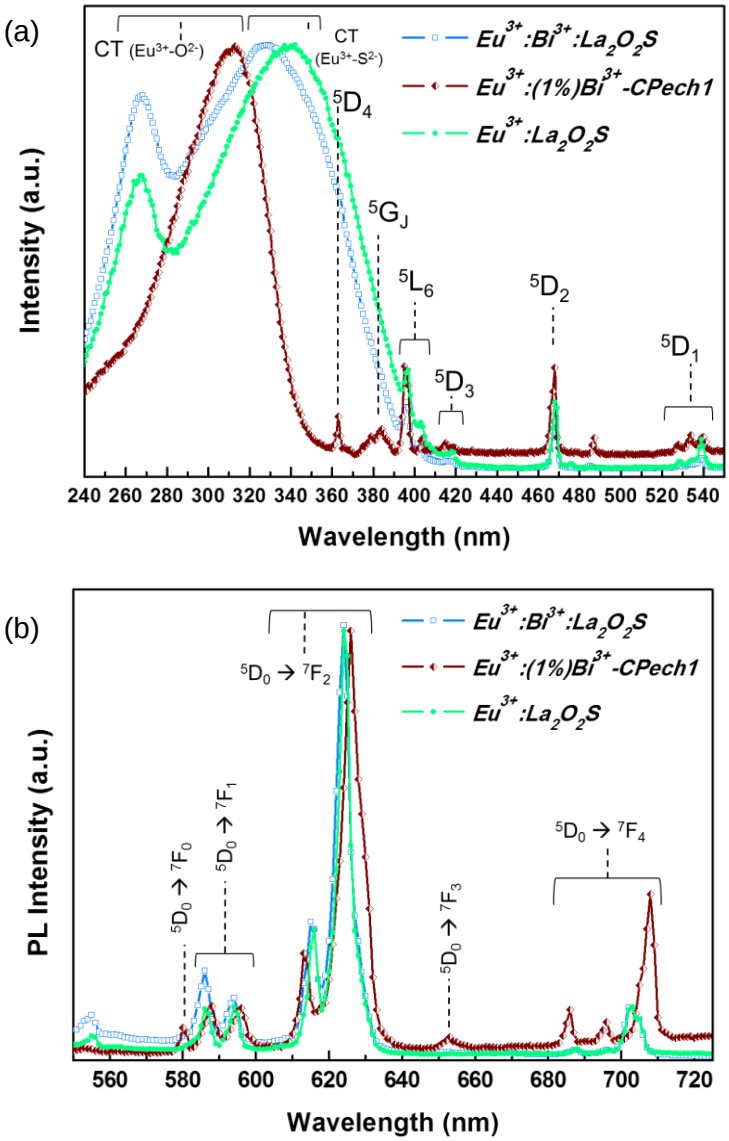

Figure 4.18.(a) Excitation and **(b)** emission spectra of the Eu^{3+}:Bi^{3+}:La_2O_2S, Eu^{3+}:(1%)Bi^{3+}-*CPech1* and Eu^{3+}:La_2O_2S samples.

With the addition of the Bi^{3+} ions (Eu^{3+}:Bi^{3+}:La_2O_2S sample), the position for the maximum of the Eu^{3+}-S^{2-} CT band shifted from 340 nm to 330 nm whereas the Eu^{3+}-O^{2-} CT band appeared at the same position in comparison with the Eu^{3+}:La_2O_2S sample, at 266 nm (see

Fig. 4.18(a)). While in both excitation spectra for the Eu^{3+}:La_2O_2S and Eu^{3+}:Bi^{3+}:La_2O_2S samples, the Eu^{3+}-S^{2-} CT band was dominant, there was also a slight difference between the relative intensity between this band and the Eu^{3+}-O^{2-} band for these two samples. The Eu^{3+}-O^{2-} band of the sample containing 1 mol% Bi^{3+} (Eu^{3+}:Bi^{3+}:La_2O_2S) was more intense than that for the sample without Bi^{3+} ions (Eu^{3+}:La_2O_2S). According to previous studies reported [179], the Eu^{3+}-O^{2-} band is dominant at low concentrations due to the shorter Eu-O bond distances in comparison to Eu-S bond distances. Then, when increasing the concentration gradually, the Eu^{3+}-S^{2-} band becomes dominant reaching its maximum for concentrations of 5 mol% Eu^{3+} [179]. However, for Eu^{3+} ions concentration from 10 to 40 mol%, the Eu^{3+}-O^{2-} band becomes dominant again. The Eu^{3+}:Bi^{3+}:La_2O_2S and Eu^{3+}:La_2O_2S samples were prepared by using the combustion method. With that, we can assume similar Eu^{3+} concentration for the two samples and thus, the attention is focused in some changes produced by the presence of Bi^{3+} ions. The fact of having Bi^{3+} in the sample could enhance the probability of appearance of the Eu^{3+}-O^{2-} band up to higher concentrations since Bi^{3+} can transfer efficiently the energy to Eu^{3+} ions, as we have seen before.

Fig. 4.18(b) shows the emission spectra for these samples. Each emission spectrum was recorded by pumping at the maximum of the Eu^{3+}-S^{2-} CT band for the Eu^{3+}:Bi^{3+}:La_2O_2S and Eu^{3+}:La_2O_2S samples, 327 and 340 nm, respectively, and at the maximum of the Eu^{3+}-O^{2-} CT band for the Eu^{3+}:*(1%)*Bi^{3+}*-CPech1* sample, 313 nm. The emission spectra of the Eu^{3+}:Bi^{3+}-La_2O_2S and Eu^{3+}:La_2O_2S samples were similar but the Eu^{3+}:Bi^{3+}:La_2O_2S sample showed a more intense peak at 585 nm corresponding to the $^5D_0 \rightarrow {}^7F_1$ transition. The I_2, I_1 and I_4 values for this sample were 6.9, 3.1 and 0.6, respectively, lower than the ratios obtained for the Eu^{3+}:La_2O_2S sample (I_2 = 8.2, I_1 =3.3 and I_4 =1). This was opposite to the results obtained when introducing 1 mol % Bi^{3+} in the La_2O_3 host, but in agreement with those obtained when introducing 3 mol% Bi^{3+} in the La_2O_3 host. This might be attributed to that quenching effects depending on the dopant ion concentration varies depending on the hosts.

Table 4.6. CT band position, asymmetry ratio (I_2), fluorescence ratio (I_1) and I_4 values obtained from the emission spectra of the Eu^{3+}:La_2O_2S and Eu^{3+}:Bi^{3+}:La_2O_2S samples.

Sample	CT band position (nm)	I_2 (asymmetry ratio)	I_1 (fluorescence ratio)	I_4
Eu^{3+}:La_2O_2S (Eu^{3+}-O^{2-})	266	3.8	3.2	0.5
Eu^{3+}:La_2O_2S (Eu^{3+}-S^{2-})	340	8.2	3.3	1.0
Eu^{3+}:Bi^{3+}:La_2O_2S	327	6.9	3.1	0.6

4.2.8. Spectroscopic characterization of praseodymium doped lanthanum oxide

In order to explore the possibilities of exploiting the spectroscopic characteristics of other active lanthanide ions for developing materials with CT bands located more in the visible region, Pr^{3+} doped La_2O_3 nanoparticles were prepared by the sol-gel Pechini method. We prepared samples with a different Pr^{3+} content: *(x%)Pr^{3+}-Pech1* (*x*= 0.5, 1, and 3 mol%). Figures 4.19(a) and 4.19(b) show the excitation spectra between 250-550 nm and 250-330 nm, respectively, for *(0.5%)Pr^{3+}-Pech1*, *(1%)Pr^{3+}-Pech1* and *(3%)Pr^{3+}-Pech1* samples. These spectra were recorded monitoring the emission at 667 nm corresponding to the emission from the $^3P_0 \rightarrow {}^3F_2$ transition [88] at room temperature. In Figure 4.19(a) the excitation spectra show several lines in the region 440-500 nm, corresponding to transitions within the $4f^2$ configuration ($^3H_4 \rightarrow {}^3P_{0,1,2}$ and $^1I_6$). Besides, as observed in the case of Eu^{3+} doped La_2O_3, the broad band localized at about 290 nm was ascribed to the excitation via host lattice absorption corresponding to Pr^{3+}-O^{2-} energy transfer (CT band). These results obtained were in good agreement with the excitation spectra of Pr^{3+}:La_2O_3 observed by other authors [93,186]. However, when we compared the position of the maximum of the CT band in detail for samples doped with a different Pr^{3+} concentration (Fig. 4.19(b)), some discrepancies appeared. De Mello et al. [88] found that at higher Pr^{3+} concentration, the maximum of the CT band was located at lower energies. Nevertheless, in our case, *(1%)Pr^{3+}-Pech1* and *(3%)Pr^{3+}-Pech1* samples showed both CT bands centred at 292 nm while the *(0.5%)Pr^{3+}-Pech1* sample showed a CT band centred at 296 nm, thus at lower energies. Other factors such as the transformation from Pr^{3+} to Pr^{4+} due to oxidation processes, which could be confirmed by the changing observed in the sample colour from white to brown, or the calcination times, are needed to be considered.

Figure 4.20 shows the emission spectrum recorded for the *(0.5%)Pr^{3+}-Pech1* sample from 450 to 800 nm and recorded under 290 nm at room temperature.The emission lines corresponded to the $^3P_0 \rightarrow {}^3H_{4,5,6}$ and $^3P_0 \rightarrow {}^3F_{2,3,4}$ transitions. The spectrum was dominated by the $^3P_0 \rightarrow {}^3F_2$ transition situated at 667 nm. In the literature [88], one can find that the emission peak from the $^1D_2 \rightarrow {}^3H_4$ transition and situated at about 610 nm, should appear for samples containing less than 1 mol% Pr^{3+}. However, we did not observe this peak and this may be attributed to a pronounced concentration quenching effect of the $^1D_2$ emission in our sample.

Since the CT band of these samples is located at similar wavelengths than that of Eu^{3+}:La_2O_3 samples, we did not extended the study of the Pr^{3+}:La_2O_3 nanoparticles.

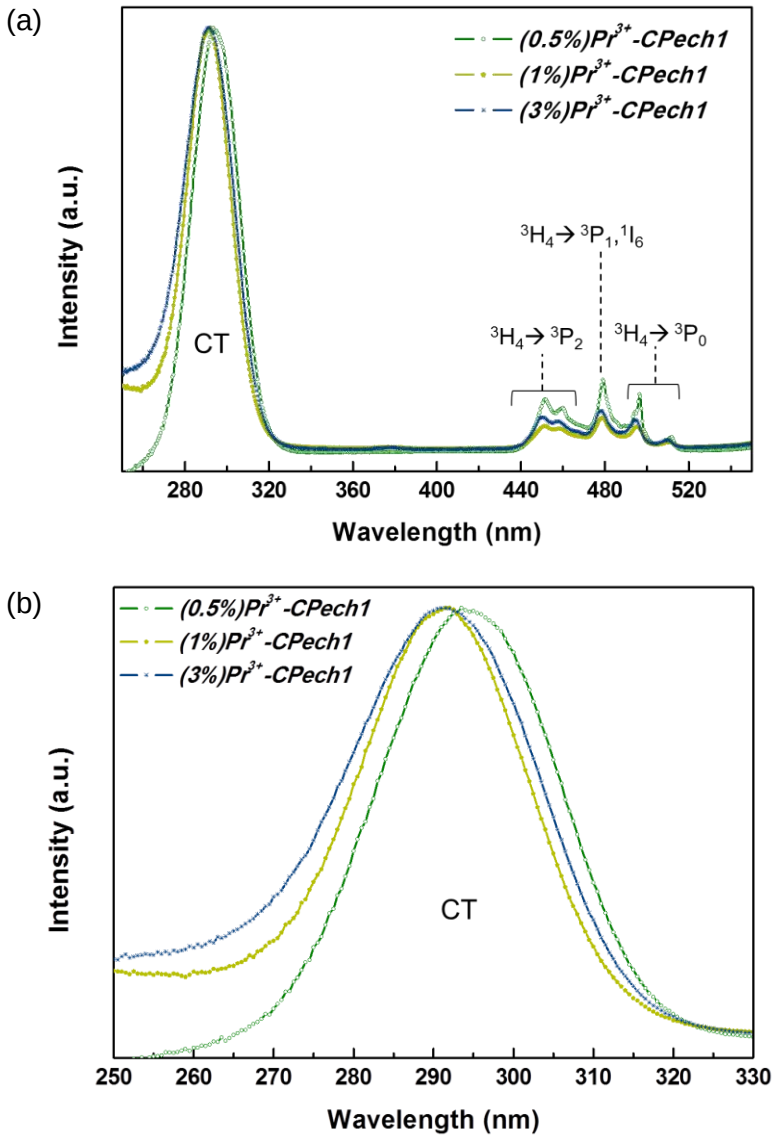

Figure 4.19. (a) Excitation spectra of several *(x%)Pr*$^{3+}$*-CPech1* samples and **(b)** magnification of the region in the spectra where the CT bands are located.

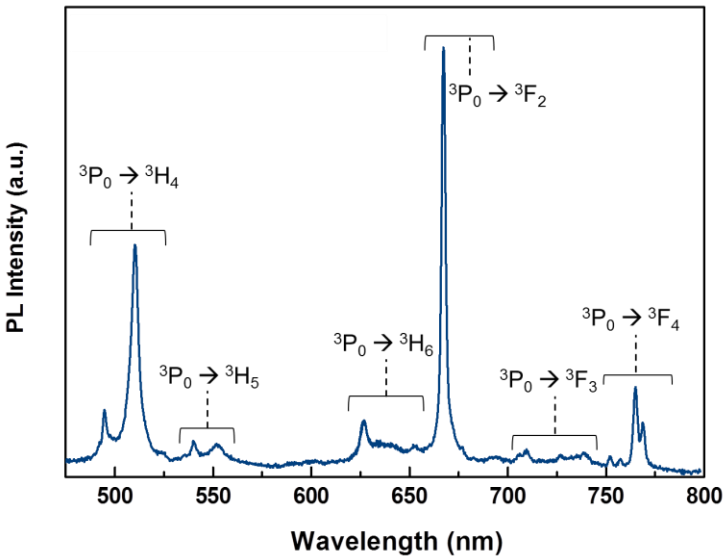

Figure 4.20. Emission spectrum recorded for the *(0.5%)Pr^{3+}-CPech1* sample.

4.3. Cathodoluminescence of doped lanthanum compounds

By the cathodoluminescence (CL) technique we studied the luminescence in detail after excitation by electron bombardment of some of the non-calcined and calcined samples synthesized. Therefore, the CL spectra of the Eu^{3+}:$La(OH)_3$, Eu^{3+}:La_2O_3 and Pr^{3+}:La_2O_3 nanoparticles have been studied at room temperature. We also analysed the spectra of *Eu^{3+}-H-24* and *Eu^{3+}-CH-24* samples at low temperature. To the best of our knowledge this is the first time that CL has been used to characterize Eu^{3+} in these matrices ($La(OH)_3$ and La_2O_3).

4.3.1. Cathodoluminescence of europium doped lanthanum hydroxide (Eu^{3+}:$La(OH)_3$) nanoparticles

Figures 4.21(a) and 4.21(b) show the CL spectra of a representative non-calcined sample of Eu^{3+}:$La(OH)_3$ nanoparticles (*Eu^{3+}-Pvu*). All the peaks were identified in these figures with the corresponding transitions from the ^5D_J (J = 0, 1) states to the $^7F_{J'}$ (J' = 0-4) states. Figure 4.21(a) shows the CL spectrum between 500-740 nm and exhibits the most intense peak of the emission spectrum at 615 nm which corresponded to the $^5D_0 \rightarrow {}^7F_2$ transition. To observe in detail the weak peaks appearing at low wavelengths, which corresponded to the $^5D_1 \rightarrow {}^7F_{J'}$ (J' = 1, 2) transitions, Figure 4.21(b) shows the CL spectrum between 500-600 nm. Maybe due to the low luminescent efficiency of lanthanide hydroxides, from the best of our knowledge, there are no previous works that report the CL properties of Eu^{3+}:$La(OH)_3$ material and only a few works that report their PL properties [84,201].

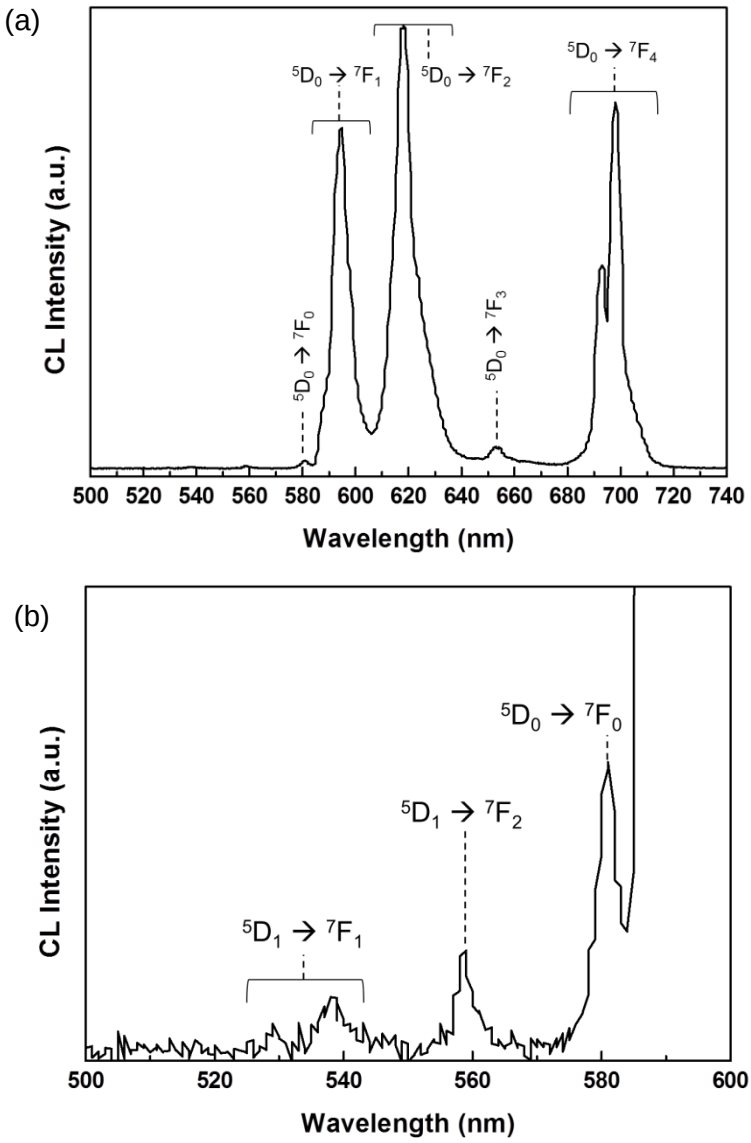

Figure 4.21. (a) CL spectra from 500 to 740 nm and **(b)** from 500 to 600 nm of the Eu^{3+}:$La(OH)_3$ nanoparticles (*Eu^{3+}-Pvu* sample).

The CL spectra of several non-calcined samples synthesized by different methods are shown in Figure 4.22. All the spectra were normalized in intensity at about 615 nm. The results showed that all samples prepared by the co-precipitation and hydrothermal methods present a very similar spectrum with the same number of peaks whereas the sample doped by the wetness impregnation method (*Eu^{3+}-H-24-IMP*) present a higher number of peaks. For instance, the $^5D_0 \rightarrow {}^7F_1$ and $^5D_0 \rightarrow {}^7F_2$ transitions showed two peaks instead of one as found for the rest of the samples. This should be clearly attributed to that while lanthanum hydroxide was the main phase for the rest of the samples, in the *Eu^{3+}-H-24-IMP* sample, the

main phase was $LaCO_3OH$ [107], as observed by XRD patterns (see Fig. 3.15). Thus, Eu^{3+} had a different environment surrounding it and consequently it showed different emission peaks, probably some of them coming from the $La(OH)_3$ phase and others coming from the $LaCO_3OH$ phase. For instance we believe that the peaks located at 600 and 611 nm can be attributed to this last phase, since they were not observed in the CL spectra of the rest of the samples which were formed only by the $La(OH)_3$ phase (see Fig. 3.15).

Furthermore, while there were some samples that showed the $^5D_0 \rightarrow {}^7F_2$ transition as the most intense peak in the spectra and located at about 615 nm (*Eu^{3+}-Pvu*, *Eu^{3+}-H-0* and *Eu^{3+}-H-24-IMP*), others showed the $^5D_0 \rightarrow {}^7F_4$ transition as the most intense peak at about 696 nm (*Eu^{3+}-H-24*, *Eu^{3+}-H-1*, *Eu^{3+}-MwH-323-5* and *Eu^{3+}-MwH-323-15*). Since the $^5D_0 \rightarrow {}^7F_0$ transition appeared in all the CL spectra, this would indicate that Eu^{3+} in $La(OH)_3$ is located in a low symmetry site, that would correspond to the S_3 position, the crystallographic site occupied by La^{3+} in this structure [143,202].

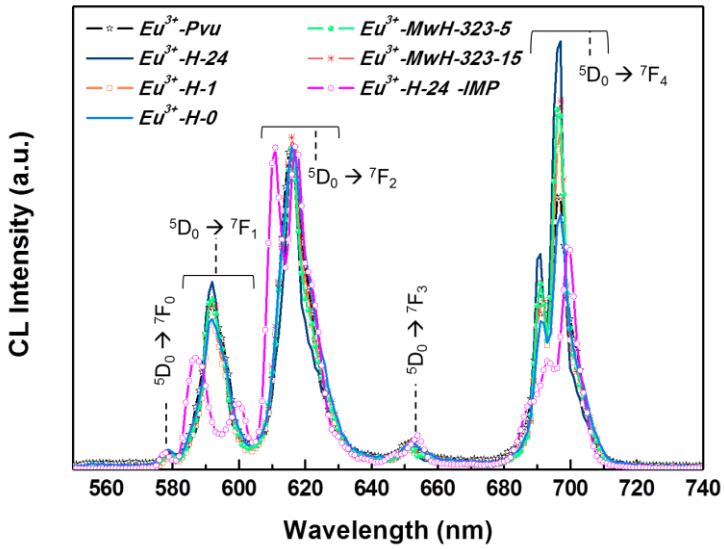

Figure 4.22. CL spectra of several Eu^{3+}:$La(OH)_3$ samples synthesized by different methods.

The asymmetry ratio, I_2, was calculated for these samples (see Fig. 4.23 and Table 4.7) and as usual, it was obtained from the intensity ratio of the $^5D_0 \rightarrow {}^7F_1$ and $^5D_0 \rightarrow {}^7F_2$ transitions. In the case of the samples doped by co-precipitation and hydrothermal method, the peaks of such transitions were located at 615 and 591 nm. For the *Eu^{3+}-H-24-IMP* sample, it was difficult to distinguish the peaks coming from the $LaCO_3OH$ and $La(OH)_3$ phase, thus, we considered the peaks located at 616 and 586 nm as the suitable peaks to calculate the I_2 ratio. The I_2 values for all the samples ranged 1.7-2.9. In comparison with the I_2 for Eu^{3+}:La_2O_3 nanoparticles obtained by photoluminescence, we could say that non-calcined samples showed lower I_2 values. Such low values might indicate that the Eu^{3+} coordination polyhedra are less distorted in the $La(OH)_3$ matrix when compared to the La_2O_3 matrix, having then a

higher degree of symmetry. Also, the covalency degree of the structure should be also considered when studying the I_2 parameter. In agreement with our results, recently, Sunding et al. [203] reported that La-O bonds present larger covalency in La_2O_3 compared to $La(OH)_3$. This low value of I_2 would also indicate that this matrix causes a weak crystal field in the short range and consequently, low emission intensities. Here it is also important to note that some of the spectra are not dominated by the $^5D_0 \rightarrow {}^7F_2$ transition. Instead, the peak corresponding to the $^5D_0 \rightarrow {}^7F_4$ transition had a similar intensity than that corresponding to the $^5D_0 \rightarrow {}^7F_2$ transition in some cases. Thus, by comparing these two structures, we should expect that, although in both cases Eu^{3+} was located in a low symmetry site (S_3 in $La(OH)_3$ and C_{3v} in La_2O_3), the oxygen atoms surrounding Eu^{3+} formed a more regular polyhedron in $La(OH)_3$ than in La_2O_3 in agreement with the lower I_2 ratio obtained for the samples formed by the $La(OH)_3$ phase. In fact, the coordination polyhedron of La^{3+} in $La(OH)_3$ is formed by 9 oxygen atoms, 3 of which located at a distance of 2.551 Å, and the other 6 additional oxygen atoms located at a distance of 2.588 Å [204]. In contrast, for La_2O_3, La^{3+} is surrounded by 7 oxygen atoms located at distances ranging from 2.356 to 2.743 Å. The distortion of the polyhedron is defined as:

$$\Delta d = (1/t)\sum_{n=1-t} \left\{ \left[d(La-O)_n - \langle d(La-O) \rangle \right] / \langle d(La-O) \rangle \right\}^2 \qquad \textbf{(Eq. 4.1)}$$

where t is the number of surrounding oxygen atoms around La and $\langle d(La-O) \rangle$ is the mean La-O distance [205]. Thus, the polyhedra distortions were 4.6×10^{-5} and 5.2×10^{-3} for $La(OH)_3$ and La_2O_3 structures, respectively. It is easy to note that the value for the distortion of the LaO_7 polyhedron in La_2O_3 was two orders of magnitude higher than the value obtained for the LaO_9 polyhedron in the $La(OH)_3$ structure, justifying in this way that the $^5D_0 \rightarrow {}^7F_2$ transition is not the most intense in some of this last host matrix. The weaker crystal field in $La(OH)_3$ in comparison to that for the La_2O_3, was also confirmed by studying the I_4 values of these samples (see Table 4.7) which were within the 1.6-2.3 range, whereas the I_4 studied previously for the *Eu^{3+}-CPech1* sample was slightly higher, 2.8, indicating again that the crystal field in the $La(OH)_3$ structure was weaker than in the La_2O_3 structure.

Table 4.7. I_2 and I_4 values calculated for several Eu^{3+}:$La(OH)_3$ samples.

Sample	I_2	I_4
Eu^{3+}-Pvu	1.9	1.6
Eu^{3+}-H-24	1.7	2.3
Eu^{3+}-H-1	2.1	2.2
Eu^{3+}-H-0	2.2	1.7
Eu^{3+}-MwHd-323-5	1.9	2.2
Eu^{3+}-MwHd-323-15	2.0	2.3
Eu^{3+}-H-24-IMP	2.9	2.0

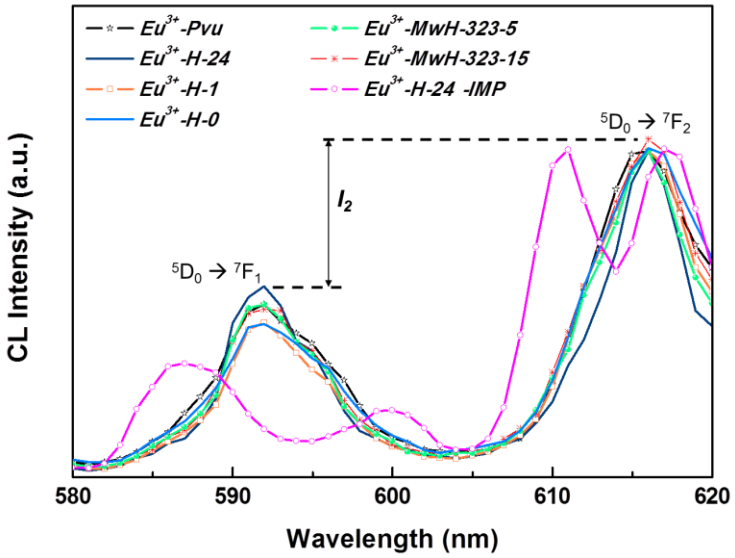

Figure 4.23. CL spectra of several Eu^{3+}:$La(OH)_3$ samples from 580 to 620 nm, indicating how the I_2 parameter was calculated.

4.3.2. Cathodoluminescence of Eu^{3+}:$La(OH)_3$ nanoparticles at low temperature

During the CL and PL analyses presented in previous sections of this chapter, we suggested that Eu^{3+} was located in a structural site without an inversion centre and replacing the crystallographic site occupied by La^{3+}, S_3 in the $La(OH)_3$ structure. In addition, the observation of the $^5D_0 \rightarrow {}^7F_0$ transition in these structures also indicates that Eu^{3+} was located in these crystallographic sites, since this transition might be partially allowed in the presence of a linear crystal field term. It is known that the $2J + 1$ degeneracy of the free ion may be broken by the crystal field at its location. The levels with $J = 0$ are non-degenerate; therefore, if only one structural position for Eu^{3+} in the crystalline structure exists, the $^5D_0 \rightarrow {}^7F_0$ transition should have only one peak, while the $^5D_0 \rightarrow {}^7F_1$ transition should exhibit three peaks and the $^5D_0 \rightarrow {}^7F_2$ transition should show five peaks. Up to now, the $^5D_0 \rightarrow {}^7F_0$ transition had only one peak in Eu^{3+}:$La(OH)_3$ structures for the samples studied. However, the other transitions did not show the corresponding theoretical number of peaks according to the degeneracy selection rule ($2J + 1$): the $^5D_0 \rightarrow {}^7F_1$ and the $^5D_0 \rightarrow {}^7F_2$ transitions showed several shoulders in the case of Eu^{3+}:$La(OH)_3$ nanoparticles (see Figs. 4.22 and 4.23). We carried out CL measurements at low temperature (6K) to verify the existence of one or more positions for Eu^{3+} in this structure.

Fig. 4.24 shows the CL spectrum of the *Eu^{3+}-H-24* sample measured at 6 K. The spectrum recorded at low temperature showed only one peak for the $^5D_0 \rightarrow {}^7F_0$ transition, confirming that only one structural position for Eu^{3+} exists in the crystalline structure of the $La(OH)_3$

matrix. However, despite that we were able to observe a larger number of peaks at low temperature, the fine structure of the $^5D_0 \rightarrow {}^7F_1$ and the $^5D_0 \rightarrow {}^7F_2$ transitions was still not well resolved, since the system does not allow a recording resolution for the spectra smaller than 0.5 nm.

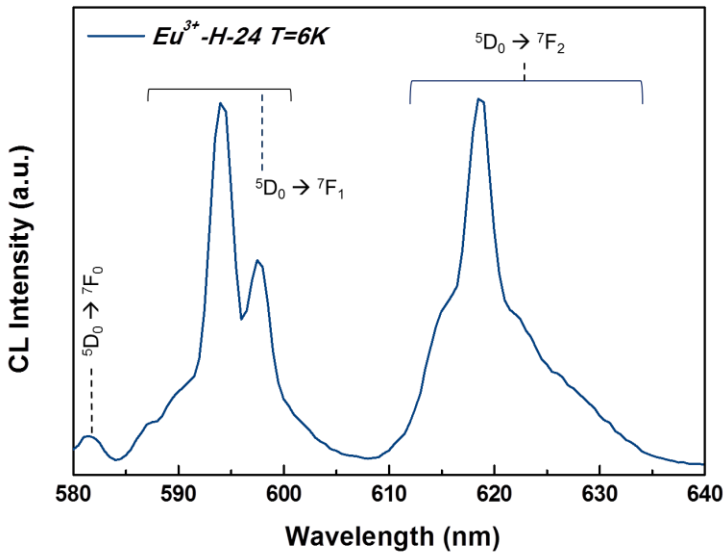

Figure 4.24. CL spectra of the *Eu^{3+}-H-24* sample recorded at low temperature.

4.3.3. SEM and CL images of Eu^{3+}:$La(OH)_3$ nanoparticles

Figures 4.25-4.30 show the SEM images and the corresponding CL images recorded for the Eu^{3+}:$La(OH)_3$ samples. The CL images were recorded either panchromatic or monochromatic (corresponding to the wavelength of the most intense emission peaks) in order to observe where the light emitted by the nanoparticles originates at the different emission wavelengths. Figs. 4.25 (a) and 4.25(b) exhibit the SEM image and the corresponding panchromatic CL image, respectively, of the *Eu^{3+}-Pvu* sample. The CL image showed brightness coming from all the particles forming this sample. This confirmed that Eu^{3+} doping was homogeneous in the sample.

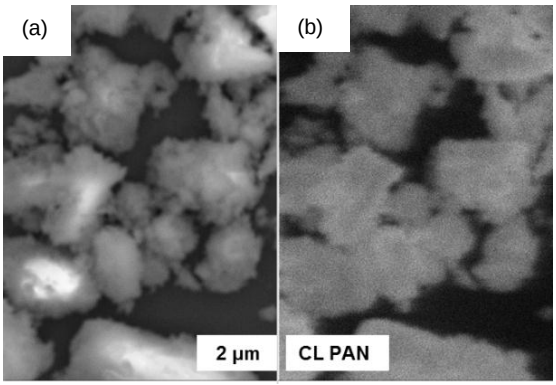

Figure 4.25. (a) SEM and **(b)** panchromatic CL images recorded for the Eu^{3+}-*Pvu* sample.

Figures 4.26(a) and 4.26(b) show the SEM images with their corresponding panchromatic CL images, respectively, of the Eu^{3+}-*H-24* sample. The CL image shown in Fig. 4.26(b) looked homogeneous because the nanoparticles emitted throughout the entire sample, as observed for the previous sample.

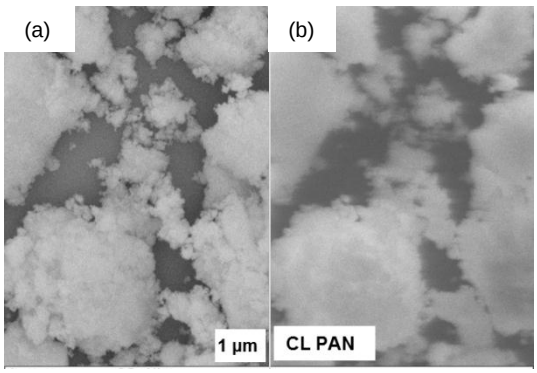

Figure 4.26. (a) SEM and **(b)** panchromatic CL images recorded for the Eu^{3+}-*H-24* sample.

SEM images and the corresponding panchromatic and monochromatic CL images at 592 nm and 696 nm for the Eu^{3+}-*H-1* sample are shown in Figs. 4.27(a-d). These two different wavelengths were chosen because corresponded to the two different emission peaks observed in the CL spectra for this sample (Fig. 4.22). The panchromatic image shown in Fig. 4.27(b) showed the clearest image because here the intensity emitted at all wavelengths was recorded. The less clear image was the monochromatic CL image recorded at 592 nm, since the intensity of this peak, which corresponded to the $^5D_0 \rightarrow {}^7F_1$ transition, was lower than that of the peak at 696 nm, which corresponded to the $^5D_0 \rightarrow {}^7F_4$ transition.

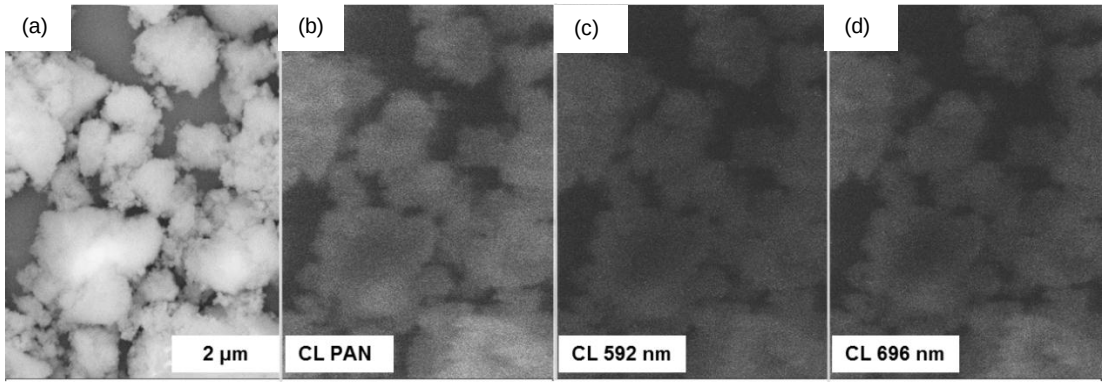

Figure 4.27. (a) SEM, **(b)** panchromatic CL and **(c-d)** monochromatic CL images at 592 nm and 696 nm, respectively, recorded for the *Eu^{3+}-H-1* sample.

Figures 4.28(a-c) and 4.28(b-d) exhibit the SEM images with their corresponding panchromatic CL images, respectively, of the *Eu^{3+}-H-0* sample. The panchromatic CL images (Fig. 4.28(b-d)) show emission light arising from all the parts of the sample indicating a good doping homogeneity. Similar results were observed for the *Eu^{3+}-MwH-323-5* sample. Figure 4.29(a-b) shows the SEM image of this sample with its corresponding panchromatic CL image.

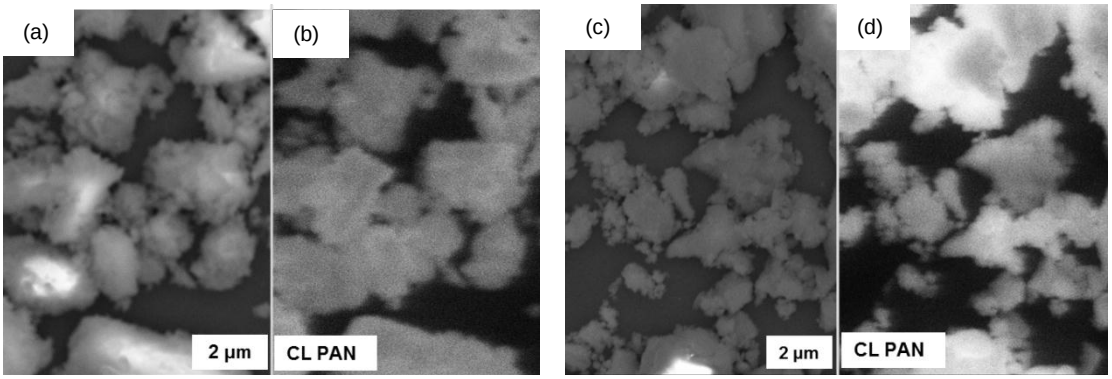

Figure 4.28. (a-c) SEM and **(b-d)** panchromatic CL images recorded for the *Eu^{3+}-H-0* sample.

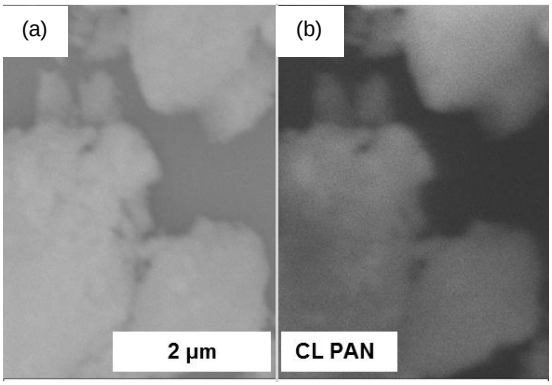

Figure 4.29.(a) SEM and **(b)** panchromatic CL images recorded for *Eu^{3+}-MwH-323-5* sample.

Figure 4.30(a) shows the SEM image, Fig. 4.30(b) the panchromatic CL image and Fig. 4.30(c-d) the monochromatic CL images at 611 nm and 616 nm corresponding to the different emission peaks observed in its CL spectrum and attributed to the $LaCO_3OH$ and $La(OH)_3$ phases, respectively (see Fig. 4.22), for the sample doped by the wetness impregnation method (*Eu^{3+}-H-24-IMP*). This sample showed a panchromatic CL image very brilliant and this might be attributed to the fact that the Eu^{3+} ion concentration at the surface of the sample is expected to be higher than that of the rest of the samples analysed. However monochromatic images showed no significant differences between the two phases observed in this sample, which would indicate a good mixing between these two phases.

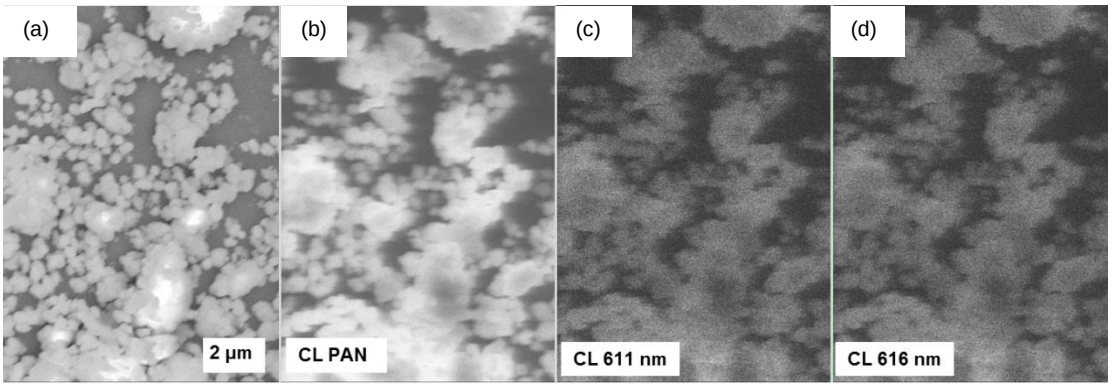

Figure 4.30.(a) SEM, **(b)** panchromatic CL and **(c-d)** monochromatic CL images at 611 nm and 616 nm recorded for the *Eu^{3+}-H-24-IMP* sample.

4.3.4. Cathodoluminescence of europium doped lanthanum oxide (Eu^{3+}:La_2O_3) nanoparticles

Figures 4.31(a) and 4.31(b) show the CL spectra of a representative sample of Eu^{3+}:La_2O_3 (*Eu^{3+}-CH-24*) with all the peaks identified with the corresponding transitions already observed in the previous photoluminescence results. Thus, the peaks were attributed to the transitions from ^5D_J (J = 0, 1, 2) states to $^7F_{J'}$ (J' = 0, 1, 2, 3, 4) states. Figure 4.31(a) shows

the CL spectrum between 450-740 nm and dominated by the $^5D_0 \rightarrow {}^7F_2$ transition at 626 nm. Figure 4.31(b) shows the CL spectrum but between 450-575 nm in order to observe the low intense transitions which corresponded to transitions from the $^5D_1$ and $^5D_2$ states. All the peaks observed in the spectrum in Fig. 4.31(a) correspond to the same transitions observed in the PL spectrum of Eu^{3+}:La_2O_3 nanoparticles (see Fig. 4.5), and thus, indicating that Eu^{3+} in this matrix can be efficiently excited by means of electron bombardment. However, Fig. 4.31(b) shows emission peaks at lower wavelengths which were not observed by the PL technique.

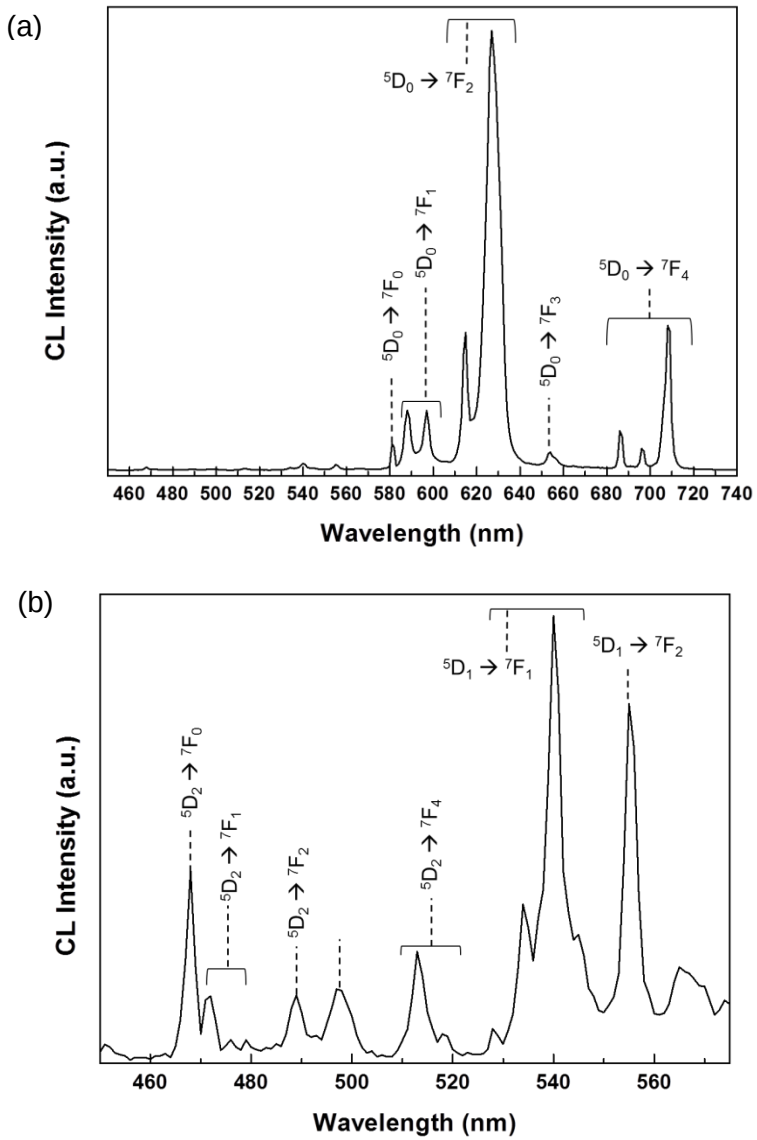

Figure 4.31. Cathodoluminescence spectra of the *Eu^{3+}-CH-24* sample **(a)** from 450 to 750 nm and **(b)** from 450 to 575 nm.

Figure 4.32 shows the CL spectra of Eu^{3+}:La_2O_3 samples synthesized by using different methods and after applying an annealing treatment at 973K for 2 h. Apparently, no significant differences were found in the CL spectra between these samples. Even, the *Eu^{3+}-CH-24-IMP* sample, which showed differences in the CL spectrum before the annealing treatment (see Fig. 4.22) due to the presence of the $LaCO_3OH$ phase (see Fig. 3.15), once it was calcined, the spectrum showed the same peaks demonstrating that the carbonate hydroxide phase was transformed into the oxide phase, as observed in the XRD patterns (see Fig. 3.21).

The I_2 values were calculated from the peaks with higher intensity corresponding to the $^5D_0 \rightarrow {}^7F_2$ and $^5D_0 \rightarrow {}^7F_1$ transitions and localized at about 626 nm and 585 nm, respectively, for all the samples. All the I_2 ratios were within 6.2-8.4 values (see Table 4.8). The *Eu^{3+}-CH-0* was the sample with the highest I_2 value. Apart from taking in consideration all the parameters studied in the PL section that can affect the I_2 parameter such as Eu^{3+} concentration, structure distortion, etc., this sample was formed by small particles with one of the lowest crystallite sizes among the synthesized samples (see Table 3.7). If we compare the I_2 values obtained by CL to those obtained by PL (see Table 4.1) we observed a similar trend in both cases. Thus, *Eu^{3+}-CPvu* and *Eu^{3+}-CH-24-IMP* samples show the lowest I_2 values. However, in general, the I_2 values calculated were higher from the CL spectra due to the fact that samples were calcined several times, that seems to affect to the polyhedron distortion.

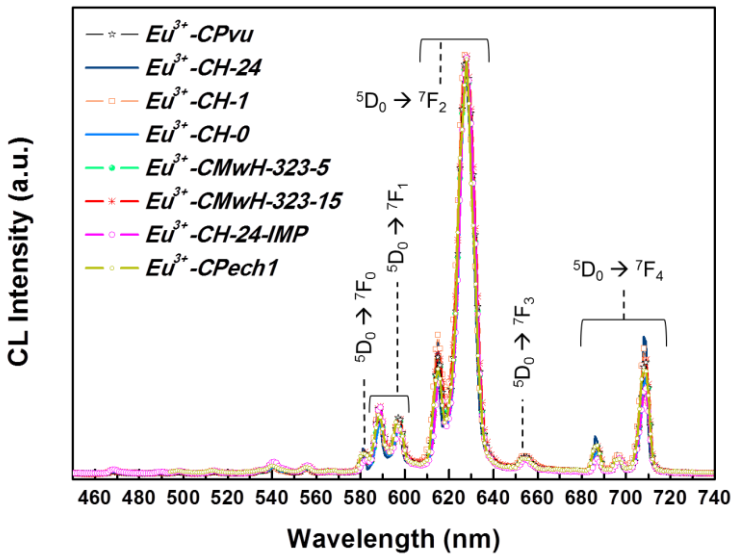

Figure 4.32. Cathodoluminescence spectra of some Eu^{3+}:La_2O_3 samples synthesized by using different methods.

Table 4.8. I_2 values of some Eu^{3+}:La_2O_3 samples.

Sample	I_2	I_1
Eu^{3+}-CPvu	6.4	3.6
Eu^{3+}-CH-24	7.6	3.2
Eu^{3+}-CH-1	6.8	3.0
Eu^{3+}-CH-0	8.4	4.3
Eu^{3+}-CMwH-323-5	7.2	3.6
Eu^{3+}-CMwH-323-15	6.2	3.5
Eu^{3+}-CH-24-IMP	6.3	4.6
Eu^{3+}-CPech1	7.1	4.0

The I_1 values were calculated from the $^5D_0 \rightarrow {}^7F_2$ transition which consisted of two peaks at 615 nm and 626 nm. The values obtained were within 3-4.6 (see Table 4.8), with the *Eu^{3+}-CH-24-IMP* sample showing the highest value. This result was in good agreement with the fact that by the CL technique, we are analysing the samples more superficially, together with the fact that by doping the sample by the wetness impregnation method, we should observe a higher amount of Eu^{3+} near the surface of this sample (see section 4.2.4).

4.3.5. Cathodoluminescence of Eu^{3+}:La_2O_3 nanoparticles at low temperature

Fig. 4.33 shows the CL spectrum of the *Eu^{3+}-CH-24* sample measured at 6 K. This spectrum recorded at low temperature presented only one peak for the $^5D_0 \rightarrow {}^7F_0$ transition, confirming that only one structural position for Eu^{3+} exists in the La_2O_3 crystalline structure. However, despite that we were able to observe a larger number of peaks at low temperature, the fine structure of the $^5D_0 \rightarrow {}^7F_1$ and the $^5D_0 \rightarrow {}^7F_2$ transitions was still not well resolved, since the system does not allow a recording resolution for the spectra smaller than 0.5 nm, as previously observed for the *Eu^{3+}-H-24* sample (see Fig. 4.24).

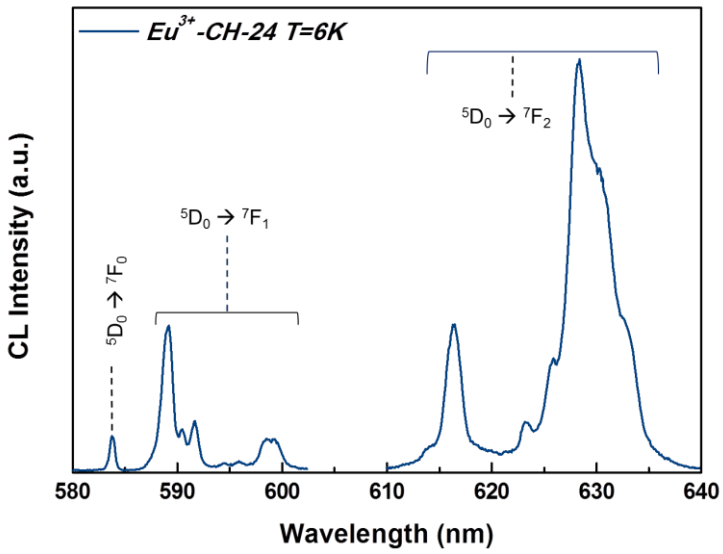

Figure 4.33. CL spectra recorded at low temperature for the *Eu^{3+}-CH-24* sample.

4.3.6. Cathodoluminescence at different accelerating voltage

Figure 4.34 shows the CL spectra recorded for a representative Eu^{3+}:La_2O_3 sample (*Eu^{3+}-CPech1*) as a function of the accelerating voltage. In this way we are analysing the CL spectra at different depths of the material. As we can see, the CL intensity increases when raising the accelerating voltage from 3 to 10 keV that corresponds to a higher volume of material being excited at high voltages. The fact that no additional peaks appear at high voltages indicates that there are not other minority phases in this sample, according to the X-ray diffraction results.

By comparing the results obtained by using different voltages one can also extract more information about the distribution of Eu^{3+} in the La_2O_3 nanoparticles, so that, the I_1 and I_2 parameters were calculated from the different CL spectra obtained (see Table 4.9). The I_1 ratio can be considered to be the same for all the voltages used. This parameter has been used to indicate the doping concentration of Eu^{3+} ions in the sample [71]. With that, as observed by other techniques, we corroborate the good Eu^{3+} distribution in the La_2O_3 nanoparticles for the *Eu^{3+}-CPech1* sample because we would expect a higher I_1 value at low accelerating voltage in the case of having more Eu^{3+} in the surface of the nanoparticles than in the bulk. However, the I_2 ratio decreased when increasing the accelerating voltage (see Table 4.9). This could be related to some quenching effects due to the higher amount of Eu^{3+} ions that were being excited when we used high accelerating voltages. For instance, Mhlongo et al. [206] reported that when the beam voltage increases, the local heating by energetic electrons occurs, and thus temperature also increases which can cause thermal quenching.

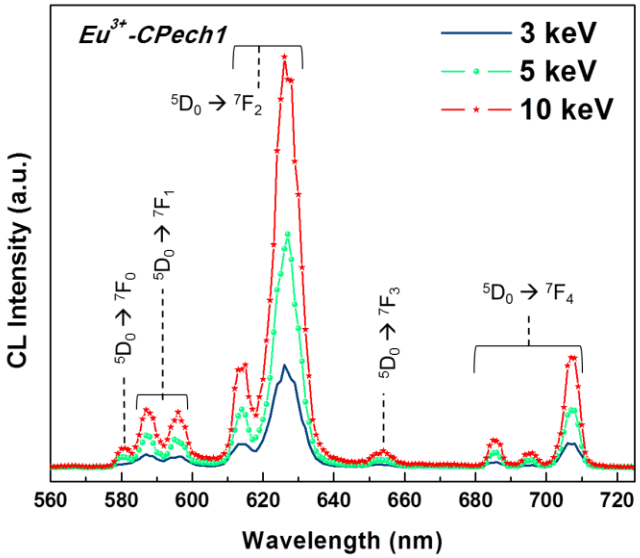

Figure 4.34. Cathodoluminescence spectra of the *Eu*$^{3+}$*-CPech1* sample recorded at different accelerating voltages.

Table 4.9. I_1 and I_2 values calculated from the CL spectra taken at different voltages for the *Eu*$^{3+}$*-CPech1* sample.

Accelerating voltage (keV)	I_1	I_2
3	4	8.9
5	4	8.7
10	4.1	7.3

4.3.7. SEM and CL images of Eu^{3+}:La_2O_3 nanoparticles

Figures 4.35(a-d) show a SEM image of the Eu^{3+}:La_2O_3 nanoparticles (*Eu*$^{3+}$*-CPech1*) together with a panchromatic CL image and two monochromatic CL images of the same region of the sample taken at 595 and 626 nm, coinciding with the peaks corresponding to the Eu^{3+} $^5D_0 \rightarrow {}^7F_1$ and $^5D_0 \rightarrow {}^7F_2$ transitions, respectively. These images confirm that the luminescence observed in the CL spectra arises from the Eu^{3+}:La_2O_3 nanoparticles. Figure 4.35(b) shows that the luminescence intensity recorded for the nanoparticles of calcined samples (Eu^{3+}:La_2O_3) was significantly higher in comparison with the luminescence intensity recorded for nanoparticles of non-calcined samples (Eu^{3+}:$La(OH)_3$) (see Figs. 4.25-4.30). Monochromatic images confirm that the different emissions observed are generated at the same parts of the samples.

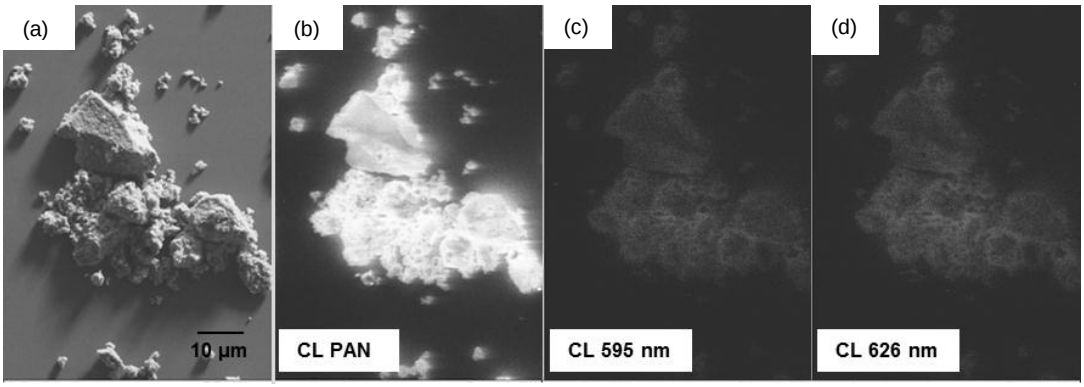

Figure 4.35. (a)SEM, **(b)** panchromatic CL and **(c-d)** monochromatic CL images at 595 and 626 nm recorded for the Eu^{3+}-*CPech1* sample.

Fig. 4.36 shows the SEM and CL images recorded for the Eu^{3+}-*CPech1* sample, but studied in other region than that shown in Fig. 4.35 and taking monochromatic CL images at additional wavelengths.

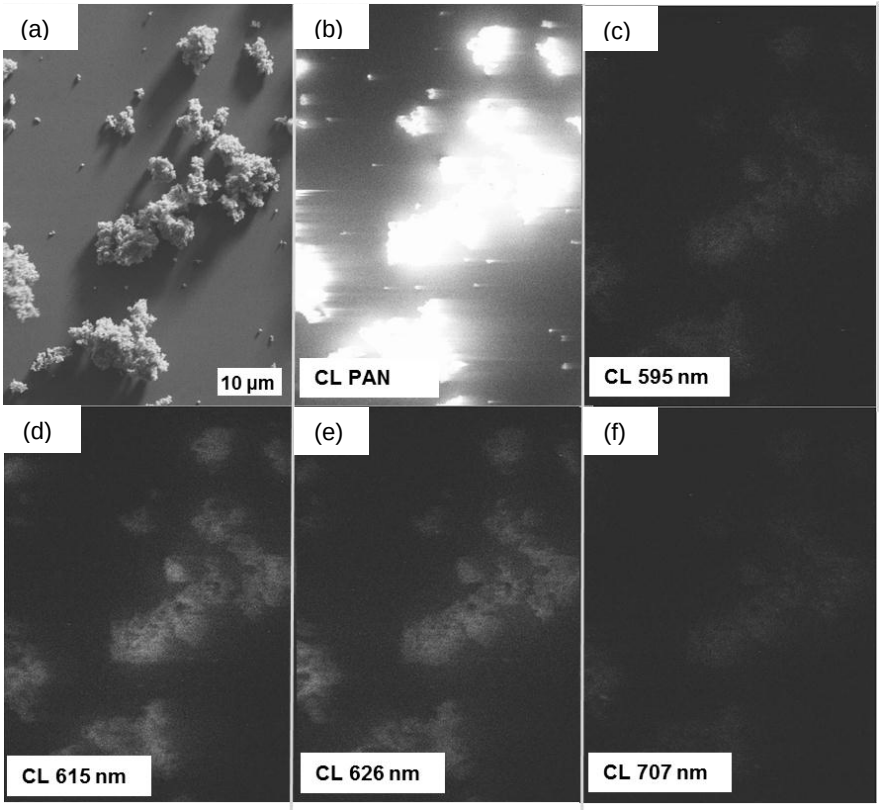

Figure 4.36. (a) SEM, **(b)** panchromatic CL and **(c-f)** monochromatic CL images at 595, 615, 626 and 707 nm recorded for the Eu^{3+}-*CPech1* sample.

Therefore, Figs 4.36(a-f) show a SEM image of the *Eu^{3+}-CPech1* sample together with a panchromatic CL image and four monochromatic CL images of the same region of the sample taken at 595, 615, 626 and 707 nm, coinciding with the peaks corresponding to the Eu^{3+} $^5D_0 \rightarrow {}^7F_1$, $^5D_0 \rightarrow {}^7F_2$ and $^5D_0 \rightarrow {}^7F_4$ transitions. As we expected, the panchromatic image showed the highest luminescence intensity and the monochromatic images exhibited lower luminescence intensities depending on the intensity of the emission peaks from which they have been recorded. Since all images show the same regions of the particles, then we can conclude that Eu^{3+} is well distributed on the nanoparticles.

4.3.8. Cathodoluminescence of praseodymium doped lanthanum oxide (Pr^{3+}:La_2O_3)

CL spectra of the *(5%)Pr^{3+}-Pech1* sample are shown in Figs. 4.37(a) and 4.37(b) for the visible and near infrared (NIR) parts of the electromagnetic spectrum. The peaks observed in Fig. 4.37(a) corresponded to the $^3P_0 \rightarrow {}^3H_{4,5,6}$ and $^3P_0 \rightarrow {}^3F_{2,3,4}$ transitions and the $^3P_0 \rightarrow {}^3F_2$ transition located at 667 nm was the most intense, as observed in the PL emission spectrum for that sample (see Fig. 4.20). Fig. 4.37(b) shows the CL spectrum at longer wavelengths with the peaks corresponding to the $^1D_2 \rightarrow {}^3F_J$ (J = 3, 4) transitions and the $^1D_2 \rightarrow {}^1G_4$ transition [178]. The peak located at 1030 nm which corresponded to the $^1D_2 \rightarrow {}^3F_4$ transition was the most intense. If we compare the peaks observed in the PL emission spectrum (see Fig. 4.20) with those observed in the CL spectrum for the same electromagnetic spectral region, both presented the same peaks but with some differences in their relative intensities. For example, in the PL spectrum, the peaks attributed to the $^3P_0 \rightarrow {}^3H_6$ transition had a lower intensity than the peaks attributed to the $^3P_0 \rightarrow {}^7F_4$ transition, whereas an opposite behaviour was observed in the CL spectrum for these two peaks. This might be due to the different excitation mechanisms involved in these two excitation processes.

Additionally, for the *(5%)Pr^{3+}-Pech1* sample, SEM images together with the corresponding panchromatic CL images were taken for the visible and infrared regions of the electromagnetic spectrum and are shown in Figures 4.38(a-b) and 4.38(c-d), respectively. The panchromatic CL images confirmed the low luminescence intensity emitted by Pr^{3+}, since the images were not as brilliant as the panchromatic CL images observed for Eu^{3+}:La_2O_3 nanoparticles and even less brilliant than those recorded for the Eu^{3+}:$La(OH)_3$ nanoparticles. For this reason, we were not able to record monochromatic CL images for this sample. From the images recorded, we can conclude that Pr^{3+} was distributed homogeneously in the samples.

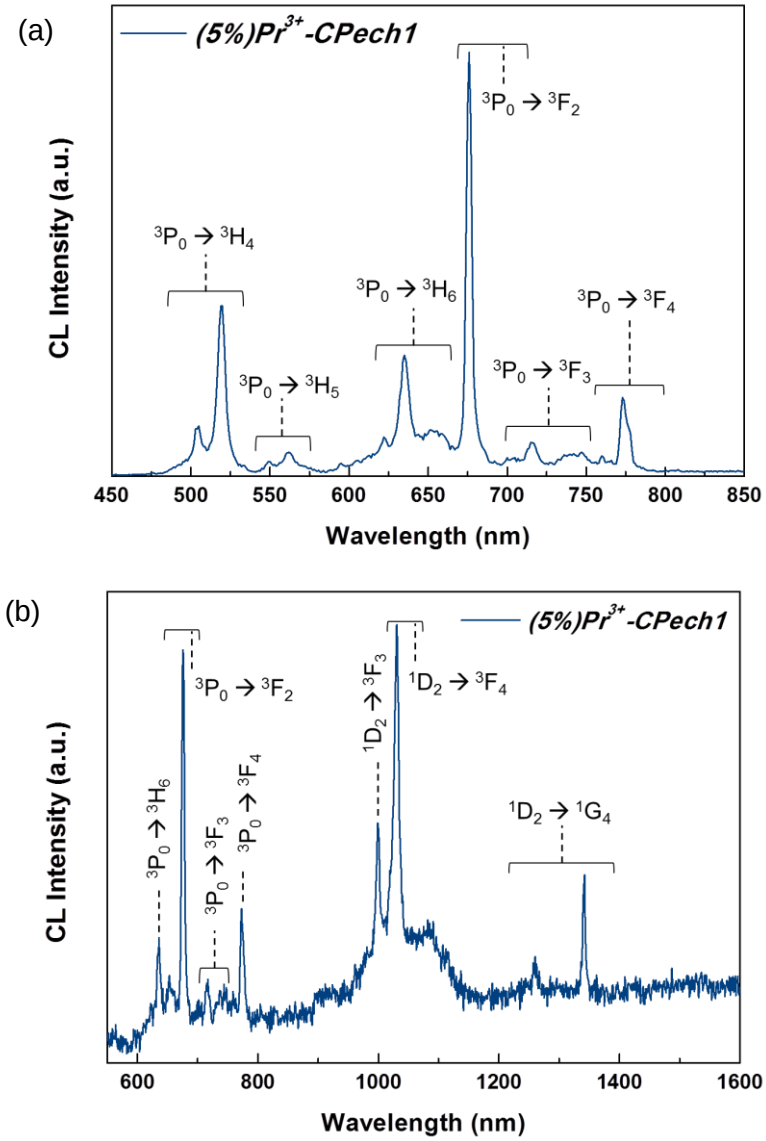

Figure 4.37. (a) CL spectrum from 450 to 850 nm and **(b)** CL spectrum from 575 to 1600 nm of the *(5%)Pr^{3+}-CPech1* sample.

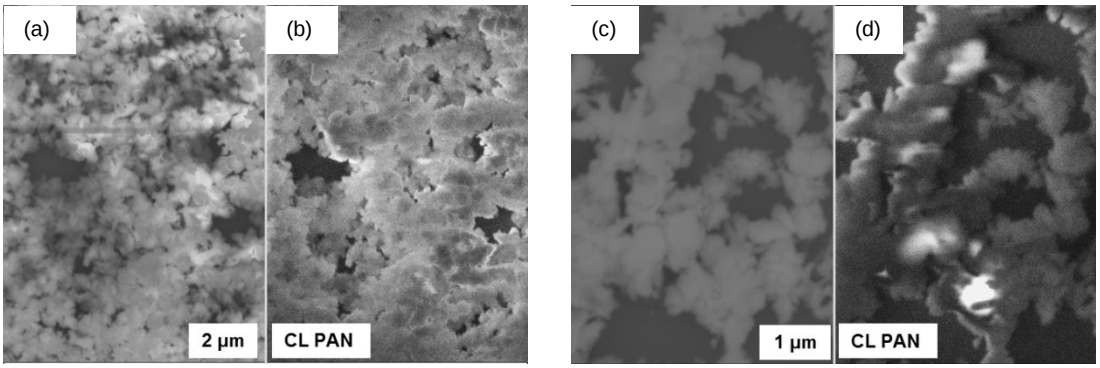

Figure 4.38. (a-b) SEM and panchromatic CL images recorded in the visible region of the electromagnetic spectrum and **(c-d)** SEM and panchromatic CL images recorded in the infrared region of the electromagnetic spectrum for the Pr^{3+}-*CPech1* sample.

Chapter 5

Structural stability studies of La_2O_3 and La_2O_2S hosts: re-hydroxylation process

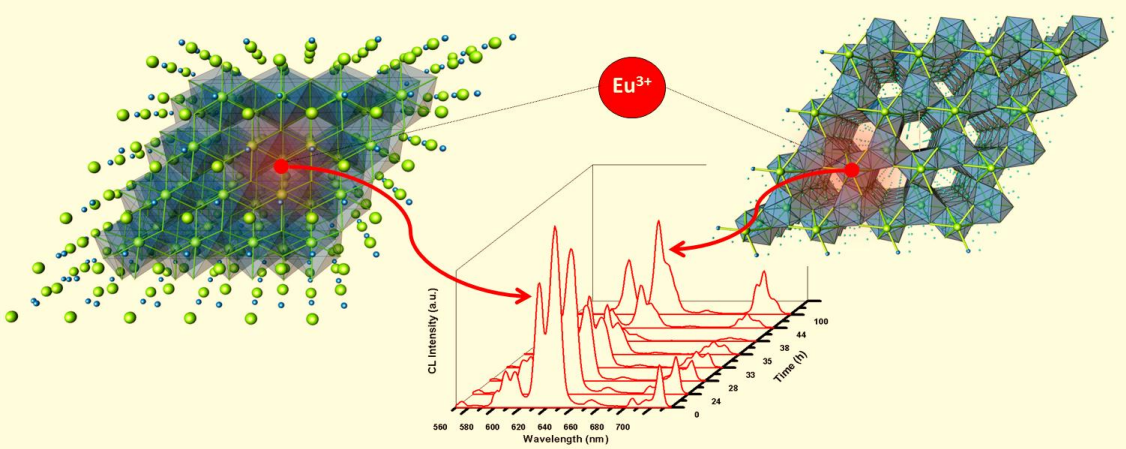

During many years, materials with different structural properties have been used as hosts for luminescent active ions. One of the desired properties for the host materials is their structural and chemical stability. In Chapter 5, we will study the stability of the hosts used in this thesis, lanthanum oxide (La_2O_3) and lanthanum oxysulfide (La_2O_2S), from their characterization by different techniques such as XRD, N_2 physisorption, TEM, PL and CL. The different emission Eu^{3+} signatures observed depending on the host, have been specially used as an advantageous tool to follow the stability of these hosts. Other studies of stability as a function of time and calcination temperature will be also presented in this chapter.

5.1. Overview

During many years, several hosts with different structural properties have been doped with small amounts of luminescent active ions. As we commented in Chapter 4, a good host for luminescent ions must hold some special properties, for example to be transparent for visible and infrared light and, among others, to have a good chemical and structural stability.

Structural stability of La_2O_3

Lanthanum oxide (La_2O_3) is becoming of increasing interest in recent years due to the wide number of applications of this material together with the possibility of reducing production costs. When compared with other rare earth host materials (Y_2O_3, Gd_2O_3, etc.), inorganic compounds containing lanthanum are relatively low-cost host materials [139]. However, lanthanum oxide powders have to be handled carefully because they are very sensitive to the atmospheric conditions reacting relatively fast with water/carbon dioxide to form hydroxyl, carbonate and mixed phases [144,207-210].

All the lanthanide oxides absorb water and/or carbon dioxide onto their surface forming a layer of hydrate, carbonate or hydroxyl-carbonate. In accordance with the phase diagram for the lanthanide sesquioxides [211] shown in Figure 5.1, five different structural varieties have been identified as a function of the ionic radius of the lanthanide ions, known as A, B, C, H, and X types.

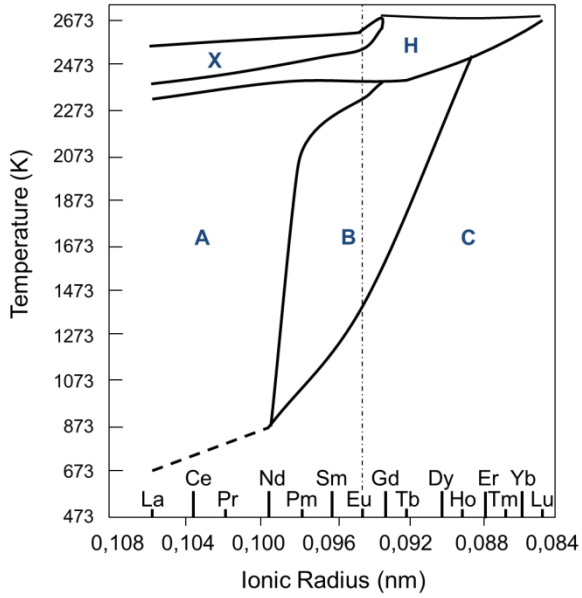

Figure 5.1. Polymorphic transformation for the lanthanide sesquioxides (Ln_2O_3).

Three of these polymorphs, the trigonal A-type (in most cases space group $P\bar{3}m1$), the monoclinic B-type (in most cases space group C2/m), and the cubic C-type (in most cases

space group Ia3), are known to occur at room temperature, and atmospheric pressure, whereas H and X forms have only been observed at temperatures above 2273 K [211,212]. For the lighter members of the series, from La to Nd, the trigonal A-type form is the most usually found and together with the B-type are able to absorb water and/or carbon dioxide from the atmosphere faster than the other forms [211]. Jeon et al. [213] studied the hygroscopic nature of some lanthanide oxides (Pr_2O_3, Sm_2O_3, Gd_2O_3 and Dy_2O_3) and found that the higher the ionic radius of the lanthanide and the lower the electronegativity, the higher the reactivity with water. Lanthanum oxide belongs to the A-type trigonal oxides and it is well known for being the most hygroscopic compound of the lanthanide series [211,213]. Many authors, interested in the properties of these oxides as high-k gate dielectric materials, have considered the hygroscopic nature of La_2O_3 a major problem in its use. Re-hydroxylation of lanthanum oxide in air can be completed after 24 h, and can drive to mechanical weakness of monolithic pieces. A complete study on the reaction kinetics of the re-hydroxylation reaction of La_2O_3 has been published [214], indicating that bulk reaction of powders with water vapour proceeds extremely fast. More recently, Fleming et al. [214] published a study about the reactivity of various lanthana powders by passing water-saturated vapour across the lanthanum oxide samples, which were obtained after calcining several lanthanum hydroxides synthesized by different procedures at different temperatures. These authors conclude that the rate of re-hydroxylation can be related to the crystallite size of the lanthana samples. However, no information about the mechanism involved in this re-hydroxylation process has been reported.

Structural stability of La_2O_2S

All the elements of the lanthanide series, along with yttrium, can form compounds with the composition Ln_2O_2S and with trigonal $P\bar{3}m1$ structure [88,215]. In general the polycrystalline Ln_2O_2S compounds, apart from Ce_2O_2S, are stable in air up to 773 K. Since the oxysulfides can be considered as intermediates between the oxides and the sulphides of the corresponding elements, many features of their properties and structure are similar [179]. However, we do not have to consider hydroxylation processes when we regard to oxysulfides, since lanthanide hydroxide sulfides do not exist. Some preliminary studies of Machida et al. [216] revealed that the oxysulfides are generally decomposed into a mixture of oxides and sulfates when heated in the presence of O_2.

5.2. Re-hydroxylation studies of un-doped and europium-doped lanthanum oxide nanoparticles

First, we present and discuss the studies of the re-hydroxylation process of several un-doped lanthanum oxide samples whose precursors were synthesized by different procedures. After that, we report the use of cathodoluminiscence as a novel characterization technique to follow the lanthanum oxide re-hydroxylation reaction versus time according to different annealing procedures for several europium-doped lanthanum oxide samples. Finally, we also follow the

re-hydroxylation process of doped samples by recording excitation and emission photoluminescence spectra, specially focusing our interest on the charge transfer band.

5.2.1. Characterization of the re-hydroxylation process for un-doped lanthanum oxide to lanthanum hydroxide ($La_2O_3 \rightarrow La(OH)_3$)

In order to study the effect that the lanthanum hydroxide preparation method has on the surface and re-hydroxylation properties of the La_2O_3 nanoparticles, several lanthanum oxide samples (*CPv, CPvu, CH-0, CH-1, CH-48* and *CMwH-323-5),* whose precursors were obtained by different methods (*see Chapter 3, section 3.2.1.*), were exposed to re-hydroxylation in atmospheric air for 80 h.

Table 5.1 shows some characterization data of the re-hydroxylated samples, such as crystallite size calculated from XRD patterns, and BET areas, calculated from N_2 physisorption. Those samples were named with an *R* after their identification names (e.g. *CPv-R* is the re-hydroxylated sample of the *CPv* sample).

Table 5.1. Characterization of the re-hydroxylated La_2O_3 samples

Sample	Crystallite phases (XRD)	Crystallite size (nm)[a]	BET Area ($m^2 \cdot g^{-1}$)[b]
CPv-R	$La(OH)_3$	25.5	16.5
CPvu-R	$La(OH)_3$	25.8	17.9
CH-0-R	$La(OH)_3$	22.4	17.8
CH-1-R	$La(OH)_3$	24.3	17.6
CH-48-R	$La(OH)_3$	26.3	18.5
CMwH-323-5-R	$La(OH)_3$	24.3	14.8

[a] Calculated from XRD patterns.[b] Calculated from nitrogen physisorption.

XRD patterns of these samples only showed the presence of the $La(OH)_3$ phase. This confirms that total re-hydroxylation occurred. Also, there was a decrease of the crystallite size while increasing the BET surface when comparing to their respective calcined samples. Crystallite sizes of calcined samples were ranging from 48 to 65 nm and BET surface values were ranging from 1 to 4 $m^2 \cdot g^{-1}$ (see Table 3.7 and 3.8). Crystallite sizes of the re-hydroxilated samples ranged from 22 to 27 nm, while BET surface values ranged from 14 to 18 $m^2 \cdot g^{-1}$. The details for each re-hydroxylated sample can be found in Table 5.1. These results confirmed that the re-hydroxylation process occurred in these samples, and led to similar crystallite sizes and similar BET areas for all samples. It is important to note that the BET surface areas of the re-hydroxylated samples were lower than those of the starting synthesized lanthanum hydroxides, which were ranging from 28 to 146 $m^2 \cdot g^{-1}$ (see Table 3.6). This can be explained by the presence of atmospheric CO_2 during the re-hydroxylation

process that could difficult the recovery of the surface area lost after calcination, as previously reported [217].

Since the adsorption of water and/or carbon dioxide entails the increase of mass and volume of lanthanum oxide [214], we took advantage of that to study the kinetics of the re-hydroxylation process and compare the behaviour of these calcined samples, whose precursors were synthesized by using different methods. Once they were calcined, they were immediately weighed, considering that measure as the weight at time 0. Samples were weighed at the same time intervals within the 0-80 h period to be compared and at controlled humidity and temperature conditions (50-70% and 293-298 K) in order to be compared among them. Finally, the study was considered as finished when the weight stopped increasing. Figure 5.2 shows the conversion of La_2O_3 to $La(OH)_3$ with time for the *CPv*, *CPvu*, *CH-0*, *CH-1*, *CH-48* and *CMw-H-323-5* samples. After 80 h of re-hydroxylation, all the La_2O_3 samples were completely transformed to $La(OH)_3$.

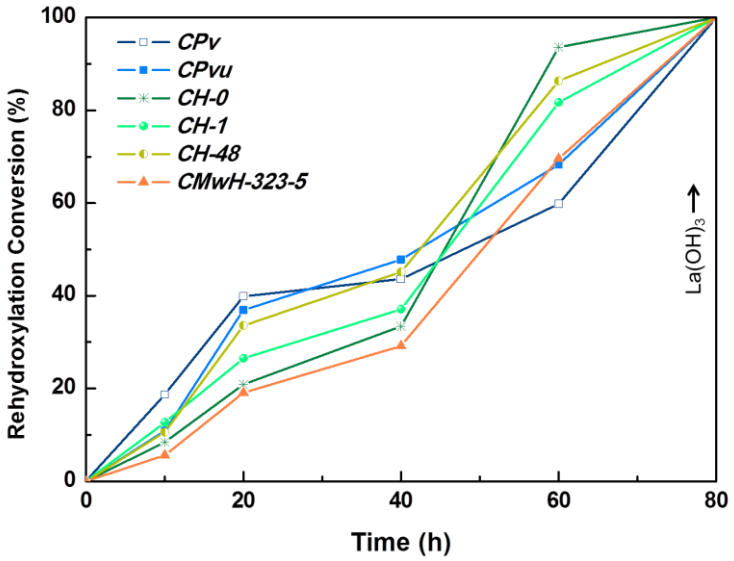

Figure 5.2. Re-hydroxylation study of several La_2O_3 samples synthesized by different methods as a function of time exposure to controlled humidity and temperature conditions.

From this graph, we can observe that the progress of the re-hydroxylation process with time takes place in several steps at different rates. Initially, the reaction is quite slow and similar for all samples until 10 h, except for the *CPv* sample, which showed a higher re-hydroxylation conversion than the rest of samples. In this period, surface adsorption of water and reaction with the surface of lanthanum oxide should be expected. The initial slow rate could be associated with some diffusion limitations in La_2O_3 from the surface to the bulk [214]. More differences in the behaviour of the samples were observed at 20 h with re-hydroxylation conversion values between 20 and 40 % depending on the sample. At this reaction time, the re-hydroxylation process occurred in the order *CPv* > *CPvu* > *CH-48* >

CH-1 > *CH-0* > *CMwH-323-5* for the different samples, being faster that of the *CPv* sample. The reaction rate could be related to factors such as the surface area, the particle size and the morphology of the nanoparticles, as well as to the presence of surface defects that would facilitate the transport of hydroxyl/water species from the surface to the bulk of the nanoparticles. Thus, samples with lower particle sizes (e.g. *CPv* sample) re-hydroxylate faster than those that had higher particle sizes, such as *CH-48* or *CMwH-323-5* samples (Fig. 3.14). After 20 h, the reaction rate is apparently constant over a period of time, suggesting that mass transport in both, surface and bulk, is invariant. After 40 h, the re-hydroxylation rate increased significantly for all samples, but especially for the three samples which showed a lower reaction rate during the first 20 h of the re-hydroxylation process: *CH-0*, *CH-1* and *CMwH-323-5*. This acceleration of the re-hydroxylation process is probably accompanied by a process of formation of defects allowing a faster mass transport process. Interestingly, the initial surface area of these samples (*CH-0*, *CH-1* and *CMwH-323-5*) was lower than that of the rest of the samples (see Table 3.8). Therefore, samples with a lower initial surface area require longer reaction times to increase the re-hydroxylation rate. In the final phase of the reaction, the rate slows again toward completion and it is apparent that mass transport limitations become important again. This is probably related to the decreasing concentration of sites for hydroxylation and the fact that these sites would be deep inside the materials, and far from the surface requiring a more complex mass transport process [214]. We observed that the total weight gained was about an 8-9% over the initial weight but apparently, the sample looked two or three times bigger than the initial one.

The evolution of the transformation of the crystalline phases during re-hydroxylation with time was followed taking XRD patterns. The patterns were recorded from 25 to 35^{o} because in this region is possible to see the maximum intensity peaks of both La_2O_3 and $La(OH)_3$ phases, (002) and (101) peaks, respectively, and they were recorded at different re-hydroxylation times until 30 h for four representative calcined samples (see Fig. 5.3). As we can observe, the $La(OH)_3$ phase was formed at different times for the different samples analysed. For the *CPv* sample, the peaks corresponding to $La(OH)_3$ appeared well defined after 10 h from the beginning of re-hydroxylation (see Fig. 5.3(a)) whereas the observation of $La(OH)_3$ was more progressive with time for the *CH-48* sample (see Fig. 5.3(d)). Finally, for *CH-0* and *CMwH-323-5* samples, 19 and 20 h of re-hydroxylation were necessary to detect the $La(OH)_3$ phase, respectively (see Fig. 5.3(b) and (c)).

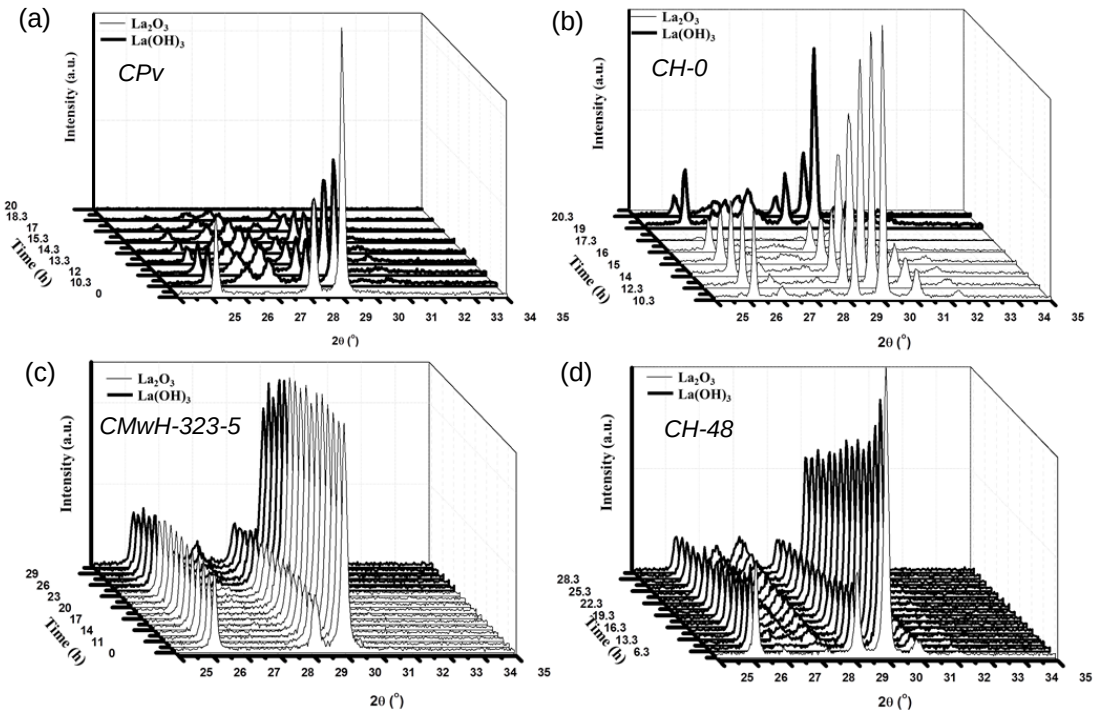

Figure 5.3. Evolution of the XRD patterns versus re-hydroxylation time for the **(a)** *CPv*, **(b)** *CH-0*, **(c)** *CMwH-323-5* and **(d)** *CH-48* samples.

The particle size of the re-hydroxylated samples was smaller (Fig. 5.4 (a-c) than that of their respective calcined samples, as observed by TEM (see Fig. 5.4(d-f). This can be attributed to the interlayers formed between the particles by the generation of the covering $La(OH)_3$ phase on the surface of the particles, which can cause the separation of the big aggregates formed during the calcination process. The *CH-48-R* sample showed particles much bigger (see Fig. 5.4(b)) than those whose precursors were precipitated without aging or aged with microwaves or by conventional heating at shorter aging times (e.g. see Fig. 5.4(a) and 5.4(c)). This could be related to the different re-hydroxylation rate observed for each La_2O_3 sample. Thus, smaller La_2O_3 particles easily transform to $La(OH)_3$.

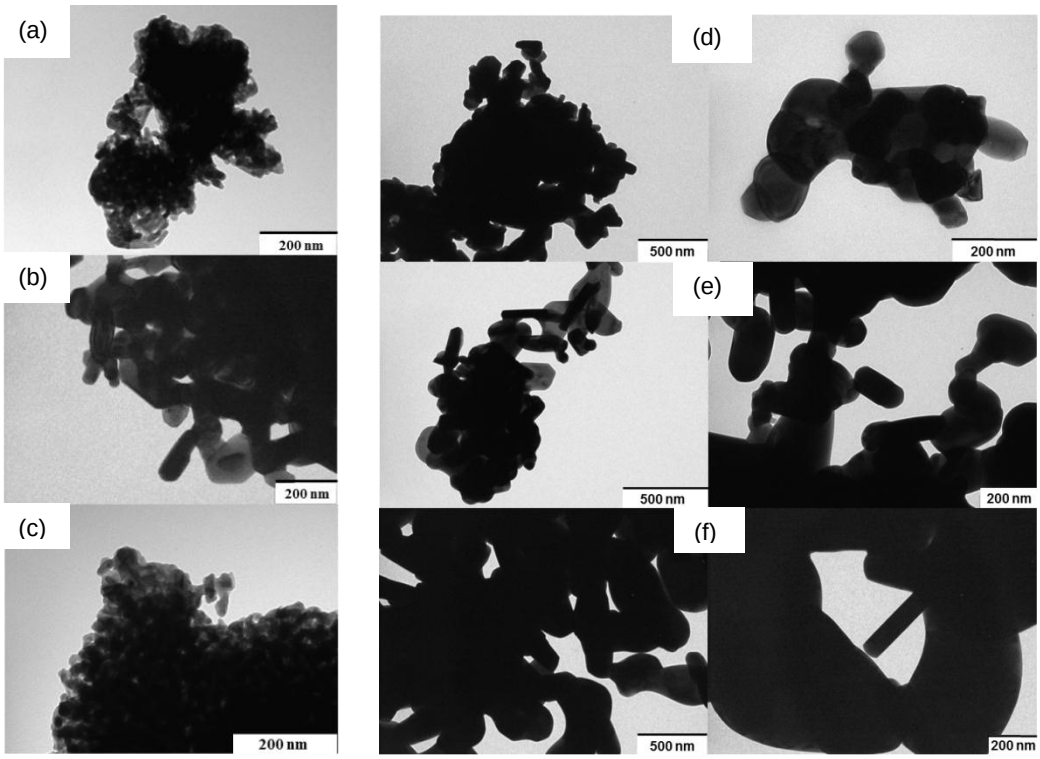

Figure 5.4. TEM images of several re-hydroxylated La_2O_3 samples: **(a)** *CPv-R*, **(b)** *CH-48-R* and **(c)** *CMwH-323-5-R* and their corresponding just calcined La_2O_3 samples: **(d)** *CPv*, **(e)** *CH-48* and **(f)** *CMwH-323-5*.

From these studies, we can conclude that the re-hydroxylation rate mainly depended on the particle size and surface area of the starting lanthanum oxide sample. Therefore, the method used to prepare the initial lanthanum hydroxide affects the re-hydroxylation properties of the subsequent lanthanum oxide sample. However, after re-hydroxylation, the particle size and surface area were similar for all samples (see Table 5.1), independently from the method from which these samples were prepared initially.

5.2.2. Characterization of the re-hydroxylation process for europium doped lanthanum oxide to europium doped lanthanum hydroxide (Eu^{3+}:La_2O_3 → Eu^{3+}:$La(OH)_3$)

The re-hydroxylation process of a representative europium doped lanthanum oxide sample was characterized by the XRD technique. Thus, we monitored the evolution of the re-hydroxylation reaction of Eu^{3+}:La_2O_3 nanoparticles (*Eu^{3+}-CH-24* sample) with time by XRD (see Fig. 5.5). We previously calcined the Eu^{3+}:$La(OH)_3$ precursor at 1273 K for 2 h to guarantee only the presence of the oxide phase. The range of measurement was also restricted from 25 to 35º. We marked with a triangle the three most intense diffraction peaks of the La_2O_3 phase. These peaks correspond to the (100), (002) and (101) reflections of the La_2O_3

phase [115]. We could note that the La_2O_3 phase was stable up to 30 h and at the same time we also observed that the La_2O_3 phase started to disappear when the $La(OH)_3$ phase began to appear at about 25 h. Thus, in the range between 25-30 h, both phases were present.

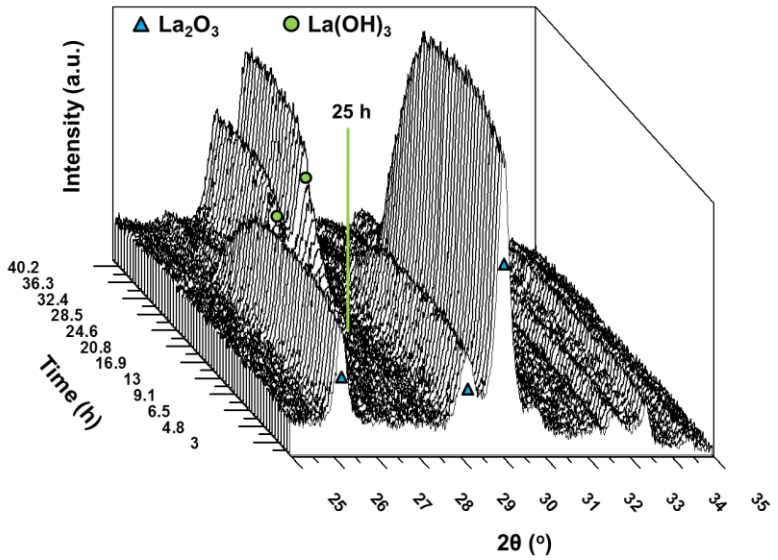

Figure 5.5. XRD patterns of the evolution of the *Eu^{3+}-CH-24* sample versus time after exposure to air atmosphere at room temperature.

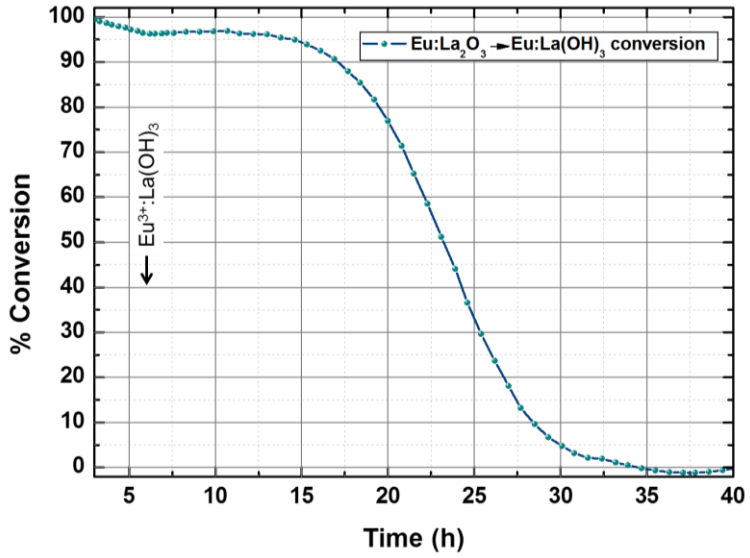

Figure 5.6. Kinetic curve of the re-hydroxylation process after calcining the *Eu^{3+}-H-24* sample at 1273 K for 2 h applying a heating rate of 10 K min^{-1} and evaluated by XRD.

We evaluated the kinetic curve of the re-hydroxylation reaction by correlating the intensity of the (101) diffraction peak of the $La(OH)_3$ phase with its concentration in the sample. The

result is presented in Figure 5.6. More than 22 h were needed to convert 50% of La_2O_3 to $La(OH)_3$, and after 35 h, La_2O_3 was completely re-hydroxylated.

We can observe whether the presence of the doping Eu^{3+} ions has any effect on the re-hydroxylation rate of La_2O_3 by comparing Figs. 5.2 and 5.6. Fig. 5.2 shows that after 25 h of the calcination of the sample, the *CH-48* sample was 40% transformed into $La(OH)_3$ whereas for the *Eu^{3+}-H-24* sample the transformation reach values of 70% after 25 h of the calcination of the sample. Thus, we suggest that the fact of having 5 mol% Eu^{3+} in the La_2O_3, could be accelerating the rate of the re-hydroxylation process. Two of the parameters taken into account when studying the re-hydroxylation rate for the un-doped samples, and exposed in the section *5.2.1,* were the crystallite size and the surface area. To compare the particle size between un-doped and Eu^{3+} doped samples, we analysed the *CH-1* and *Eu^{3+}-CH-1* samples, that where synthesized under the same conditions with the only difference of the introduction of Eu^{3+} as a doping ion in the second sample. If we compare the values of the crystallite size obtained for the *CH-1* and the *Eu^{3+}-CH-1* samples, we observed some significant differences. They showed different crystallite sizes, being 58.6 and 48.7 nm, respectively. In conclusion, the crystallite size of the particles was generally smaller when Eu^{3+} ions were present in La_2O_3. Consequently, this fact could accelerate the La_2O_3 re-hydroxylation process, in the case of Eu^{3+} doped samples.

Cathodoluminescence as a function of calcination conditions

Since Eu^{3+} showed different emission peaks depending on the host containing the active ion (La_2O_3 or $La(OH)_3$), as we already observed in Chapter 4, the CL technique was also useful to follow the re-hydroxylation process. The sample used to carry out these analyses was *Eu^{3+}-CH-24*. Table 5.2 lists the wavelengths of the different emission bands observed at room temperature in Eu^{3+}:$La(OH)_3$ and Eu^{3+}:La_2O_3 (see Figs. 4.21 and 4.31, respectively). After following the evolution of the re-hydroxylation by XRD of the sample annealed at 1273 K for 2 h by applying a heating rate of 10 K min^{-1} and studying its corresponding kinetic curve, we analysed what happened if we applied rapid thermal annealing conditions: 973 K for 1 min (*A-Eu^{3+}-CH-24* sample), 1073 K for 1 min (*B-Eu^{3+}-CH-24* sample), 1173 K for 1 min (*C-Eu^{3+}-CH-24* sample), and 1173 K for 2 min (*D-Eu^{3+}-CH-24* sample).

Just after annealing the (*A-D)-Eu^{3+}-CH-24* samples at different experimental conditions, the CL spectra showed the typical bands of Eu^{3+} in La_2O_3, as expected. However, we observed that the relative intensity between the two peaks corresponding to the $^5D_0 \rightarrow {}^7F_2$ transition, located at 613 and 626 nm (the fluorescence intensity ratio, I_1) changed significantly by time, with a reduction of the intensity of the peak located at 626 nm. At longer time, the re-hydroxylation progressed and I_1 further decreased. Finally, the 613 nm band, corresponding to the $^5D_0 \rightarrow {}^7F_2$ transition in $La(OH)_3$, dominated the spectra. At the same time, the emission band located at 707 nm, corresponding to the $^5D_0 \rightarrow {}^7F_4$ transition in Eu^{3+}:La_2O_3 lost intensity whereas the emission band located at 695 nm, corresponding to the same transition but in

Eu^{3+}:$La(OH)_3$, was more and more intense. Figure 5.7(a-d) shows the CL spectra of the (*A-D)-*Eu^{3+}*-CH-24* samples. The cathodoluminescence spectra were recorded at different times after the annealing process (0, 24, 28, 33, 35, 38, 44 and 100 h). From these spectra, we observed that the $La(OH)_3$ phase appeared after 24 h of annealing, but the sample was not completely transformed to La_2O_3 until 35-38 h after the beginning of the re-hydroxylation process, at which time the cathodoluminescence spectra of the sample did not change any more. However, the kinetics of the re-hydroxylation reaction progressed differently depending on the annealing procedure (time and temperature).

Table 5.2. Wavelength values of the cathodoluminescence peaks of Eu^{3+} in $La(OH)_3$ and La_2O_3 phases.

Transition	**$La(OH)_3$ peak position (nm)**	**La_2O_3 peak position (nm)**
$^5D_2 \rightarrow {}^7F_0$	-	468
$^5D_2 \rightarrow {}^7F_1$	-	472, 475, 479, 489
$^5D_2 \rightarrow {}^7F_2$	-	497
$^5D_2 \rightarrow {}^7F_3$	-	512
$^5D_1 \rightarrow {}^7F_1$	524, 534	533, 540
$^5D_1 \rightarrow {}^7F_2$	555	554
$^5D_0 \rightarrow {}^7F_0$	577	581
$^5D_0 \rightarrow {}^7F_1$	591	588, 596
$^5D_0 \rightarrow {}^7F_2$	613	614, 626
$^5D_0 \rightarrow {}^7F_3$	648	653
$^5D_0 \rightarrow {}^7F_4$	688, 694	708

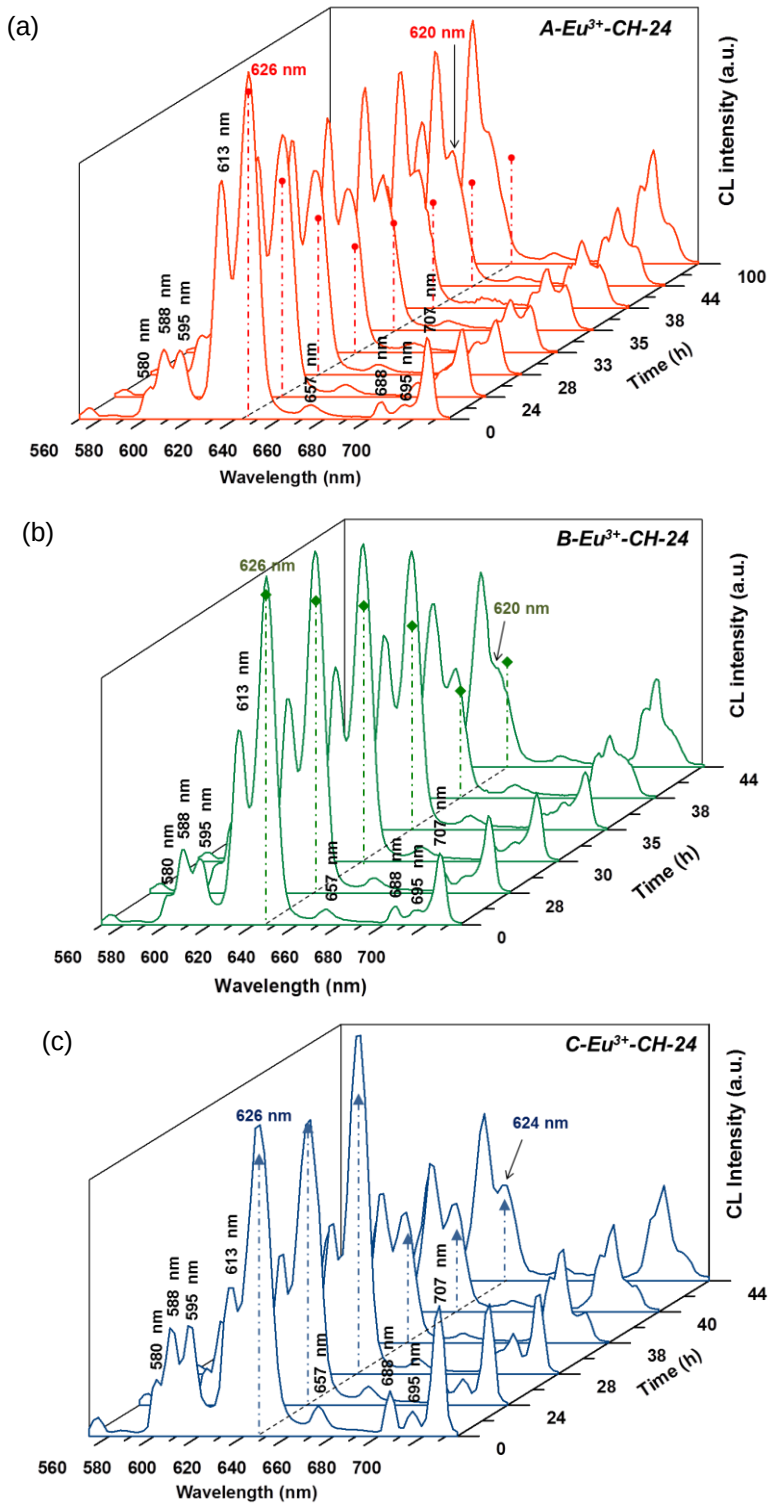

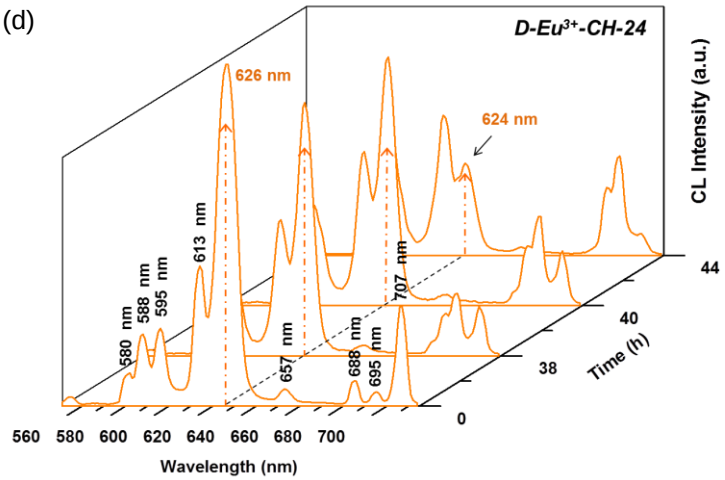

Figure 5.7. Cathodoluminescence spectra of the **(a)** *A-Eu^{3+}-CH-24* sample annealed at 973 K for 1 min, **(b)** *B-Eu^{3+}-CH-24* sample annealed at 1073 K for 1 min, **(c)** *C-Eu^{3+}-CH-24* sample annealed at 1173 K for 1 min, and **(d)** *D-Eu^{3+}-CH-24* sample annealed at 1173 for 2 min.

The kinetic curves were calculated for the *(A-D)-Eu^{3+}-CH-24* samples by using the relative intensities of the peaks located at 613 and 626 nm since the first one can be assigned to the $La(OH)_3$ phase, while the second one can be assigned to the La_2O_3 phase. The curves were obtained in order to observe the differences with respect to the annealing procedure more in detail. Figure 5.8 shows the kinetic curves depending on the temperature (Fig. 5.8(a), 973 K, 1073 K and 1173 K) and depending on the time applied in the rapid thermal annealing process (Fig 5.8(b), 1 min and 2 min). Time 0 h corresponds to the measurements taken just after the annealing procedure. After that, the samples were exposed to air at room temperature. We observed that when the annealing temperature was higher, the re-hydroxylation process evolved more slowly (see Fig. 5.8(a)). On one hand, the *A-Eu^{3+}-CH-24* sample, which was annealed at 973 K, showed 100% of conversion after 38 h of annealing whereas the *B-Eu^{3+}-CH-24* and *C-Eu^{3+}-CH-24* samples (annealed at 1073 K and 1173 K, respectively) showed about 88% and 82% of conversion at this time, respectively. On the other hand, the shape of the curve of re-hydroxylation was also significant. For instance, we observed that by increasing the temperature from 973 K to 1073 K, after 30 h of the annealing process, the *A-Eu^{3+}-CH-24* sample transformed 75% of the oxide phase to the hydroxide phase while the *B-Eu^{3+}-CH-24* sample just transformed 12% of the oxide phase. Fig. 5.8(b) shows the kinetic curve after annealing the sample at 1173 K for 1 min (*C-Eu^{3+}-CH-24* sample) and 2 min (*D-Eu^{3+}-CH-24* sample). After 40 h, only ~50% of the *D-Eu^{3+}-CH-24* sample was converted to Eu^{3+}:$La(OH)_3$, while almost 85% of the *C-Eu^{3+}-CH-24* sample was already converted to Eu^{3+}:$La(OH)_3$. Thus, at the same annealing temperature, the re-hydroxylation process evolved slowly when we increased the time of annealing. However, the full conversion of the material was achieved at the same time, indicating that the reaction evolved slowly at the beginning for the *D-Eu^{3+}-CH-24* sample, but fast at the end. These

results could be comparable with the kinetic curves depending on the temperature because the most significant difference between the *(A-C)-Eu^{3+}-CH-24* samples and the *(C-D)-Eu^{3+}-CH-24* samples was the resistance time of Eu^{3+}:La_2O_3 to be re-hydroxylated. Thus, everything indicated that after a certain degree of conversion was achieved, the reaction evolved faster. When comparing these results with those obtained previously by conventional annealing techniques (1273 K for 2 h) and shown in Fig. 5.6, we could see that rapid thermal annealing increased the stability of the La_2O_3 phase, which constituted a benefit to manipulate this compound under a non-controlled atmosphere.

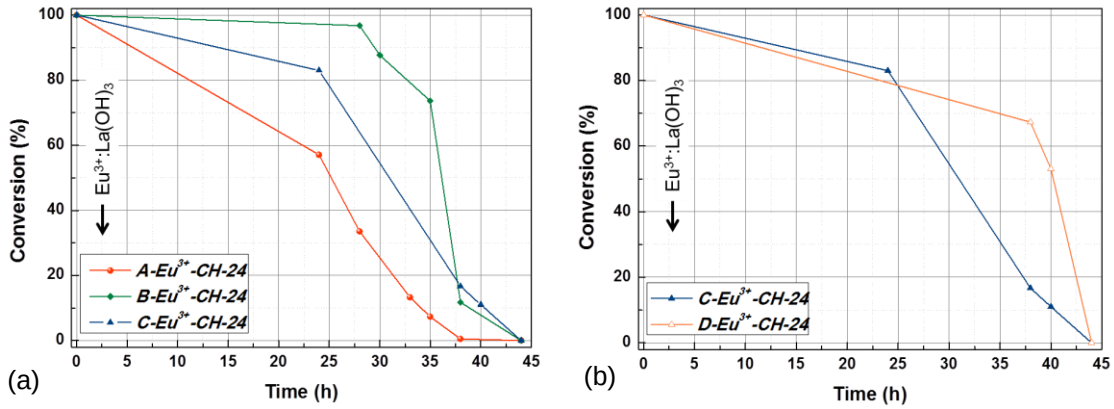

Figure 5.8. Kinetic curves of the re-hydroxylation process after a rapid thermal annealing process depending on **(a)** temperature and **(b)** time used in the annealing process.

Photoluminescence studies versus re-hydroxylation time

The re-hydroxylation of Eu^{3+}:La_2O_3 directly affects the luminescence properties of the Eu^{3+} ion as we have seen by the CL study presented in *section 4.3.1*. Since we are interested in exploiting the absorption cross section of the charge transfer (CT) band because it is orders of magnitude higher than that of the f-f transitions of Eu^{3+} in the UV-visible spectral region, we analysed what happen to this CT band during the re-hydroxylation process. Then, by the PL technique we followed the re-hydroxylation process versus time of the Eu^{3+}:La_2O_3 nanoparticles and the changes in the CT band were analysed.

Figures 5.9(a) and 5.9(b) show the excitation spectra of the *Eu^{3+}-CH-1* sample from 0h to 164 h after the calcination of the sample from two different perspectives. In order to compare the changes of the CT band versus time, all the spectra were normalized in intensity at ~233 nm (see Fig. 5.9(b)) corresponding to the host absorption band from the O 2 p valence band to the La (5d6s) conduction band. Fig. 5.9(a-b) depicte that within the first 45 h, the CT band became quite stable, whereas above 50 h after the calcination of the sample, the intensity of the CT band became lower and lower until it was not able to be distinguished from the host absorption band. Fig. 5.9(c) shows the excitation spectrum after 150 h of calcination in more detail. Since the small peaks appearing at higher wavelengths are due to Eu^{3+} f-f transitions,

they were still observed in the excitation spectrum after 150 h of the calcination of the samples.

Other authors have already observed changes in the luminescence behaviour of the materials due to the effects that water adsorption or hydroxyl groups formation can cause. For instance, Schmechel et al. [218] observed, when studying Eu^{3+}:Y_2O_3 nanoparticles that the relative excitability on the charge transfer process decreased drastically in the presence of water. This is commonly attributed to the fact that the water molecules efficiently quench the luminescence of lanthanide ions through non-radiative exchange of electronic energy from the Ln^{3+} ions to the high vibrational modes of OH groups.

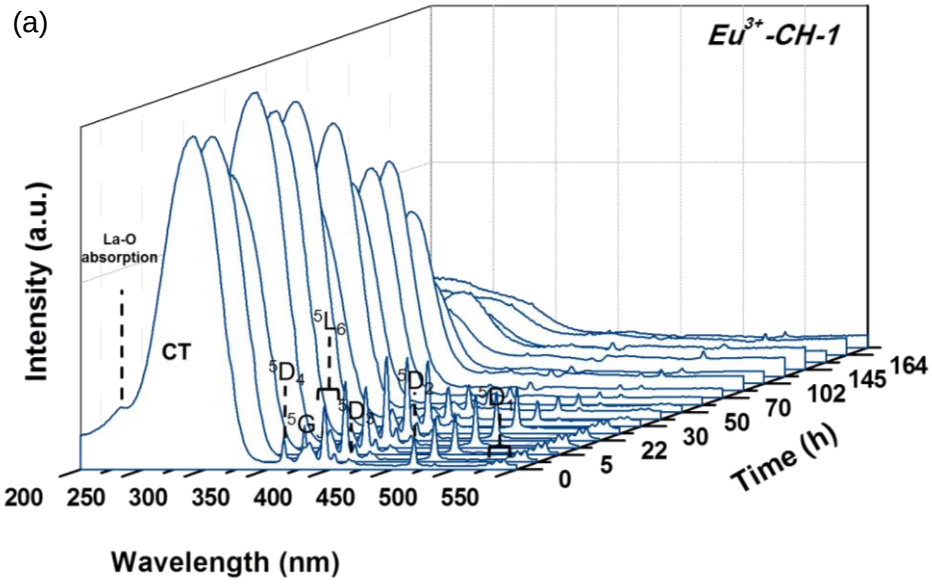

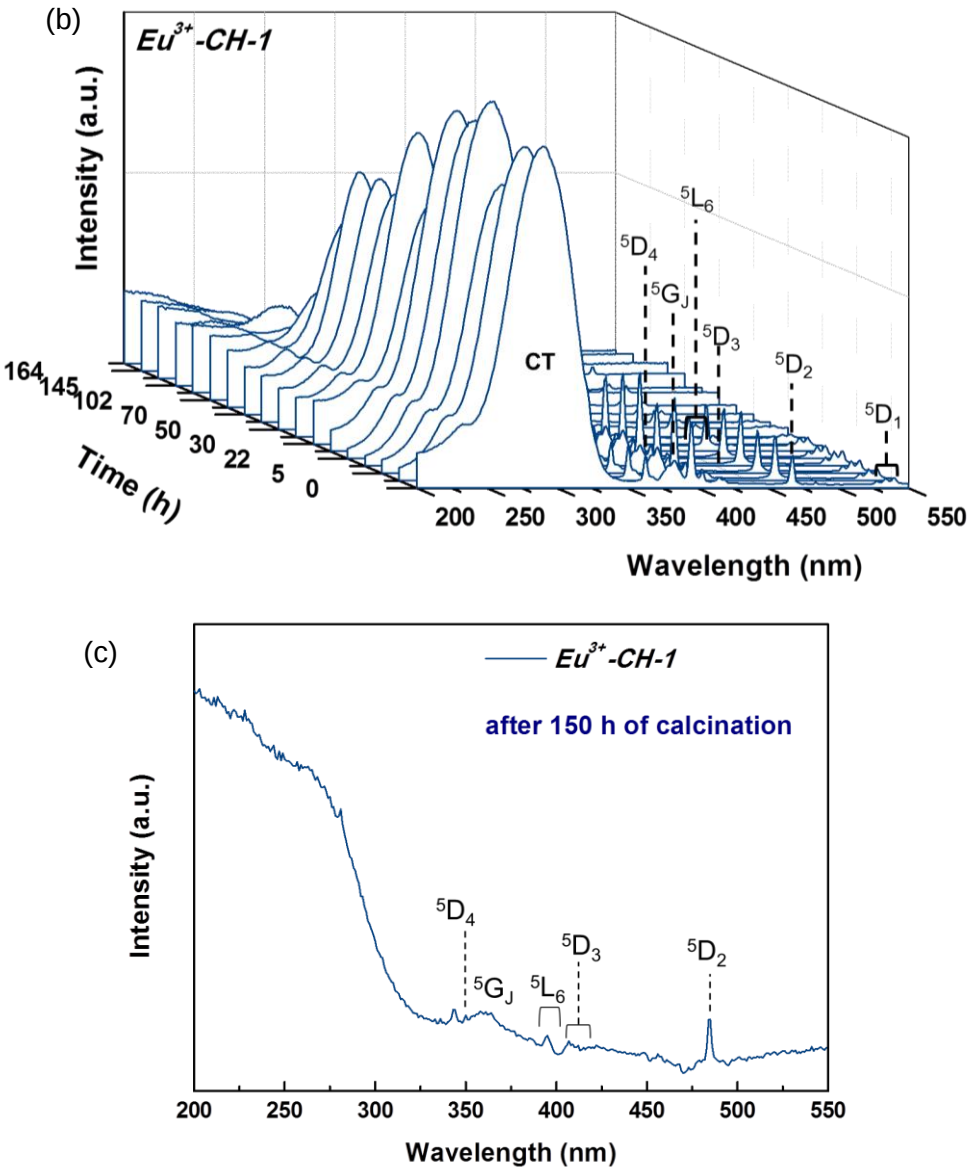

Figure 5.9. Excitation spectra of the *Eu^{3+}-CH-1* sample from 0 to 164 h after its calcination **(a)** tilted towards the left site, **(b)** tilted towards the right site, and **(c)** at 150 h after its calcination.

If we take in consideration the results obtained by the XRD technique (see Figs. 5.5 and 5.6), La_2O_3 and $La(OH)_3$ were present in the sample within the range of 25-35 h which corresponded to the range of time during which the intensity of the CT band was quite stable (see Fig. 5.9(a-b)). In the XRD patterns, after 40 h only the $La(OH)_3$ phase was detected. This time matched well with the time after which the CT band started to decrease in intensity. Thus, the reduction in intensity of the CT band could be related to the re-hydroxylation

process what meant on one hand the gradual disappearance of the La_2O_3 phase in the sample and on the other hand, the gradual formation of the $La(OH)_3$ phase.

Hoefdraad et al. [166] observed that the CT band position varies as a function of the host lattice and concluded that this variation was proportional to the Eu-O distance. In fact, as Fig. 5.10 shows, the CT band shifted slightly towards shorter wavelengths during the re-hydroxylation process. In the excitation spectrum of the as-calcined *Eu^{3+}-CH-1* sample, the CT band is centered at 290 nm whereas for the *Eu^{3+}-CH-1* sample after 45 and 80 h of its calcination, the CT bans is centered at 286 and 283 nm, respectively. In agreement with these results, a similar observation was made on Eu^{3+}:Y_2O_3 nanoparticles [218], where the CT band position shifted from ~238 nm to ~230 after 3 months of exposure in air.

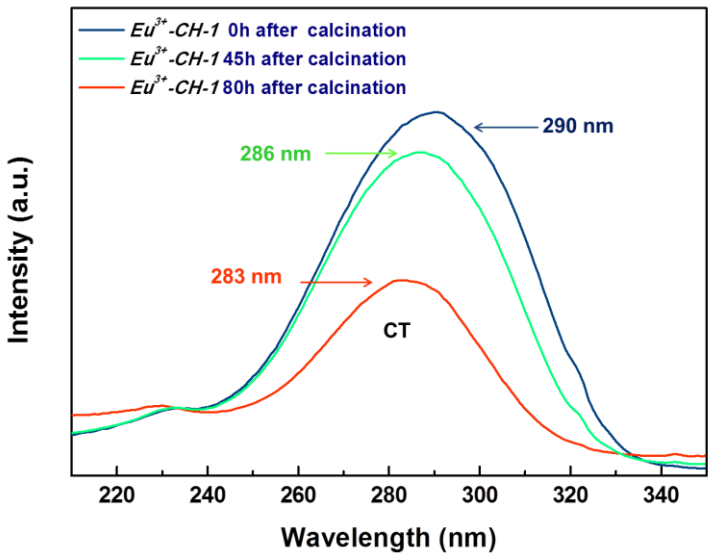

Figure 5.10. Excitation spectra of the as-calcined *Eu^{3+}-CH-1* sample and the *Eu^{3+}-CH-1* sample after 45 and 80 h of its calcination.

Figs. 5.11(a) and 5.11(b) show the emission spectra of the *Eu^{3+}-CH-1* sample versus time. In agreement with the results observed in the excitation spectra, the emission intensity has a similar behaviour during the re-hydroxylation process, as expected since the excitation wavelength used corresponded to the maximum of the CT band for each emission spectrum recorded. All the spectra were normalized in intensity at 615 nm for comparison. The asymmetry ratio I_2, calculated at different times after the calcination of the sample by using the intensity ratio between the peaks at 626 and 595 nm, confirmed the trend of the emission intensity of the *Eu^{3+}-CH-1* sample versus time. The emission intensity decreased at the beginning of the re-hydroxylation process, later, the emission intensity increased within the period of 25-50 h, and finally, through a progressive disappearance of the peaks, there was not emission coming from the sample. The I_2 obtained were 4.0, 3.3, 3.1, 3.4, 3.0, 2.8, and

0.7 for the sample after being exposed to air at 0, 10, 25, 50, 70, 80, and 140 h, respectively (see Fig. 5.12).

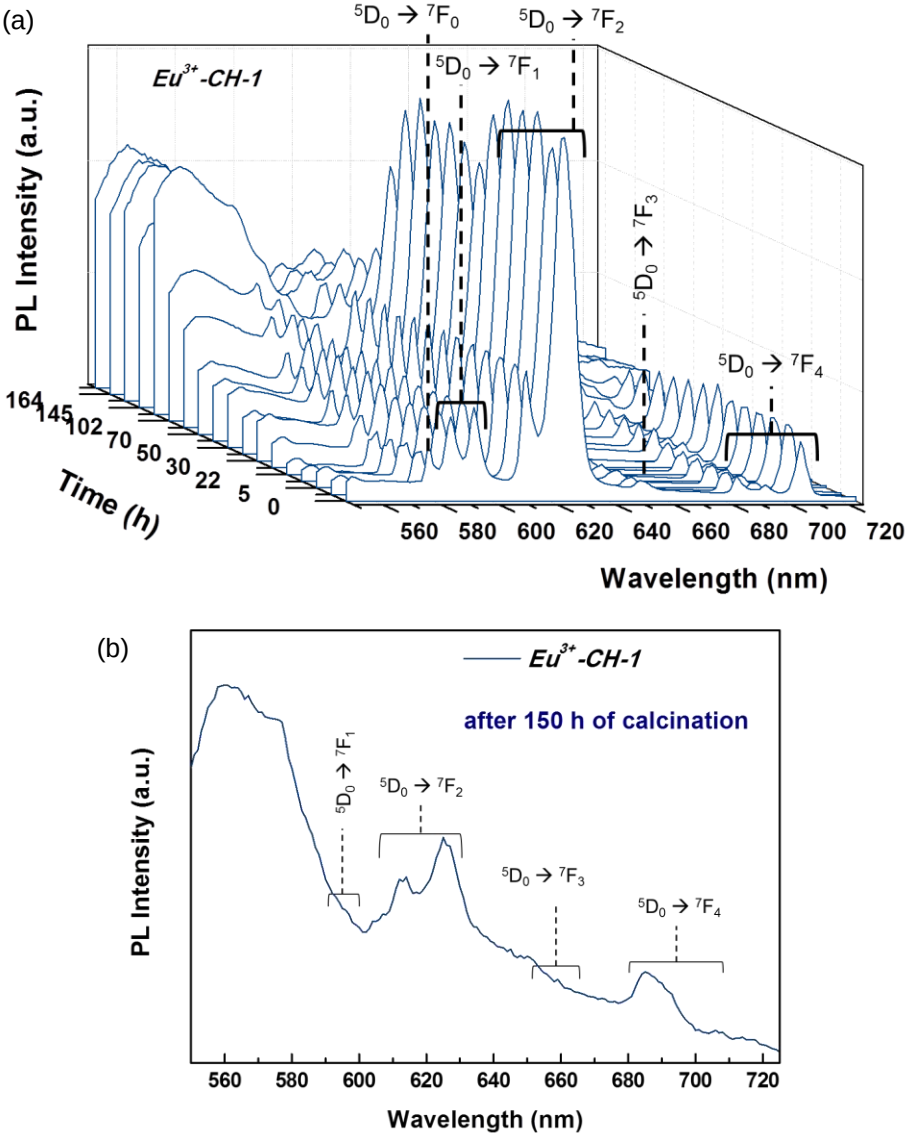

Figure 5.11. Emission spectra of *Eu^{3+}-CH-1* sample **(a)** from 0 to 164 h **(b)** and at 150 h after calcination.

We suggest that at the beginning of the re-hydroxylation process the surface of the sample is covered by water molecules relatively fast and consequently decreasing the emission intensity. However, after 20-25 hours approximately, the water might be creating interlayers between the particles. As observed by TEM images (see Fig. 5.4(a-c)), the re-hydroxylated samples showed smaller particle sizes than their respective calcined samples (see Fig. 5.4(d-

f). Thus, these interlayers separate the big aggregates formed during the calcination step which could be related to a slight increase in the emission efficiency. However, after a certain time, and when more water molecules are found surrounding the sample, the emission drastically decline, coinciding with a faster transformation of La_2O_3 into $La(OH)_3$. Furthermore, although the un-doped samples showed a slower re-hydroxylation rate, in agreement with the results observed by PL, Fig. 5.2 also shows that during the first 20 h after the calcination of the sample, the re-hydroxylation went faster than during the following 20 hours, and the re-hydroxylated rate increased again after 60 h of the calcination of the *CH-1* sample. Fig. 5.11(b) shows the emission spectrum after 150 h of the calcination of the sample. Here, the peaks were much less intense making difficult its identification with the corresponding transition. Since we could not obtain the emission spectra of the Eu^{3+}:$La(OH)_3$ samples by PL, we believe that this decrease in the intensity of the emission peaks is also related to the formation of the $La(OH)_3$ phase.

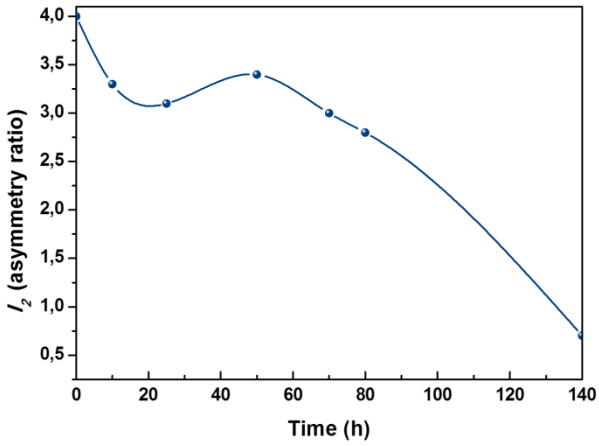

Figure 5.12. I_2 ratio versus time of the *Eu^{3+}-CH-1* sample during atmosphere exposure.

In order to confirm the decrease in the emission efficiency, the fluorescence lifetime of the Eu^{3+}:$La(OH)_3$ nanoparticles was measured. Figure 5.13(a) shows the fluorescence lifetime at room temperature of the *Eu^{3+}-CPech1* sample after several days and consequently re-hydroxylated (*Eu^{3+}-CPech1*). From the results observed in the re-hydroxylation studies, we suggest that this sample should be only partially re-hydroxylated. Additionally, Fig. 5.13(b) shows the emission spectrum of this sample which corroborated that the re-hydroxylation was not complete since it still showed several emission peaks. This spectrum was recorded from 550 to 750 nm by using the OPO laser under pumping at 394 nm. The decay curves were monitored at 615 nm. The lifetime derived from the single exponential fitting was 460 μs. In comparison with the lifetime obtained for the *Eu^{3+}-CPech1* sample, which was 1.02 ms (see Fig. 4.17), the lifetime for the *Eu^{3+}-CPech1-R* sample was significantly lower. Other authors have already observed a decrease in the lifetimes due to the increased nonradiative decay processes involving the vibrational modes of the water molecules at the surface [218].

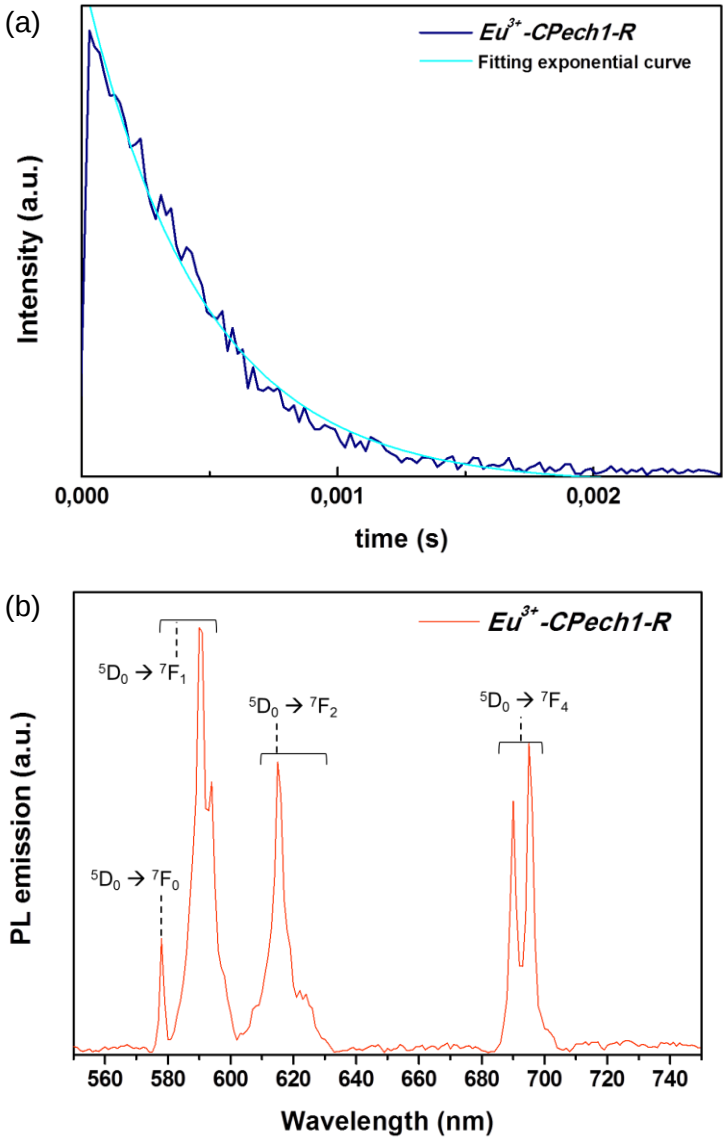

Figure 5.13. (a) Lifetime decay of the *Eu*$^{3+}$*-CPech1-R* sample recorded at room temperature and **(b)** its emission spectrum.

Changes on the position of the Charge Transfer (CT) Band

In order to explain the disappearance of the CT band during the re-hydroxylation process, we focused our attention on the Eu-O distance. To study the Eu-O distance in the $La(OH)_3$ structure, the X-ray diffraction patterns of the *Eu*$^{3+}$*-Pvu*, *Eu*$^{3+}$*-H-1*, *Eu*$^{3+}$*-MwH-323-5* and *Eu*$^{3+}$*-H-24-IMP* precursors were recorded at slow conditions (an angular step of 0.02º at 16 s per step). Additionally, the Eu-O distance was also studied in $La(OH)_3$ generated from the La_2O_3 re-hydroxylation process of the *Eu*$^{3+}$*-CH-1* sample. The resultant re-hydroxylated sample was named *Eu*$^{3+}$*-CH-1-R*. The lattice parameters of these precursors and of this re-

hydroxylated sample were refined from the respective X-ray diffraction patterns using the Full-Prof software based on the Rietveld method (see Fig. 5.14). The lattice parameters of un-doped $La(OH)_3$ were taken as reference, listed in the 36-1481 reference pattern of the JCPDS database, that are a=b= 6.5286 Å, and c= 3.8588 Å [110]. As we did for lanthanum oxide, we refined 10 different parameters: one overall scale factor, six background parameters, five shape parameters and three cell parameters.

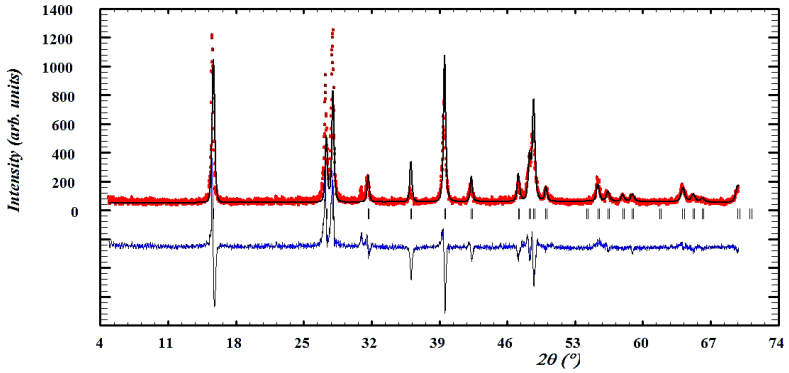

Figure 5.14. Experimental (black line), calculated (red line), and difference (bottom) results of XRD refinement for the *Eu^{3+}-CH-1-R* sample by the Fullprof software.

Then, the La-O distances were calculated by using the ATOMS software and introducing for each sample their experimental lattice parameters obtained with the refinement performed in the Full-Prof software. Assuming that Eu^{3+} was replacing La^{3+} in the structure of $La(OH)_3$, occupying the S_3 symmetry sites, the La-O distance calculated, can be considered as the Eu-O distance. The structure of the $La(OH)_3$ is hexagonal and belongs to the $P6_3/m$ space group. The coordination polyhedra of La in this structure can be described as a trigonal prism with the lanthanum located at its center. Lanthanum is nine-coordinated with two unique metal-oxygen bond distances (La-O(1) = 2.551(3) Å and La-O(2) = 2.588(3) Å). Six of the nine coordinating oxygens are located at each of the corners of the trigonal prism. Those are the apical oxygens, O(2), with longer bond distances, three above and three below the mid-horizontal plane. The remaining three coordinating oxygens, O(1), are equatorial with shorter bond distances, and being located near the center of the rectangular faces of the trigonal prism. The atomic coordinates of the $La(OH)_3$ structure are listed in Table 5.3. Figure 5.15 shows three projections of the structure of $La(OH)_3$ along the three crystallographic axes.

Table 5.3. Coordinates of the La, O and H atoms for the $La(OH)_3$ structure.

	x	y	z
La	1/3	2/3	0.25
O	0.3916	0.3095	0.25
H	0.225	0.152	0.25

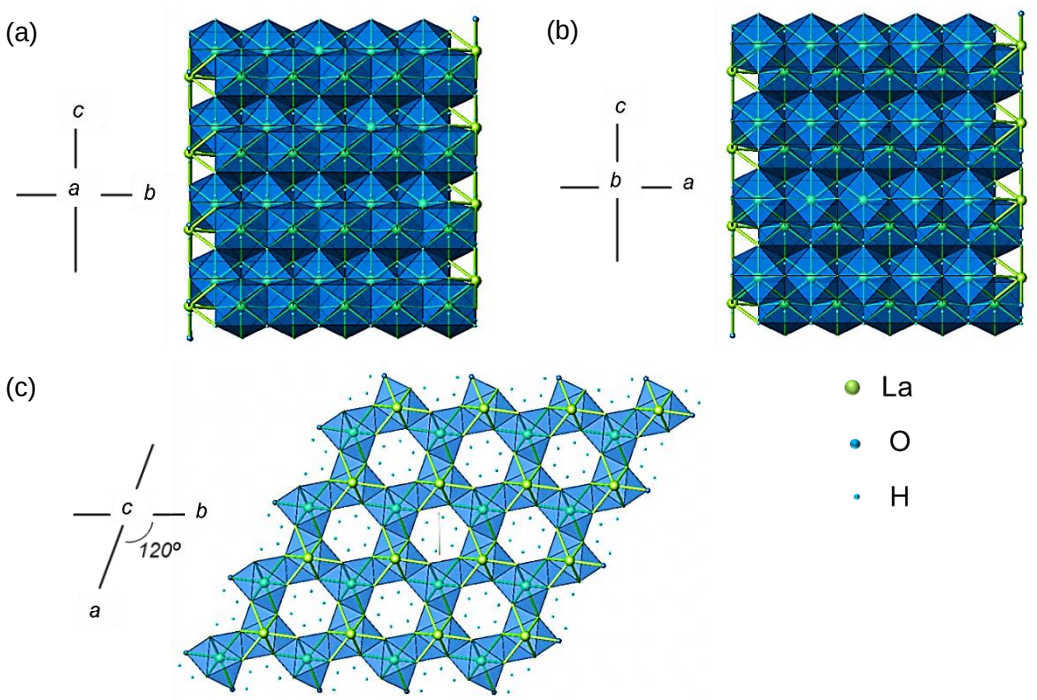

Figure 5.15. Image depicting three projections of the $La(OH)_3$ structure along the **(a)** *a*, **(b)** *b* and **(c)** *c* crystallographic axes.

Table 5.4. Experimental lattice parameters and average Eu-O distances of the precursor $La(OH)_3$ samples prepared by using different methods.

Sample	Lattice parameters (Å)		Average Eu-O distance (Å)
	a=b	c	
Eu^{3+}-Pvu	6.5288(3)	3.8588(4)	2.5652
Eu^{3+}-H-1	6.5286(7)	3.8585(0)	2.5651
Eu^{3+}-MwH-323-5	6.5287(9)	3.8587(6)	2.5652
Eu^{3+}-H-24-IMP	6.5286(0)	3.8588(4)	2.5651
Eu^{3+}-CH-1-R	6.5230(8)	3.8528(3)	2.5625

The experimental results of Eu-O distances for the precursor and the re-hydroxylated samples synthesized by using different methods are listed in Table 5.4. As was already observed in Chapter 4, *section 4.2.6*, the smaller lattice parameters for $La(OH)_3$ doped with Eu^{3+} in comparison with pure $La(OH)_3$ could be attributed to the introduction of europium in the structure of the crystals. The results of the Eu-O bond distances were within the range 2.5651-2.5652 Å for the precursor samples and 2.5625 Å for the re-hydroxylated sample.

Therefore, the $La(OH)_3$ sample generated by the re-hydroxylation process had shorter Eu-O bond distances and smaller lattice parameters than the $La(OH)_3$ precursors. From these results, we can say that by using different synthesis methods to prepare the Eu^{3+}:$La(OH)_3$ nanoparticles, the Eu-O distance was not affected significantly.

According to Hoefdraad et al. [166], the shorter the Eu-O bond distance, the shorter the wavelength where the CT band is found. Therefore, since the Eu-O distance in $La(OH)_3$ is larger than that of La_2O_3 one would expect a shift of the CT towards longer wavelengths. Since we compare the Eu^{3+}-O^{2-} CT band position in these two different hosts, $La(OH)_3$ and La_2O_3, the covalency of the compound might be also an important parameter to be considered. Bouchard et al. [167] observed that as the covalency increases, the interaction between the electrons is reduced, so that they spread out over wider orbitals and consequently the CT band shifts to longer wavelengths. Recenty, Sunding et al. [203] reported that La-O bonds present larger covalency in La_2O_3 compared to $La(OH)_3$. Thus, this would explain the fact of having the CT band at shorter wavelengths in $La(OH)_3$ than in La_2O_3. However, we observed that when the time of exposure of the sample to air increased, the CT band was not formed. This fact has been already observed in other hosts and it could be directly related to the Eu-O distance length. Table 5.5 shows different Eu^{3+} doped hosts with the position of their corresponding CT band and the Eu-O distance. Thus, it seems that it exists a limitation for the Eu-O distance for which the CT band can be formed. Whereas for the La_2O_3 host, which has a Eu-O distance of ~ 2.5342 Å, the CT band can be successfully formed, for $La(OH)_3$, which has a Eu-O distance of ~ 2.5652 Å, the CT band could not formed.

Table 5.5. Examples of several Eu^{3+} doped hosts with the position of their corresponding CT band and their Eu-O distance.

Host	CT band position (nm)	Eu-O distance (Å)	Ref.
Y_2O_3	~ 250	2.297	[219]
$Ln_2(WO_4)_3$	~ 260	2.387-2.495	[220]
NaGdW	~ 261	2.450-2.478	[221]
La_2O_3	~ 290	2.5342	This work
KLuW	Not observed	2.217-2.765	[222]
$La(OH)_3$	Not observed	2.5652	This work

Thus, we believe that the Eu-O distance in La_2O_3 is already almost at the limit value for which the CT band can be formed, and a further increase of this distance, as it is produced in the $La(OH)_3$ phase, produces the disappearance of this CT band.

5.3. Chemical stability of Eu^{3+}:La_2O_2S nanoparticles

The spectroscopic results obtained at different times after the synthesis of the Eu^{3+}:La_2O_2S sample were rather different (see Figs. 5.16(a) and 5.16(b)) than those obtained for the Eu^{3+}:La_2O_3 samples versus time.

Figure 5.16(a) shows the excitation spectra versus time from 0 h to 40 days after the synthesis of the Eu^{3+}:La_2O_2S sample. The 3D graph was normalized at 395 nm in intensity and the excitation spectra monitored at 624 nm. The two broad bands, located at 264 and 340 nm corresponding to the Eu^{3+}-O^{2-} and Eu^{3+}-S^{2-} CT bands, respectively, remained unchanged and the sample seemed not being structurally affected by the environmental moisture. Figure 5.16(b) shows the emission spectra monitored under excitation at 340 nm and shows that the luminescence intensity was maintained also unchanged for at least 40 days after the Eu^{3+}:La_2O_2S sample synthesis.

Therefore, we can say that La_2O_2S is more stable than La_2O_3 to be affected by CO_2 and water. Thus, using Eu^{3+}:La_2O_2S nanoparticles instead of Eu^{3+}:La_2O_3 nanoparticles allow us to use almost the same optical properties of the Eu^{3+} ion observed in La_2O_3 nanocrystal but avoiding the problems of re-hydroxylation that presents La_2O_3.

The XRD pattern of the as-synthesized *Eu^{3+}:La_2O_2S* sample presented the La_2O_2S as the main phase, but traces of $La_2O_2SO_4$ and La_2O_3 were also found (see Fig. 5.17). In order to corroborate the study about the chemical stability of the La_2O_2S phase, we also recorded XRD patterns of this sample after several days of its synthesis. As Fig. 5.17 shows, we observed that the traces of La_2O_3 present in the as-synthesized sample were transformed into traces of $La(OH)_3$. On one hand, we can say that the La_2O_2S did not avoid the La_2O_3 transformation into $La(OH)_3$. But on the other hand, as there were only few amounts of lanthanum oxide/hydroxide in these samples, the luminescence properties were not affected.

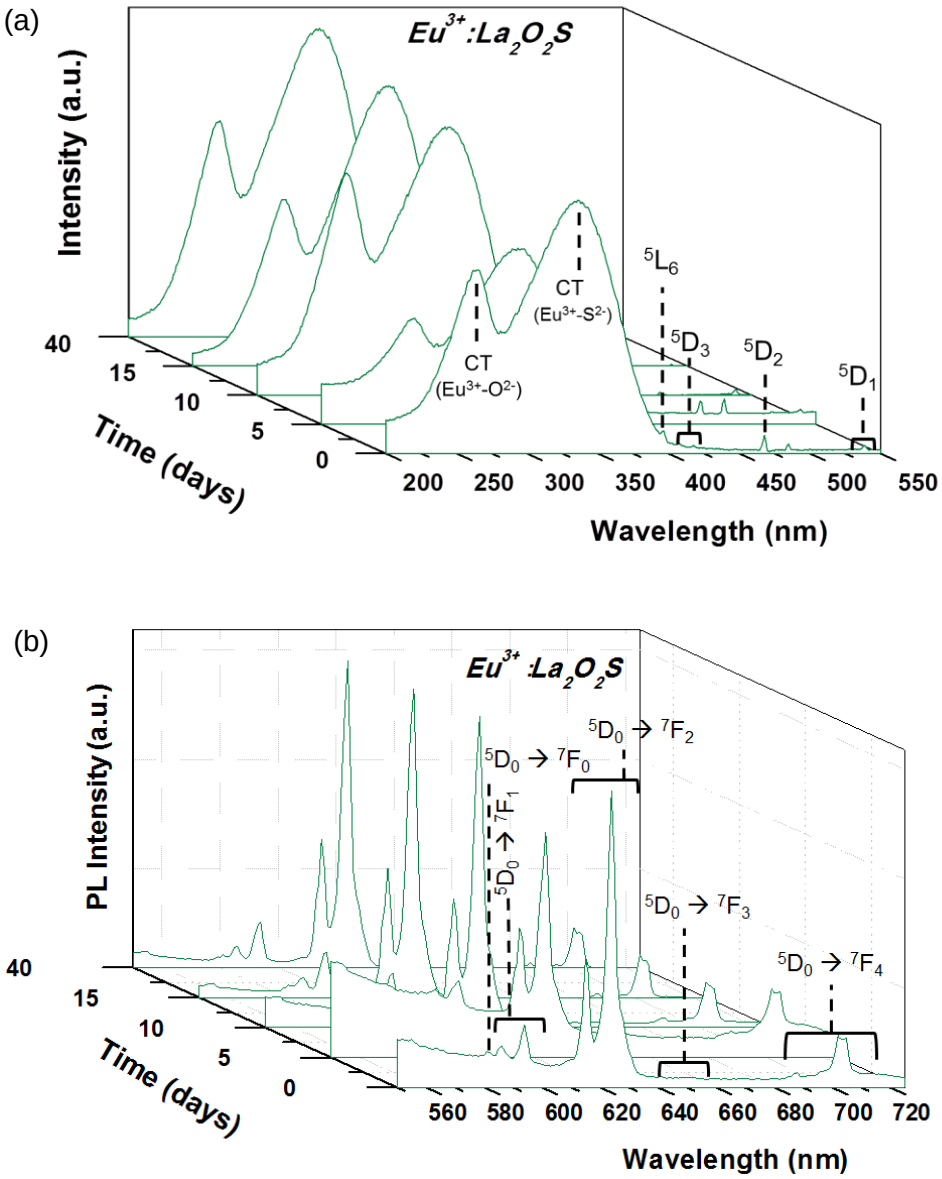

Figure 5.16. (a) Excitation and **(b)** emission spectra versus time of the $Eu^{3+}:La_2O_2S$ sample.

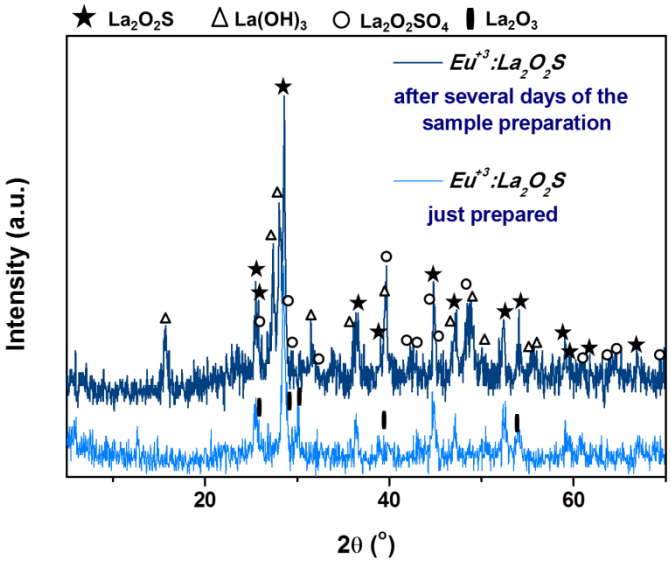

Figure 5.17. XRD pattern of as-synthesized Eu^{3+}:La_2O_2S nanoparticles and after 40 days of its synthesis.

Chapter 6

Dispersion of doped lanthanum compound nanoparticles by mechanical techniques and functionalization methods

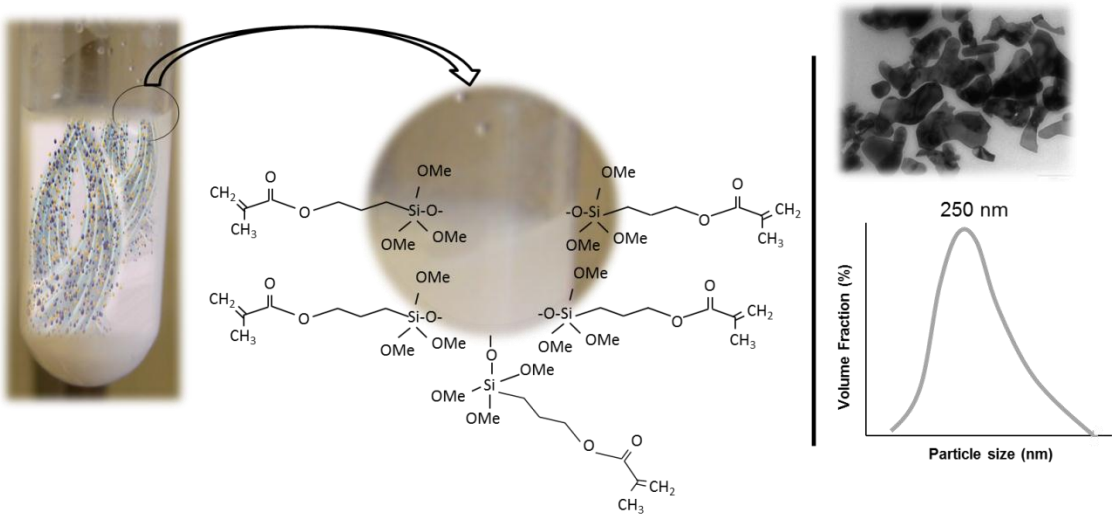

A good dispersion of particles with sizes in the nanoscale is essential to profit their unique size-dependent properties in which fundamentally they differ from those of the bulk materials. In this chapter, we will present the methods and techniques that we used to disperse lanthanum-doped compound nanoparticles. Different characterization techniques have been applied to study the dispersion of Eu^{3+}:La_2O_3, Eu^{3+}:Bi^{3+}:La_2O_3 and Eu^{3+}:La_2O_2S nanoparticles: dynamic light scattering (DLS), TEM; and their functionalization: TGA and IR. Finally, we have studied the luminescent properties of the Eu^{3+} ion and the chemical stabilization of the La_2O_3 and La_2O_2S hosts after the functionalization process by using the PL technique.

6.1. Overview

Nanoparticles are valuable for their unique properties due to their small sizes in which fundamentally they differ from those of bulk materials and therefore have great potential for use in electronic, chemical, mechanical, and biological industries [223]. However, the particles can not always be considered to belong to the nanoscale because when they become sufficiently small and the surface energy is significantly high, spontaneous agglomeration occurred [224]. Additionally, nanoparticles frequently display their particular properties only when they are dispersed and uniformly distributed while aggregation and agglomeration produce unpredictable crystal size distributions and shapes, both of which are key factors characterizing the physical properties of the powder product [225]. In nanocomposites, agglomeration can be also an important problem due to the combination of organic and inorganic materials. A clear example is the increasing number of studies in obtaining homogeneous, stable and aggregate-free nanoparticle-polymer blends [226]. Some of the earliest and most well-known organic-inorganic representatives are certainly derived from painting and polymer industries, where inorganic pigments of fillers are dispersed in organic components (solvents, surfactants, polymers, etc.) in order to improve their optical and mechanical properties [226].

Agglomerates consist of two or more individual particles. They can be classified as soft or hard agglomerates. Soft agglomerates are bonded by Van der Waals forces, whereas hard agglomerates are sintered. Only soft agglomerates can be disaggregated [40]. During the aggregation step, the individual particles (also so-called primary particles) collide with each other, leading to adhesion based on a weak physical attraction between the particles [225]. This physical attraction is held together by Van der Waals forces as well as strong and weak chemical or sintering bonds [227], especially in the case of particles in the nanometer size range, where the interaction between the particles is very strong due to their high specific surface and small particle size. Several decades ago, four authors developed a theory to explain the observed instability of a colloidal dispersion against irreversible aggregation in solutions of high ionic strength. According to the DLVO (Derjaguin-Landau-Verwej-Overbeeek) theory, the sum of the interaction potentials between two particles yields the total interaction [228,229]. Near the particle surface the cumulative interaction potential often shows a minimum, resulting in strong attractive forces and thus leading to stable agglomerates when particles are getting close to each other. Therefore, it is not difficult to comprehend that high stresses are needed for de-agglomeration. It is well known that the resistance against fracture (agglomerate strength) depends on the size of the surface defects and the fracture toughness of the particles assembly [230].

De-agglomerated nanoparticles can be obtained during or after their synthesis by functionalizing their surfaces, and by applying mechanical techniques such as sonication, high shear mixing, mechanical milling, and high-pressure processing. Surface

functionalization involves covalent [231-233] and non-covalent [234] bonds between the functionalizing agent and the nanoparticle surface whereas the use of mechanical techniques does not modify the chemical surface of the nanoparticles.

Marković et al. [235] used ultrasonication to break up barium titanate ($BaTiO_3$) agglomerated powders in an isopropanol suspension. The average of the particle sizes was 1.4 μm without sonication and 64 nm after 3 h of sonication. However, several studies concluded that the most influential factor on agglomeration is the agitation of the suspension [236]. Therefore, agitation has a complicated and an opposite effect on the agglomeration process because on one hand, it promotes more collisions among the particles but on the other hand, the aggregates formed can be broken by the turbulent motion generated by the agitation [237]. Sonication is a very common technique, and its influence on aggregation/agglomeration is mainly determined by the sonic frequency, the sonication power, the treatment time, and solution characteristics, such as the surface tension, the gas solubility, the vapour pressure, and the viscosity [235,238]. Other authors have established also that the shape of the experimental vessel exerts an important effect on the intensity of the sonication [235]. Thus, sonication in a flat-bottom vial generated a random effect on the contents of the vessel whereas when a round-bottom tube was used, the effects of sonication were considerably more consistent.

Functionalization is usually employed for surface modification in order to achieve desired surface properties such as water repellent for automobile windscreen but is also used to link molecules such as fluorescent dyes, proteins and other compounds of interest for a variety of applications such as sensors or catalysts [239]. Eu^{3+} doped $La(OH)_3$ nanophosphors, have been recently functionalized by C. Sun et al. [201] for bioimaging applications. Thus, the surface of Eu^{3+}:$La(OH)_3$ was modified by functionalization with aminopropyltriethoxysilane (APTES) in toluene to improve chemical stability and provide amine functional groups for conjugation of biomolecules. Another related example was the functionalization of lanthanum hydroxide nanowires by atom transfer radical polymerization [240]. The $La(OH)_3$ nanowires have been found to have high potential in the field of biological labelling.

Recently, Krüger et al. [224] reported an easy way to functionalize nanodiamond surfaces: the silanization reaction. It consists of a simple condensation reaction between hydroxyl groups and (3-acryl-oxypropyl)trimethoxysilane (APTMS) in dry THF and under ultrasonic irradiation. Using the bead-assisted sonication technique (zirconia beads), Krüger et al. in 2010 [224] developed a versatile and efficient method for the simultaneous de-agglomeration and surface functionalization of strongly agglomerated nanoparticles. The results showed homogeneously functionalized nanodiamond particles in a colloidal solution with sizes around 8 nm.

The interest in de-agglomerating the nanoparticles synthesized in this thesis is mainly their application in organic solar cells. If nanoparticles form large aggregates, the structure of the final device, which is usually fabricated of thin organic films with thicknesses of around a

few hundred nanometers, will be further affected by those aggregates. The structure of organic solar cells is directly related with the properties of the device, and they require high homogeneity and smooth surfaces.

6.2. Mechanical techniques for nanoparticle dispersion

Throughout Chapter 3 we observed how the particle sizes were in the nanoscale but at the same time, they were forming large aggregates becoming particles in the microscale. Therefore, in the first part of this chapter, we analyse the dispersion degree of Eu^{3+}:Bi^{3+}:La_2O_3 nanoparticles (sample *Eu^{3+}:(1%)Bi^{3+}-CPech1*) after using several mechanical dispersion techniques such as an ultrasound bath or an ultrasonic processor, and also with the application of an air flow to Eu^{3+}:$La(OH)_3$ nanoparticles (sample *Eu^{3+}-H-1*) during the calcination step to get Eu^{3+}:La_2O_3 nanoparticles instead of using static air.

6.2.1. Sonication of the nanoparticles by using an ultrasound bath and an ultrasonic processor

Effect of the sonication time on the dispersion of the nanoparticles

In order to find out the optimum time of sonication when using the ultrasound bath and the ultrasonic processor with a 5 mm micro tip, several tests were carried out in Eu^{3+}:Bi^{3+}:La_2O_3 nanoparticles. Figures 6.1(a) and 6.1(b) show the photographs of the ultrasound bath and the ultrasonic processor, respectively, used in this thesis. The ultrasonic processor is more powerful than the ultrasound bath because, among others, it holds a tip, which is responsible for emitting the sonic waves, and is directly introduced into the suspension to be dispersed.

All tests were performed at room temperature but the use of ice was necessary in most cases to balance the increase of temperature produced from the agitation waves applied for long times. We focused the study on the effect of the sonication time on the dispersion of nanoparticles. Thus, only tetrahydrofuran (THF) solvent was used and the sonication power was kept always constant. *Eu^{3+}:(1%)Bi^{3+}-CPech1* was the sample used to carry out these tests. Round-bottom tubes were used as sonication vessels, and all the samples were prepared with 10 mg of *Eu^{3+}:(1%)Bi^{3+}-CPech1* nanopowder in 1 ml of THF. We used this amount of nanoparticles on the basis of the previous results reported [224], as well as the election of THF as solvent.

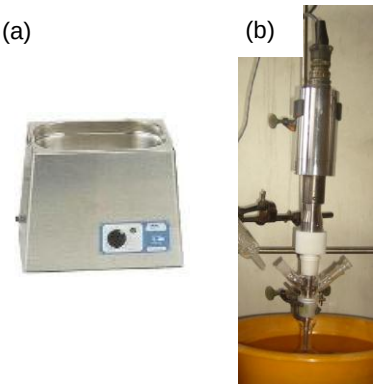

Figure 6.1. Photographs of **(a)** the ultrasound bath and **(b)** the ultrasonic processor equipment used to disperse the nanoparticles.

The tests performed using the ultrasound bath were carried out for 1, 2, 5, 10, 60 and 120 minutes and the tests performed using the ultrasonic processor were carried out for 1, 5, 10, 60, 120, 210, 300 and 420 min. Figure 6.2 shows a photograph of the *Eu^{3+}:(1%)Bi^{3+}-CPech1* nanopowder after its dispersion in THF solvent by using the ultrasound bath technique.

Figure 6.2. Photograph of the *Eu^{3+}:(1%)Bi^{3+}-CPech1* nanopowder after its dispersion in THF solvent by using the ultrasound bath technique.

Figures 6.3(a) and 6.3(b) show the nanoparticle dispersion results obtained for this sample by the dynamic light scattering (DLS) characterization technique. It was not possible to take the measurement at time 0 min due to the large particle size, which maintained them at the bottom of the cuvette.

Fig. 6.3(a) shows the DLS results obtained after using the ultrasound bath to disperse the nanoparticles. The curve obtained after using the ultrasounds for 1 min showed that the particle size average was around 1.15 μm. When we increased the ultrasound time from 1 min to 2 min, two different bands appeared. That is known as polydispersion, and means that the nanoparticles have different particle sizes but at the same time well distributed in more than one group. However, most of the particles had sizes around 1150 μm, since the percentage of the volume fraction was higher than that for the band centred at 5 μm. It is clear, that by increasing the ultrasound time up to 60 min did not show a significant

improvement, making this technique not powerful enough to disperse the particles, or the aggregates, to a nanometer scale.

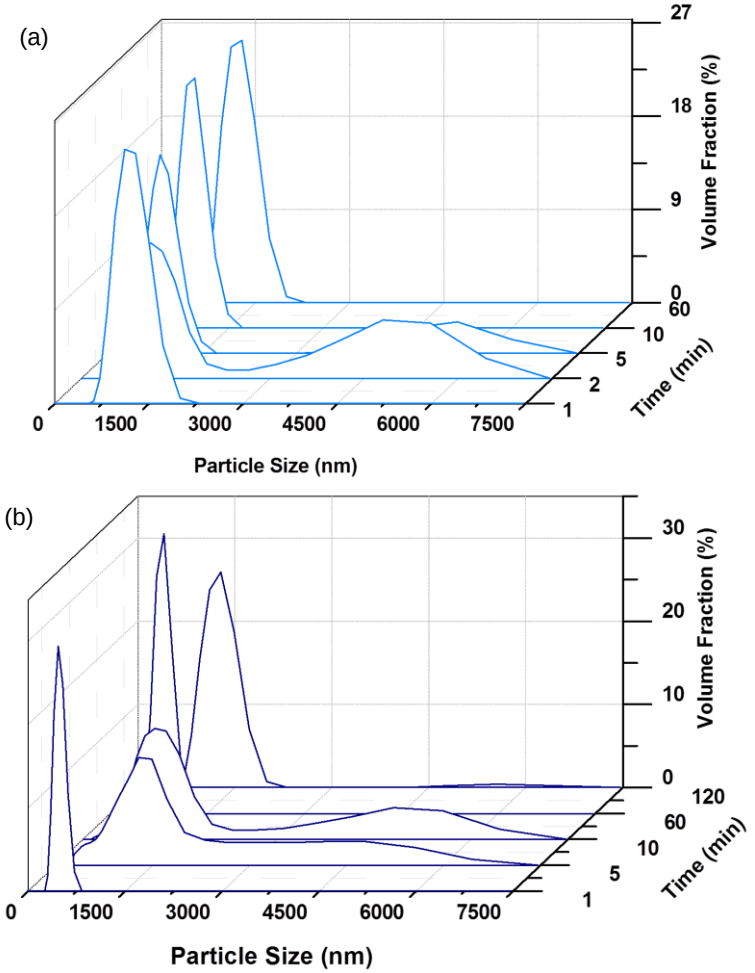

Figure 6.3. DLS results for the tests carried out by the **(a)** ultrasound bath and the **(b)** ultrasonic processor for different sonication times for the *Eu^{3+}:(1%)Bi^{3+}-CPech1* sample.

The DLS results obtained for the *Eu^{3+}:(1%)Bi^{3+}-CPech1* sample dispersed by using the ultrasonic processor are shown in Figure 6.3(b). The dispersion results after 1 min of sonication, showed particles with sizes around 500 nm. These particles were smaller than those obtained by using the ultrasound bath technique for 1 min. Nevertheless, the results after sonication of the sample for 5 min showed a polydispersion with most of the particles with sizes around 1.3 μm (Figure 6.3(b)). This indicates that the collisions of the particles lead to an increase of aggregates formation, as previously reported by other authors [225]. However, after 60 min of sonication the sample presented monodispersion with sizes around 800 nm and after 120 min of sonication the sizes of the particles were larger again and around 1.2 μm. These fluctuations observed in the particle size might be related with the time

between stopping the sonication and starting to measure the particle size distribution in the sample. At longer times, the larger particles would tend to precipitate at the bottom of the cuvette faster than the smaller particles, and thus, the equipment would be detecting a higher percentage of smaller particles. Figure 6.4 shows the DLS results of a sample measured immediately after the sonication process (1st measurement), which showed polydispersion and large particle sizes, and after 2 minutes, approximately (2nd measurement), which in contrast, showed smaller particles and monodispersion. Figure 6.5 shows the photograph of the samples taken immediately after the sonication (image on the top) and taken after 15 minutes approximately (image on the bottom), which shows most of the particles precipitated at the bottom of the vial.

Therefore, as previously observed in the results obtained by mechanical means it was not possible to de-agglomerate effectively the synthesized nanoparticles.

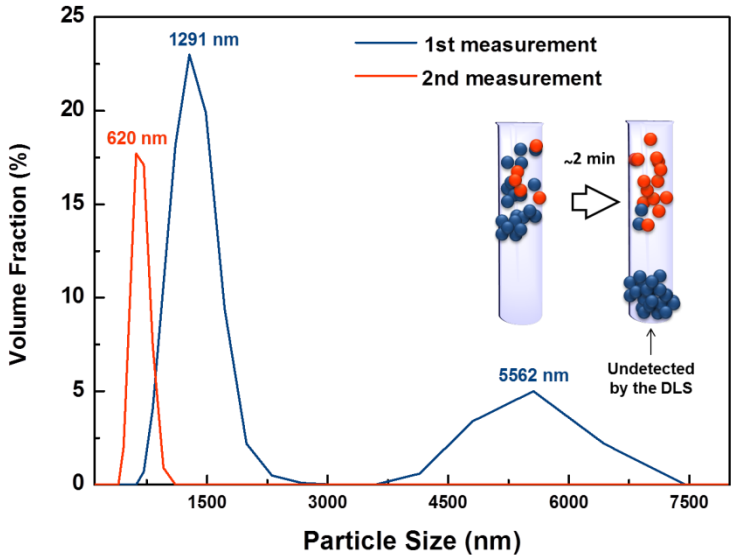

Figure 6.4. DLS results for the *Eu^{3+}:(1%)Bi^{3+}-CPech1* sample measured immediately after the sonication process and measured after 2 min approximately.

Figure 6.5. Photograph of several vials containing portions of the *Eu^{3+}:(1%)Bi^{3+}-CPech1* sample taken immediately after sonication (image on the top) and later on after 15 minutes approximately (image on the bottom).

Effect of the solvent used on the dispersion of nanoparticles by using the ultrasonic processor

The solvent was another parameter studied in the attempts to disperse the nanoparticles. When dealing with applications in which lanthanum compound nanoparticles have to be dispersed in polymer matrices, non-aqueous dispersion media are often required. In other words, polymers are often soluble in polar aprotic solvents. So, by using this kind of solvents to disperse the particles is a better approximation for the later co-existence of both materials. The solvent used up to now was the THF; now other dispersion tests were carried out to disperse the *Eu^{3+}:(1%)Bi^{3+}-CPech1* sample but using other polar aprotic solvents: *o*-dichlorobenzene (*o*-DCB), dimethyl sulfoxide (DMSO) and N-methylpyrrolidone (NMP). The chemical structure of these solvents is shown in Figure 6.6.

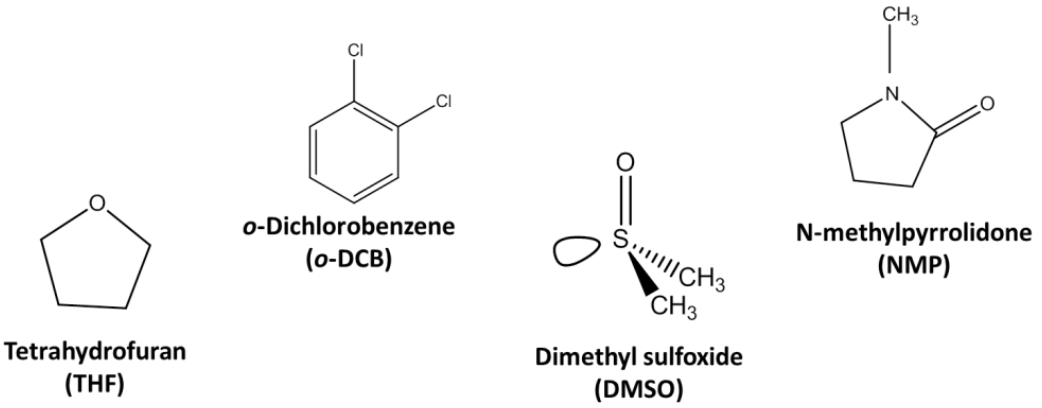

Figure 6.6. Chemical structure of the solvents used in the non-functionalization dispersion tests by mechanical meanings.

The *o*-DCB solvent was chosen specially for its good solubility of conjugated polymers [240]. These conjugated polymers (see later in Chapter 7) are often used in photonic applications. Then, having a stable colloidal solution of particles in the same solvent might represent an advantage. Solvents with high polarities generally tend to disperse particles and DMSO has been reported to do so even more efficiently than water [239]. One of the reasons for this is that DMSO is one of the strongest hydrogen-bonding acceptors known, several orders of magnitude stronger than water. This property causes efficient breaking up of any hydrogen bonding present on the surface of a single particle, as well as interparticle hydrogen bonding. NMP had similar chemical properties than DMSO.

In the tests carried out by using *o*-DCB, we visually observed how the solution containing the particles changed from white colour to light brown until becoming completely dark brown after increasing the sonication time (see Fig. 6.7(a-b)). Other authors also observed this peculiar characteristic with haloaromatic solvents [240]. This is due to the decomposition of the solvent and its polymerization when it is subjected to ultrasonication. These compounds are known as sonopolymers.

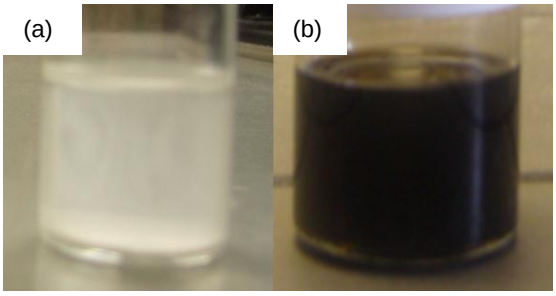

Figure 6.7. Photograph of the *Eu^{3+}:(1%)Bi^{3+}-CPech1* sample dispersed in *o*-DCB solvent **(a)** before and **(b)** after using the ultrasonic processor.

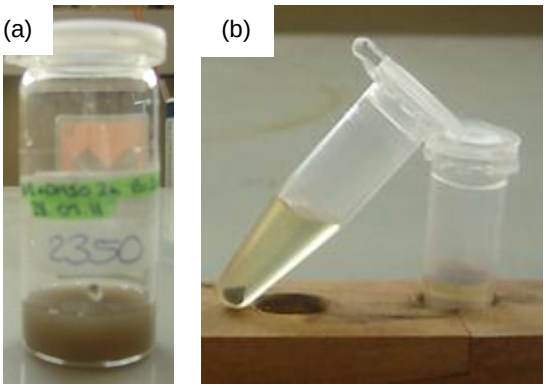

Figure 6.8.(a) Photograph of the *Eu^{3+}:(1%)Bi^{3+}-CPech1* sample dispersed in DMSO solvent by using the ultrasonic processor and **(b)** photograph of the solution after the centrifugation and washing treatment.

The tests using DMSO solvent did not present better results than those obtained with *o*-DCB since DMSO also seemed to decompose under ultrasonication taking into account that the solution changed from white colour to brown (see Fig. 6.8(a)). In order to isolate the particles from the decomposed organic solvent, a washing treatment with acetone and centrifugation was performed. However, the particles precipitated at the bottom and maintained the brown colour, indicating that the solvent might be attached irreversibly on the surface of the particles (see Fig. 6.8(b)).

Figure 6.9 shows the results obtained by using the NMP solvent. Although this polymer did not seem to decompose/polymerize, the particle sizes observed by DLS were within the range of the results already observed by using THF. This figure shows the DLS measurements of the *Eu^{3+}:(1%)Bi^{3+}-CPech1* sample performed after using ultra sonication for 10 min, recorded immediately after the sonication process, and 2 and 4 min approximately after stopping the sonication process. As explained above, the measurements recorded at 2 and 4 min after the sonication process showed a higher percentage of smaller particles than the measurement recorded immediately after the sonication process because the larger particles precipitate at the bottom of the cuvette faster than the smaller nanoparticles.

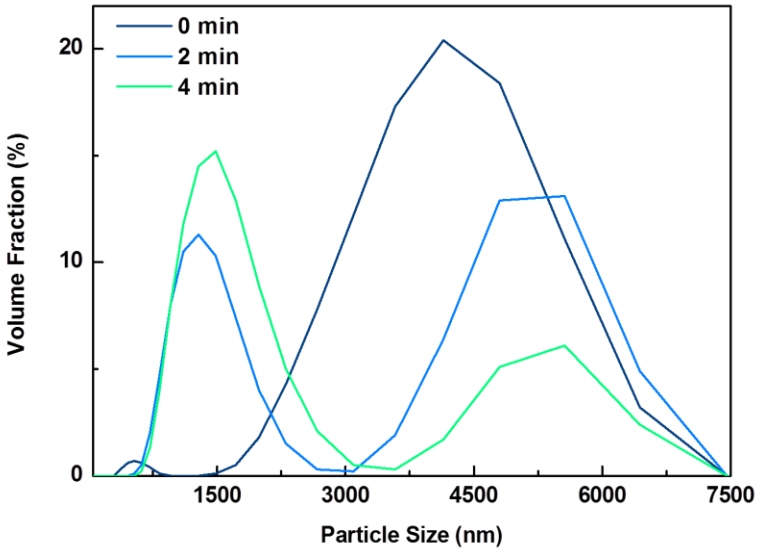

Figure 6.9. DLS results for the *Eu^{3+}:(1%)Bi^{3+}-CPech1* sonicated by ultrasonic processor and using NMP solvent recorded immediately after the sonication process, and 2 and 4 min later.

From these results, we concluded that another strategy was necessary to obtain de-agglomerated particles.

6.2.2. Calcination of the nanoparticles using air flow

One of the main reasons of having the particles forming large aggregates was the high calcination temperature (1173-1273 K) used during the synthesis process. This temperature is necessary in order to obtain the lanthanum oxide as the unique crystalline phase. Thus, we proposed to pass an air flow through the nanopowder during the calcination step in order to favour the elimination of the water formed during calcination, and therefore, obtain lanthanum oxide nanoparticles with a lower degree of aggregation. To make this test, the *Eu^{3+}-H-1* sample was introduced in a quartz reactor covered with a porous membrane, which allows the pass of air.

Figs. 6.10(a) and 6.10(b) show the nanoparticles obtained after calcination under an air flow (2 $mL \cdot s^{-1}$) at 1173 K for 2 h. The aggregation degree of the nanoparticles was similar to that of the *Eu^{3+}-CH-1* sample calcined without applying an air flow (see Fig. 3.25). Therefore, this technique was not useful to obtain disaggregated lanthanum compound nanoparticles.

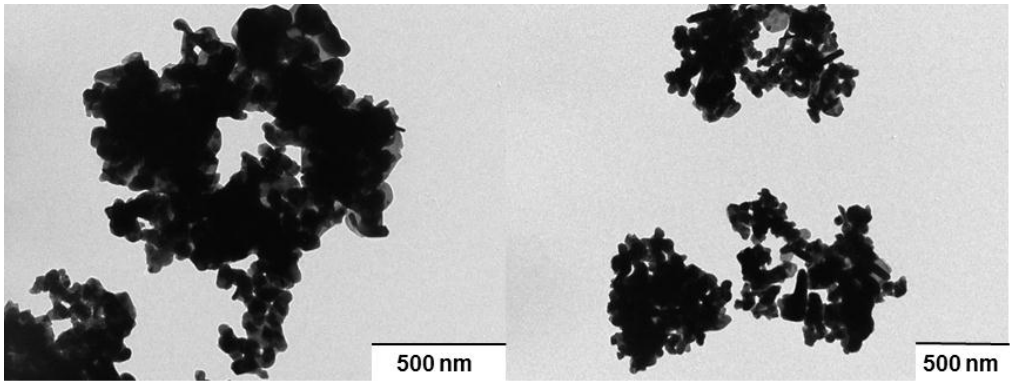

Figure 6.10. TEM images of *Eu^{3+}-CH-1* sample after calcination at 1173 K for 2 h and using an air flow.

6.3. Functionalization methods for the disaggregation of Eu^{3+}:La_2O_3 nanoparticles

In Chapter 5 we observed how lanthanum oxide nanoparticles can react with water and be transformed into lanthanum hydroxide very fast. This fact is not an advantage for the luminescence properties, since we could not detect any absorption band and only very low emission intensities in Eu^{3+}:$La(OH)_3$ nanoparticles (see Figs. 5.9 and 5.11). However, at the same time, we can take benefit from this important hygroscopic behaviour, because the surface of La_2O_3 might be fast surrounded by OH groups from the adsorbed water, and these OH groups can be used to functionalize the surface of the nanoparticles. Functionalization of nanoparticles, also called modification or coating of the surface, can allow us de-agglomerate those particles. Therefore, functionalization was applied during the synthesis of the

Eu^{3+}:$La(OH)_3$ nanoparticles by using polyacrylic acid (PAA) and to Eu^{3+}:Bi^{3+}:La_2O_3 and Eu^{3+}:La_2O_2S nanoparticles by using (3-acryl-oxypropyl)trimethoxysilane (APTMS).

6.3.1. Functionalization by polyacrylic acid: @PAA

In order to obtain a better dispersion and smaller nanoparticles, the use of an organic compound, in this case PAA which is able to react with the Eu^{3+}:$La(OH)_3$ surface, was used during the synthesis of the nanoparticles. The PAA chemical structure is shown in Figure 6.11.

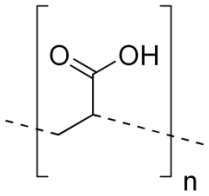

Figure 6.11. Chemical structure of the polyacrylic acid.

Thus, one test was carried out to functionalize the Eu^{3+}:$La(OH)_3$ surface by using PAA. 1 g of PAA (Aldrich, M.W 250,000.) was dissolved in 50 ml of distilled water. Then, NaOH (Merck, 99%) was added to have pH = 6 in order to obtain the sodium polyacrylate. Finally, a solution 0.04 M of $La(NO_3)_3 \cdot 6H_2O$ and $Eu(NO_3)_3 \cdot 5H_2O$ was added to the sodium polyacrylate solution. The Eu^{3+}:$La(OH)_3$ nanoparticles precipitated very fast due to the basicity of the solution. The Eu^{3+}:$La(OH)_3$ sample obtained was named *Eu^{3+}:$La(OH)_3$@PAA*. These nanoparticles were characterized by TEM (see Fig. 6.12(a-b)). Fig. 6.12(a) shows small nanoparticles with sizes between 50 and 150 nm. However, as Fig. 6.12(b) shows, most of the nanoparticles were found still forming aggregates.

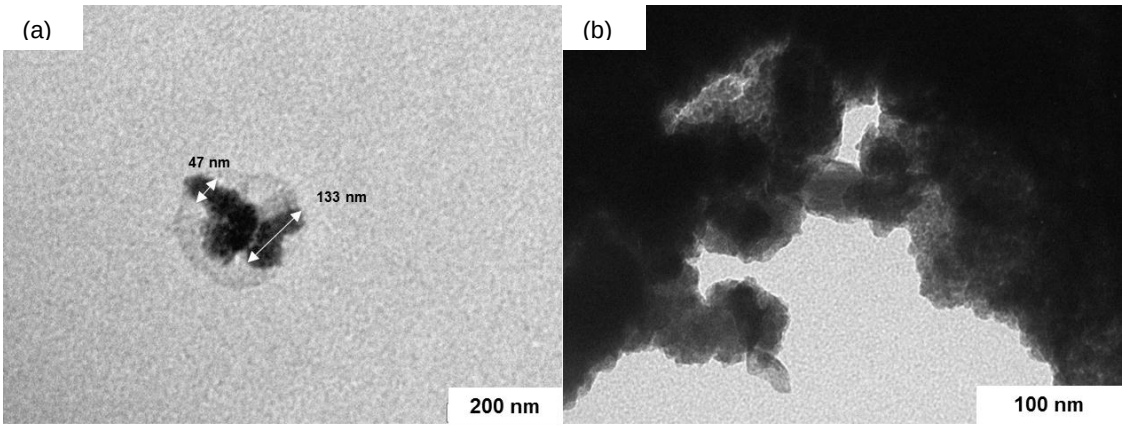

Figure 6.12.(a-b) TEM images of the *Eu^{3+}:$La(OH)_3$@PAA* sample.

6.3.2. Functionalization by (3-acryl-oxypropyl)trimethoxysilane: @APTMS

Based on the method developed by Krüger et al. [224], we used the (3-acryl-oxypropyl)trimethoxysilane (APTMS) to functionalize several doped lanthanum compound nanoparticles. In that method, Krüger et al. used zirconia beads and a mixture of APTMS and THF solvent to disperse agglomerated nanodiamonds. Beads were not used in our process because lanthanum compound nanoparticles are soluble in strong acids and zirconia beads require strong acids to be removed from the sample. From the results of some preliminary tests, another modification was introduced in the method. Instead of using a mixture of THF as the medium of dispersion and APTMS as the functionalizing agent, we used APTMS for both functions.

Figure 6.13 shows a schematic representation of the reaction between the Eu^{3+}:Bi^{3+}:La_2O_3 nanoparticles represented by 7-fold coordinated La_2O_3 polyhedra, surrounded by OH groups from the water adsorbed from the atmosphere, and the APTMS compound. The silanization reaction is a simple condensation reaction between these -OH groups and the -OMe of the (3-acryl-oxypropyl)trimethoxysilane (APTMS). With an excess of APTMS we can assure the maximum reaction rate and consequently, the maximum separation rate of the particles.

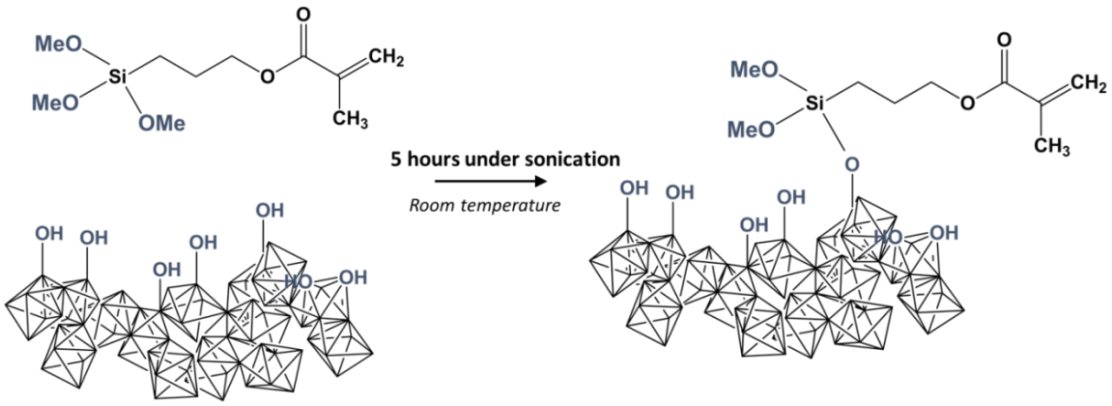

Figure 6.13. Schematic representation of the silanization reaction between the -OH groups surrounding the Eu^{3+}:Bi^{3+}:La_2O_3 nanoparticles and the -OMe groups of the APTMS.

The samples used in the functionalization tests were *Eu^{3+}:(1%)Bi^{3+}-CPech1* and *Eu^{3+}:La_2O_2S* because they exhibited the most interesting luminescence results to be used in solar cells applications (Chapter 4, section *4.2.6*). In order to functionalize the nanoparticles, 100 mg of nanopowders were mixed with 5 ml of APTMS (Serva, 85%) into a round-bottom flask. Then, the solution was agitated for 5 hours in the ultrasonic processor using a 5 mm micro tip. The process was carried out at room temperature, with the round-bottom flask submerged in a water bath to palliate the increase of temperature due to the agitation process. The mixture was stable, since the particles did not precipitate at the bottom of the flask for several

hours (see Fig. 6.14). The excess of APTMS compound was removed in order to have only the functionalized nanoparticles for the desirable applications.

Figure 6.14. Photograph of the Eu^{3+}:Bi^{3+}:La_2O_3 functionalized nanoparticles in the APTMS solution.

To remove the excess amount of APTMS, the particles were washed with acetone. Therefore, 5 ml of acetone were added to the mixture and immediately ultrasonicated for 5 min. Finally, the mixture was centrifuged at 15000 rpm for 3 min to separate the functionalized nanoparticles by depositing them at the bottom of the flask. The washing step was repeated three times, until the supernatants became colourless. The functionalized samples were named by adding @APTMS, e. g. the *Eu^{3+}:(1%)Bi^{3+}-CPech1@APTMS* sample was the *Eu^{3+}:(1%)Bi^{3+}-CPech1* sample after the functionalization and washing processes.

The particle sizes of the *Eu^{3+}:(1%)Bi^{3+}-CPech1@APTMS* sample were analysed by the DLS technique. Among other parameters such as the cuvette dimensions, the temperature, etc., the viscosity of the solvent is another important parameter to take into account to get an appropriate measurement of the size of the particles when using this technique. Thus, the viscosity of APTMS was measured at 298 K, using a Ubbelohde viscometer, operating at a controlled temperature. The kinematic viscosity in $mm^2 \cdot s^{-1}$ was extracted from the following equation:

$$\nu = kt \qquad \textbf{(Eq. 6.1)}$$

where *k* is a constant provided by the Ubbelohde viscometers tables and *t* is the flow through time. The viscosity average obtained for the APTMS was 2.4 $mm^2 \cdot s^{-1}$.

Figure 6.15 shows the particle size distribution obtained by the DLS technique. The curves correspond to the *Eu^{3+}:(1%)Bi^{3+}-CPech1@APTMS* sample before and after the acetone washing process. It is clear that the washing process did not affect significantly the particle size, and for both samples, the nanoparticles exhibited sizes around 250 nm. The curves exhibited ranging sizes from 100 to 450 nm approximately.

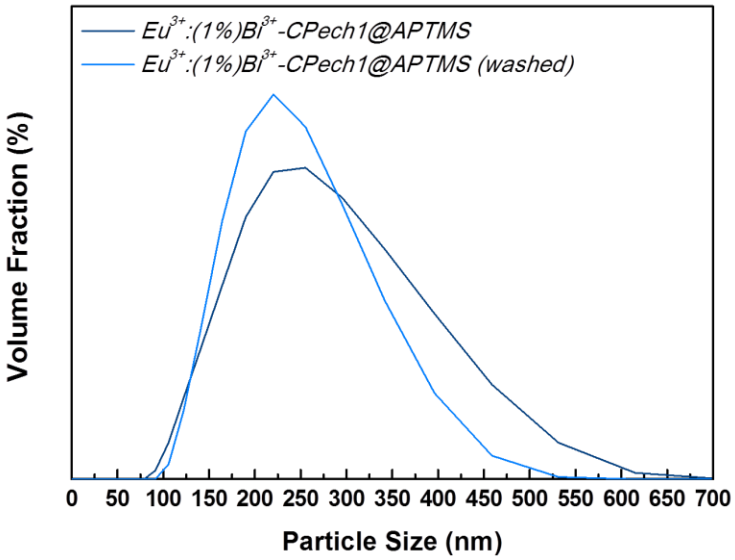

Figure 6.15. Particle size distribution of the *Eu^{3+}:(1%)Bi^{3+}-CPech1@APTMS* sample before and after the acetone washing process.

TEM images exhibited significant differences after the functionalization process. Figure 6.17(a) shows a TEM image of the *Eu^{3+}:(1%)Bi^{3+}-CPech1* sample whereas Figures 6.17(b-e) show several TEM images of the *Eu^{3+}:(1%)Bi^{3+}-CPech1@APTMS* sample. It can be clearly observed the effect of the sonication and the functionalization in the dispersion of the particles, which allows distinguishing in a better way the size and the morphology of the nanoparticles.

The particles were irregular with round borders. A possible explanation for these round borders might be that the collisions between the particles during the sonication process fracture their surface. The dispersion of the nanoparticles was more efficient than that obtained by using mechanical techniques. This was confirmed because several particles could be found individually. Additionally, the contrast of the particles in the TEM images was lower (see Fig. 6.11(e)) than that in the non-functionalized sample, which showed particles with high contrast (see Fig. 6.11(a)). As previously observed in the results obtained by Krüger et al. [224], APTMS was not identified in the TEM images.

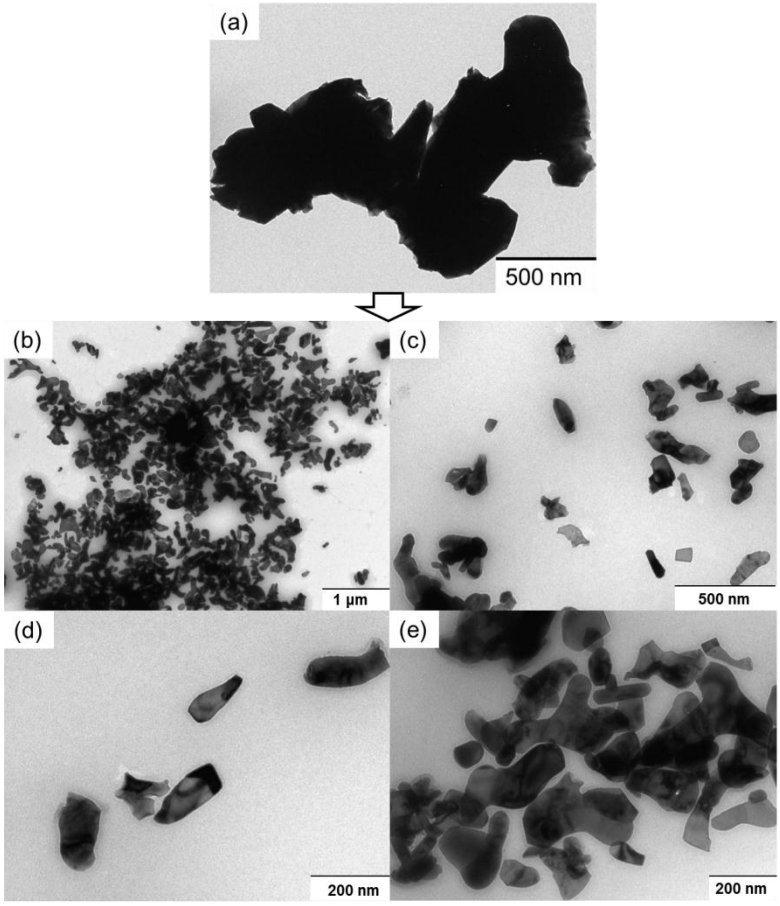

Figure 6.16. TEM images of **(a)** the *Eu^{3+}:(1%)Bi^{3+}-CPech1*sample and **(b-e)** the washed *Eu^{3+}:(1%)Bi^{3+}-CPech1@APTMS* sample.

The silanization reaction was followed by infrared (IR) spectroscopy and thermogravimetric analysis (TGA). Figure 6.17 shows the infrared spectrum of the as-calcined nanoparticles (*Eu^{3+}:(1%)Bi^{3+}-CPech1*), the spectrum of the nanoparticles after an ultrasound bath sonication for 5 min, the spectrum of the functionalized nanoparticles (*Eu^{3+}:(1%)Bi^{3+}-CPech1@APTMS*) and the spectrum of a representative Eu^{3+}:$La(OH)_3$ sample (*Eu^{3+}-H-24*). The spectrum of the calcined sample, analysed already in Chapter 3 (see Figs. 3.22 and 3.23) shows slight differences with the spectrum taken after ultrasound bath sonication. The sonication process allows the introduction of water and carbonate species into the sample by the cavitation and waves formed. The absorption peaks at 3614 and 3439 cm^{-1} were attributed to the stretching vibration mode of the O-H bond and the bending vibration of H-O-H, respectively. Thus, the peak at 3614 cm^{-1}, not present in the as-calcined sample, was indicative of the presence of $La(OH)_3$, which was in good agreement with the spectrum of the *Eu^{3+}-H-24* sample. Additionally, new peaks from the vibration modes ν_{1-4} of the CO_3^{2-} within the 1636-652 cm^{-1} range can be also observed in the spectrum taken after ultrasound bath

sonication in comparison with the as-calcined sample. However, the most notable differences appeared when analysing the functionalized sample. It exhibited absorption bands corresponding to acrylate groups (H_2C=CH-C(=O)-) within the range 1110-1700 cm^{-1} [224] together with the peaks appearing at 2942 and 2840 cm^{-1} which might be also attributed to the C-H stretching vibration from the acrylate groups. Other authors [240] had assigned the two intense peaks located in the range 100-1200 cm^{-1} to the stretching of the Si-O-Si group, which in our case it would corroborate the successful silanization. The high intensity band at 1718 cm^{-1} became stronger in comparison with the non-functionalized samples due to the ester group (C=O) vibration, which corresponded to the methacrylate groups of the organosilane compound attached to lanthanum oxide nanoparticles. The typical band attributed to the La-O stretching vibration mode shifted from 649 cm^{-1} in the non-functionalized sample to 630 cm^{-1} in the functionalized sample. We suggest that, this can be due to the Si atoms linked to O atoms, giving rise to the ν(La-O-Si) vibration [161]. With these bands observed in the infrared spectra we could confirm the successful functionalization of the nanoparticles by the silanization reaction.

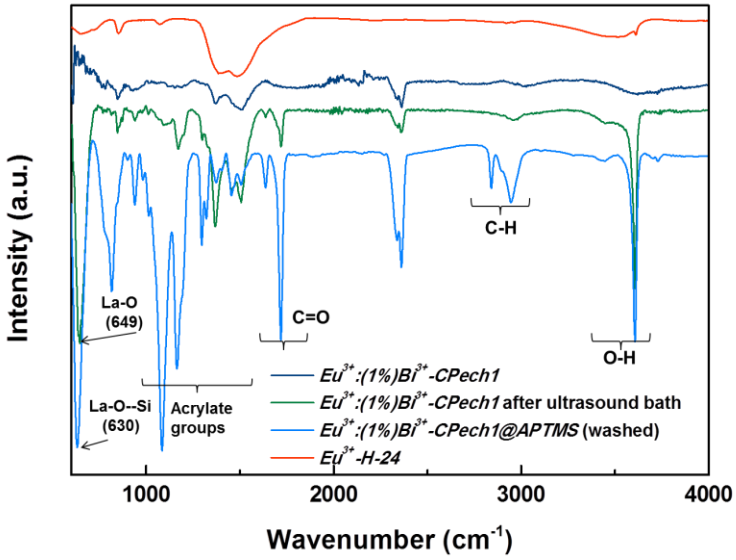

Figure 6.17. Infrared spectra of the as-calcined *Eu^{3+}:(1%)Bi^{3+}-CPech1* , *Eu^{3+}:(1%)Bi^{3+}-CPech1* after ultrasound bath sonication and *Eu^{3+}:(1%)Bi^{3+}-CPech1@APTMS* samples.

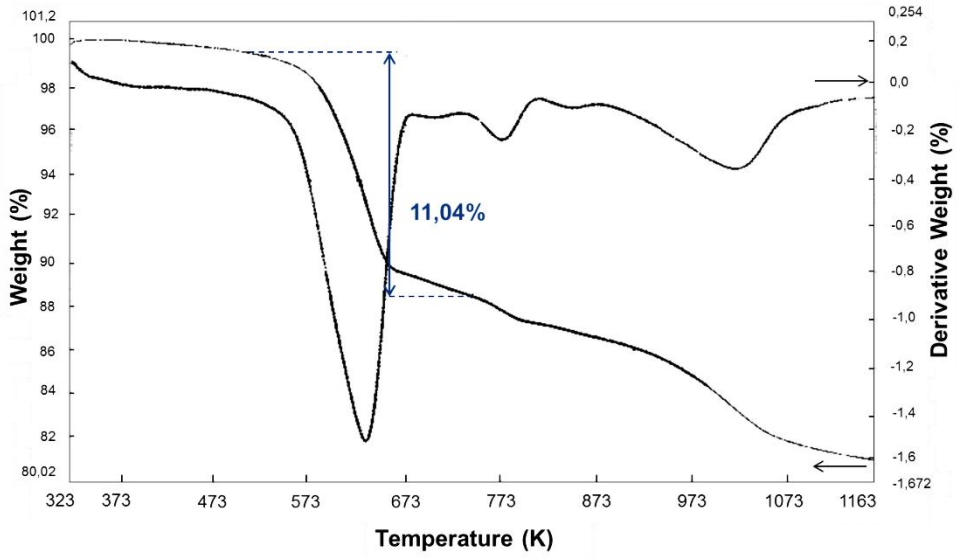

Figure 6.18. TGA curve of the *Eu^{3+}:(1%)Bi^{3+}-CPech1@APTMS* sample.

Thermogravimetric analysis also corroborated the successful functionalization of the *Eu^{3+}:(1%)Bi^{3+}-Pech1* sample (see Fig. 6.18). The sample was heated at a rate of 10 K·min^{-1} from 298 K to 1173 K under a nitrogen atmosphere. Since the *Eu^{3+}:(1%)Bi^{3+}-CPech1@APTMS* was the functionalized sample of *Eu^{3+}:(1%)Bi^{3+}-CPech1*, it was already calcined and therefore no important weight losses in the thermograms should be expected. However, the functionalized sample presented a remarkable weight loss at around 623 K (11.04%). That might be attributed to the presence of APTMS, which present the boiling point at 526 K and it was around this temperature when we observed that the sample weight started to decrease. Other weight losses were at 773 K and at 1023 K (see Fig. 6.18) and could correspond to the loss of hydroxyl and carbonate species formed during the dispersion/functionalization process. In the infrared spectrum of this sample, some peaks related to hydroxyl and carbonate species were also observed (see Fig. 6.17). However, the percentage of their weight loss was very low in comparison with that related with the APTMS loss. The surface loading ratio informs us about the capability of the organic compound to react with the nanoparticle surface [42]. The surface loading obtained was 0.71 mmol·g^{-1} and was calculated by the following equation:

$$\text{Surface loading (mmol/g)} = \frac{\text{Weight loss (\%)}}{\text{sample weigth (mg)}\cdot\text{MW of APTMS } (\frac{g}{mol})} \qquad \textbf{(Eq. 6.2)}$$

According to Krüger et al [42], depending on the choice of alkoxy groups, the surface loading can be tuned between 0.3 and 1.5 mmol·g^{-1}. We can say that the value obtained in our case is within this range. However, further studies should be done in order to increase this ratio if necessary.

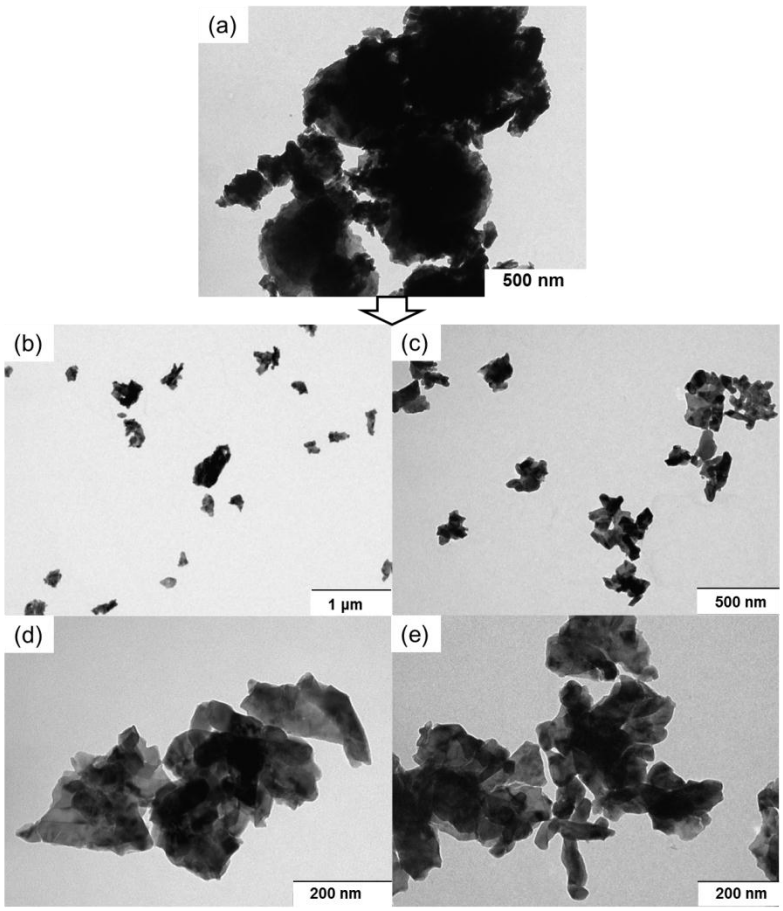

Figure 6.19. TEM images of **(a)** the Eu^{3+}:La_2O_2S sample and **(b-e)** the washed Eu^{3+}: La_2O_2S@APTMS sample.

The Eu^{3+}:La_2O_2S@APTMS sample was also functionalized by APTMS and the resulting nanoparticles are shown in the TEM images of Fig. 6.19(a-e). In agreement with what was observed in the Eu^{3+}:(1%)Bi^{3+}-Pech1 sample, the nanoparticles after the sonication/functionalization process, were irregular and showed lower contrast (see Fig. 6.19(b-e) than the Eu^{3+}:La_2O_2S sample (see Fig. 6.19(a)). These images confirmed that this process allowed us to have smaller particles and a better dispersion also for the Eu^{3+}:La_2O_2S nanoparticles.

The Eu^{3+}:La_2O_2S@APTMS sample was also studied by X-ray diffraction (XRD) as a representative functionalized sample. Figure 6.20 shows the XRD patterns of the Eu^{3+}:La_2O_2S@APTMS and the Eu^{3+}:La_2O_2S samples. The same crystalline peaks corresponding to La_2O_2S, $La(OH)_3$ and $La_2O_2SO_4$ phases were observed in both samples. Therefore, we can conclude that the APTMS did not have any influence in the crystallinity of the nanoparticles.

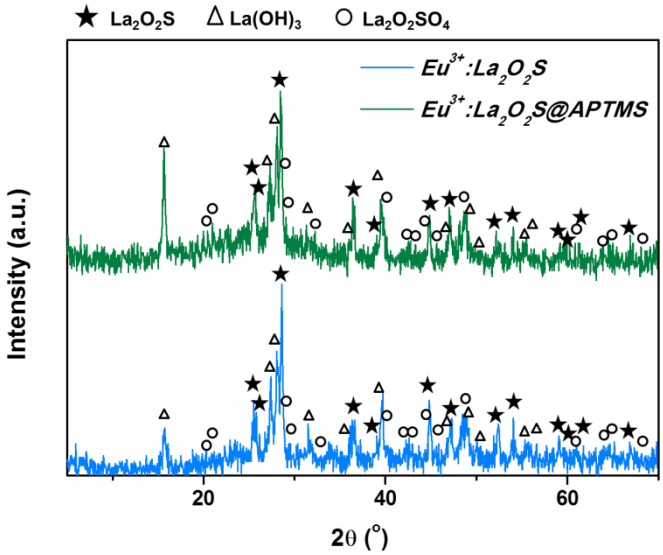

Figure 6.20. XRD patterns of the *Eu^{3+}:La_2O_2S@APTMS* and *Eu^{3+}:La_2O_2S* samples.

Photoluminescence studies of the functionalized lanthanum compound nanoparticles

The luminescence of the *Eu^{3+}:(1%)Bi^{3+}-CPech1@APTMS* and the *Eu^{3+}:La_2O_2S@APTMS* samples was studied by the photoluminescence technique (Figs. 6.21(a-b) and Figs. 6.22 (a-b)), respectively.

Figures 6.21(a) and 6.21(b) show the excitation and emission spectra, respectively, of the functionalized *Eu^{3+}:(1%)Bi^{3+}-CPech1@APTMS* sample. In this figure we added also the spectra recorded for the non-functionalized *Eu^{3+}:(1%)Bi^{3+}-CPech1* sample and the spectra recorded for the *Eu^{3+}-CPech1* sample for means of comparison. The excitation spectra were normalized in intensity at 312 nm. The spectrum of the *Eu^{3+}:(1%)Bi^{3+}-CPech1@APTMS* sample showed two different absorption bands associated to Eu^{3+}: one centered at 280 nm and the other centered at 301 nm. That meant that, contrary to the non-functionalized sample, now the Eu^{3+}-O^{2-} CT band was not overlapped to the band attributed to the Bi^{3+} absorption, and thus both bands could be distinguished as it happens for instance in Eu^{3+}:Bi^{3+}:Y_2O_3 nanoparticles [193]. The small band attributed to the host excitation was also observed at around 228 nm. In addition, the CT band of Eu^{3+} was blue shifted to respect the position of the CT band recorded in the *Eu^{3+}-CPech1* sample. The position of the maximum of the Eu^{3+}-O^{2-} CT band was shifted ~8 nm towards short wavelengths in comparison with that recorded in the *Eu^{3+}-CPech1* sample, which showed its CT band at 288 nm. Furthermore, the Eu^{3+} f-f transitions for the *Eu^{3+}:(1%)Bi^{3+}-CPech1@APTMS* sample also showed considerably less intensity than those observed for the non-functionalized sample.

The emission spectra shown in Fig. 6.21(b) were normalized in intensity at 626 nm. All the spectra showed the same emission peaks, corresponding to the $^5D_0 \rightarrow {}^7F_J$ (J = 0-4) transitions.

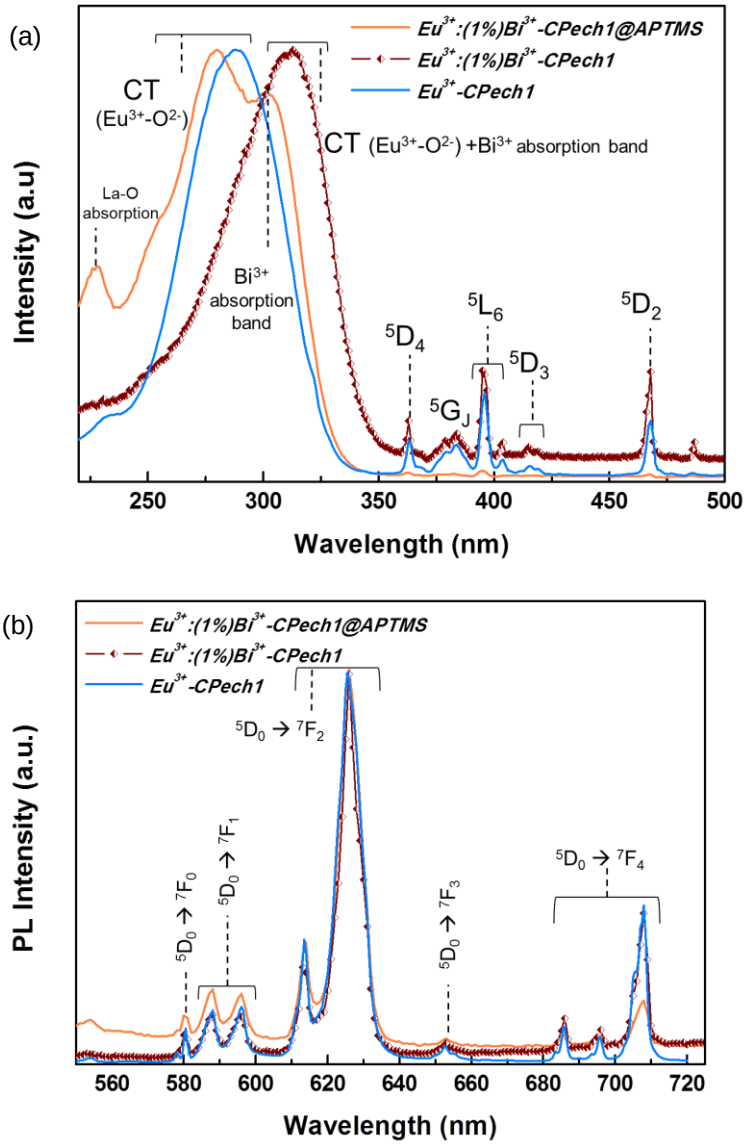

Figure 6.21.(a) Excitation and **(b)** emission spectra of the *Eu^{3+}:(1%)Bi^{3+}-CPech1*, *Eu^{3+}:(1%)Bi^{3+}-CPech1@APTMS*, and *Eu^{3+}-CPech1* samples.

The asymmetry intensity ratio (I_2) and the fluorescence intensity ratio (I_1) were compared for all the samples. The I_2 values obtained for the *Eu^{3+}:(1%)Bi^{3+}-CPech1* and for the *Eu^{3+}-CPech1* samples were 8.2 and 6.7, respectively, while for the *Eu^{3+}:(1%)Bi^{3+}-CPech1@APTMS* sample was 5.4 (see Table 6.1). This decrease in the I_2 parameter obtained for the functionalized sample could be attributed to some changes in the covalency of the Eu-O bond [103]. This would explain the shifts in the excitation bands (see Fig. 6.21(a)). Since the silanization reaction was successfully achieved, Si atoms were linked to O atoms of the surface of the nanoparticles and this might affect the Eu-O and the Bi-O bond distances as

well as to the covalency of these bonds. Wu et al. [193] reported the excitation spectra of Eu^{3+}:Bi^{3+}:Y_2O_3 nanoparticles which also shows two different wide bands, one from the CT of Eu^{3+}-O^{2-} and the other at longer wavelengths attributed to the Bi^{3+} absorption. In the *Eu^{3+}:Bi^{3+}-CPech1* sample, the two bands were found overlapped (see Fig. 6.21(a)) whereas for the *Eu^{3+}:(1%)Bi^{3+}-CPech1@APTMS* sample, the bands were separated as for the Eu^{3+}:Bi^{3+}:Y_2O_3 nanoparticles.

The I_1 values obtained for the *Eu^{3+}:(1%)Bi^{3+}-CPech1* and for the *Eu^{3+}-CPech1* samples were 4 and 3.2, respectively, while the I_1 value for the *Eu^{3+}:(1%)Bi^{3+}-CPech1@APTMS* sample was 3.3 (Table 6.1). The value for the functionalized sample was within the values obtained by the other samples, indicating that the concentration of Eu^{3+} did not change during the functionalization process, as it would be expected.

Table 6.1. Asymmetry ratio (I_2), fluorescence ratio (I_1) and I_4 ratio calculated from the emission spectra of the *Eu^{3+}:(1%)Bi^{3+}-CPech1*, *Eu^{3+}:La_2O_2S* and their respective functionalized samples.

Sample	I_2 (asymmetry ratio)	I_1 (fluorescence ratio)	I_4 (crystal strength at long distances)
Eu^{3+}:(1%)Bi^{3+}-CPech1@APTMS	5.4	3.3	1.0
Eu^{3+}:(1%)Bi^{3+}-CPech1	8.2	4.0	2.7
Eu^{3+}-CPech1	6.7	3.2	2.8
Eu^{3+}:La_2O_2S@APTMS	4.9	2.2	0.9
Eu^{3+}:La_2O_2S	8.1	3.3	1.0

More significant changes were observed in the I_4 parameter, which informs us about the crystal strength at long distances. The *Eu^{3+}:(1%)Bi^{3+}-CPech1@APTMS* sample had a I_4 value of 1 which was clearly lower in comparison with the I_4 value of 2.7 and 2.8 obtained for the *Eu^{3+}:(1%)Bi^{3+}-CPech1* and *Eu^{3+}-CPech1* samples, respectively (Table 6.1). This low I_4 value confirmed to have a weak crystal field strength at long distances and so that, shorter Eu-O distances when the Si was linked to the O atoms.

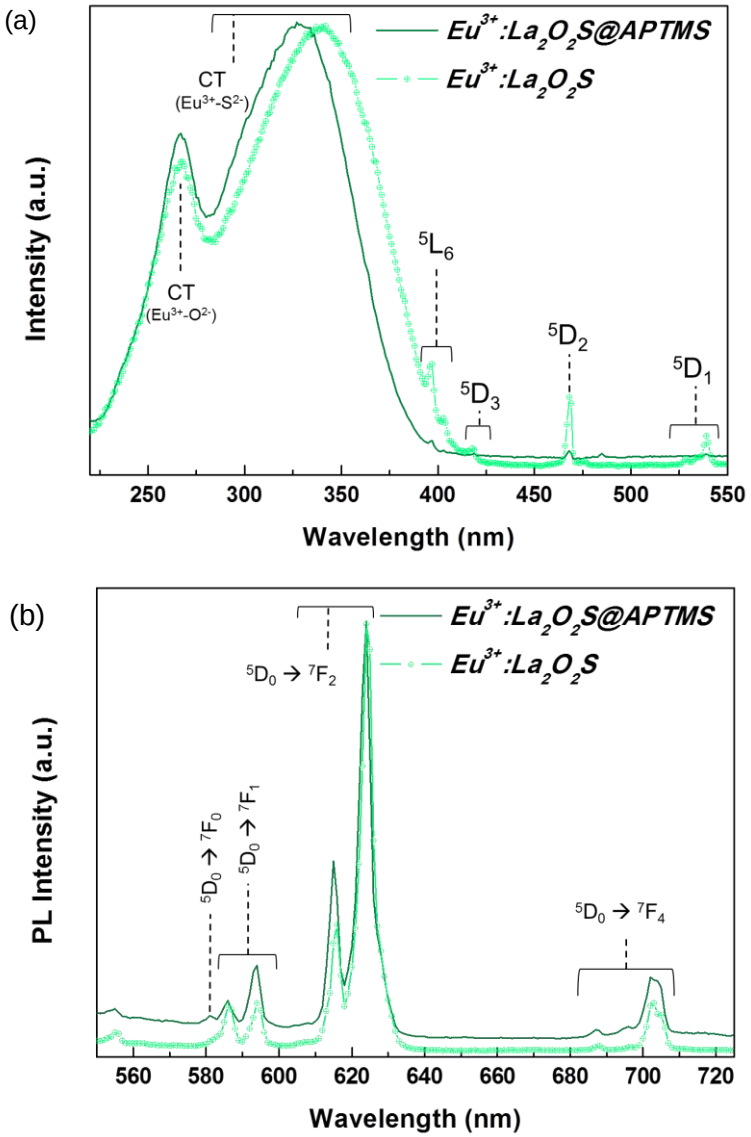

Figure 6.22.(a) Excitation and **(b)** emission spectra of the Eu^{3+}: La_2O_2S@*APTMS* and Eu^{3+}:La_2O_2S samples.

Figures 6.22(a) and 6.22(b) show the excitation and emission spectra, respectively, of the Eu^{3+}:La_2O_2S@*APTMS* sample. We also added the spectra recorded for the non-functionalized Eu^{3+}: La_2O_2S sample for comparison. The excitation spectra were normalized in intensity at 340 nm. Here, the functionalized sample also showed a blue shift in the position of the CT band (Eu-S). The CT band of the Eu^{3+}:La_2O_2S@*APTMS* sample was centred at 328 nm while that of the Eu^{3+}:La_2O_2S sample was centred at 340 nm. Apart from that, the peaks at longer wavelengths corresponding to the Eu^{3+} f-f transitions: $^7F_J \rightarrow {}^5D_J$ (J =

1-4), $^7F_J \rightarrow {}^5G_J$ and $^7F_J \rightarrow {}^5L_6$ were also less intense in comparison with the those recorded in the non-functionalized sample.

The emission spectrum of the *Eu^{3+}:La_2O_2S@APTMS* sample showed the same peaks located at the same wavelengths than those of the *Eu^{3+}:La_2O_2S* sample (see Fig. 6.22(b)). However, the relative intensities among the peaks were different, as previously observed for the *Eu^{3+}:(1%)Bi^{3+}-CPech1@APTMS* sample. The I_2, I_1 and I_4 parameters calculated for the *Eu^{3+}:La_2O_2S* sample were 8.1, 3.3, and 1 respectively, while for the *Eu^{3+}:La_2O_2S@APTMS* sample were 4.9 and 2.2, and 0.9 respectively. These smaller parameters obtained confirmed also the lower Eu-O covalency when the Si is linked to the surface of the sample.

In Chapter 5, the chemical stability of the different hosts used in this thesis (La_2O_3 and La_2O_2S) was studied by photoluminescence and cathodoluminescence. In this chapter, we again analysed the chemical stability of the functionalized samples by PL. Therefore, the re-hydroxylation of the *Eu^{3+}:(1%)Bi^{3+}-CPech1@APTMS* and the *Eu^{3+}:La_2O_2S@APTMS* samples was followed by photoluminescence.

Figures 6.23(a) and 6.23(b) show the excitation spectra of the *Eu^{3+}:(1%)Bi^{3+}-CPech1@APTMS* sample recorded from 0 h to 150 h and the excitation spectrum at 150 h, respectively. For this study, some drops of the functionalized sample cleaned with acetone were let dry on a quartz substrate. All the spectra were normalized in intensity at 395 nm to be compared. The curves showed a decrease in the intensity of the CT band with time. This is due to the formation of the $La(OH)_3$ phase. Thus, this indicates that the functionalization of the nanoparticles with APTMS did not avoid the easy re-hydroxylation process from the La_2O_3 phase to the $La(OH)_3$ phase. Furthermore, if we compare the re-hydroxylation rate of the *Eu^{3+}:(1%)Bi^{3+}-CPech1@APTMS* functionalized sample with the non-functionalized sample studied (see Fig. 5.9(a-b)), the rate is very similar. In both samples, at 70 h, the CT band decreased significantly, and at about 130 h the CT band almost disappeared.

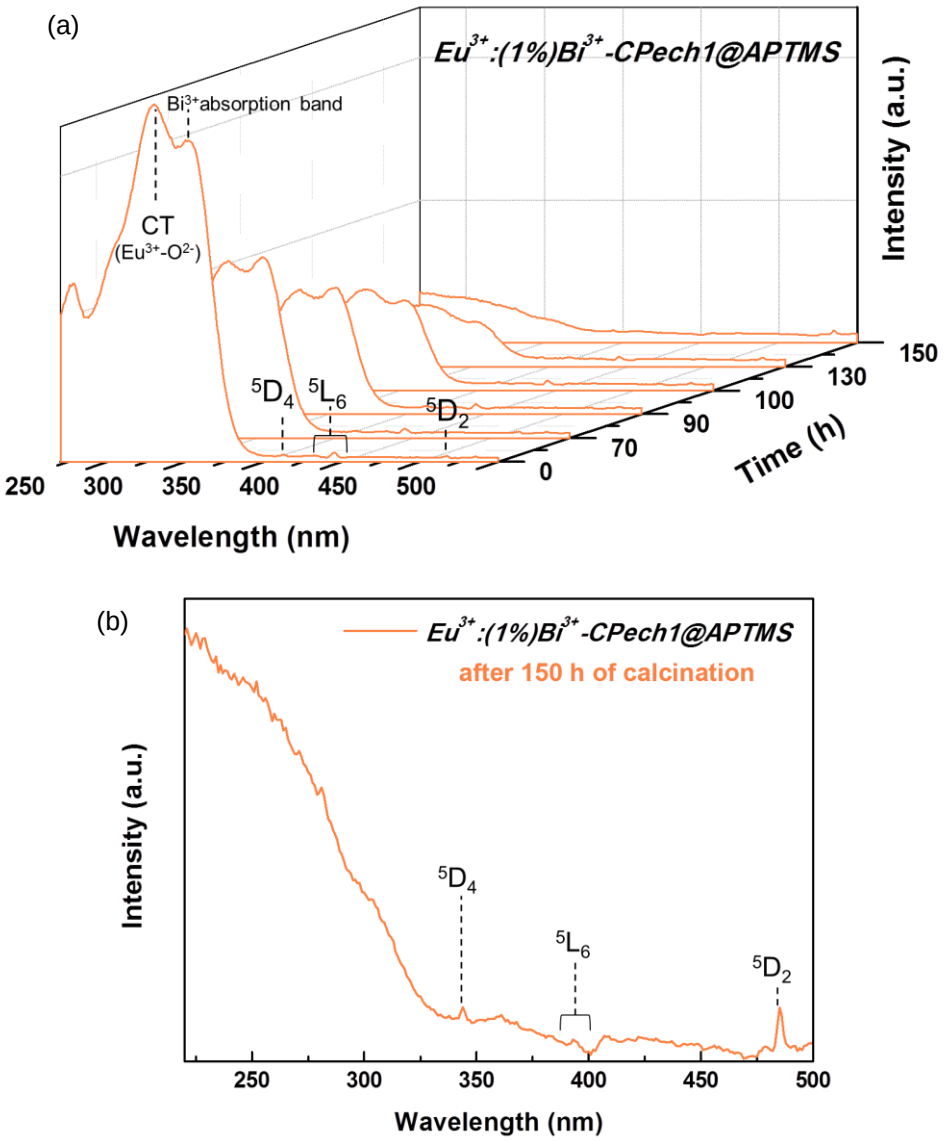

Figure 6.23. Excitation spectra recorded at **(a)** 0-150 h and at **(b)** 150 h for the *Eu^{3+}:(1%)Bi^{3+}-CPech1@APTMS* sample.

Similar results were observed in the emission spectra recorded versus time (Figs. 6.24(a) and 6.24(b)). All the spectra were normalized in intensity at 615 nm. We observed that all Eu^{3+} emissions in La_2O_3 decreased in intensity as the time increased.

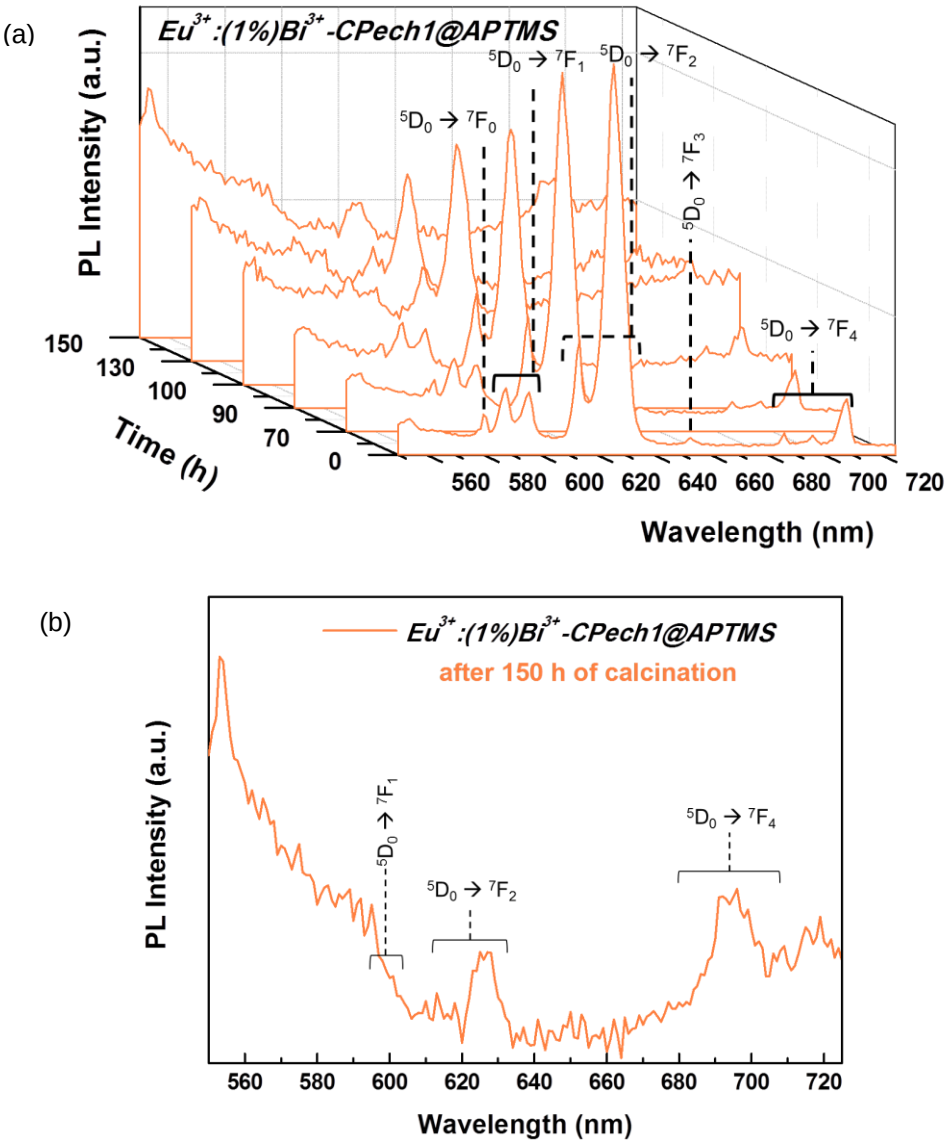

Figure 6.24. Emission spectra recorded at **(a)** 0-150 h and at **(b)** 150 h for the *Eu^{3+}:(1%)Bi^{3+}-CPech1@APTMS* sample.

Regarding to the re-hydroxylation studies of the *Eu^{3+}:La_2O_2S@APTMS* sample, we can conclude that Eu^{3+}:La_2O_2S kept stable also after being functionalized with the APTMS compound, as observed in Figure 6.25.

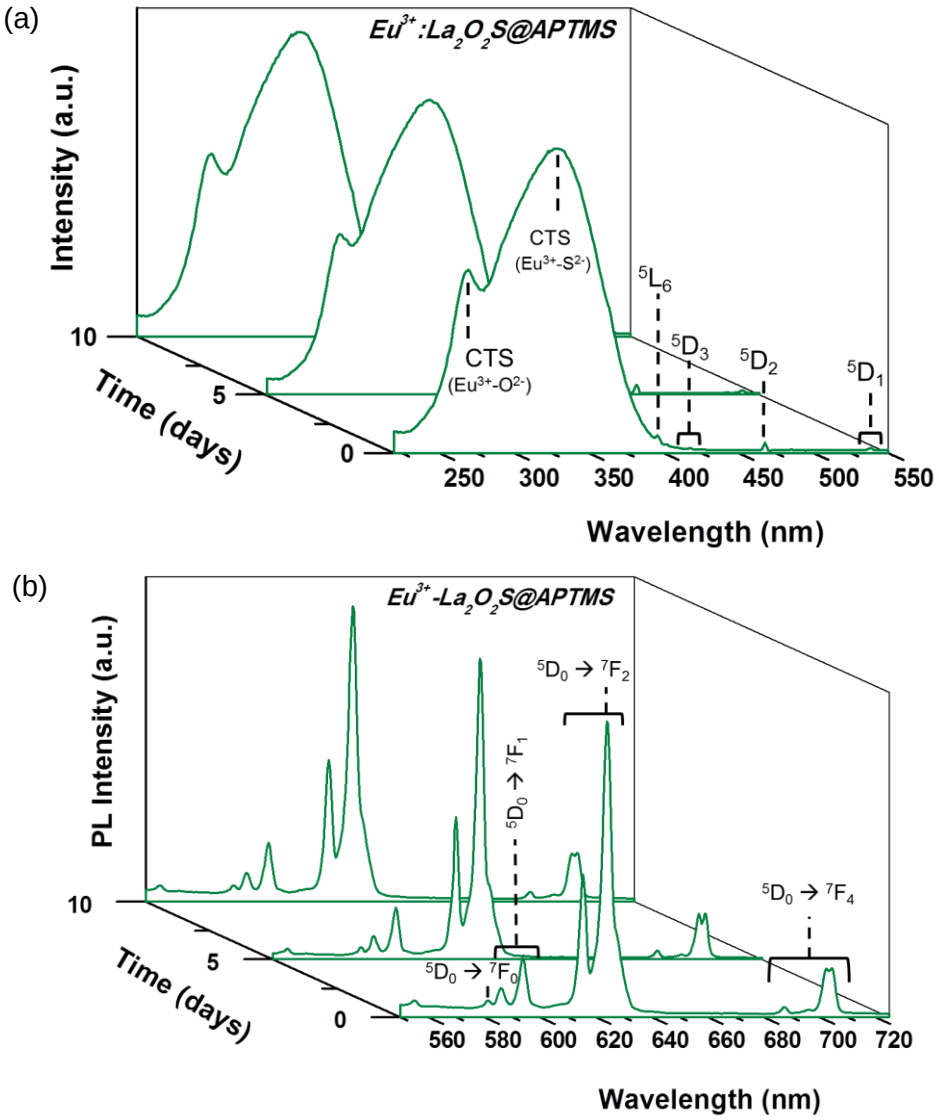

Figure 6.25. (a) Excitation and **(b)** emission spectra recorded from 0 to 10 days for the *Eu^{3+}:La_2O_2S@APTMS* sample.

Chapter 7

Fabrication and characterization of polymer-based nanocomposites

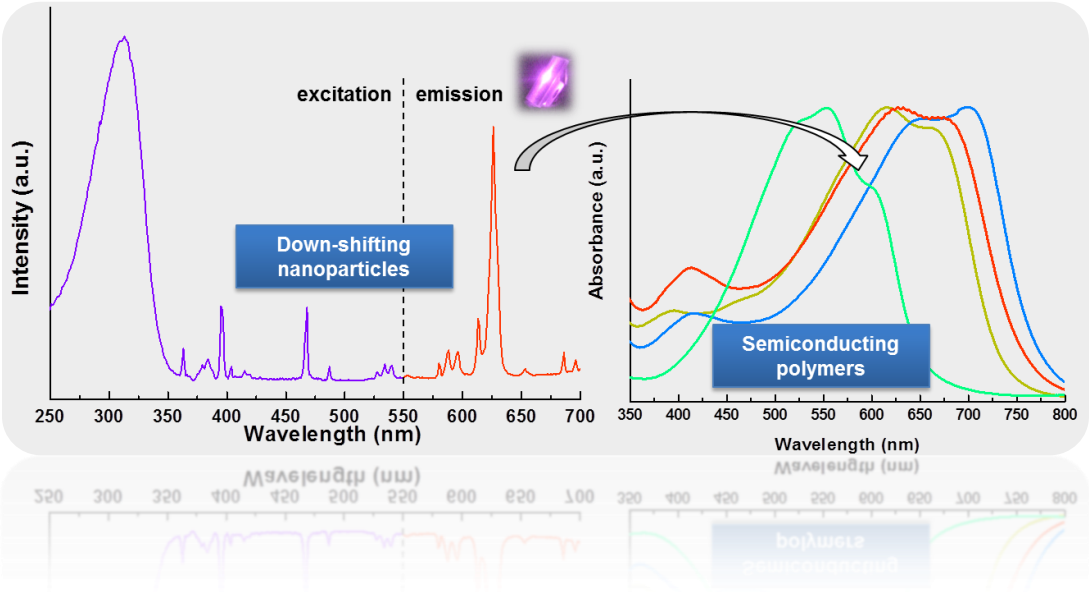

The comprehension of the organic-inorganic hybrid materials is essential for the well working of the final nanocomposites. Thus, Chapter 7 is mainly focused on the fabrication of polymer-based nanocomposite samples by the spin-coating technique and their characterization by different techniques (AFM, Raman, UV, PL, CL, ESEM and TEM). Furthermore, an approach of the fabrication and characterization of structured polymer-based nanocomposites using macroporous silicon in the template-assisted method is also shown in this chapter.

7.1. Overview

Nanocomposite materials are solids resulting from the combination of two or more simple materials that develop a continuous phase (polymer, ceramic, etc.), and a disperse phase, such as carbon particles, silica powder, etc. [241] and where at least one of the phases has one dimension below than 100 nm. Within the wide collection of inorganic-organic hybrid materials, nanocomposites are an emerging group that received a great deal of attention overall for their variety of applications ranging from biology to optoelectronics [242].

Nanocomposite materials include a very large family of materials, thus, one can find different ways to classify them. One way is depending on the matrix nature (ceramic, metal, polymer). Another is depending on the way the organic and inorganic components are associated, the first type includes composites made of inorganic materials embedded in a polymer matrix and the second type includes those made of a polymer deposited in an inorganic template [243].

The main motivation for the fabrication of organic-inorganic hybrid materials is that, as nanocomposites, they present advantages from both components: the easy manipulation and applicability of oxide nanopowders and the improvement of the polymer properties. For example, inorganic nanoparticles (clay) embedded in a polymer matrix such as polypropylene and polyethylene are used for automotive applications due to their excellent mechanical properties (light weight, high tensile strength, and high stability) and low cost [244]. Another common motivation is the improvement of optics and photonics properties. Here the use of conjugated polymers is required for the good synergy of both organic and inorganic materials, as it happens, for instance, in CdSe nanoparticles embedded in P3HT thin films for photovoltaic applications [245].

Inorganic-organic nanocomposites may be easily fabricated by incorporating (also called embedding or introducing) inorganic nanoparticles usually of oxides or semiconductors, in a controlled manner, into a matrix of a polymer solution [243]. Alternative techniques have been used owing to the fact that isolated colloids of primary particles are not usually successful. They form strongly connected aggregates difficult to separate from each other during the procedures applied for the nanocomposite fabrication [246]. As a consequence, nanocomposites have been prepared through the synthesis of the inorganic particles in situ, for instance in solution, where the solvent can also be a monomer and the nanocomposites are formed by in situ polymerization. Other techniques use chemical reactions, for instance, metal-oxide nanoparticles in a polyimide film were formed by a chemical reaction between the metal thin films and polyamic acid (PAA) [247].

In this chapter, we have focused our attention on the preparation of lanthanide doped lanthanum compounds embedded in polymer-based nanocomposites. Recently, a work about the luminescence properties of Er^{3+}:Y_2O_3, Pr^{3+}:Y_2O_3 and Pr^{3+}:$LaAlO_3$ nanopowders embedded in poly(methyl)methacrylate (PMMA)-based composites have been published [248]. However, up to now there are only few reports about embedding nanoparticles into

other polymers, such as for example in conjugated polymers (polythiophene (P3HT), polyfluorenes (PF), poly(*p*-phenylene vinyle) (PPV), etc.). Lin et al. [249], embedded semiconductor FeS_2 nanoparticles into P3HT for photovoltaic applications. Additionally, for these photovoltaic applications, new semiconducting polymers with thieno[3,4-*b*]thiophene and benzodithiophene alternating units have been developed [250]. These polymers, known as PTBx (x =1-7), have low bandgaps and exhibit efficient absorption throughout the region of greatest photon flux in the solar spectrum (around 700 nm). The absorption region of the PTBx polymers is in good agreement with the emission light of Eu^{3+} doped nanocompounds. In this thesis, the polymers involved in the polymer-based nanocomposite fabrication were: P3HT, poly(thienothiophene-benzodithiophene) (PTB1), and poly[4,8-bis-substituted-benzo[1,2-b:4,5-b']dithiophene-2,6-diyl-alt-4-substituted-thieno[3,4-b]thiophene-2,6-diyl] (PBDTTT-CF). The structure of these polymers is shown in Figure 7.1.

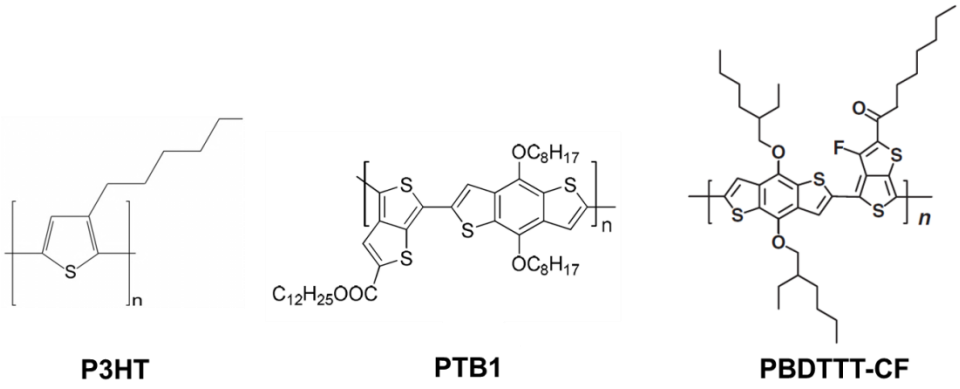

Fig. 7.1. Structure of the different polymers involved in the polymer-based nanocomposites.

Structured nanocomposites, known as nanocomposites with a desired morphology, have been investigated in recent years [251]. Lithography, electrospinning, self-assembly and template-assisted are some of the common methods used for the fabrication of structured nanocomposites [252]. Template-assisted has been the method used for the fabrication of the structured nanocomposites in this thesis. This method consists on the infiltration of a specific material into a cavity (called template) with a well-defined shape and, then, the template is removed (when a free structure is required) to obtain the inverse replica of the template [253]. Macroporous silicon and nanoporous alumina are attractive materials to be used as templates for many reasons, since they can be fabricated in a large scale, and the porosity, pore size and depth can be tuned under appropriate preparation conditions. Due to the size of the nanoparticles we chose the macroporous silicon templates fabricated by electrochemical dissolution in hydrofluoric acid-based solutions, for the structured polymer-based nanocomposite fabrication. Since the first studies of Uhlir [254] and Turner [255], the preparation of porous silicon by electrochemical dissolution of silicon wafers in solutions based on hydrofluoric acid (HF) has been developed [256]. Structured materials have a wide

range of potential applications in different fields, such as medicine, sensors, actuators and opto-electronic devices [257]. Among them, one of the most interesting applications for structured materials is in photovoltaic devices [258].

7.2. Fabrication of polymer-based nanocomposite samples

Different polymer-based nanocomposite samples were fabricated. All of them could be included in the general synthesis scheme shown in Fig. 7.2.

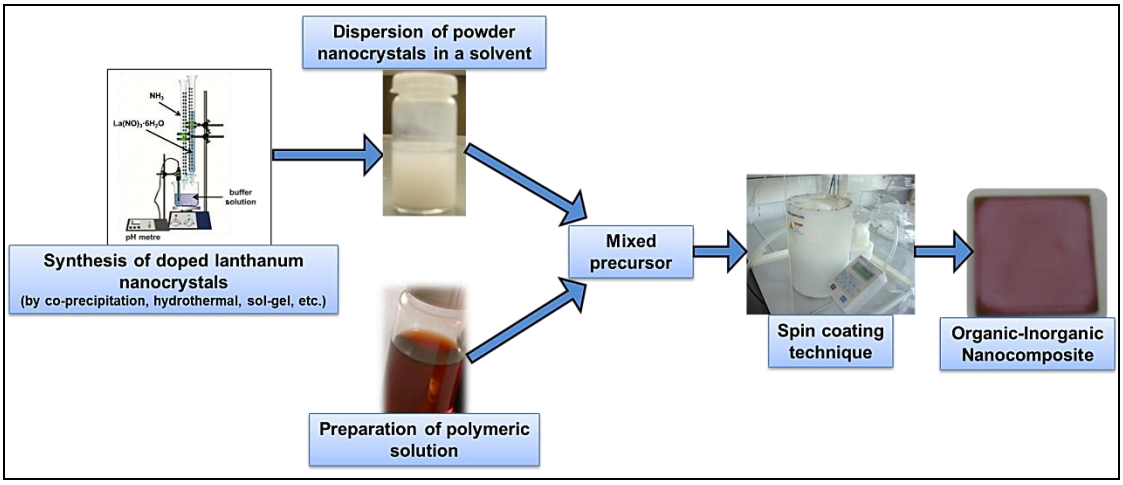

Figure 7.2. General scheme for the synthesis of polymer-based nanocomposite films.

On one hand, doped lanthanum nanoparticles synthesized by different methods (Chapter 3) were dispersed into an organic solvent. Then, that solution was kept for several hours in an ultrasonic processor to avoid the presence of particle aggregates. On the other hand, the commercial polymeric powder was dissolved in the suitable organic solvent (the same used to disperse the nanoparticles). Finally, to fabricate the polymer-based nanocomposite films, both solutions were mixed carefully and stirred to assure good homogeneity. After several hours, the films were deposited on a substrate, such as quartz or glass, by the spin-coating technique.

Depending on the property to measure, samples were fabricated with some slight differences with respect to the procedure shown in Fig. 7.1, as indicated in Table 7.1.

Five samples were fabricated onto indium tin oxide (ITO) for the morphological and electrical characterization. One sample was prepared as a blank (*P3HT-ITO)*. The P3HT powder was stirred overnight in a vial with chloroform solvent in a ratio of 1 ml of chloroform ($CHCl_3$) to 10 mg of P3HT. The solution was stirred in the dark overnight to ensure the complete dissolution of the powders. Organic films were prepared by spin coating this solution onto pre-cleaned ITO-coated glass substrates, yielding a film thickness of approximately 100 nm as measured by AFM. ITO coated substrates were cleaned in an ultrasound bath with soap for 10 min and after rinsing them with acetone they were annealed

at 723 K for 30 min. This procedure has already been demonstrated to be very important to obtain reliable current voltage results [259,260]. Spin coating conditions were 2000 rpm for 1 min after adding 0.2 ml of polymeric solution on the ITO-coated glass substrates.

Table 7.1. Fabrication conditions of polymer-based nanocomposite samples.

Sample	Solvent	Nature of sample	Method - amount/rpm/time	Substrate
P3HT-ITO	$CHCl_3$	Film	SC – 0.2 ml / 2000 rpm / 1 min	ITO
Eu^{3+}-CPech1(10%)-P3HT	$CHCl_3$	Film	SC – 0.2 ml / 2000 rpm / 1 min	ITO
Eu^{3+}-CPech1(35%)-P3HT	$CHCl_3$	Film	SC – 0.2 ml / 2000 rpm / 1 min	ITO
Eu^{3+}-CPech1(65%)-P3HT	$CHCl_3$	Film	SC – 0.2 ml / 2000 rpm / 1 min	ITO
Eu^{3+}-CPech1(80%)-P3HT	$CHCl_3$	Film	SC – 0.2 ml / 2000 rpm / 1 min	ITO
P3HT-Quartz	THF	Film	SC - 1 ml / 500 rpm / 2 min	Quartz
Eu^{3+}-CPech1(15%)-P3HT	THF	Film	SC - 1 ml / 500 rpm / 2 min	Quartz
Eu^{3+}-CPech1(100-97%)-P3HT	$CHCl_3$	Solution	-	Quartz cuvette
PTB1-Quartz	DCB	Film	SC - 1 ml / 500 rpm / 2 min	Quartz
Eu^{3+}-CPech1(100-97%)-PTB1	ODCB	Solution	-	Quartz cuvette
PBDTTT-CF-Quartz	CB	Film	SC - 1 ml / 500 rpm / 2 min	Quartz
Eu^{3+}-CPech1(100-97%)-PBDTTT-CF	CB	Solution	-	Quartz cuvette

THF: Tetrahydrofuran, $(CH_2)_4O$

DCB: Dichlorobenzene, $C_6H_4Cl_2$

CB: Chlorobenzene, C_6H_5Cl

ITO: Indium tin oxide, $In_2O_3(90\%)SnO_2(10\%)$

SC: Spin coating technique

For the fabrication of polymer-based nanocomposite films, Eu^{3+} doped lanthanum oxide nanoparticles synthesized by the sol-gel Pechini method (*Eu^{3+}-CPech1*) were dispersed in the $CHCl_3$ solvent using an ultrasonic processor for 3 h. Then, the films were prepared in the same way than P3HT films but adding different amounts of the solution containing the

dispersed nanoparticles to the P3HT solution in chloroform. The mixture was stirred using an ultrasound bath for 30 min to assure a good dispersion of the nanoparticles in the P3HT matrix. Four more samples were fabricated from this solution (*Eu^{3+}-CPech1(10%)-P3HT*, *Eu^{3+}-CPech1(35%)-P3HT*, *Eu^{3+}-CPech1(65%)-P3HT* and *Eu^{3+}-CPech1(80%)-P3HT*).

Two more P3HT-based nanocomposite films were fabricated onto quartz substrates for spectroscopic and optical characterization. Thus, samples, *P3HT-Quartz* and *Eu^{3+}-CPech1(15%)-P3HT*, were fabricated following the same procedure previously explained but using tetrahydrofuran (THF) as the organic solvent and changing the spin-coating conditions in order to develop a thicker film.

Two additional polymer-based nanocomposite films were made of PTB1 and PBDTTT-CF (*PTB1-Quartz* and *PBDTTT-CF-Quartz)* on quartz substrates. In order to study the spectroscopic properties of the nanoparticles into these polymeric matrices, the *Eu^{3+}-CPech1(99-97%)-P3HT*, *Eu^{3+}-CPech1(99-97%)-PTB1* and *Eu^{3+}-CPech1(99-97%)-PBDTTT-CF* samples were analysed in liquid state and inside a quartz cuvette.

7.3. Characterization of polymer-based nanocomposite samples

Since the behaviour of the nanocomposites greatly depends on the combination of several parameters such as concentration, structure, size, and shape, it requires a well comprehension and control of their properties. Thus, polymer-based nanocomposite samples fabricated were well characterized in the next part of this chapter. The results were separately exposed for the morphologic, spectroscopic and optics, and electric characterization.

7.3.1. Dispersion studies of the nanoparticles into a polymeric matrix

Raman scattering was used to study the dispersion of the nanoparticles into a polymeric matrix. *P3HT-Quartz* and *Eu^{3+}-CPech1(15%)-P3HT* were the samples used in this study. As we can see in Figure 7.2, Eu^{3+}:La_2O_3 nanoparticles showed a vibrational peak with maximum intensity at 407 cm^{-1} while the P3HT polymer showed the vibrational peak with maximum intensity at 1450 cm^{-1}, well separated from the peak corresponding to the Eu^{3+}:La_2O_3 nanoparticles. Furthermore, we did not observe any vibrational peak at around 407 cm^{-1} corresponding to the polymer, so a Raman map of the *Eu^{3+}-CPech1(15%)-P3HT* sample was analysed collecting the signal at 407 cm^{-1} and plotting the intensity of this peak as a function of the position. Figure 7.3 shows an optical microscopy image where we observed the dispersion of the nanoparticles into the polymeric matrix. In the right hand image, the Raman map plotting the intensity of the 407 cm^{-1} vibrational peak confirms the presence of the nanoparticles in the polymer, corresponding to the black spots as observed in the optical image.

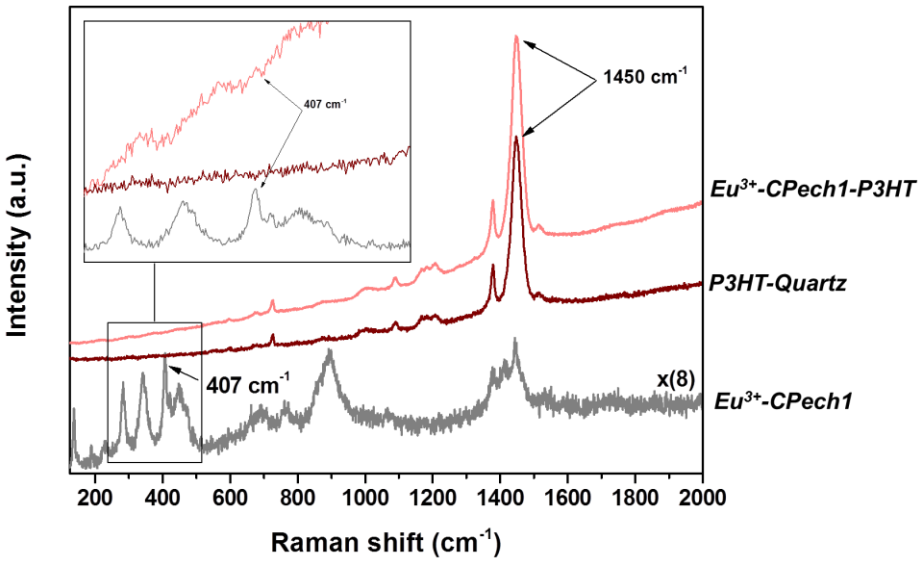

Figure 7.3. Raman scattering showing the vibrational peaks of the *Eu*$^{3+}$*-CPech1*, *P3HT-Quartz* and *Eu*$^{3+}$*-CPech1-P3HT* samples.

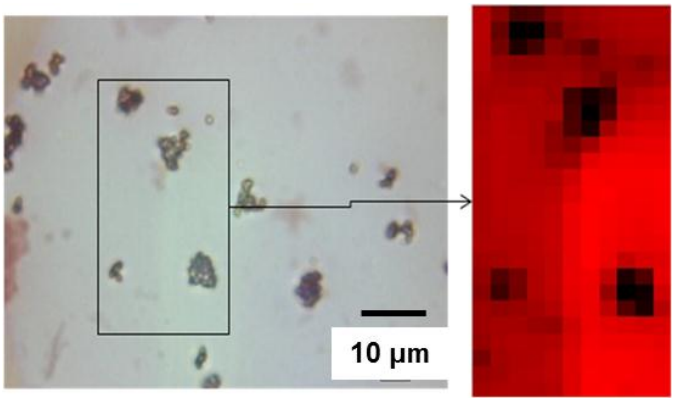

Figure 7.4. Image of the *Eu*$^{3+}$*-CPech1-P3HT* sample obtained by optical microscopy (left), and its map obtained by Raman and plotting the intensity of the 407 cm^{-1} vibrational peak.

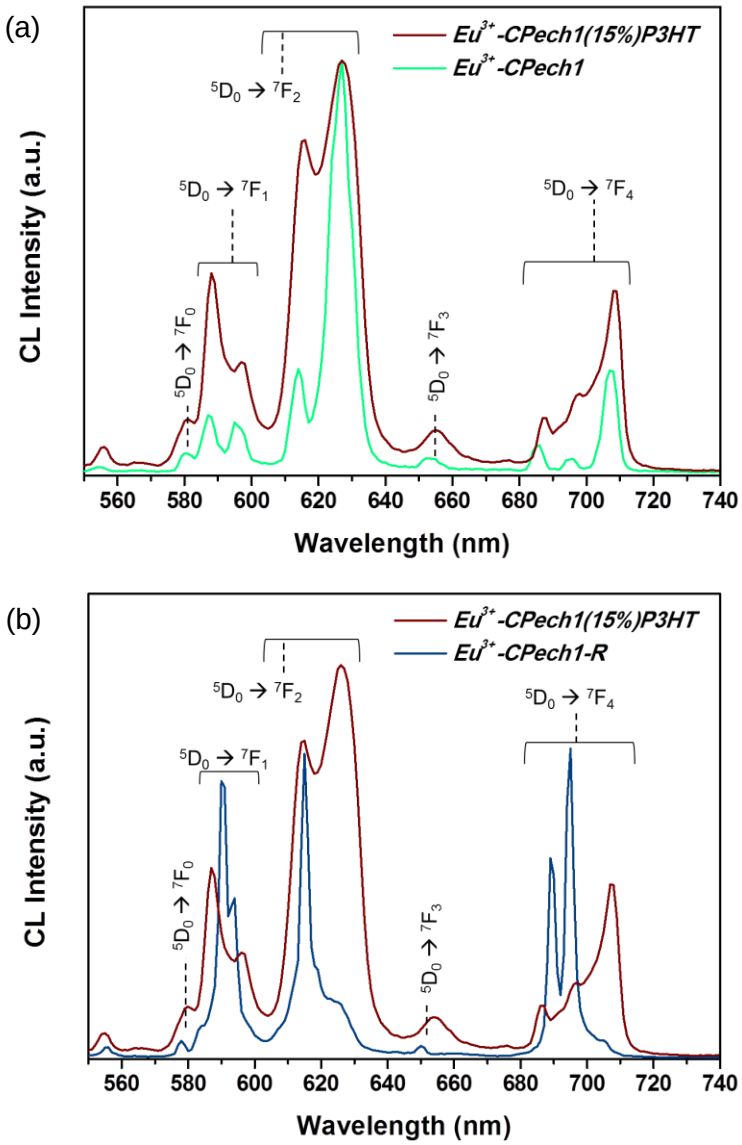

Figure 7.5.(a) CL spectra of the *Eu^{3+}-CPech1(15%)P3HT* sample compared to the CL spectra of the *Eu^{3+}-CPech1* sample and **(b)** CL spectra of the *Eu^{3+}-CPech1(15%)P3HT* sample compared to the CL spectra of the *Eu^{3+}-CPech1-R* sample.

Figure 7.5(a) and 7.5(b) shows the cathodoluminescence (CL) spectra of *Eu^{3+}-CPech1* and *Eu^{3+}-CPech1(15%)-P3HT* samples and *Eu^{3+}-CPech1-R* and *Eu^{3+}-CPech1(15%)-P3HT* samples, respectively. Both *Eu^{3+}-CPech1* and *Eu^{3+}-CPech1(15%)-P3HT* CL spectra showed the typical peaks from the $^5D_0 \rightarrow {}^7F_J$ (J = 0-4) transition of Eu^{3+} observed in the Eu^{3+}:La_2O_3 nanoparticles (see Chapter 4). These bands are located at the same position than those observed for the nanoparticles, however, with different intensity ratios (Fig. 7.5(a)). Depending upon the environment around the Eu^{3+} ions, the luminescence properties are affected, as observed in Chapter 4. The asymmetry ratios, I_2, calculated from the intensity

relation between the $^5D_0 \rightarrow {}^7F_2$ (626 nm) and $^5D_0 \rightarrow {}^7F_1$ (595 nm) transitions, were 7.85 and 2.08 for *Eu^{3+}-CH-24* and *Eu^{3+}-CPech1(15%)P3HT*, respectively. The low I_2 value obtained for the nanocomposite film was within the values obtained for europium doped hydroxide samples (1.71-2.16). However, this does not mean that the nanoparticles were hydroxylated but the sample was kept stable thanks to the polymer matrix. Fig. 7.5(b) corroborates this affirmation, because when we compared the CL spectrum of the *Eu^{3+}-CPech1(15%)P3HT* sample with that of the *Eu^{3+}-CPech1-R* sample, significant differences were observed. These spectra were normalized in intensity at the peak located at 614 nm. Then, we might attribute the differences in the asymmetry ratios to a decrease of covalency of the structure or to a distortion of the bonds surrounding the active ion.

Other intensity ratio differences were also interesting. The CL spectrum of the *Eu^{3+}-CPech1(15%)P3HT* sample had a similar ratio between peaks at 595 and 714 nm whereas the CL spectrum of the *Eu^{3+}-CPech1* sample showed the peak at 714 nm with double intensity value in comparison with the peak at 595 nm (Fig. 7.5(a)). Since nanoparticles were embedded into a P3HT polymeric matrix, that matrix could be absorbing part of the light emitted by the nanoparticles. The absorbance spectrum of P3HT and more luminescence results from nanocomposites are explained in section 7.3.2 of this chapter.

The dispersion of the nanoparticles embedded into a P3HT matrix was also studied by SEM and CL images (Figs. 7.6 and 7.7). The results for the *Eu^{3+}-CPech1(15%)P3HT* sample are shown in Figure 7.6. The images of the *Eu^{3+}-CPech1(15%)P3HT* sample exhibited well dispersed nanoparticles through all the film, as observed by Raman scattering, although forming large aggregates. We also concluded from CL images, that the polymeric matrix, in which the nanoparticles are embedded, do not block neither the excitation nor the emission of the nanoparticles.

Figure 7.7 shows SEM and CL images of the *Eu^{3+}-CPech1(15%)P3HT* sample at different wavelengths These wavelengths were chosen because they corresponded to the $^5D_0 \rightarrow {}^7F_2$ (623 nm) and $^5D_0 \rightarrow {}^7F_4$ (708 nm) transitions with higher intensity in the spectra (see Fig. 7.4(a)). The image recorded at 623 nm was brighter than that recorded at 708 nm, according to the higher intensity of the $^5D_0 \rightarrow {}^7F_2$ transition when compared to the intensity of the $^5D_0 \rightarrow {}^7F_4$ transition.

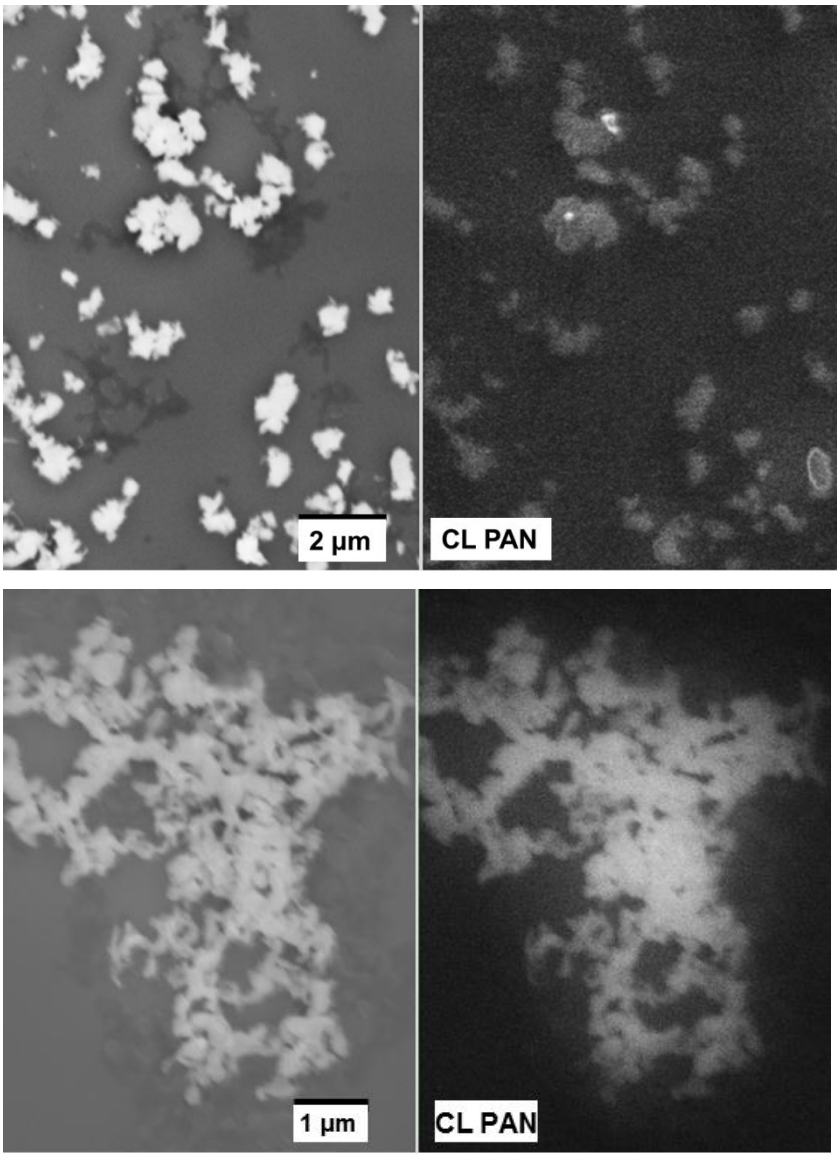

Figure 7.6. SEM (left) and CL panchromatic (right) images of the *Eu^{3+}-CPech1(15%)P3HT* sample.

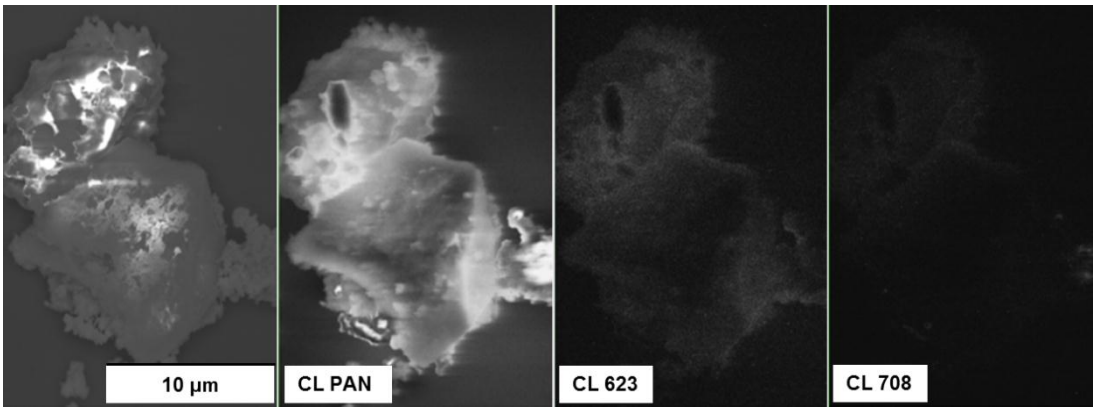

Figure 7.7. SEM images of the *Eu^{3+}-CPech1(15%)P3HT* sample recorded under CL excitation at different wavelengths.

7.3.2. Thickness and roughness studies of the nanoparticles into a polymeric matrix

By using atomic force microscopy (AFM) we studied the surfaces of some samples in order to confirm the dispersion of the nanoparticles in the polymeric matrix. The 3D topography images of the *P3HT-ITO* and *Eu^{3+}-CPech1(65%)-P3HT* samples are depicted in Figs 7.8(a) and (b), respectively. These topography images showed a maximum roughness of the surface film in this area, of 28 nm and 578 nm for the *P3HT-ITO* and *Eu^{3+}-CPech1(65%)-P3HT* samples, respectively. We attributed this significant increase of roughness to the existence of agglomerates of the La_2O_3 nanoparticles. However, we considered that the NPs were covered by a P3HT thin layer. We could attribute this effect to the higher viscosity of the polymer when compared to the viscosity of the chloroform, which does not contribute to have a good deagglomeration of the nanoparticles.

The dispersion of the NPs in the *Eu^{3+}-CPech1(15%)-P3HT* sample was also observed by ESEM. Figs. 7.9(a-b) show a top view of the sample taken by two different detectors (the Secondary Electrons detector and the Back Scattered Electrons detector). Here, it was possible to observe once again the degree of dispersion of the aggregated particles occupying almost all the polymer film. Additionally, in Fig. 7.9(c) we could observe the roughness of these films and in the image taken with the Back Scattered Electrons detector we corroborate that this roughness arises from the nanoparticles (Fig. 7.9(d)), in these lateral views of the sample.

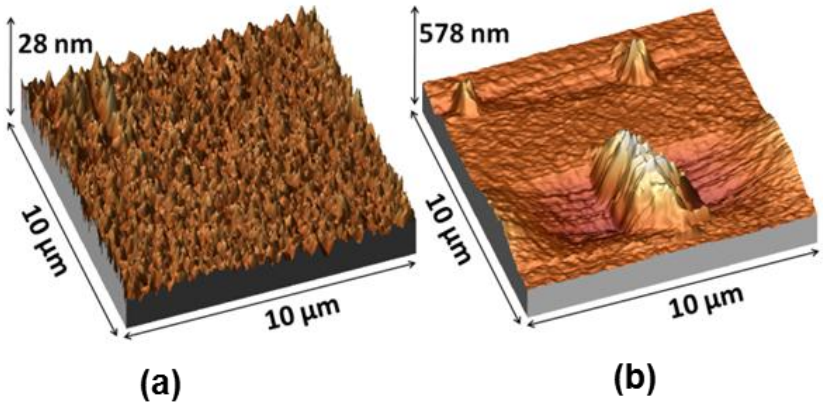

Figure 7.8. 3D topography AFM images of **(a)** *P3HT-ITO* and **(b)** *Eu^{3+}-CPech1(65%)-P3HT* samples.

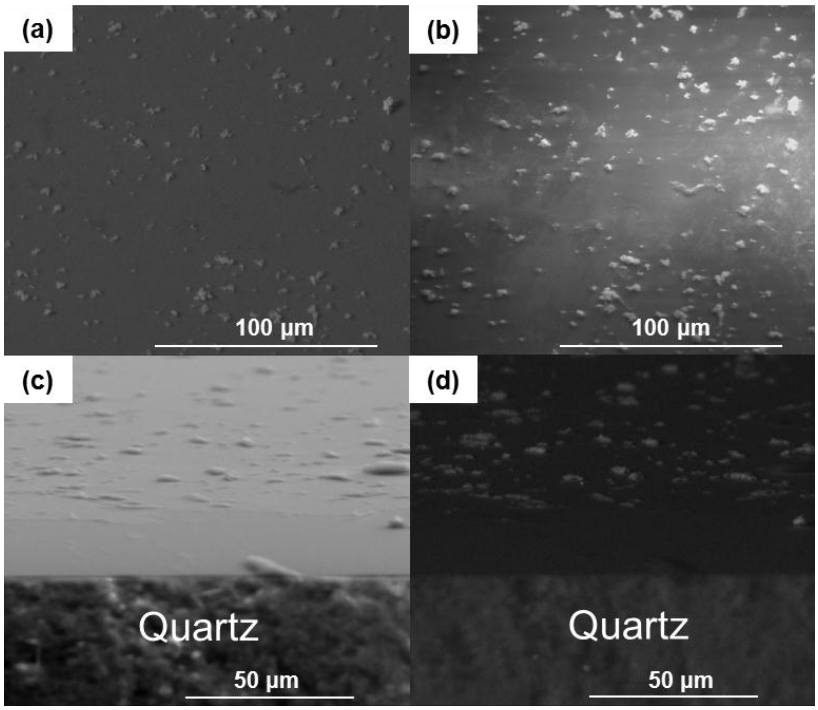

Figure 7.9. ESEM images, **(a-b)** top view and **(c-d)** 45º tilted, of the *Eu^{3+}-CPech1(15%)-P3HT* sample.

7.3.3. Spectroscopic and optical characterization

UV-Visible absorption and photoluminescence of polymers

The absorption spectra of the polymers used in the fabrication of the nanocomposite samples were recorded in the range from 350 to 800 nm. Fig. 7.10 shows the absorption spectra of the

P3HT, PBDTTT-CF and PTB1 polymers, all of them measured onto quartz substrates. The intensities were normalized by to the maximum intensities of the absorption bands in order to be compared. Typically, the absorption of polymers is known for its wide band width in the visible part of the electromagnetic spectrum. The absorption of the P3HT polymer comprised a range between 400-650 nm with maximum absorbance at 554 nm. The absorption of PBDTTT-CF and PTB1 polymers comprised a range between 500-800 nm and both presented a weak shoulder at around 415 nm. The maximum absorbance was found at 630 nm and 700 nm for PBDTTT-CF and PTB1, respectively. From these results, we could say that the use of polymers such as PTB1 or PBDTTT-CF, which have the absorption band more centered in the region of emission of the Eu^{3+}:La_2O_3 nanoparticles (626 nm), would be more efficient because they would absorb a higher amount of the light emitted by the nanoparticles.

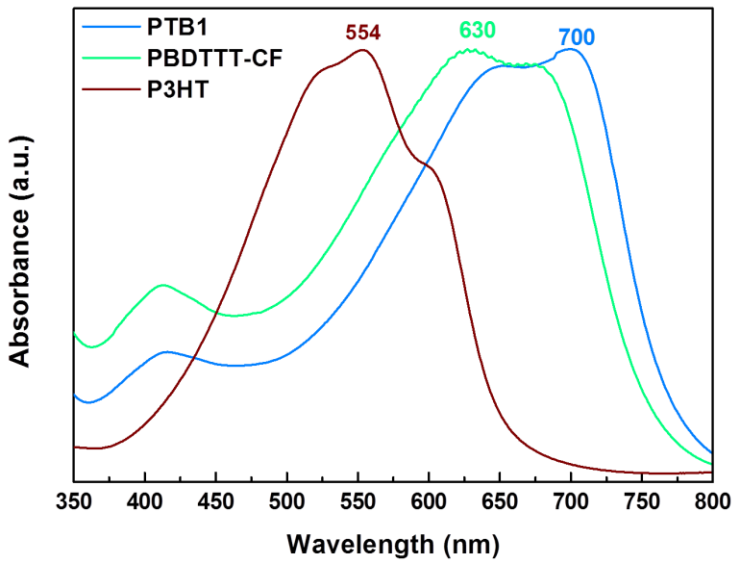

Figure 7.10. Absorption spectra of the polymers used for the fabrication of the nanocomposite samples.

Conjugated polymers are photoluminescent. Figs. 7.11(a) and 7.11(b) show the photoluminescence (PL) spectra of P3HT and PBDTTT-CF polymers, respectively. Spectra were recorded pumping at the wavelength of maximum absorption, thus at 554 and 630 nm, respectively.

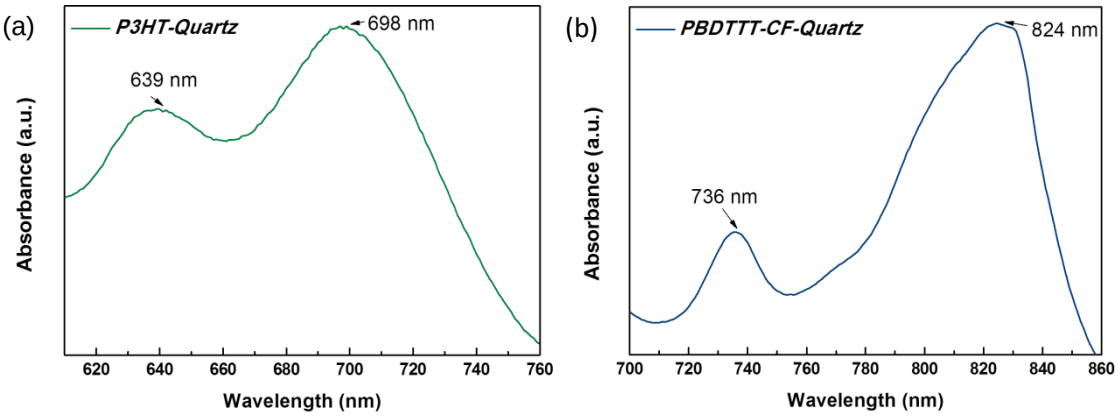

Figure 7.11. Photoluminescence spectra of the **(a)** *P3HT-Quartz* and **(b)** *PBDTTT-CF-Quartz* samples.

Photoluminescence characterization of polymer-based nanocomposite samples

Photoluminescence properties of the polymer-based nanocomposites samples were studied in terms of excitation and emission spectra of the Eu^{3+}:La_2O_3 nanoparticles in order to analyse how the polymeric matrix affected their luminescence properties and if existed some energy transfer process from the nanoparticles to the polymeric matrix. Fig. 7.12(a) shows the excitation spectra of the *Eu^{3+}-CPech(100-97%)-P3HT* samples, monitoring the emission of the $^5D_0 \rightarrow {}^7F_2$ transition at 626 nm. All the excitation spectra were normalized in intensity at 289 nm to be compared. The *Eu^{3+}-CPech(100%)* sample presented the typical band peaking at ~290 nm corresponding to the charge transfer state (CTS) band, well-studied in Chapter 4. That excitation spectrum also presented the typical Eu^{3+} f-f transitions. When the amount of nanoparticles decrease in the composite with respect to the P3HT (*Eu^{3+}-CPech(99-97%)-P3HT*) the CT band decrease in intensity and we observed also a slight shift in its position. Furthermore, we could not observe the Eu^{3+} f-f transitions.

Fig. 7.12(b) shows the emission spectra of the *Eu^{3+}-CPech(100-97%)-P3HT* samples after pumping into the CT band at 290 nm. All the emission spectra were normalized in intensity at 626 nm to be compared. The emission spectra of the *Eu^{3+}-CPech(99%)* and *Eu^{3+}-CPech(100%)* samples were dominated by the $^5D_0 \rightarrow {}^7F_2$ transition which consisted of two peaks at 613 and 626 nm, respectively. However, for samples with a lower concentration of nanoparticles, the emission spectra were dominated by the peak at 710 nm which corresponded to the $^5D_0 \rightarrow {}^7F_4$ transition whereas the peak at 626 nm started to disappear when the P3HT amount increased in the nanoparticles solution. This was attributed to the absorption from the P3HT polymer of the light emitted by the nanoparticles.

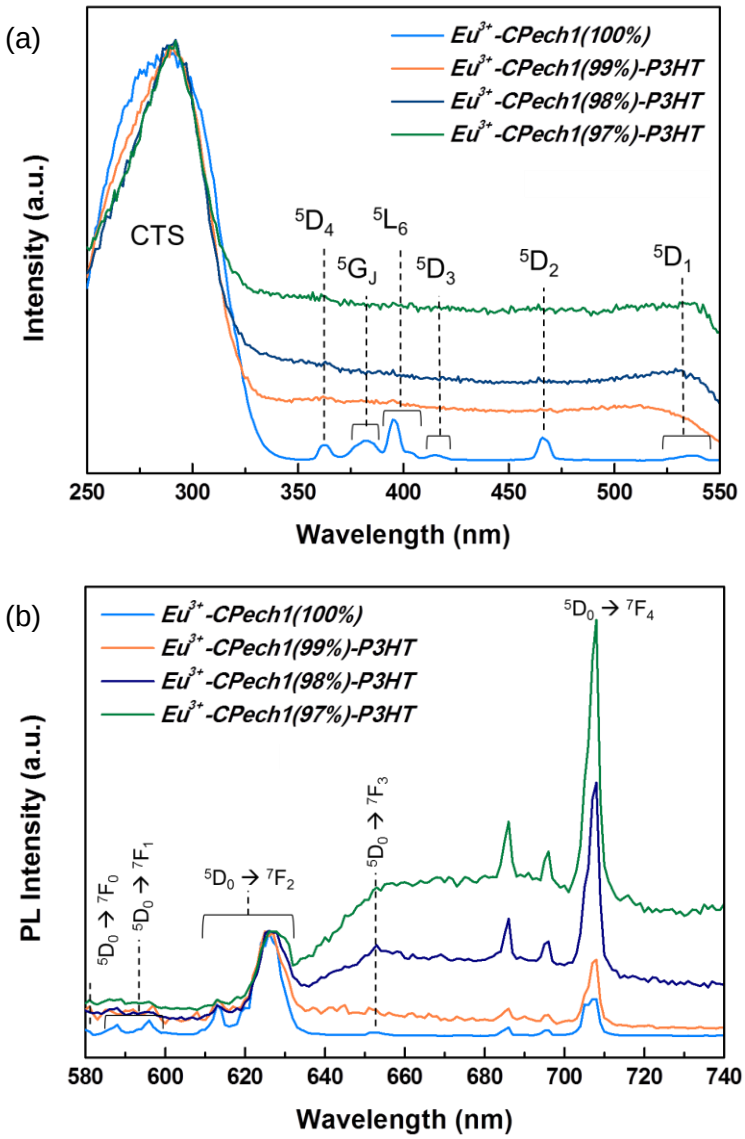

Figure 7.12. (a) Excitation and **(b)** emission spectra of the *Eu^{3+}-CPech1(100-97%)-P3HT* sample normalized in intensity at 289 nm and at 626 nm, respectively.

In order to use a better polymer matrix with its absorption band centered at 626 nm, the emission spectra of the *Eu^{3+}-CPech1(100-97%)-PTB1* and *Eu^{3+}-CPech1(100-97%)-PBDTTT-CF* samples were also recorded (Fig. 7.13(a-b)). As observed by UV-Visible absorption, the absorption region of these polymers had maximum bands at 630 and 700 nm for the *PTB1* and *PBDTTT-CF* polymers, respectively. Therefore, the emission spectra presented a different behaviour in comparison to those when the P3HT polymer was used. All the emission peaks of the Eu^{3+}:La_2O_3 nanoparticles were decreasing in intensity when the

concentration of polymer increased. Thus, that meant that these polymers were able to absorb a higher part of the light emitted by the nanoparticles.

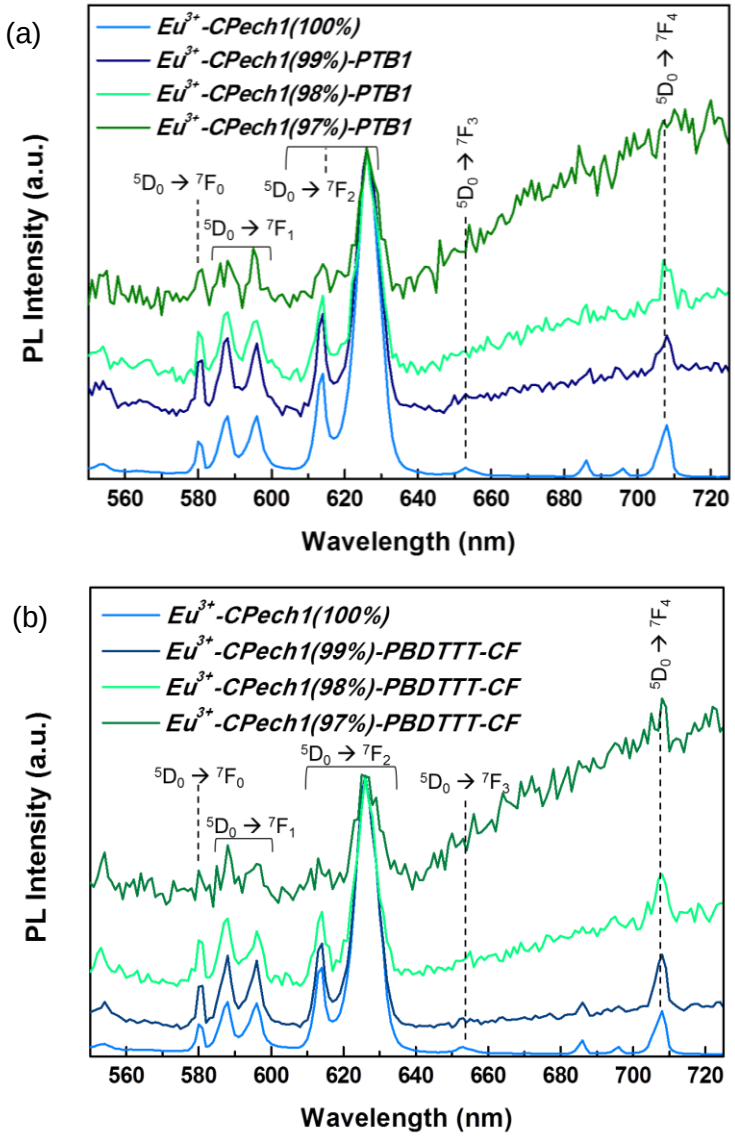

Figure 7.13. Emission spectra of the **(a)** *Eu^{3+}-CPech1(100-97%)-PTB1* and **(b)** *Eu^{3+}-CPech1(100-97%)-PBDTTT-CF* samples.

Unfortunately, since the detector used could not measure lifetimes shorter than 200 μs, it was not possible to measure the lifetime of the nanoparticles embedded in the polymeric films. However, this indicated that the polymers were shortening the emission lifetime of the nanoparticles (1.05 ms), as observed, for instance, in other P3HT-based nanocomposites [261].

7.3.4. Electrical characterization

Samples fabricated onto ITO substrates (*P3HT-ITO* and *Eu^{3+}-CPech1(10-80%)-P3HT*) were characterized by the current sensing atomic force microscopy (CS-AFM) technique. AFM measurements were done in air under ambient conditions using a commercial scanning probe microscope. The AFM images were collected in tapping mode from 4 to 7 V of peak amplitude depending on the roughness of the sample and with a speed of 1 line/s. The CS-AFM studies were performed in contact mode in the dark. For CS-AFM measurements, electrically conductive platinum-chromium coated cantilevers (Multi75E-G with a resonant frequency of 75 kHz and a force constant of $3 N \cdot m^{-1}$ from Budgetsensors) were used to scan the nanocomposite while the current was measured between the tip and the ITO substrate. A representation of our experiment is shown in Figure 7.14, where the electronic components, as well as the apparatus for topographic imaging, are omitted for simplification. One electrical contact is placed on the conductive ITO film, while the other contact is provided by the tip in contact with the surface of the sample.

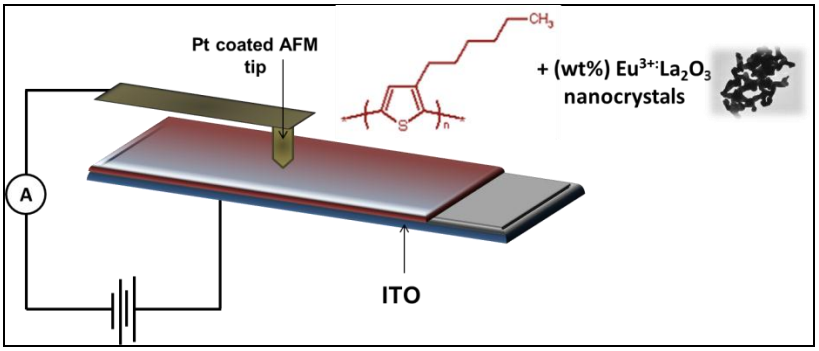

Figure 7.14. Simplified diagram of the CS-AFM setup for the *P3HT-ITO/Eu^{3+}-CPech1(10-80%)-P3HT* samples.

A comparative energy level diagram of the studied nanocomposite, under non equilibrium conditions, is shown in Figure 7.15(a). The HOMO of P3HT has been estimated to be located in the range between 5.1 and 5.2 eV. The energy gap estimated from absorption spectroscopy is about 2.1 eV, therefore the LUMO is about 3.0 eV [262]. The work functions of Pt and ITO are about 5.6 [263] and 4.7 eV [262], respectively. Here, we did not take into account the band gap of lanthanum oxide (La_2O_3), which is about 4.3 eV [264]. The current-voltage characteristics of the Pt/P3HT/ITO nanocomposites are controlled by two basic processes: (a) injection of charge carriers from the Pt electrode into the polymer and vice versa and (b) transport of charge in the bulk of the film. To be injected into the polymer, the charge carriers must overcome the potential barrier at the metal/polymer interface. We are refereeing to the potential barrier as a simple geometric shape (rectangular, trapezoidal, triangular) as it is possible to observe in Figure 7.15(b). Although these barriers are oversimplifications, the important feature is the prediction of a transition from direct tunnelling through a barrier (trapezoidal type) to field emission through the top of the barrier (triangular type) [265-267].

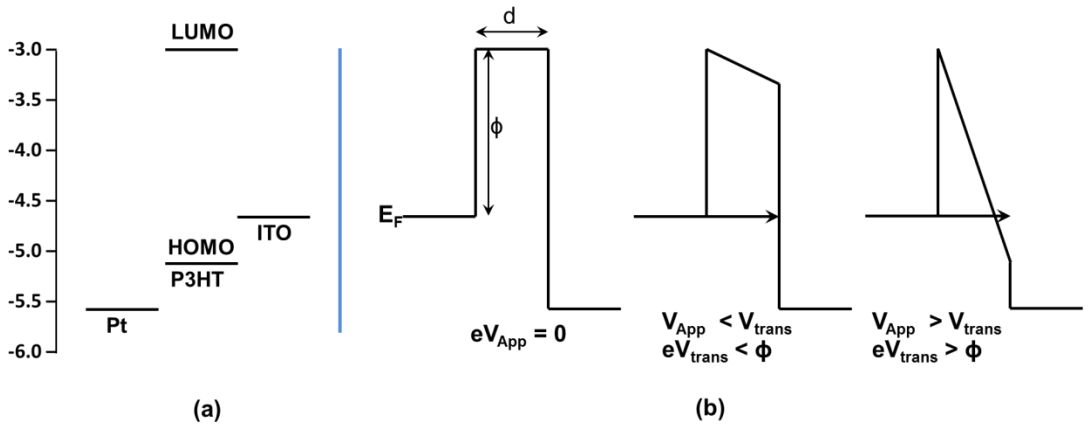

Figure 7.15.(a) Energy level diagram of the nanocomposites studied (under nonequilibrium conditions). **(b)** Here, a molecule is depicted as a tunnel barrier of height Φ and length *d*, for clarity we picture electron tunnelling only (left). When a bias voltage is applied, the barrier is tilted (center). When $eV \geq \Phi$ the barrier becomes triangular and electrons tunnel by field emission (right).

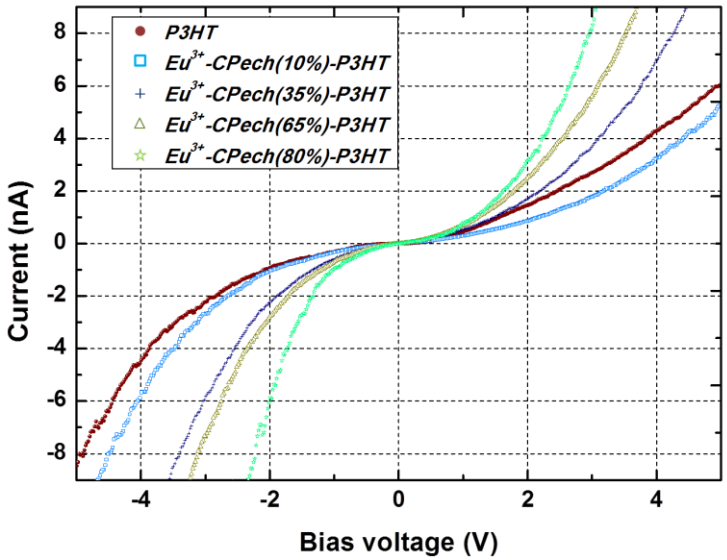

Figure 7.16. Current-voltage curves of Pt/*P3HT-ITO*/ITO, Pt/Eu^{3+}-*CPech1(10-80%)-P3HT*/ITO and *vice versa* obtained by the current-sensing atomic force microscopy technique.

Figure 7.16 shows the characteristics of the current (I) versus voltage (V) of the Pt/*P3HT-ITO*/ITO and Pt/ Eu^{3+}-*CPech1(10-80%)-P3HT* /ITO nanocomposites. The direct and inverse polarizations of the nanocomposite show nonequivalent behaviour. The asymmetrical nature of the curves is attributed to the difference in the work functions of the electrodes, implying different barriers at each electrode/polymer interface. In positive values of the axes, curves were lower than in negative values of the axes. This effect could be associated to the higher work function of the Pt compared to that of the ITO ($5.6(\Phi_{Pt}) > 4.7(\Phi_{ITO})$). Furthermore, the

different nanocomposites showed different I-V curves. The current rose at a lower voltage when the weight percentage of Eu^{3+}:La_2O_3 nanoparticles was higher.

These differences between them can be attributed to a thinner polymer film due to the higher percentage of nanoparticles. In fact, when we increase the wt% of nanoparticles, we are decreasing the wt% of P3HT of the nanocomposite because we used the same amount of solution (0.2 ml) to fabricate every nanocomposite independently of the wt% nanoparticles used and they occupied a certain volume which was not occupied by the polymer. Parker et al. observed differences between MEH-PPV nanocomposites changing the thickness of the polymer layer [268]. They demonstrated that the I-V characteristics depend, not on the voltage as for conventional nanocomposites, but instead on the electric-field strength. The thickness of the polymer was then obtained by scrapping off part of the thin polymer film, and using the atomic force microscopy in tapping work mode. The results obtained from the nanocomposites showed different thickness: 100, 115, 97, 75, 60 nm for the *P3HT-ITO*, *Eu^{3+}-CPech1(10%)-P3HT*, *Eu^{3+}-CPech1(35%)-P3HT*, *Eu^{3+}-CPech1(65%)-P3HT*, and *Eu^{3+}-CPech1(80%)-P3HT* samples, respectively, as expected. The thicknesses almost totally agreed with the I-V curves, unless the thickness taken for the *P3HT-ITO* and *Eu^{3+}-CPech1(10%)-P3HT* samples. Since spin coating is considered a very good technique to fabricate thin films with a good control of their thickness, the differences in the thickness of the samples might be attributed to the space of volume that nanoparticles are occupying: the higher the percentage of nanoparticles, the thinner the films were. Another reason could be the lack of precision of measuring the thickness by scrapping the samples.

The representation of current (I) versus the electric field strength (F) can be observed in Figure 7.17. While this plot can be drawn for either positive or negative voltages, conventionally [27], the positive half of the I-V characteristics was chosen. This corresponds to a *scenario* where the negative voltage is applied to the cantilever tip. Considering the thickness of each nanocomposite, the curves showed less significant differences between them. However, the *P3HT-ITO* nanocomposite appeared quite different, because it presented a lower slope than the other curves corresponding to the nanocomposites containing nanoparticles.

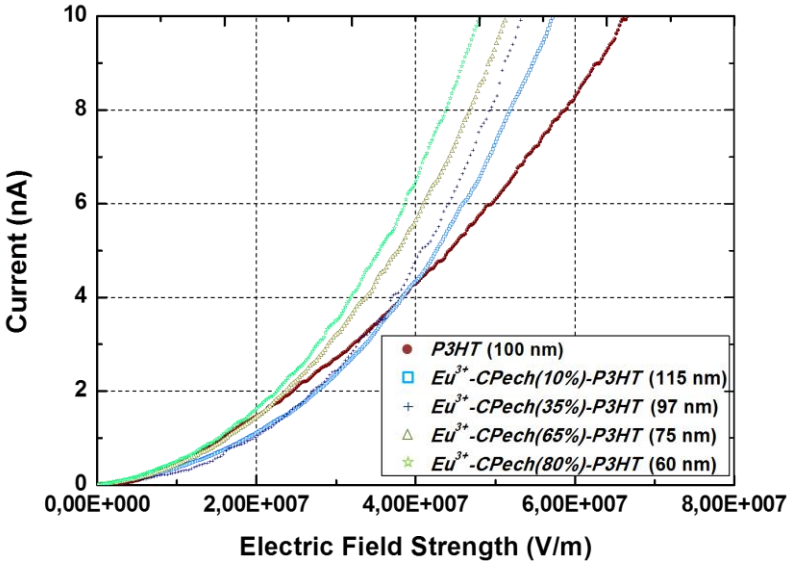

Figure 7.17. I-F characteristics taking into account the different thickness of the nanocomposites.

Figure 7.18 shows the current-voltage characteristics in a logarithmic scale. We observed two linear regions with different slopes (α). At low voltages (V < 1 V) the slope was about 1, suggesting an Ohmic behaviour. At higher voltages the slope tended to increase to a value around 2-2.5. If the slope is greater than 2, it indicates the existence of traps within the bulk of the organic semiconductor. This power dependence of current on voltage is typical of space charge limited mechanism [262].

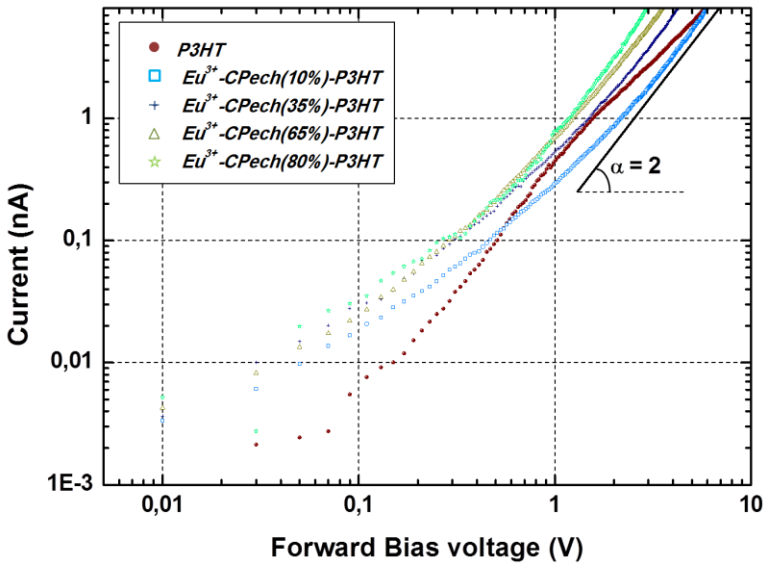

Figure 7.18. I-V curves in log-log scale for hole injection through the ITO/P3HT interface. The angles (α) correspond to the slope that forms the tangent of the curve with the horizontal.

Fowler-Nordheim (FN) plots were used to estimate the position of the molecular orbital closest to the Fermi level. However, by performing transition voltage spectroscopy (TVS), technique which has been established recently, it was not possible to directly determine the identity of the closest molecular orbital. TVS of Pt/*P3HT-ITO*/ITO and vice versa was analyzed by plotting a FN curve, $\ln(I/V^2)$ against $(1/V)$. These curves are shown in Figure 7.19(a-b). All the curves exhibited a clear minimum, called transition voltage (V_{trans}), which is expected to indicate, approximately, the energetic separation between the Fermi level and the closest molecular orbital.

The results of the V_{trans} were 2.19, 3.12, 2.53, 2.07, and 1.84 V for Pt/*P3HT-ITO*/ITO, Pt/*Eu^{3+}-CPech1(10%)-P3HT*/ITO, Pt/*Eu^{3+}-CPech1(35%)-P3HT*/ITO, Pt/*Eu^{3+}-CPech1(65%)-P3HT*/ITO, and Pt/*Eu^{3+}-CPech1(80%)-P3HT*/ITO, respectively. For the reverse case the V_{trans} results were 1.98, 2.11, 2.07, 1.61, and 1.1 V for ITO/*P3HT-ITO*/Pt, ITO/*Eu^{3+}-CPech1(10%)-P3HT* /Pt, ITO/*Eu^{3+}-CPech1(35%)-P3HT*/Pt, ITO/*Eu^{3+}-CPech1(65%)-P3HT*/Pt, and ITO/*Eu^{3+}-CPech1(80%)-P3HT*/Pt, respectively. The results were in good agreement with the different height barrier, which needs to be broken by the charge transport mechanisms [9,24]. So, the V_{trans} values were lower in the ITO/sample/Pt nanocomposites than in the Pt/sample/ITO nanocomposites. In the case of P3HT FN representation, it was quite different with respect to the other ones because it had two minimum peaks. We took into account the minimum at lower voltages.

Fig. 7.20(a) and (b) show a AFM topography image of the *Eu^{3+}-CPech1(65%)-P3HT* sample and the current mapping image, respectively. On the one hand, the topography image showed significant topographic changes due to the Eu^{3+}:La_2O_3 nanoparticles dispersed into the P3HT polymeric matrix. On the other hand, the current mapping showed that the current was homogeneously distributed throughout the film surface, just increasing its intensity at the edge of every nanoparticle. When both measurements topography and current mapping, were plotted together, we observed a total correlation between the peaks (see Figure 7.20(c)). This means that at the edge of the nanoparticles, the intensity of the current was about 300 times higher than at the polymeric surface. These results agreed with the thickness-current relationship studied above (at thinner thicknesses of the layer more intense current). Thus, on one hand we could attribute the increase of the current to the polymer thickness, that we assume is thinner on the nanoparticle surface than in direct contact with the ITO substrate. On the other hand, we could attribute the higher intensity of the current to a better electric contact between the tip and the surface of the sample.

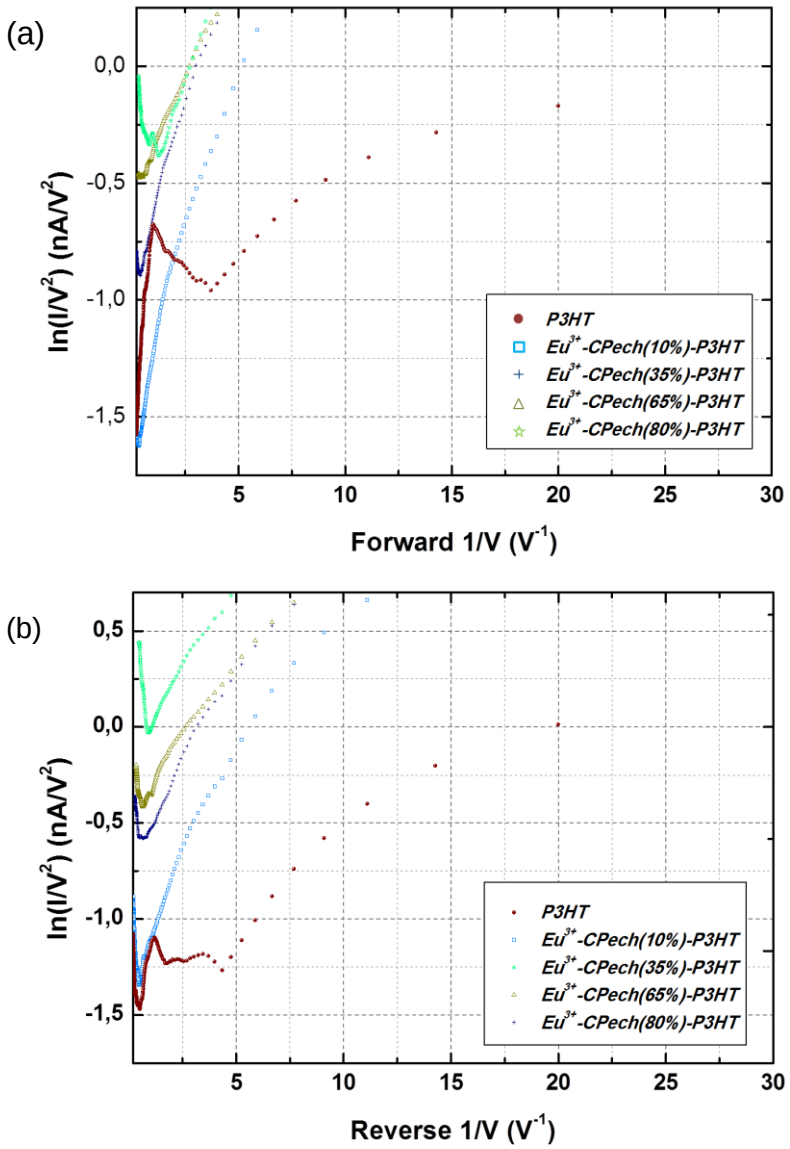

Figure 7.19. Fowler-Nordheim plots for the tunnelling of electrons **(a)** from ITO into the *Eu*$^{3+}$-*CPech1(10-80%)-P3HT* sample and **(b)** from Pt into the *Eu*$^{3+}$-*CPech1(10-80%)-P3HT* sample.

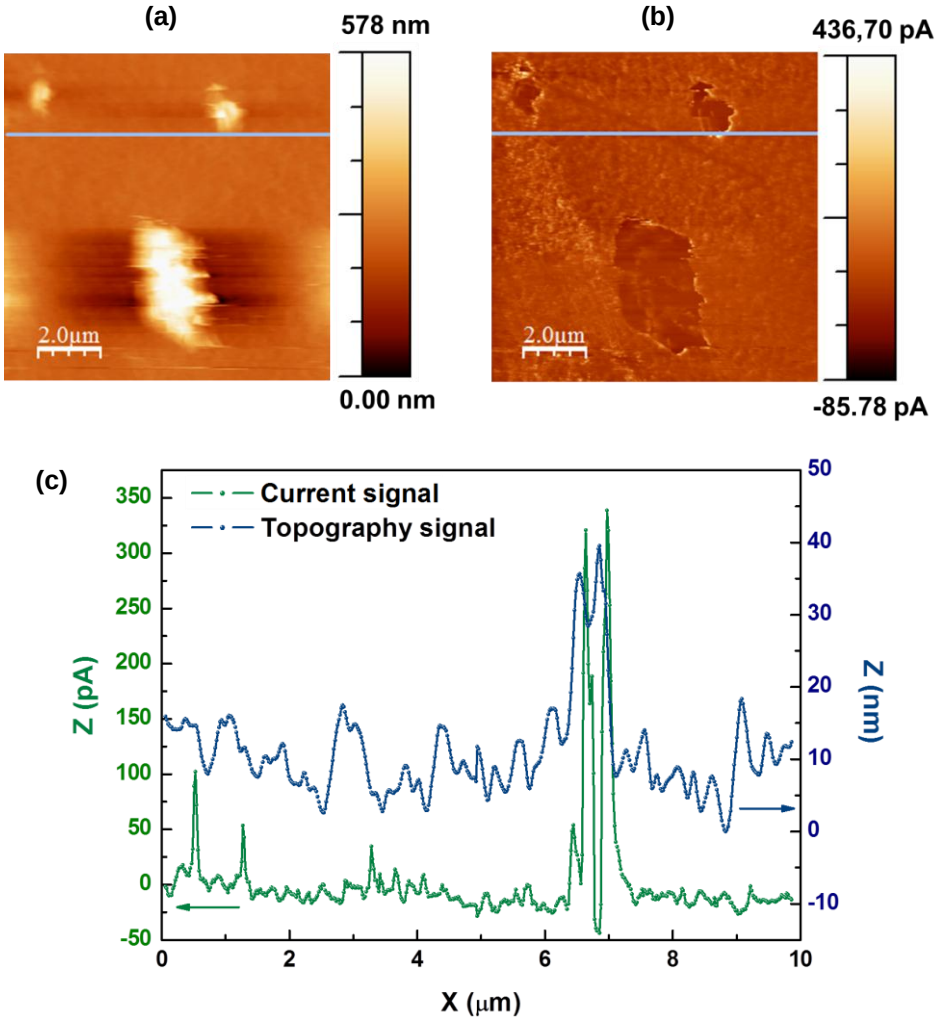

Figure 7.20. (a) AFM topography and **(b)** AFM current mapping of the *Eu*$^{3+}$*-CPech1(65%)-P3HT* sample. **(c)** AFM topography (blue line-right scale) and current (green line-right scale) profiles corresponding to the images shown in (a) and (b) (sky blue line), respectively.

7.4. Fabrication and characterization of disordered macroporous silicon templates

Macroporous silicon templates were prepared by electrochemical etching in hydrofluoric acid (HF) solution. This method is based on growing pores randomly on a flat polished silicon wafer by HF electrolyte. The surface of the silicon wafer is in contact with a solution containing HF and with the anode (in that case Au deposited by the sputtering technique) on the back side. After applying a voltage (in the right direction) between the wafer backside

contact and an electrode in the solution, the pore growth by the silicon dissolution starts. A general scheme of the process is shown in Fig. 7.21.

In order to prepare porous silicon, the current at the silicon/electrolyte interface must be carried by holes, injected from the bulk towards the interface. The current must be kept between zero and the electropolishing threshold and if the current exceeds the electropolishing threshold, the anodization results in progress. This limit depends on the etching parameters and wafer doping.

The global anodic semi-reaction during pore formation can be written as:

$Si + 6HF \rightarrow H_2SiF_6 + H_2 + 2H^+ + 2e^-$

H_2SiF_6 is the final and stable product for silicon in HF (or some of its ionized forms). It follows that during the pore formation only two of four available silicon electrons participate in an interface charge transfer while the remaining two participate in hydrogen formation (bubbles).

Pores grow preferentially along the [100] direction and the silicon dissolution occurs mainly at the pore tips, where enough holes are available, making the dissolution process to progress only towards the tips of the pore (Fig. 7.21).

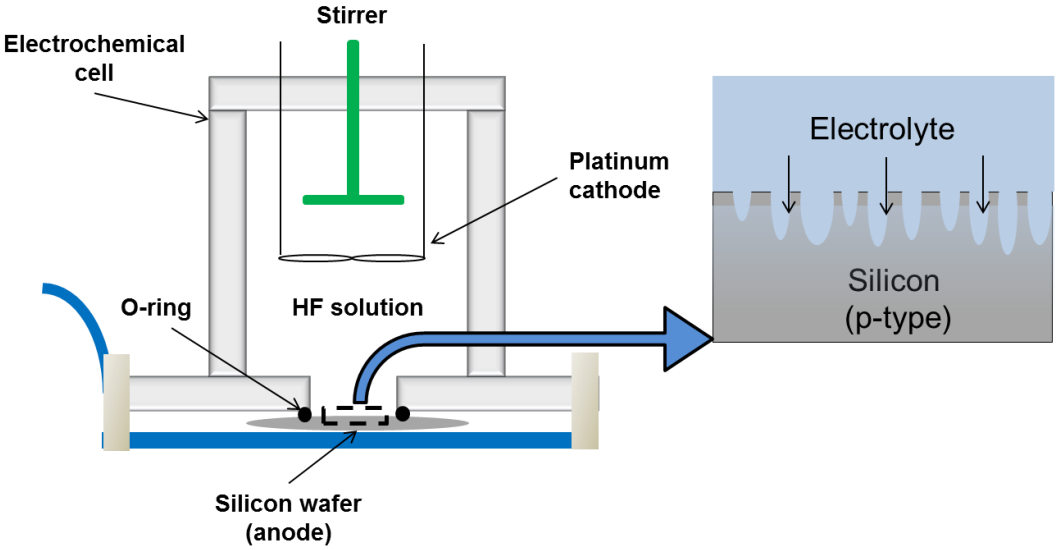

Figure 7.21. Scheme of the electrochemical cell for porous silicon template fabrication.

The most important parameters that determine the characteristics of porous silicon obtained by electrochemical etching are: the doping of the silicon wafer (type and resistivity), the electrolyte composition, the current density across the wafer and the time of current application [269-270].

The silicon wafers used in this work for macroporous template fabrication were p-type (boron doped) with (100) orientation. The thickness of the wafers was between 330 and 430 μm and the resistivity was between 10 and 30 Ω·cm.

The silicon porous templates fabricated were characterized by ESEM (see Fig. 7.22(a-b)). The pores on the surface appeared randomly disordered with about 2 μm of diameter and 10 μm of pore depth. In Fig. 7.22(a), the different black-grey tonality corresponded to a different pore depth: the darker the colour, the deeper the pore was.

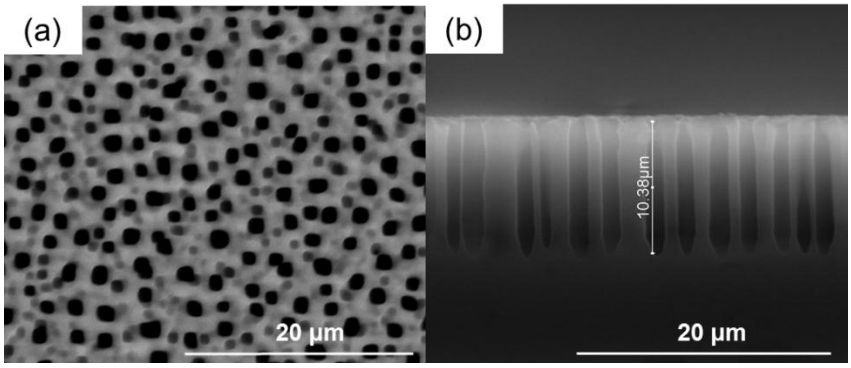

Figure 7.22. ESEM images of disordered macroporous silicon, **(a)** top view showing pores with about 2 μm of diameter and **(b)** cross-section showing pores with 10 μm of depth.

7.5. Fabrication and characterization of structured P3HT-based nanocomposites

Two different ways of preparation were carried out for the fabrication of structured P3HT-based nanocomposites (Fig. 7.23). In one case we proceed as in the non-structured nanocomposite film fabrication process. Thus, first the organic solutions which contained the Eu^{3+}:La_2O_3 nanoparticles and the polymer were mixed. Then, after stirring this solution for several hours, it was added onto the silicon porous template drop by drop and letting the volatile organic solvent to evaporate (Fig 7.23, left hand). In order to facilitate the entrance of the solution inside the pores we applied vacuum at the bottom of the template. Another way of preparation was similar to the previous one, but this time, the solution containing the nanopowder was introduced into the silicon pores separately from the polymeric solution (Fig 7.23, right hand). Polymer solutions have generally a high viscosity, leading to the formation of more particle aggregates. By using this second way of preparation we tried to avoid this effect.

Finally, the last step consisted on removing the silicon template from the nanocomposite. Thus, the nanocomposite still with the silicon template was introduced into an aqueous solution of potassium hydroxide (KOH, 40%) previously prepared. After stirring overnight, the silicon was completely removed.

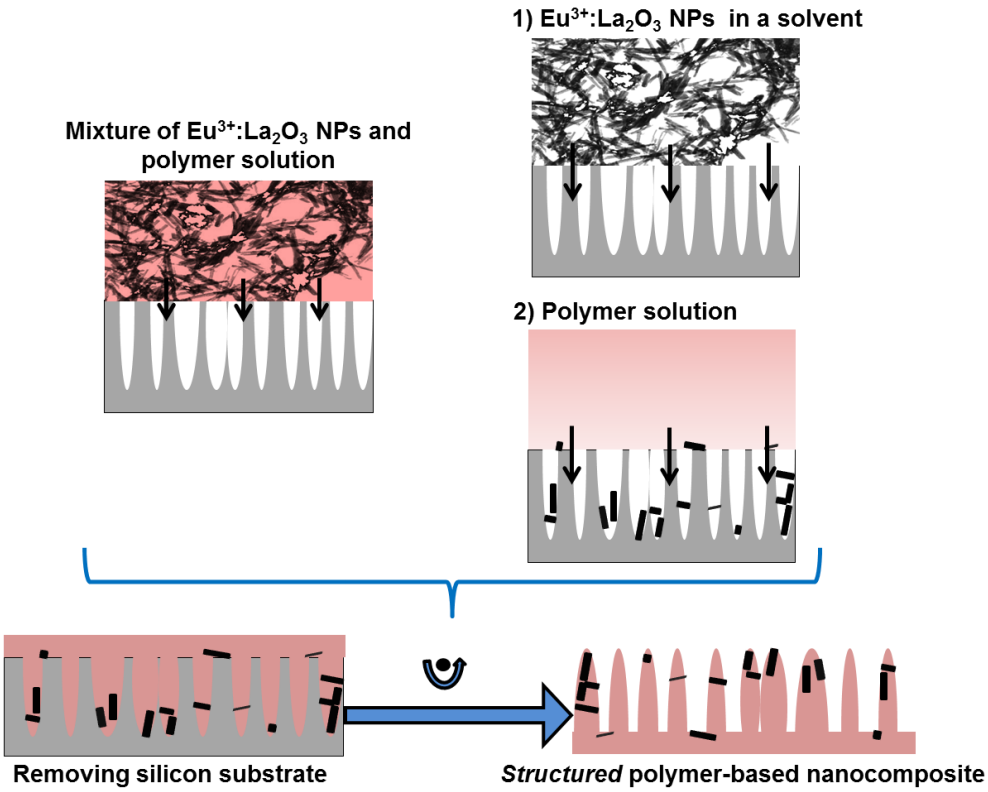

Figure 7.23. Scheme showing the two different ways of preparation used to fabricate structured P3HT-based nanocomposite samples.

One sample was successfully fabricated by the first process of synthesis, as observed in Fig. 7.24(a-d). ESEM images showed micropillars with sizes about 11 μm in length and1.5 μm in diameter (Fig. 7.24(b-c)). The micropillars were aggregated on their tips forming small groups. This fact might be caused by electrostatic charges, very common in nanowire shaped materials. Additionally, due to that some pores were not fully developed by electrochemically etching (Fig 7.24(a)), some micropillars were very short. Using a back scattered electron detector, we had the chance to observe differences in the images depending on the atomic weight of the elements. However, it was difficult to assure if the nanoparticles were inside the micropillars.

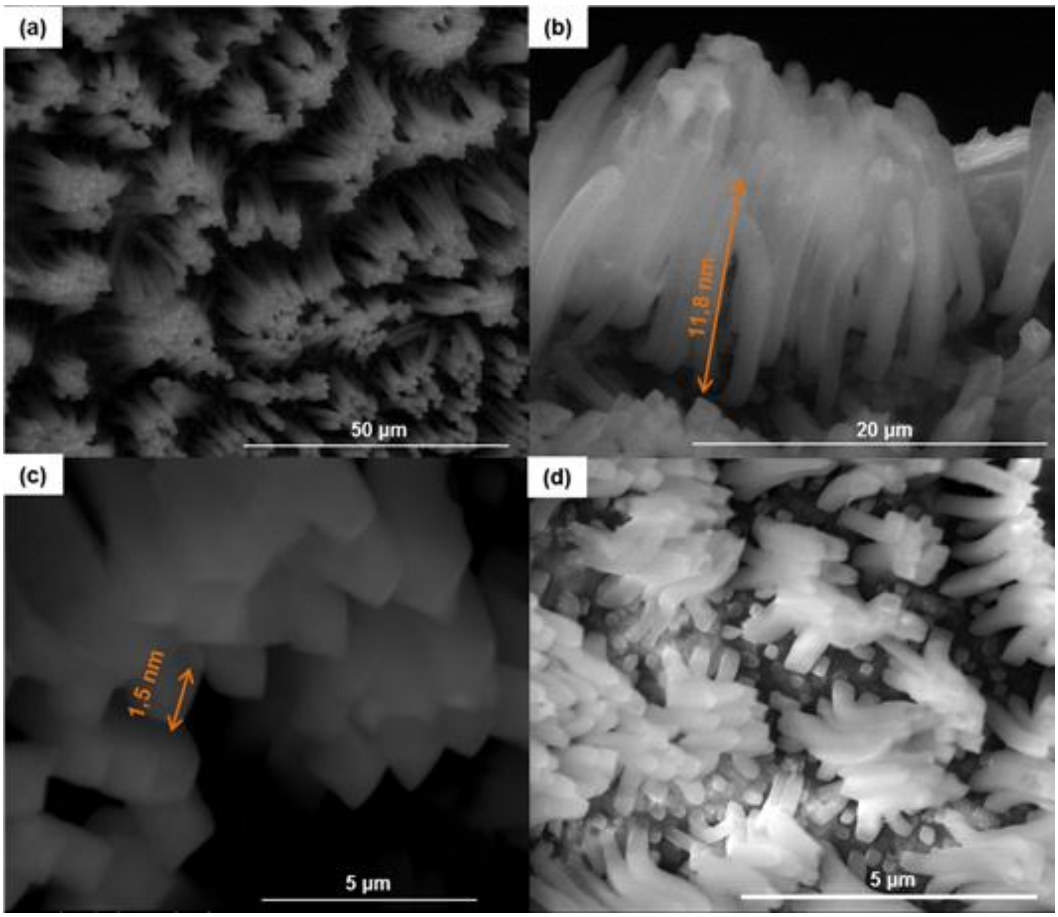

Figure 7.24.(a-d) ESEM images of the structured P3HT-based nanocomposite sample fabricated by introducing a solution containing the polymer and the nanoparticles into the Si template.

In order to corroborate whether the nanoparticles were inside the micropillars, the sample was observed by TEM. Fig. 7.25(a-b) show that the majority of the nanoparticles were at the base but not inside the pillars, what meant that the nanoparticles were not entering together with the mixed solution inside the silicon porous template. The aggregate sizes could be the main reason to difficult the entrance of the nanoparticles in the pillars. Micropillars also showed some nanoparticles at their tips but looking more carefully at their morphologies they might be some silicon particles which were not removed during the substrate dissolution step with KOH (Fig. 7.25(c-d)).

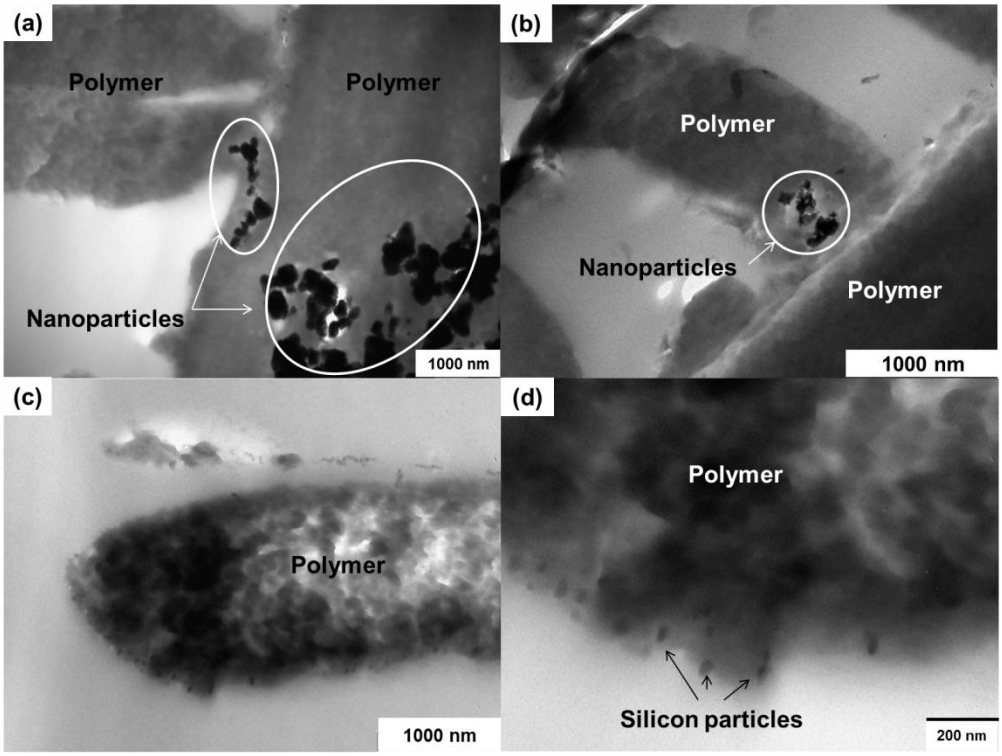

Figure 7.25.(a-d) TEM images of the structured P3HT-based nanocomposite sample fabricated by introducing a solution containing the polymer and the nanoparticles into the Si template.

The samples prepared by the second procedure were characterized by ESEM. Figure 7.26(a-d) shows the silicon porous template after wetting with the dispersed nanopowder solution. The top views showed some pores with particles inside them (Fig. 7.26(a-b). However, cross section images showed that most of the particles remained on the surface (Fig. 7.26(c)), and only a few single particles were at the bottom of the silicon pores (Fig. 7.26(d)).

From these images we concluded that de-agglomeration of the nanoparticles was required in order to fabricate the P3HT-based nanocomposites. However, we did not performed these experiments.

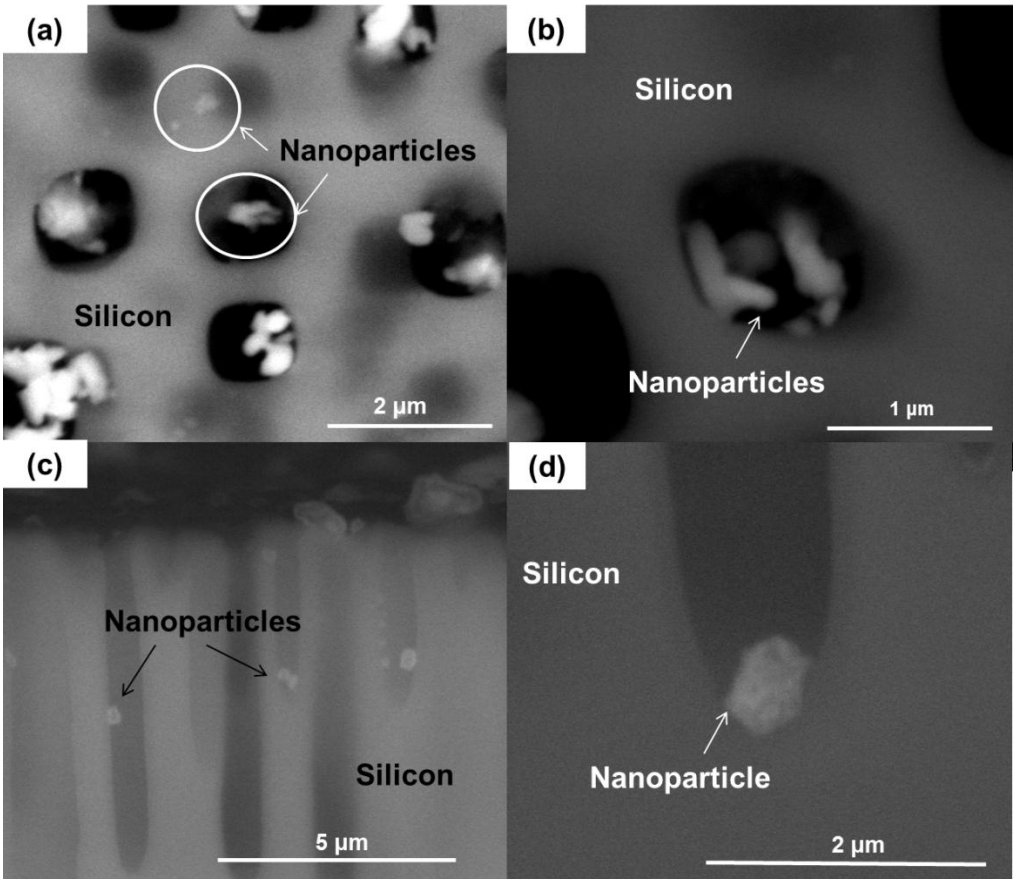

Figure 7.26.(a-d) ESEM images of the Eu^{3+}:La_2O_3 nanoparticles introduced inside the silicon porous template.

Chapter 8

Fabrication and characterization of bulk heterojunction organic and hybrid solar cells

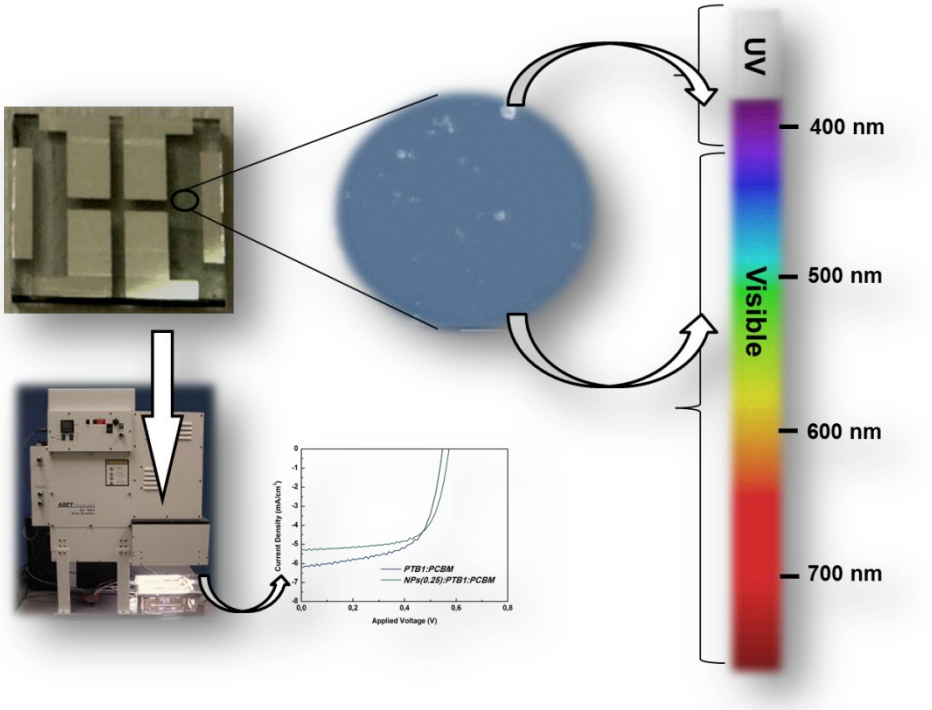

In this chapter, the down-shifting properties of the Eu^{3+} doped lanthanum compounds are tested in bulk heterojunction (BHJ) polymer-fullerene photovoltaic cells. The fabrication and the characterization of the bulk heterojunction organic and hybrid solar cells based on polymer-fullerene and nanoparticles are explained. The Eu^{3+}:La_2O_3 and Eu^{3+}:La_2O_2S nanoparticles have been embedded into P3HT:PCBM and PTB1:PCBM-based solar cells. The characterization is basically focused on the energy conversion efficiency of the devices. Thus, a solar simulator with the appropriate filters has been used for such studies.

8.1. Overview

Since the first modern silicon p-n junction solar cell was invented at Bell labs [271] in 1954, many attempts have been focused to obtain high efficiency low-cost solar cells but it was not until 2006, that the "40% efficient barrier" was broken [272]. However, in parallel to such development, many other researches have gone beyond the inorganic world and have been attracted by the organic photovoltaic (OPV) solar cells.

Despite their low efficiency, the devices made from organic semiconductors have shown promise for future commercialization due to their low cost, easy and large-area fabrication from a simple solution, mechanical flexibility, and small environmental impact compared to silicon and heavy metal based semiconductors [16-19]. Organic semiconducting polymers have been also used in organic light-emitting diodes (OLEDs) [273], printed electronic circuits [274], biosensors [275] and supercapacitors [276].

In the OPV solar cells, the electron donor is a semiconducting polymer and together with the electron acceptor forms the active layer. This layer is the responsible for absorbing the light from the Sun and is where the photon transformation into free charges takes place. The morphology of the active layer has become an important issue [29] and different structures such as single layers and double layers have been designed [25]. However, the bulk heterojunction (BHJ) structure has shown the best results in terms of efficiency [26]. In the case of a BHJ cell, the donor and acceptor have a higher interfacial area for exciton dissociation in comparison to the single and double layer cells and that increases the efficiency of the devices [30]. In addition, the structured BHJ, also known as "ordered BHJ", has been proposed [277]. In such a structure, polymer and acceptor have straight pathways towards the electrodes to reduce carrier recombination and increase charge collection efficiency. However, the efficiency of these structured cells is currently low and one of the challenges to improve their efficiency includes the formation of nanostructured porous materials such as those studied in Chapter 7. Several fabrication methods such as spin-coating, doctor blading, ink jet printing, etc. have been used in the OPV solar cells fabrication.

Several organic semiconducting polymers have been used as electron donor in the fabrication of OPV solar cells [29]. Figure 8.1 shows the chemical structure of some representative semiconducting polymers: MEH-PPV, P3HT, PFO-DBT and PCDTBT. Recently, low bandgap polymers, are also under investigation for OPV solar cells [258]. Fig. 8.1 also shows the chemical structure of some representative low bandgap polymers: PTB1, PCPDTBT and PCPBBT.

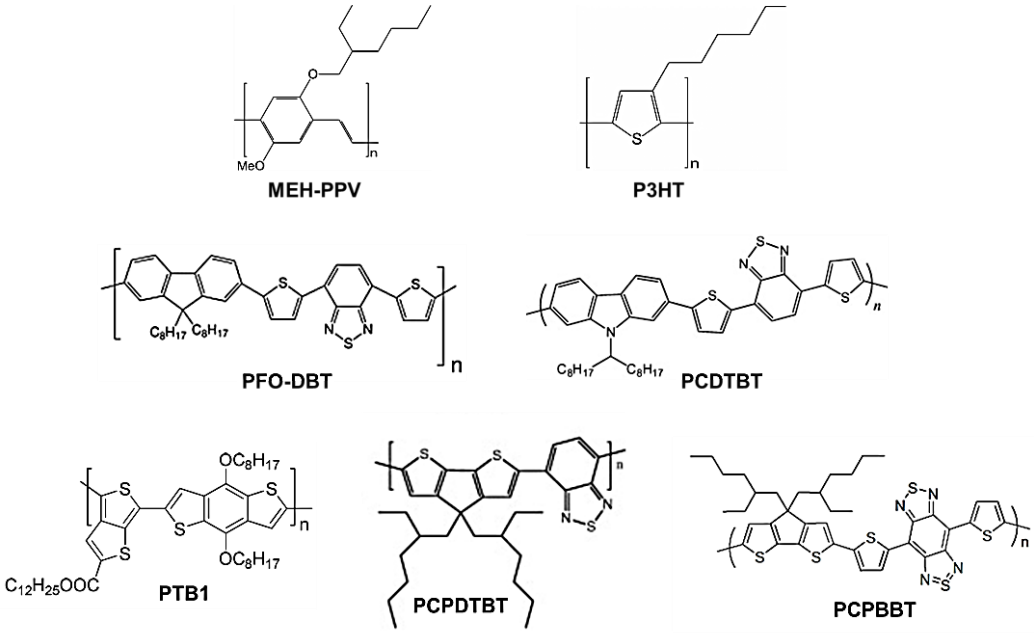

Figure 8.1. Example of some organic electron donors used in polymer solar cells.

Among the electron acceptor materials used, there are polymers like CN-MEH-PPV, F8BT, and small molecules (fullerenes), C_{60} and soluble derivatives of C_{60} and C_{70} namely $PC_{60}BM$ and $PC_{70}BM$ [29]. Fullerenes are considered to be the best electron acceptor for polymer solar cells so far mainly because the photoinduced charge transfer between the donor polymers and fullerenes is ultrafast (~45 fs) [14], which becomes very important to obtain higher power conversion efficiencies (PCE). That is because fullerenes have an energetically deep-lying low unoccupied molecular orbital (LUMO) [31] which endows the molecule with a high electron affinity. The triply degenerate LUMO of fullerenes also allows the molecule to be reversibly reduced with up to six electrons, illustrating its ability to stabilize negative charge [31]. The chemical structures of the electron acceptor materials are shown in Figure 8.2.

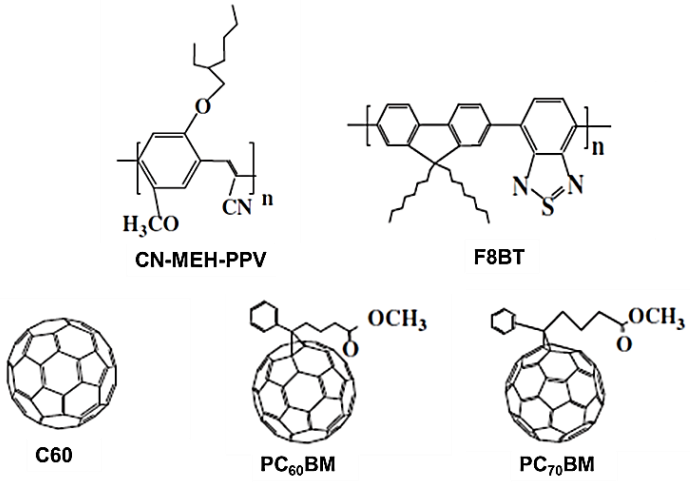

Figure 8.2. Example of some organic electron acceptors used in polymer solar cells.

The full names of the above representative organic materials are:

MEH-PPV: poly[2-methoxy-5-(2'-ethyl-hexyloxy)-1,4-phenylene vinylene].

P3HT: poly(3-hexylthiophene).

PFO-DBT: poly[2,7-(9,9-dioctyl-fluorene)-alt-5,5-(4,7'-di-2-thienyl-2',1',3'-benzothiadiazole).

PCDTBT: poly[N-9'-hepta-decanyl-2,7-carbazole-alt-5,5-(4',7'-di-thienyl-2'1',3'-b3nzothiadizaole)].

PTB1: poly(thienothiophene-benzodithiophene).

PCPDTBT: poly[2,6-(4,4-bis-(2-ethylhexyl)-4H-cyclopenta[2,1-b;3,4-b']-dithiophene)-alt-4,7-(2,1,3-benzothiadiazole)].

PCPBBT: poly[2,6-(4,4-bis(2-ethylhexyl)-4H-cyclopenta[2,1-b;3,4-b']dithiophene)-alt-5,5-(4,8-di-2-thienyl-2$\lambda^4\delta^2$-[1,2-c:4,5-c']bis[1,2,5]thiadiazole.

CN-MEH-PPV: poly-[2-methoxy-5,2'-ethylhexyloxy]-1,4-(1-cyanovinylene)-phenylene.

F8TB:poly(9,9'-dioctylfluorene-co-bis-N,N'-(4-butylphenyl)-bis-N,N'-phenyl-1,4-phenylenediamine.

PC60BM: 6,6-phenyl-C61-butyricacidmethylester.

PC70BM: 6,6-phenyl-C71-butyricacidmethylester.

In this thesis, we used the P3HT:PC60BM (P3HT:PCBM) and PTB1:PC60BM (P3HT:PCBM) active layers with the BHJ structure. The P3HT:PCBM is the active layer most studied up to now for the fabrication of organic and hybrid solar cells [29]. Recently, W. Ge [278] reported a PCE as high as 5% for a P3HT:PCBM-based OPV cell, which is an unusual efficiency in cells made of organic materials. However, it is still very far from the efficiencies obtained in cells based on silicon. In order to increase such efficiencies, many reports are focused on the study of different parameters such as the morphology [279], the concentration ratio between the P3HT and PCBM [279], the effect of thermal and solvent

annealing [280], and the comprehension of the carrier transport [281]. Some remarkable results have been found when applying an annealing treatment of 423 K for 10 min because the PCE increases from 0.34% for the untreated cell to 2.8% for the annealed cell [282]. Other studies revealed that the best PCE is found for P3HT:PCBM-based cells with 1:1 concentration in weight, in comparison to that obtained for systems with 1:0.5 and 1:2 concentrations. However, Ma et al. [283] were more precise and found 1:0.8 the best ratio and the chlorobenzene the best organic solvent. The organic solvent to prepare the blend causes differences purely morphological as has been proved spectroscopically [29].

Other attempts of improving the efficiency of the P3HT:PCBM-based solar cells has been the use of inorganic nanoparticles. For instance, using monodisperse Cu_2S nanodisks, the efficiency of the hybrid device increases by 22.7% compared to that obtained in pure P3HT:PCBM–based solar cells [284]. The reason is that Cu_2S nanodisks improve the electronic mobility of the system. Nam et al. [285] used a layer of PbSe nanoparticles coupled with the organic blend and the efficiency increased by 31%. These nanoparticles provide a broad-range photon harvesting ability and an efficient charge transportation. Many other examples using FeS_2, TiO_2, ZnO, etc., are found in the literature [286-288]. While FeS_2 nanoparticles can efficiently improve charge transport and exciton dissociation of P3HT:PCBM solar cells, TiO_2 and ZnO can act as a metal oxide buffer layer between the active layer and the cathode. Qian et al. [288] speculated that the ZnO layer prevents diffusion of cathode atoms into the active layer and that it also has the potential to improve the environmental stability of the OPV. Apart from these inorganic materials, the presence of other nanoparticles such as amorphous Si nanocones [289] and Au [290] has also advantages for P3HT:PCBM solar cells. Si nanocones extend the absorption to near infrared and solve the difficulty of carrier transport forcing the holes move to the anode and electrons move to the cathode, with that, Pei et al. [289] observed that the power conversion efficiency was increased from 1.73% to 2.22% (28% enhancement). Au nanoparticles exhibit localized surface plasmon resonances which offer the possibility of enhanced absorption and enhanced photogeneration of mobile carriers. In terms of efficieny, Wang et al. [291] reported that by using Au nanoparticles in a P3HT:PCBM system, the efficiency increased from 3.54% to 4.36%. Furthermore, semiconductor materials with very small sizes (quantum dots, QDs) such as CdSe [292] and CdS [293] have been also introduced in P3HT-based systems to act as electron acceptors. They have useful absorption in the visible region, appopiate energy levels when coupled with most conjugated polymers and well established synthesis methods. The PCEs by using CdSe and CdS QDs in P3HT-systems range around 2% and 4%, respectively [292,293].

The use of lanthanide (Ln^{3+}) ions in silicon solar cells [8,294] and dye sensitized solar cells (DSSC) [295] has been investigated. Nevertheless, their use in OPV cells has not attracted many researchers.

The other active layer used has been the PTB1:PCBM in the BHJ structure. The PTB1 polymer is considered a low bandgap polymer [250]. In general, the low bandgap polymers have been used recently because of the necessity to increase the efficiencies of the OPV cells together with the necessity to reduce the relatively large bandgap and high HOMO energy level of polymers such as P3HT, which limit the possibility of further improving the device performance. The PCE reported up to now for the PTB1:PCBM system is 4.76%, however it reaches 5.6% when using $PC_{70}BM$ instead of $PC_{60}BM$ [282]. In addition, low bandgap polymers show a wide absorption band centered between the 600-700 nm region of the electromagnetic spectrum [250] which make them to be a suitable electron donor in our hybrid solar cells since the maximum emission of the Eu^{3+} doped lanthanum compounds nanoparticles is within such region [103]. Very few works with PTB1:PCBM system have been reported and from our best knowledge, there are no works related with the introduction of nanoparticles in the PTB1:PCBM-based solar cells.

8.2. Fabrication of the bulk heterojunction organic and hybrid solar cells

In Chapter 7 we observed how the different polymers absorb the light emitted by the Eu^{3+} doped lanthanum compound particles but an approach of the use of these nanoparticles in a photovoltaic system as down-shifting material is exposed throughout this chapter. Thus, here, we explain the fabrication of two different types of bulk heterojunction (BHJ) organic and hybrid solar cells. One type was made of P3HT:PCBM blend for the organic cell and using Eu^{3+}:La_2O_3 nanoparticles for the corresponding hybrids. Those devices were fabricated in collaboration with the Institute of Chemical Research of Catalonia (ICIQ). The other type was made of PTB1:PCBM blend and using Eu^{3+}:La_2O_2S@APTMS nanoparticles.

Figure 8.3 shows a schematic diagram for the fabrication process of BHJ organic and hybrid solar cells.

1) The first step consisted in cleaning the indium tin oxide (In_2O_3(90%)SnO_2(10%), ITO) coated glass substrates. The ITOs purchased by Ikerlan Co. had an area of 15×15 mm^2 and were covered by a photo-resin which was removed by rinsing the films in acetone followed by an ultrasonic bath for 5 min in acetone. Afterwards, two consecutive ultrasonic baths of 10 min in isopropyl alcohol were applied. The substrates were dried with the help of an air stream and placed on an oven at 353 K during 10 min in order to dry them completely. Finally, for the case of P3HT:PCBM-based photovoltaic (PV) devices, the ITO conductive layer was exposed to an ozone-containing atmosphere for 30 min in order to remove the organic remainings.

2) The second step was the deposition of the intermediate layer (IL): PEDOT:PSS. For that purpose, a solution of the copolymer mixture (PEDOT:PSS) was diluted with isopropyl alcohol (IPA) 4:1 in weight, respectively. The mixture was stirred vigorously to its previous

use during at least 30 min in dark conditions, after which it was filtered using acetate cellulose filters of 0.2 μm diameter pores. The spin coating was performed using 8 drops of the PEDOT:PSS:IPA mixture, and the spin coating conditions were first 4400 rpm for 30 s followed by 30 s at 3500 rpm. With these conditions, the IL had a thickness of ~30 nm. The IL was deposited in atmospheric conditions. In order to use the ITO as anode in the final device, the edges of the ITO coated glass substrates were discovered removing the PEDOT:PSS carefully by using water.

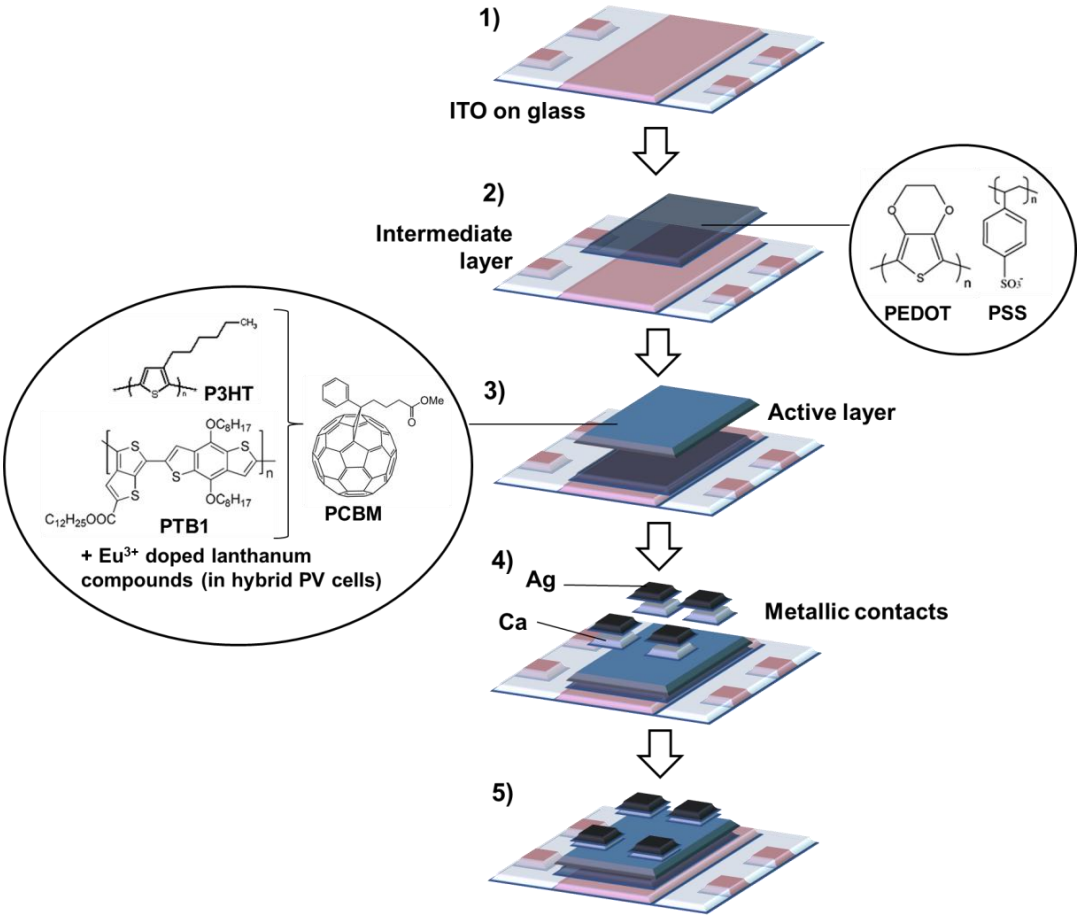

Figure 8.3. Schematic diagram for the fabrication of the BHJ organic and hybrid solar cells.

3) Then, two different solutions were prepared separately, one by mixing the P3HT and the $PC_{60}BM$ and the other by mixing the PTB1 and the $PC_{60}BM$ in an organic solvent and under nitrogen atmosphere. For the case of P3HT:PCBM-based devices, the concentration ratio was 10 $mg \cdot ml^{-1}$ of polymer and 8 $mg \cdot ml^{-1}$ of fullerene with chlorobenzene (CB) being the solvent used. In contrast, for the case of PTB1:PCBM-based devices, the concentration ratio was 15 $mg \cdot ml^{-1}$ of polymer and 15 $mg \cdot ml^{-1}$ of fullerene, using *orto*-dichlorobenzene (*o*-DCB) as

solvent. Table 8.1 shows the different organic and hybrid solar cells fabricated. The solutions containing the active layer were kept under vigorous stirring overnight.

For the P3HT:PCBM-based devices, the spin coating conditions were 75 µl of the mixture at 900 rpm for 3 min and for PTB1:PCBM-based devices were 70 µl of the mixture at 1000 rpm for 1.5 min. This latter polymer-fullerene blend was filtered with a 0.2 µm polytetrafluoroethylene (PTFE) filter before of being spin-coated. The amount of nanoparticles (Eu^{3+}:La_2O_3 or Eu^{3+}:La_2O_2S@APTMS) used in the devices is measured as percentage in weight with respect to the polymeric/fullerene blend. The edges of the devices were cleaned by CB solvent to discover the ITO. The following step for the P3HT:PCBM-based devices was an annealing treatment at 423 K during 15 minutes under nitrogen atmosphere.

Table 8.1. Materials used for the fabrication of BHJ organic and hybrid solar cells.

Sample	Polymer	Fullerene	Lanthanum compound nanoparticles	Solvent
P3HT:PCBM	P3HT	$PC_{60}BM$	-	CB
NPs(0.25):P3HT:PCBM	P3HT	$PC_{60}BM$	Eu^{3+}:La_2O_3	CB
NPs(0.5):P3HT:PCBM	P3HT	$PC_{60}BM$	Eu^{3+}:La_2O_3	CB
NPs(0.75):P3HT:PCBM	P3HT	$PC_{60}BM$	Eu^{3+}:La_2O_3	CB
PTB1:PCBM	PTB1	$PC_{60}BM$	-	*o*-DCB
NPs(0.25):PTB1:PCBM	PTB1	$PC_{60}BM$	Eu^{3+}:La_2O_2S@APTMS	*o*-DCB
NPs(0.5):PTB1:PCBM	PTB1	$PC_{60}BM$	Eu^{3+}:La_2O_2S@APTMS	*o*-DCB

CB: chlorobenzene (C_6H_5Cl). *o*-DCB: orto-dichlorobenzene ($C_6H_4Cl_2$).

4) Finally, 15 nm of calcium were deposited by evaporation under high vacuum followed by 150 nm of silver.

5) The final solar cell was obtained and was ready to be characterized (Figure 8.4).

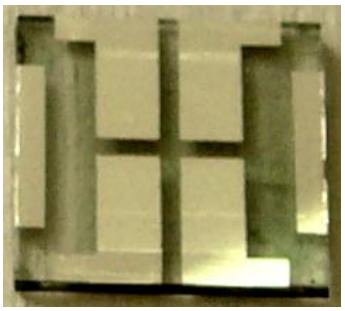

Figure 8.4. Photograph showing a representative final hybrid solar cell (*NPs(0.25):PTB1:PCBM).*

Two additional samples for the optical characterization were fabricated. Thus, two different films, one made of P3HT and another made of PCBM were spin-coated on ITO substrates and an annealing treatment of 423 K for 15 min was also applied to compare them with the corresponding blends. These samples were simply labelled as *P3HT* and *PCBM*.

8.3. Characterization of the bulk heterojunction organic and hybrid solar cells

Here, we present the optical characterization of the P3HT:PCBM-based cells and the photovoltaic characterization of the P3HT:PCBM and PTB1:PCBM-based cells. Therefore, power energy conversion efficiencies were measured for all the devices fabricated (PEC or η) and the incident photon-to-current conversion efficiency (IPCE), also known as external quantum efficiency (EQE), was measured for the case of P3HT:PCBM-based solar cells.

8.3.1. Characterization of *P3HT:PCBM* and *NP(x):P3HT:PCBM* (x=0.25, 0.5 and 0.75) solar cells

The absorption of the polymers used in this thesis was studied in Chapter 7. However, the active layers were fabricated by mixing those polymers with the $PC_{60}BM$ fullerene. Thus, to study the absorption effect of the PCBM in the active layer, the UV-Vis absorption spectra of *P3HT*, *PCBM*, *P3HT:PCBM* and *NPs(0.5):P3HT:PCBM* samples were recorded in the range between 250-800 nm. Figure 8.5 shows that the visible absorption between 400 and 650 nm was caused by the P3HT polymer whereas the absorption below 400 nm was caused by PCBM. Slight differences in the position of the maximum of the absorption band were observed between the *P3HT* sample and the *P3HT:PCBM* and *NPs(0.5):P3HT:PCBM* devices. However, these results were in good agreement with those obtained by other authors [29,296]. The modification of the absorption spectra for the samples containing PCBM can be attributed to the interaction between the polymer chains and the PCBM molecules, where the presence of PCBM molecules lowers the interaction among the P3HT chains upon an increased disordering in the blends.

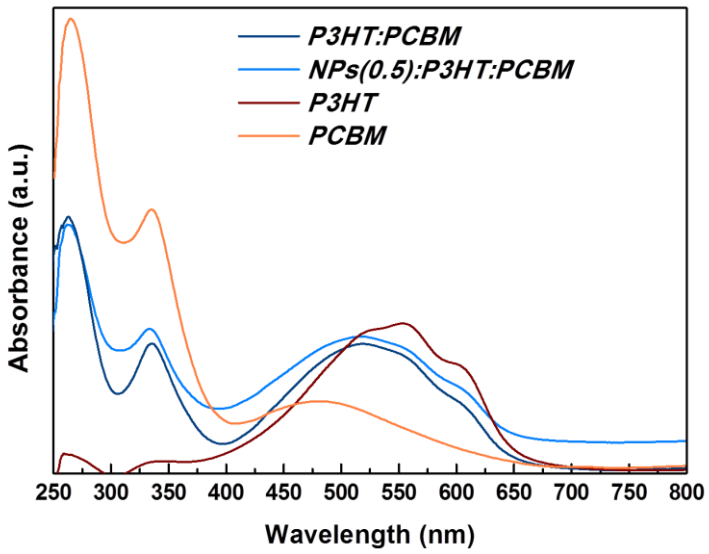

Figure 8.5. Absorption spectra of *P3HT:PCBM*, *NPs(0.5):P3HT:PCBM*, *P3HT* and *PCBM* samples.

The *P3HT:PCBM* and *NPs(x):P3HT:PCBM (x=0.25, 0.5 and 0.75)* samples were well characterized in collaboration with the Institute of Chemical Research of Catalonia (ICIQ).

Figure 8.6 shows the current-voltage characteristics of the *P3HT:PCBM* device measured in the dark and under simulated AM 1.5G illumination at 10 $mW \cdot cm^{-2}$ and 100 $mW \cdot cm^{-2}$. The photovoltaic performance of the device measured at 10 $mW \cdot cm^{-2}$ shows a short circuit current density (J_{sc}) of 0,8 $mA \cdot cm^{-2}$, an open circuit voltage (V_{oc}) of 0.55 V and a fill factor (*FF*) of 68.74%, resulting in a power conversion efficiency (*PCE*) of 3.35% (see Table 8.2). The photovoltaic performance of the device measured at 100 $mW \cdot cm^{-2}$ shows a short circuit current density (J_{sc}) of 5,7 $mA \cdot cm^{-2}$, an open circuit voltage (V_{oc}) of 0.62 V and a fill factor (*FF*) of 65.09%, resulting in a power conversion efficiency (PCE) of 2.6% (see Table 8.2). The PCE obtained can be considered low in comparison to other efficiencies reported [35,296]. For instance, Ge in 2009 [278] obtained a PCE of 5%, one of the highest efficiencies obtained in a P3HT:PCBM-based solar cell.

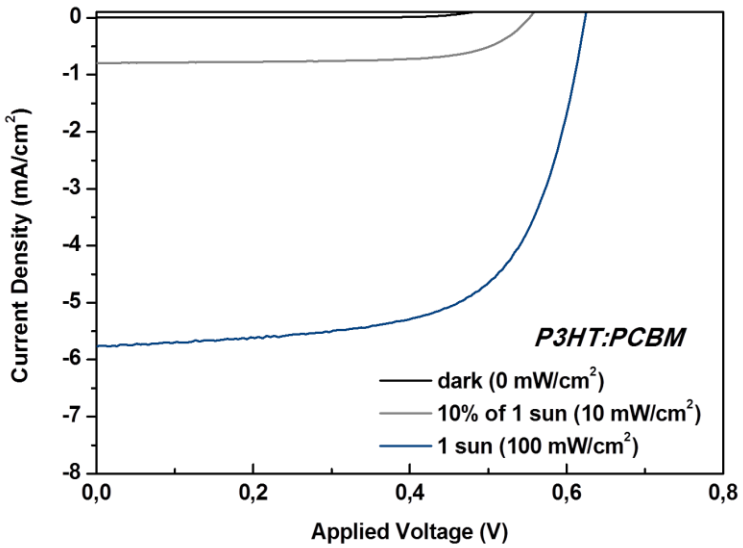

Figure 8.6. Current-voltage characteristics of the *P3HT:PCBM* device at dark and under simulated AM 1.5G illumination at 10 mW·cm^{-2} and 100 mW·cm^{-2}.

Table 8.2. Photovoltaic parameters for *P3HT:PCBM* sample under different illumination conditions.

Illumination Power	J_{sc} (mA·cm^{-2})	V_{oc} (V)	FF (%)	PCE (%)
10 mW·cm^{-2} (10% of 1 sun)	0.8	0.55	68.74	3.35
100 mW·cm^{-2} (1 sun)	5.7	0.62	65.09	2.60

The current-voltage and the incident photon-to-current conversion efficiency (IPCE) of the P3HT:PCBM-based solar cells is shown in Figures 8.7 and 8.8, respectively. Figure 8.7 shows the curves for *P3HT:PCBM*, *NPs(0.25):P3HT:PCBM*, *NPs(0.5):P3HT:PCBM* and *NPs(0.75):P3HT:PCBM* samples obtained under simulated AM 1.5G illumination at 100 mW·cm^{-2}. It is clearly observed that the higher the concentration of nanoparticles, the lower the J_{sc}, the V_{oc} and the FF. Consequently, the PCE were also lower when increasing the concentration of nanoparticles in the P3HT:PCBM-based hybrid devices. Table 8.3 lists the results obtained for these devices. Thus, the maximum PCE was 2.6% obtained for the P3HT:PCBM device and the minimum PCE was 0.28% obtained for the *NPs(0.75):P3HT:PCBM* device.

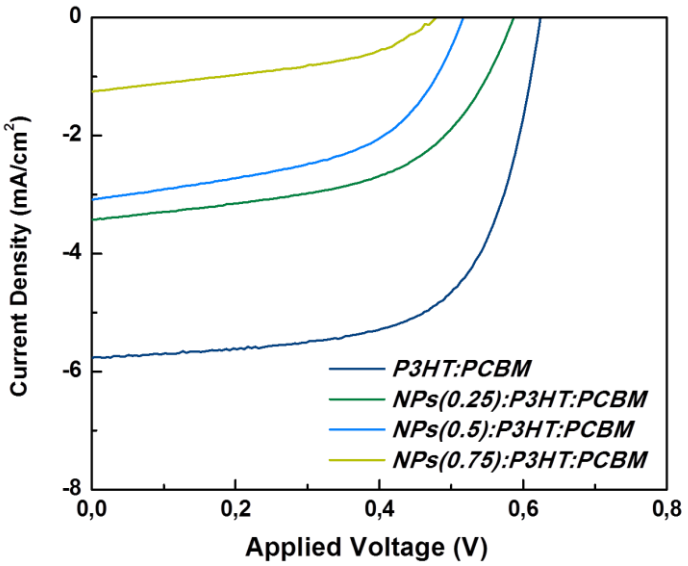

Figure 8.7. Current-voltage characteristics of the *P3HT:PCBM*, *NPs(0.25):P3HT:PCBM*, *NPs(0.5):P3HT:PCBM*, *NPs(0.75):P3HT:PCBM* solar cells.

Table 8.3. Photovoltaic parameters for *P3HT:PCBM* and *NPs(x):P3HT:PCBM* (x=0.25, 0.5 and 0.75) samples.

Sample	J_{sc} (mA·cm^{-2})	V_{oc} (V)	FF (%)	PCE (%)
P3HT:PCBM	5.7	0.62	65.09	2.6
NPs(0.25):P3HT:PCBM	3.4	0.58	54.22	1.2
NPs(0.5):P3HT:PCBM	3.0	0.51	51.72	0.91
NPs(0.75):P3HT:PCBM	1.2	0.47	42.16	0.28

The main reason to obtain lower efficiencies for the devices containing Eu^{3+}:La_2O_3 nanoparticles might be due to the fact that the nanoparticles were not really excited by using the light emitted by the solar simulator equipment. Solar simulator equipment is designed in order to best mimic the spectral output of the Sun. This means that the equipment is adapted to work with the real light percentage between 300 nm and 1100 nm. Since these particles have the maximum intensity of the excitation band centered at ~290 nm and the band limits at ~320 nm, the resulting down-shifting process could be very weak to really observe its effects on the PCE values. In other words, the nanoparticles excitation region does not match very well with the solar electromagnetic spectrum that arrives to the Earth.

The fill factor is more sensitive to the polymer-metal interphase morphology, unlike other parameters such as the V_{oc} and J_{sc}. Therefore, the fact to introduce aggregate nanoparticles into the active layer seemed to be the responsible for reducing significantly the FF value.

Lower FF values were also observed when introducing carbon nanotubes [298] in a P3HT:PCBM-based solar cell. However, there are many other reports where the introduction of nanoparticles in a P3HT:PCBM-based solar cell, does not show significant fluctuations in the fill factor parameter [298].

Figure 8.8 exhibits the incident photon-to-current conversion efficiency (IPCE) of the *P3HT:PCBM* and *NPs(0.25):P3HT:PCBM* samples under illumination from 350 to 800 nm.

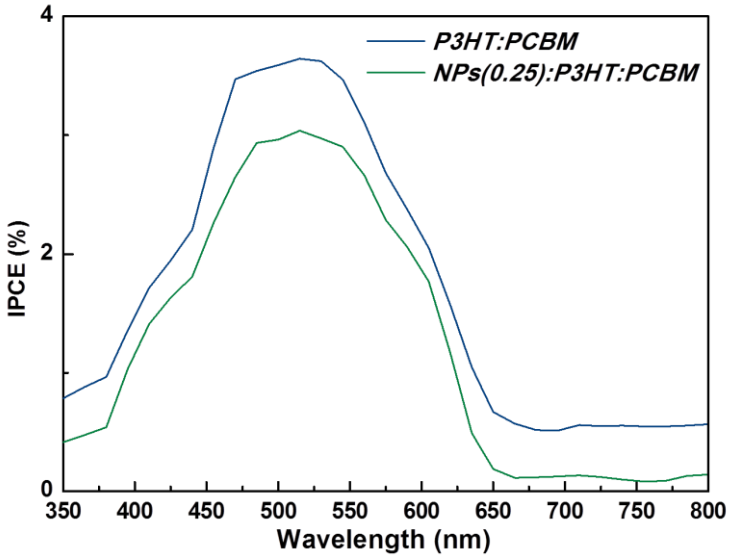

Figure 8.8. Incident photon-to-current conversion efficiency of *P3HT:PCBM* and *NPs(0.25):P3HT:PCBM* samples.

Both spectra showed the typical absorption of the P3HT polymer in the range between 400 and 650 nm (see Fig. 8.5). The spectrum obtained for the *NPs(0.25):P3HT:PCBM* sample, which contained Eu^{3+}:La_2O_3 nanoparticles, had the same shape than that obtained for the *P3HT:PCBM* sample, as expected since the excitation band of the particles should be observed at lower wavelengths, at around ~320 nm. Thus, from the results obtained we can say that the IPCE was not able to inform us about the real effect of the nanoparticles.

8.3.2. Characterization of *PTB1:PCBM* and *NP(x):PTB1:PCBM* (x=0.25, 0.5) solar cells

The PTB1:PCBM-based samples were not annealed contrary to what we did with the P3HT:PCBM-based samples. This was because Guo et al. [299] demonstrated that annealing treatment in PTB1:PCBM reduced the device power conversion efficiency from 5.24% to 1.92% due to reduced interfacial area between the electron donor and the acceptor.

The characteristic current-voltage measurements obtained for the PTB1:PCBM-based devices are shown in Figure 8.9. The curves were obtained under simulated AM 1.5G illumination at 100 $mW \cdot cm^{-2}$. The PCE obtained for the *PTB1:PCBM* sample was 2.39%. In comparison to

other power conversion efficiencies reported with values of ~6% [299], this can be considered as a low efficiency achieved. Regarding to the hybrid cells, it was not possible to obtain the measurement for the *NPs(0.5):PTB1:PCBM* sample because the device short-circuited when measuring but it was possible to measure the *NPs(0.25):PTB1:PCBM* device with a PCE of 2.28%. The PCE obtained for the *PTB1:PCBM* device was slightly higher than that obtained for the *NPs(0.25):PTB1:PCBM* device.

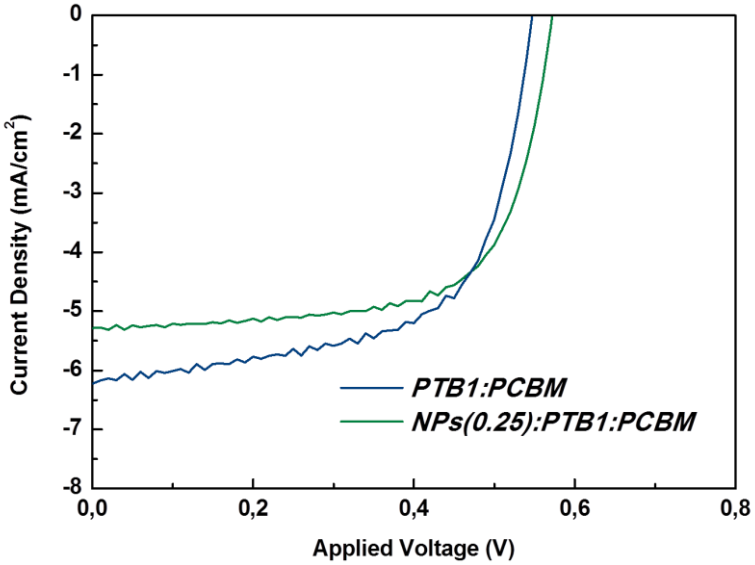

Figure 8.9. Current-voltage characteristics of the *PTB1:PCBM* and *NPs(0.25):PTB1:PCBM* samples.

Table 8.4 lists the results obtained for these devices. Therefore, as observed in P3HT:PCBM-based solar cells, the PCE decreased when the nanoparticles where introduced in the device (see Table 8.3). However, the PTB1:PCBM-based devices showed slight differences between them. This can be attributed to the higher fill factor obtained for the sample containing Eu^{3+}:La_2O_2S@APTMS nanoparticles. Notice that in the PTB1:PCBM-based devices the nanoparticles used were previously functionalized by the APTMS molecule to avoid the agglomeration of the particles. This can be causing different morphological effects in comparison to the non-functionalized Eu^{3+}:La_2O_3 nanoparticles used in the P3HT:PCBM-based devices.

Table 8.4. Photovoltaic parameters for *PTB1:PCBM* and *NPs(x):PTB1:PCBM* (x=0.25, 0.5) samples.

Sample	J_{sc} (mA·cm^{-2})	V_{oc} (V)	FF (%)	PCE (%)
PTB1:PCBM	6.9	0.55	62.8	2.39
NPs(0.25):PTB1:PCBM	5.8	0.57	68.1	2.28
NPs(0.5):P3HT:PCBM	-	-	-	-

However, the current density obtained for the *PTB1:PCBM* sample was higher than that for the *NPs(0.25):PTB1:PCBM* device. The Eu^{3+}:La_2O_2S nanoparticles have an excitation band that extends to ~420 nm. Thus, contrary to the Eu^{3+}:La_2O_3 nanoparticles, this excitation band was well matched with the solar electromagnetic spectrum. So, once the morphology and the electromagnetic spectrum did not seem to be the main causes for the low efficiencies obtained, another reason could be attributed to electrical problems. In other words, the particles might be working as interfaces/obstacles where the recombination process could be taking place. The recombination would mean the loss of the charge carriers which in theory should be transported to the corresponding electrodes.

Conclusions

The main conclusion of this thesis is the successful fabrication and characterization of down-shifting (DS) nanoparticles to be used in polymeric solar cells. Although still more efforts are required to design and develop higher efficiencies of polymeric cells using DS materials, this thesis opens a promising future for the spectrum modification concept by using lanthanide doped lanthanum based materials. Throughout this thesis, many other conclusions have been obtained, and they are summarized as follows:

Synthesis of the materials

- Lanthanum hydroxide ($La(OH)_3$) and lanthanum oxide (La_2O_3) nanoparticles have been synthesized by using precipitation and hydrothermal (by a furnace or a microwave oven) methods and applying a calcination treatment.
- $La(OH)_3$ and La_2O_3 have been successfully doped with europium (Eu^{3+}) and praseodymium (Pr^{3+}) by the wetness impregnation method and the co-precipitation and hydrothermal methods. The wetness impregnation method is a new concept for optical materials. In addition, for doped nanoparticles, the sol-gel method has been a novel method for the synthesis of the materials analysed in this thesis.
- $La(OH)_3$ and La_2O_3 have been successfully co-doped with europium and bismuth (Eu^{3+}:Bi^{3+}).
- Eu^{3+} doped and Eu^{3+}:Bi^{3+} co-doped lanthanum oxysulfide (La_2O_2S) nanoparticles have been synthesized by the ethanol-assisted solution combustion method.
- Several nanocomposites have been fabricated by embedding the nanoparticles in polymer-based films.
- Several nanoparticles have been successfully de-agglomerated and functionalized by using (3-acryl-oxypropyl)trimethoxysilane (APTMS).
- Different bulk heterojunction polymer-based solar cells have been fabricated by embedding nanoparticles into them.

Characterization of the materials

The nanoparticles have been characterized by several techniques obtaining information about their chemical and physical properties:

- We have obtained nanoparticles with different sizes, morphologies, surface areas, and decomposition temperatures by using different synthesis methods, as has been confirmed by electronic microscopy, XRD, nitrogen adsorption, and DTA-TGA techniques. From the results observed, we can say that one of the better methods used to prepare the Ln^{3+} doped La_2O_3 nanopartices is the hydrothermal treatment in autoclave using microwave: a low temperature was required to obtain the lanthanum

oxide phase, the samples showed higher surface areas, and it is a fast and clean method.

- From the spectroscopic studies by using PL and CL techniques we can say that the fact of using different methods to prepare the nanoparticles do not impact significantly in the spectroscopic results. However, the fact of using Bi^{3+} as co-dopant and La_2O_2S as a host cause important changes, shifting and broadening the charge transfer band towards the red part of the electromagnetic spectrum, which was one of the objectives of this thesis.
- The re-hydroxylation process from La_2O_3 into $La(OH)_3$ has been monitored by using the XRD, IR, PL and CL techniques. Some differences in the re-hydroxylation rate depending on different parameters have been observed:
    - The higher the temperature and the longer the calcining time, the higher the resistance to re-hydroxylation of the La_2O_3 formed.
    - The different surface area and morphology of the synthesized $La(OH)_3$ nanoparticles obtained by different methods, showed different re-hydroxylation rates for the corresponding calcined samples: smaller particle size and higher surface area make the La_2O_3 to transform easily into $La(OH)_3$.
    - The presence of active ions in the La_2O_3 structure seems to accelerate the re-hydroxylation process due to a reduction of the size of the particles.
- It has been demonstrated the high stability of the lanthanum oxysulfide host versus time by the PL technique.
- By using IR and TGA techniques we confirmed the successful functionalization of the nanoparticles by using APTMS. TEM images show the dispersion of these nanoparticles, since they did not show aggregates. The DLS results showed an average size around 250 nm.

Characterization of the devices

- By AFM, the current-voltage curves have been obtained for the polymer-based films and also for the nanocomposite samples.
- The devices have been successfully measured by a solar simulator equipment and only some of them short-circuited during measuring.
- The efficiencies of organic and hybrid solar cells have been measured with a solar simulator equipment. From the results obtained we can say that the effects that the nanoparticles could cause, such as charge transport and recombination, are significant enough to impede us to notice the improvement of efficiency by spectrum modification.
- Although the efficiencies are not higher when using the DS Ln^{3+} doped lanthanide compound nanoparticles, in the future co-doping with other Ln^{3+} ions, might generate additional energy transfer mechanisms that might allow taking advantage from new

DC mechanisms. Then, by using the DS and DC mechanisms, the probability to improve the efficiencies in OPV cells would be higher.

References

[1] O. Morton, *Nature*, 443 **2006** 19.

[2] M.A. Green, *Solar Cells; Operating Principles, Technology and Systems Application*. Englewood Cliffs, NJ, USA: Prentice-Hall **1982**.

[3] S. Wenham, M. Green, M. Watt, *Applied Photovoltaics, UNSW Photovoltaics*.

[4] A. Mishra, P. Bäuerle, *Angew. Chem. Int.* 51 **2012** 2020.

[5] M. Green, *Third Generation Photovoltaics*, Springer, Berlin, **2003**.

[6] N. Bloembergen, *Phys. Rev. Lett*, 2(3) **1959** 84.

[7] C.R. Ronda, *J. Alloys Comp*. 225 **1995** 534.

[8] B.S. Richards, *Sol. Energy Mater. Sol. Cells*, 90(9) **2006** 1189.

[9] P. Gibart, F. Auzel, J.-C. Guillaume, K. Zahraman, *13th EPVSEC, Nice, France*, **1995** 85.

[10] A. Shalav, B. Richards, T. Trupke, R. Corkish, K. Krämer, H. Güdel, M. Green, *Third conference on Photovoltaic Energy Conversion*, **2003**.

[11] H.Q. Wang, M. Batentschuk, A. Osvet, L. Pinna, C.J. Bravec, *Avd. Mater.* 23 **2011** 2675.

[12] A. Luque, A. Martí, *Theoretical Limits of Photovoltaic Conversion. In Handbook of Photovoltaic Science and Engineering*, Eds. A. Luque and S. Hegedus, **2003** 113. Chichester, U.K.:Wiley.

[13] C. Soci, I.W. Hwang, D. Moses, Z. Zhu, D. Waller, R. Guadiana, C.J. Brabec, A.J. Heeger, *Adv. Funct. Mater.* 17 **2007** 632.

[14] S. Günes, H. Neugebauer, N.S. Sariciftci, *Chem. Rev.* 107(4) **2007** 1324.

[15] J. Liu, Q. Yao, Y. Li, *Appl. Phys. Lett.* 88 **2006** 173119.

[16] X.Y. Huang, J.X. Wang, D.C. Yu, S. Ye, Q.Y. Zhang, X.W. Sun, *J. Appl. Phys.* 109 **2011** 113526.

[17] Q.G. Zeng, Z.J Ding; Z.M. Zhang, *J. Lumin.* 118 **2006** 301.

[18] C.K. Huang, Y.C. Chen, W.B. Hung, T.M. Chen, K.W. Sun, W.-L. Chang, *Prog. Photovolt. Res. Appl.* **2012**.

[19] C. Strümpel, M. McCann, G. Beaucarne, V. Arkhipov, A. Slaoui, V. Švrček, C. del Cañizo, I. Tobias, *Sol. Energy Mater. Sol. Cells*, 91 **2007** 238.

[20] R.S. Ningthoujam, R. Shukla, R.K. Vatsa, V. Duppel, L. Kienle, *J. Appl. Phys.* 105 **2009** 084304.

[21] L. Li, H.K. Yang, B.K. Moon, B.C. Choi, J.H. Jeong, K.H. Kim, *Mater. Chem. Phys.* 119 **2010** 471.

[22] T.A. Skotheim, J.R. Reynolds, *Handbook of Conducting Polymers,3rd ed.*; CRC Press: Boca Raton, FL, **2006**.

[23] F.C. Krebs, *Sol. Energy Mater. Sol. Cells* 93 **2009** 394.

[24] T.T. Larsen-Olsen, B. Andreasen, T.R. Andersen, A.P.L. Böttiger, E. Bundgaard, K. Norrman, J.W. Andreasen, M. Jørgensen, F.C. Krebs, *Sol. Energy Mater. Sol. Cells* 97 **2012** 22.

[25] G.A. Chamberlain, *Organic solar cells: A review. Solar Cells* 8 **1983** 47.

[26] J.J.M. Halls, K. Pichler, R.H. Friend, S.C. Moratti, A.B. Holmes, *Appl. Phys. Lett.* 68 **1996** 3120.

[27] G. Yu, J. Gao, J.C. Hummelen, F. Wudl, A.J. Heeger, *Science* 270 **1995** 1789.

[28] C.J. Bravec, N.S. Sariciftci, J.C. Hummelen, *Adv. Funct. Mater.* 11 **2011** 15.

[29] B.C. Thompson, J.M.J. Fréchet, *Angew. Chem. Int.* 47 **2008** 58.

[30] F. Padinger, R.S. Rittberger, N.S. Sariciftci, *Adv. Funct. Mater.* 13 **2003** 85.

[31] P.M. Allemand, A. Koch, F. Wudl, Y. Rubin, F. Diederich, M.M. Alvarez, S.J. Anz, R.L. Whetten, *J. Am. Chem. Soc.* 113 **1991** 1050.

[32] G. Greczynski, T. Kugler, M. Keil, W. Osikowicz, M. Fahlman, W.R. Salaneck, *J. Electron Spectrosc. Relat. Phenom.* 121 **2001** 1.

[33] L.S.C. Pingree, B.A. MacLeod, D.S. Ginger, *J. Phys. Chem. C* 112 **2008** 7922.

[34] W.H. Kim, G.P. Kushto, H. Kim, Z.H. Kafafi, *J. Polym. Sci. Part B: Polym. Phys.* 41 **2003** 2522.

[35] R.W. Cahn, P. Haasen, E.J. Kramer, *Materials Science and Technology, Characterization of Materials Part I*, 2A **1992**.

[36] Y. Huang, X.F. Duan, Q.-Q. Wei, C.M. Lieber, *Science* 291 **2001** 630.

[37] J. Rodriguez-Carvajal, *Reference guide for the computer program Fullprof; Laboratorie Leon Brillouin. CEA-CNRS. Saclay*, France: **2000**.

[38] H.M. Rietveld, *J. Appl. Crystallogr*. 2 **1969** 65.

[39] R.A. Young, *International union of crystallography, monographs on crystallography 5. In; Oxford University Press*, Oxford: **1995**; Chapter The Rietveld Method.

[40] G. Cao, *Nanostructures & Nanomaterials, Imperial College Press*, London **2004**.

[41] R.A. van Santen, P.W.N.M. Van Leeuwen, J.A. Moulijn, B. A. Averill, **2000**. Studies in Surface Science and Catalysis: Catalysis an integrated approach. Elsevier, Amsterdam.

[42] A. Krueger, M. Ozawa, G. Jarre, Y. Liang, J. Stegk, L. Lu, *Phys. Stat. Sol. (a)*, 204(9) **2007** 2881.

[43] E. Abbe, Beiträge zur Theorie des Mikroskops und der mikroskopischen. Wahrnehmung. Arch. Mikrosk. Anat. Entwichlungsmech. 9 **1873** 413.

[44] M.J. Sadar, Turbidity Science, Technical Information Series, 11 **1982**.

[45] Catalogue for Capillary viscometry from SCHOTT Instruments, 168.

[46] Hawleys, in Sax and R. J. Lewis, Eds. Condensed Chemical Dictionary, Van Nostrand Reinhold, 11th Edition, New York **1987** 683.

[47] L. Wang, Y. Ma, Y. Wang, S. Liu, Y. Deng, *Catal. Commun.* 12 **2011** 1458.

[48] A.A. Dakhel, *Mater. Chem. Phys.* 102 **2007** 266.

[49] J.L. Zhu, Y.H. Zhou, H.X. Yang, *J. Power Sources* 69 **1997** 169.

[50] S. Bera, R.N.P Choudhary, *Mater. Lett.* 37(3) **1998** 111.

[51] J.J. Oh, B.K. Jin, W.J. Chung, D. W. Shin, Y.G. Choi, *Curr. Appl. Phys.* 11 **2011** S15.

[52] C.-Z. Yao, H.-X. Ma, J.-H. Yao, Q.-J. Gong, H. Sun, *Mater. Chem. Phys.* 125 **2011** 595.

[53] K.S. Shankar, S. Kar, G.N. Subbanna, A.K. Raychaudhuri, *Solid State Commun.* 129 **2004** 479.

[54] S.-J. Kim, W.-K. Han, S.-G. Kang, M.-S. Han, Y.-H. Cheong, *Solid-State Phenom.* 135 **2008** 23.

[55] A.V. Murugan, S.C. Navale, V. Ravi, *Mater. Lett.* 60 **2006** 848.

[56] M. Ozawa, R. Onoe, H. Kato, *J. Alloys Compd.* 408-412 **2006** 556.

[57] C. Hu, H. Liu, W. Dong, Y. Zhang, G. Bao, C. Lao, Z.L. Wang, *Adv. Mater.* 19 **2007** 470.

[58] X. Ma, H. Zhang, Y. Ji, J. Xu, D. Yang, *Mater. Lett.* 58 **2004** 1180.

[59] N. Zhang, R. Yi, L. Zhou, G. Gao, R. Shi, G. Qiu, X. Liu, *Mater. Chem. Phys.* 114 **2009** 160.

[60] S. Wang, Y. Zhao, J. Chen, R. Xu, L. Luo, S. Zhong, *Superlattices Microstruct.* 47 **2010** 597.

[61] O. Bergadà, I. Vicente, P. Salagre, Y. Cesteros, F. Medina, J. E. Sueiras, *Microp. Mesop. Mater.* 101 **2007** 363.

[62] I. Vicente, P. Salagre, Y. Cesteros, F. Medina, J. E. Sueiras, *Appl. Clay Sci.* 48 **2010** 26.

[63] I. Vicente, P. Salagre, Y. Cesteros, F. Guirado, F. Medina, J. E. Sueiras, *Appl. Clay Sci.* 43 **2009** 103.

[64] X. Wang, M. Wang, H. Song, B. Ding, *Mater. Lett.* 60 **2006** 2261.

[65] S. Mentus, D. Jelic, V. Grudic, *J. Therm. Anal. Cal.* 90 **2007** 393.

[66] M. Salavati-Niasari, G. Hosseinzadeh, F. Davar, *J. Alloys Compd*. 509(1) **2011** 134.

[67] A. Neumann, D. Walter, *Thermochim. Acta* 445 **2006** 200.

[68] Z. Rzączyńska, A. Ostasz, S. Pikus, *J. Therm. Anal. Cal.* 82 **2005** 347.

[69] X. Wang, Y.D. Li, *Chem. Eur. J.* 9 **2003** 5627.

[70] M. Méndez, Y. Cesteros, L.F. Marsal, E. Martínez-Ferrero, P. Salagre, P. Formentín, J. Pallarès, M. Aguiló, F. Díaz, J.J. Carvajal, *Opt. Mater.* 33 **2011** 1120.

[71] H.Q. Liu, L.L. Wang, S.Q. Chen, B. Zou, *J. Luminesc.* 126 **2007** 459.

[72] H.Q. Liu, L.L. Wang, W. Huang, Z.W. Peng, *Mater. Lett.* 61 **2007** 1968.

[73] J. Chang, J.S. Xiong, H. Peng, L. Sun, S. Lu, F. You, S. Huang, J. Lumin. 122-123 **2007** 844.

[74] H.Q. Liu, L.L. Wang, S. Chen, *Mater. Lett*. 61(17) **2007** 3629.

[75] M. Galceran, M.C. Pujol, M. Aguiló, F. Díaz, *J. Sol-gel Techn*. 42 **2007** 79.

[76] Pechini MP (1967) US Patent No.3.330.697 July 1.

[77] T. Grzyb, M. Węcławiak, S.Lis, *J. Alloys Compd.* 539 **2012** 82.

[78] S.A. Hassanzadehl-Tabrizi, *Adv. Powder Techol.* 23 **2012** 324.

[79] M. Baran, Y. Zhydachevskii, A. Suchocki, A. Reszka, S. Warchol, R. Diduszko, A. Pajączkowska, *Opt. Mater.* 34 **2012** 604.

[80] S. Zhou, Z. Fu, J. Zhang, S. Zhang, J. Luminesc. 118 **2006** 179.

[81] M. Dudek, A. Jusza, K. Anders, L. Lipińska, M. Baran, R. Piramidowicz, *J. Rare Earths* 29 **2011** 1123.

[82] G.C. Aumuller, W. Koestler, B.C. Grabmaier, R. Frey, *J. Phys. Chem. Solids*, 55 **1994** 767.

[83] W. Liu, G.C. Farrington, B. Dunn, *J. Electrochem. Soc.* 143 **1996** 879.

[84] T. Xia, J. Wang, N. Lin, H. Zhao, L. Huo, G. Mountrichas, *RSC Advances* **2011**.

[85] G. Wakefield, E. Holland, P.J. Dobson, J.L. Hutchison, *Adv. Mater*. 13 **2001** 1157.

[86] Z. Wang, W. Zhang, L. Lin, B.You, Y. Fu, M. Yin, *Opt. Mater*. 30 **2008** 1484.

[87] H. Rétot, A. Bessière, B. Viana, B. LaCourse, E. Mattmann, *Opt. Mater.* 33 **2011** 1008.

[88] C. de Mello Donegá, G.J. Dirksen, H.F. Folkerts, A. Meijerink, G. Blasse, *J. Phys. Chem. Solids* 56(2) **1995** 267.

[89] S.S. Kale, K.R. Jadhav, P.S. Patil, T.P. Gujar, C.D. Lokhande, *Mater. Lett.* 59 **2005** 3007.

[90] H. Chen, H. Yu, F. Peng, H. Wang, J. Yang, M. Pan, *J. Catal.* 269 **2010** 281.

[91] H. Xu, H.M. Li, L. Xu, C.D. Wu, G.S. Sun, Y.G. Xu, J.Y. Chu, *Ind. Eng. Chem. Res.* 48 **2009** 10771.

[92] Z. Liu, X. Sun, S. Xu, J. Lian, X. Li, Z. Xiu, Q. Li, D. Huo, J.G. Li, *J. Phys. Chem. C* 112 **2008** 2353.

[93] H. Peng, S. Huang, F. You, J. Chang, S. Lu, L. Cao, *J. Phys. Chem. B* 109 **2005** 5774.

[94] J. Dhanaraj, M. Geethalakshmi, R. Jagannathan, T.R.N. Kutty, *Chem. Phys. Lett.* 387 **2004** 23.

[95] J. Bang, M. Abboudi, B. Abrams, P.H. Holloway, *J. Lumin.* 106 **2004** 177.

[96] W.H. Cao, X.X. Luo, Chinese Patent No.CN200,510,047,576.X. **2005**.

[97] X.X. Luo, W.H. Cao, *J, Alloys Compd.* 460 **2008** 529.

[98] T. Xia, W.H. Cao, X.X. Luo, Y. Tian, *J. Mater. Res.* 20(9) **2005** 2274.

[99] S.H. Shin, D.Y. Jeon, K.S. Suh, *J. Appl. Phys.* 90 **2001** 5986.

[100] X.M. Liu, J. Lin, *J. Lumin.* 122-123 **2007** 700.

[101] H. Fukada, M. Konagai, K. Ueda, T. Miyata, T. Minami, *Thin Solid Films* 517 **2009** 6054.

[102] T. Miyata, J.-I. Ishino, K. Sahara, T. Minami, *Thin Solid Films* 519 **2011** 8095.

[103] J.K. Park, S.M. Park, C.H. Kim, H.D. Park, *J. Mater. Sci. Lett.* 20 **2001** 2231.

[104] Powder Diffraction File Database PDF-2, International Center for Diffraction Data, ICDD, **2010**, File 37-1190.

[105] Powder Diffraction File Database PDF-2, International Center for Diffraction Data, ICDD, **2010**, File 49-0981.

[106] O. Yamamoto, Y. Takeda, R. Kanno, M. Fushimi, *Solid State Ionics* 17 **1985** 107.

[107] I. Djerdj, G. Garnweitner, D.S. Su, M. Niederberger, *J. Solid State Chem.* 180 **2007** 2154.

[108] A.E. Gobichon, J.P. Auffrédic, D. Louër, *Solid State Ionics* 93 **1997** 51.

[109] J.X. Zhu, Z. Gui, Y.Y. Ding, *Mater. Lett.*, 62 **2008** 2373.

[110] Powder Diffraction File Database PDF-2, International Center for Diffraction Data, ICDD, **2010**, File 36-1481.

[111] Powder Diffraction File Database PDF-2, International Center for Diffraction Data, ICDD, **2010**, File 23-0320.

[112] Powder Diffraction File Database PDF-2, International Center for Diffraction Data, ICDD, **2010**, File 48-1113.

[113] Powder Diffraction File Database PDF-2, International Center for Diffraction Data, ICDD, **2010**, File 37-0804.

[114] R.P. Turcotte, J.O. Sawyer, L. Eyring, *Inorg. Chem.* 8 **1969** 238.

[115] M. H. Mueller-Buschbaum, H.G.Z. von Schnering, *Anorg. Allg. Chem.* 340 **1965** 232.

[116] L.V. Interrante, Z. Jiang, D.J. Parking, *ACS Symp. Ser*. 77 **1998** 168.

[117] L.W. Tai, P.A. Lessing, *J. Mater. Res.* 7 **1992** 502.

[118] Powder Diffraction File Database PDF-2, International Center for Diffraction Data, ICDD, **2010**, File 73-2063.

[119] N.T. McDevitt, W.L. Baun, *Spectrochim. Acta* 20 **1964** 799.

[120] W.B. White, V.G. Keramidas, *Spectrochim. Acta* 28A **1972** 501.

[121] S. Kim, W. Han, S. Kang, M. Hang, Y. Cheong, *Solid State Phenom.* 135 **2008** 23.

[122] F. Mercier, C. Alliot, L. Bion, N. Thromat, P. Toulhoat, *J. Electron. Spectrosc. Relat. Phenom.* 150 **2006** 21.

[123] G. Bohus, V. Hornok, A. Oszkó, A. Vértes, E. Kuzmann, I. Dékány, *Colloids and Surfaces A: Physicochem. Eng. Aspects* 405 **2012** 6.

[124] Powder Diffraction File Database PDF-2, International Center for Diffraction Data, ICDD, **2010**, File 71-2098.

[125] Powder Diffraction File Database PDF-2, International Center for Diffraction Data, ICDD, **2010**, File 85-1534.

[126] C. Shang, X. Shang, Y. Qu, M. Li, *J. Appl. Phys.* 108 **2010** 094328.

[127] L. Yu, H. Song, Z. Liu, L. Yang, S. Lu, *Phys. Chem. Chem. Phys.* 8 **2006** 303.

[128] R.S. Ningthoujam, edited by S.B. Rai, Y. Dwivedi, Nova Science Publishers Inc., **2012** 145.

[129] P. Maestro, D. Huguenin, *J. Alloys Comp.* 225 **1995** 520.

[130] X. Chen, Z. Zhang, X. Li, C. Shi, *Chem. Phys. Lett.* 422 **2006** 294.

[131] G. Phaomei, R.S. Ningthoujam, W.R. Singh, R.S. Loitongbam, N.S. Singh, A. Rath, R.R. Juluri, R.K. Vatsa, *Dalton Trans.*, 40 **2011** 11571.

[132] Z. Fu, S. Zhou, T. Pan, S. Zhang, *J. Luminesc.* 124 **2007** 213.

[133] D.L. Dexter, *J. Chem. Phys.* 21(5) **1952** 836.

[134] M. Galceran, M.C. Pujol, M. Aguiló, F. Díaz, *Mater. Sci. Eng. B* 146 **2008** 7.

[135] M. Nazarov, J.H. Kang, D.Y. Jeon, S. Bukesov, T. Akmaeva, *Opt. Mater.* 27 **2005** 1587.

[136] C. Xueyuan, L. Wenqin, L. Yongsheng, L. Guokui, *J. Rare Earths* 25 **2007** 515.

[137] P.A. Tanner, L. Fu, B.-M. Cheng, *J. Phys. Chem. C* 113 **2009** 10773.

[138] L. Li, H.K. Yang, B.K. Moon, B.C. Choi, J.H. Jeong, K.H. Kim., *Mater. Chem. Phys.* 119 **2010** 471.

[139] J. Liu, X. Fei, X. Yu, Z. Tao, L. Yang, S. Yang, *J. Non Cryst. Solids* 353 **2007** 4697.

[140] Y.H. Wu, M.Y. Yang, A. Chin, W.J. Chen, C.M. Kwei, *IEEE Electron Device Lett.* 21 **2000** 341.

[141] A.M. Srivastava, *Opt. Mater.* 31 **2009** 881.

[142] W.C. Koehler, E.O. Wollan, *Acta Cryst.* 6 **1953** 741.

[143] T. Ninjbadgar, G. Garnweitner, A. Börger, L.M. Goldenberg, O.V. Sakhno, J. Stumpe, *Adv. Funct. Mater.* 19 **2009** 1819.

[144] S. Bernal, F.J. Botana, R. García, J.M. Rodríguez-Izquierdo, *React. Solids* 4 **1987** 23.

[145] P. Di Bernardo, A. Melchior, M. Tolazzi, P.L Zanonato, *Coord. Chem. Rev.* 256 **2012** 328.

[146] G. Blasse, *J. Lumin.* 1(2) **1970** 766.

[147] A. Bril, W.L. Wanmaker, *J. Electrochem. Soc.* 111 **1964** 1363.

[148] A.K. Levine, F.C. Palilla, *Appl. Phys. Lett.* 5 **1964** 118.

[149] L. Brixner, *J. Electrochem. Soc.* 114 **1967** 252.

[150] R. Reisfeld, C.K. Jorgensen, in K.A. Gschneidner Jr., L. Eyring (Eds.), *Handbook of the Physics and Chemistry of Rare Earths*, Elsevier, North Holland, Chapter 58 **1987** 1.

[151] S.S. Saleem, T.K.K. Srinivasan, *Pramana* 29 **1987** 87.

[152] K. Binnemans, C. Görller-Walrand, *Chem. Phys. Lett.* 235 **1995** 163.

[153] G. Liu, X. Chen, in: K.A. Gschneidner Jr., L. Eyring (Eds.), *Handbook of the Physics and Chemistry of Rare Earths*, Elsevier, North Holland, Chapter 37 **2007** 99.

[154] W.C. Nieupoort, G. Blasse, *Solid State Commun.* 4 **1966** 227.

[155] W. Szuszkiewicz, B. Keller, M. Guzik, T. Aitasalo, J. Niittykoski J. Hölsä, J. Legendziewicz, *J. Alloy. Compd.* 341 **2002** 297.

[156] N.A. Dulina, Y.V. Yermolayeva, A.V. Tolmachev, Z.P. Sergienko, O.M. Vovk, E.A. Vovk, N.A. Matveevskaya, P.V. Mateychenko, *J. Eu. Cer. Soc.* 30 **2010** 1717.

[157] L. Yanhong, H. Guangyan, *J. Sol. State Chem.* 178(3) **2005** 645.

[158] B.S. Barros, A.C. de Lima, Z.R. da Silva, D.M.A. Melo, S. Alves-Jr., *J. Phys. Chem. Sol.* 73(5) **2012** 635.

[159] S.A. Lourenço, N.O. Dantas, E.O. Serqueira, W.E.F. Ayta, A.A. Andrade, M.C. Filadelpho, J.A. Sampaio, M.J.V. Bell, M.A. Pereira-da-Silva, *J. Luminesc.* 131(5) **2011** 850.

[160] G. Lin, F. Luo, H. Pan, Q. Chen, D. Chen, J. Qiu, Q. Zhao, *J. Alloys Compd.* 509(22) **2011** 6462.

[161] C. Shang, H. Jiang, X. Shang, M. Li, L. Zhao, *J. Phys. Chem. C* 115 **2011** 2630.

[162] C.C. Lin, K.M. Lin, Y.Y. Li, *J. Lumin.* 126 **2007** 795.

[163] C. Martinet, A. Pillonnet, J. Lancok, C. Garapon, *J. Lumin.* 126 **2007** 807.

[164] K.R. Reddy, K. Annapurna, S. Buddhudu, *Mater. Res. Bull.* 31(11) **1996** 1355.

[165] J.K. Park, M.A. Lim, C.H. Kim, H.D. Park, C.H. Han, S.Y. Choi, *J. Mater. Sci. Lett.* 22 **2003** 477.

[166] H.E. Hoefdraad, F.M.A. Stegers, G. Blasse, *Chem. Phys. Lett.* 32 **1975** 216.

[167] R.J. Bouchard, J.L. Gillson, *Mater. Res. Bull*. 6 **1971** 669.

[168] R.S. Loiongbam, N.S. Singh, W.Rameshwor, R.S. Ningthoujam, *J. Luminesc.* **2012** in press.

[169] M. Dudek, A. Jusza, K. Anders, L. Lipińska, M. Baran, R. Piramidowicz, *J. Rare Earths* 29 **2011** 1123.

[170] R. Pragash, G. Jose, N.V. Unnikrihnan, C. Sudarsanakumar, *Bull. Mater. Sci.* 34 **2011** 955.

[171] T. Sandrock, T. Danger, E. Heumman, G. Huber, B.H.T. Chai, *Appl. Phys. B* 58 **1994** 149.

[172] P. Boutinaud, E. Pinel, M. Oubaha, R. Mahiou, E. Cavalli, M. Bettinelli, *Opt. Mater.* 28 **2006** 9.

[173] C. Pedrini, D. Bouttet, C. Dujardin, B. Moine, I. Dafinei, P. Lecoq, M. Koselja, K. Blazek, *Opt. Mater.* 3 **1994** 81.

[174] W. Seeber, E.A. Downing, L. Hesselink, M.M. Fejer, D. Ehrt, *J. Non-Cryst. Solids* 189 **1995** 218.

[175] G.C. Aumuller, W. Koestler, B.C. Grabmaier, R. Frey, *J. Phys. Chem. Solids* 55 **1994** 767.

[176] H. Retot, A. Bessiere, B. Viana, B. LaCourse, E. Mattmann, *Opt Mater.* 33 **2011** 1008.

[177] P. Boutinaud, M. Bettinelli, F. Diaz, *Opt. Mater.* 32(12) **2010** 1659.

[178] O.K. Moune, M.D. Faucher, C.K. Jayasankar, A.M. Lejus, *J. Lumin.* 85 **1999** 59.

[179] Q. Dai, H. Song, M. Wang, X. Bai, B. Dong, R. Qin, X. Qu, H. Zhang, *J. Phys. Chem. C* 112 **2008** 19399.

[180] A.M. Pires, O.A. Serra, M.R. Davolos, *J. Alloys Compd.* 374 **2004** 181.

[181] L. Ozawa, *J. Electrochem. Soc.* 124(3) **1977** 413.

[182] A.D. Sontakke, A. Tarafder, K. Biswas, K. Annapurna, *Physica B* 404 **2009** 3525.

[183] G. Ju, Y. Hu, L. Chen, X. Wang, Z. Mu, H. Wu, F. Kang, *J. Luminesc.* 132 **2012** 1853.

[184] W.J. Park, S.G. Yoon, D.H. Yoon, *J. Electroceram.* 17 **2006** 41.

[185] X.T. Wei, Y.H. Chen, X.R. Cheng, M. Yin, W. Xu, *Appl. Phys. B* 99 **2010** 763.

[186] Z. Wang, H. Liang, Q. Wang, M. Chen, M. Gong, Q. Su, *Phys. Status Solidi A* 206(7) **2009** 1589.

[187] W.J. Park, M.K. Jung, S.J. Im, D.H. Yoon, *Colloids Surf A* 313-314 **2008** 373.

[188] T. Miyata, J. Ishino, K. Sahara, T. Minami, *Thin Solid Films* 519 **2011** 8095.

[189] A.V. Prokofiev, A.I. Shelykh, B.T. Melekh, *J. Alloys. Compd.* 242 **1996** 41.

[190] R.S. Loitongbam, N.S. Singh, W.R. Singh, R.S. Ningthoujam, *J. Luminesc.* (in press) **2012**.

[191] M. Galceran, M.C. Pujol, P. Gluchowski, W. Strek, J.J. Carvajal, X. Mateos, C. Zaldo, M. Aguiló, F. Díaz, *J. Am. Ceram. Soc.* 93(11) **2010** 3764.

[192] S.S. Lee, H.I. Park, C.H. Joh, S.H. Byeon, *J. Solid State Chem.* 180 **2007** 3529.

[193] X. Wu, Y. Liang, R. Chen, M. Liu, Y. Li, *J. Mater. Sci.* 46 **2011** 5581.

[194] ATOMS Version 6.4, Shape Software, Kingsport, USA **2011**.

[195] W.H. Zachariasen, *Z. Phys. Chem.* 123 **1926** 134.

[196] W.H. Zachariasen, *Z. Phys. Chem.* 70 **1929** 187.

[197] L. Pauling, *Z. Krystallogr.* 69 **1928** 415.

[198] M. Mikami, S. Nakamura, *J. Alloys Compd*. 408 **2006** 687.

[199] E.W.J.L. Oomen, A.M.A. van Dongen, *J. Non-Cryst. Solids* 111 **1989** 205.

[200] F. Khlissa, M. Férid, M.C. Pujol, X. Mateos, J.J. Carvajal, F. Díaz, M. Aguiló, *J. Cryst. Growth* 311 **2009** 4360.

[201] C. Sun, C. Carpenter, G. Pratx, L. Xing, *Nanoscale Res. Lett.* 6 **2011** 24.

[202] T. Hahn, *International Tables for Crystallography; The Interational Union of Crytallography*; D. Reidel: Dordrecht, The Netherlands, A **1987**.

[203] M.F. Sunding, K. Hadidi, S. Diplas, O.M. Løvvik, T.E. Norby, A.E. Gunnæs, *J. Electr. Spectr. Rel. Phen.* 184 **2011** 399.

[204] W.O. Milligan, D.F. Mullica, J.D. Oliver, *J. Appl. Crystallogr.* 12 **1979** 411.

[205] C. Linares, A. Louat, *J. Physique*, 36 **1975** 717.

[206] G.H. Mhlongo, O.M. Ntwaeaborwa, M.S. Dhlamini, H.C. Swart, K.T. Hillie, *J. Mater. Sci.* 45 **2010** 5228.

[207] T.L. Van, M. Che, J.M. Tatibouet, M. Kermarec, *J. Catal.* 142 **1993** 18.

[208] S. Bernal, J.A. Díaz, R. García, J.M. Rodríguez-Izquierdo, *J. Mater. Sci.* 20 **1985** 537.

[209] B. Klingenberg, M.A. Vannice, *Chem. Mater*. 8 **1996** 2755.

[210] D. Jiawen, W. Yanli, S. Weili, L. Youngxiu, *J. Rare Earths* 24 **2006** 440.

[211] G. Adachi, N. Imanaka, *Chem. Rev.* 98 **1998** 1479.

[212] N. Dilawar, S. Mehrotra, D. Varandani, B.V. Kumaraswamy, S.K. Haldar, A.K. Bandyopadhyay, *Mater. Charact.* 59 **2008** 462.

[213] S. Jeon, H. Hwang, *J. Appl. Phys.* 93(10) **2003** 6393.

[214] P. Fleming, R.A. Farrell, J.D. Holmes, M.A. Morris, *J. Am. Ceram. Soc.* 93 **2010** 1187.

[215] O.V. Andreev, A.S. Vysokikh, V.G. Vaulin, *Physicochem. Anal. Inorg. Sys.* 53(8) **2008** 1414.

[216] M. Machida, K. Kawamura, K. Ito, *Chem. Commun.* **2004** 662.

[217] M.P. Rosynek, D.T. Magnuson, *J. Catal.* 46 **1977** 402.

[218] R. Schmehel, M. Kennedy, H. von Seggern, H. Winkler, M. Kolbe, *J. Appl. Phys.* 89 **1679** 2001.

[219] J.-S. Bae, T.E. Hong, J.H. Yoon, B. Lee, M.-S. Won, J.P. Kim, Y.S. Kim, J.H. Jeong, *J. Anal. Sci. & Tech.* 1 **2010** 92.

[220] C.A. Kodrira, H.F. Brito, O.L. Malta, O.A. Serra, *J. Luminesc.* 101 **2003** 11.

[221] E.W.J.L. Oomen, A.M.A. van Dongen, *J. Non-Cryst. Solids* 111 **1989** 205.

[222] J.J. Carvajal, B. Raghothamachar, O. Silvestre, H. Chen, M.C. Pujol, V. Petrov, M. Dudley, M. Aguiló, F. Díaz, *Cryst. Growth & Design*, 9 **2009** 653.

[223] I.M. Joni, R. Balgis, T. Ogi, T. Iwaki, K. Okuyama, *Colloids and Surfaces A: Physicochem. Eng. Aspects* 388 **2011** 49.

[224] Y. Liang, M. Ozawa, A. Krueger, *ACS Nano* 3(8) **2009** 2288.

[225] J.M. Kim, S.M. Chang, K.S. Kim, M.K. Chung, W.S. Kim, *Colloids and Surfaces A: Physicochem. Eng. Aspects* 375 **2011** 193.

[226] F. Müller, W. Peukert, R. Polke, F. Stenger, *Int. J. Miner. Process* 74 **2004** S31.

[227] S. Tsantilis, S.E. Pratsinis, *Langmuir* 20 **2004** 5933.

[228] B.V. Derjaguin, L. Landau, *Acta Phys. Chim. USSR*, 14 **1941** 633.

[229] E.J.W. Verwey, J.T.G. Overbeek, *Theory of the Stability of Lyophobic Colloids* Elsevier, New York **1962**.

[230] C. Sauter, H.P. Schuchmann, *Chem. Eng. Technol.* 30 **2007** 1401.

[231] J. Chen, M.A. Hamon, H. Hu, Y. Chen, A.M. Rao, P.C. Eklund, R.C. Haddon, *Science* 282 **1998**, 95.

[232] S. Niyogi, M.A. Hamon, H. Hu, B. Zhao, P. Bhowmik, R. Sen, M.E. Itkis, R.C. Haddon, *Acc. Chem. Res.* 35 **2002** 1105.

[233] V.N. Khabashesku, W.E. Billups, J.L. Margrave, *Acc. Chem. Res*. 35 **2002** 1087.

[234] J. Chen, A.M. Rao, S. Lyuksyutov, M.E. Itkis, M.A. Hamon, H. Hu, R.W. Cohn, P.C. Eklund, D.T. Colbert, R.E. Smalley, R.C. Haddon, *J. Phys. Chem. B* 105 **2001** 2525.

[235] S. Marković, M. Mitrić, G. Starčevic, D. Uskoković, *Ultrasonic Sonochemistry* 15 **2008** 16.

[236] X. Pepin, S.J.R. Simons, S. Blanchon, D. Rossetti, G. Couarraze, *Powder. Technol.* 117 **2001** 123.

[237] A. Mersmann, B. Braun, M. Löffelmann, *Chem. Eng. Sci.* 57 **2002** 4267.

[238] C. Sauter, M.A. Emin, H.P. Schuchmann, S. Tavman, *Ultrasonic Sonochemistry* 15 **2008** 517.

[239] H. Yu, P. Li, J. Robertson, *Diamond Rel. Mater.* 20(7) **2011** 1090.

[240] M. Zhou, J.Y. Yuan, W.Z. Yuan, Y.W. Yin, X.Y. Hong, *Nanotechnology* 18 **2007** 405704.

[241] N. Raman, S. Sudharsan, K. Pothiraj, *J. Saudi Chem. Soc.* 16 **2012** 339.

[242] E. Ruiz-Hitzky, P. Aranda, B. Casal, J.C. Galván, *Adv. Mater.* 7 **1995** 180.

[243] T.-P. Nguyen, *Surface & Coatings Technology* 206 **2011** 742.

[244] J.M. Garcés, D.J. Moll, J. Bicerano, R, Fibiger, D.G. McLeod, *Adv. Mater.* 12(23) **2000** 1835.

[245] W.U. Huynh, J.J. Dittmer, W.C. Libby, G.L. Whiting, A.P. Alivisatos, *Adv. Funct. Mater.* 13 (**2003**) 73.

[246] W. Caseri, *Macromol. Rapid Commun.* 21 **2000** 705.

[247] S.P. Kim, D.U. Lee, E.K. Kim, *Curr. Appl. Phys.* 10 **2010** S478.

[248] K. Anders, A. Jusza, M. Baran, L. Lipińska, R. Piramidowicz, *Opt. Mater.* 34 **2012** 1964.

[249] J.-S. Lin, M.-H. Chung, C.-M. Chen, F.-S. Juang, M.O. Liu, *J. Non-Cryst. Sol.* 355 **2009** 2143.

[250] Y. Liang, L. Yu, *Acc. Chem. Res.* 43(9) **2010** 1227.

[251] R. Palacios, P. Formentín, T. Trifonov, M. Estrada, R. Alcubilla, J. Pallarès, L. F. Marsal, *Physica Status Solidi (RRL)* **2**(5) **2008** 206.

[252] Y.-Z. Long, M.-M. Li, C. Gu, M. Wan, J.-L. Duvail, Z. Liu, Z. Fan, *Prog. Polym. Sci.* 36 **2011** 1415.

[253] J. Martín, C. Mijangos, *Langmuir* 25 **2009** 1181.

[254] A. Ulhir, *Bell System Technology Journal* 35 **1956** 333.

[255] D. R. Turner, *J. Electrochem. Soc.* 138 **1991** 807.

[256] L.F. Marsal, P. Formentín, R. Palacios, T. Trifonov, J. Ferré-Borrull, A. Rodríguez, J. Pallarès, R. Alcubilla, *Physica Status Solidi* a 205(10) **2008** 2437.

[257] J.N. Lee, C. Park, G.M. Whitesides, *Anal. Chem.* 75 **2003** 6544.

[258] E. Dovgolevsky, S. Kirmayer, E. Lakin, Y. Yang, C. J. Brinker, G. L. Frey, *J. Mater. Chem.* 18 **2008** 423.

[259] K. Sugiyama, H. Ishii, Y. Ouchi, K. Seki, *J. Appl. Phys.* 87 **2000** 295.

[260] S. Besbes, H.B. Ouada, J. Davenas, L. Ponsonnet, N. Jaffrezic, P. Alcouffe, *Mater. Sci. Eng. C* 26 **2006** 505.

[261] Y.-Y. Lin, D.-Y. Wang, H.-C. Yen, H.-L. Chen, C.-C. Chen, C.-M. Chen, C.-Y. Tang, C.-W, Chen, *Nanotechnology* 20 **2009** 1.

[262] Z. Chiguvare, J. Parisi, V. Dyakonov, *J. Appl. Phys.* 94 **2003** 2440.

[263] E. Cobas, M.S. Fuhrer, *Appl. Phys. Lett.* 93 **2008** 043120.

[264] Y.H. Wu, M.Y. Yang, A. Chin, W.J. Chen, C.M. Kwei, *IEEE Electron. Dev. Lett.* 21 **2000** 341.

[265] J.M. Beebe, B. Kim, J.W. Gadzuk, C.D. Frisbie, J.G. Kushmerick, *Phys. Rev. Lett.* 97 **2006** 026801.

[266] J.M. Beebe, B. Kim, C.D. Frisbie, J.G. Kushmerick, *ACS Nano* 2 **2008** 827.

[267] E.H. Huisman, C.M. Guédon, B.J. van Wees, S.J. van der Molen, *Nano Lett.* 9 **2009** 3909.

[268] I.D. Parker, *J. Appl. Phys.* 75 **1994** 1656.

[269] A. Bruyant, G. Lérondel, P.J. Reece, M. Gal, *Appl. Phys. Lett.* 82 **2003** 3227.

[270] H.S. Nalwa, *Silicon Based Materials and Devices*, Vol. 2: *Properties and Devices*, San Diego, Calif. [etc.]: Academic Press, cop. **2001**.

[271] D.M. Chapin, C.S. Fuller, G. L. Pearson, *J. Appl. Phys.* 25 **1954** 676.

[272] "Timeline of solar cells" from http://en.wikipedia.org/

[273] S.-J. Kim, Y. Zhang, C. Zuniga, S. Barlow, S.R. Marder, B. Kippelen, *Org. Electr.* 12(3) **2011** 492.

[274] Z. Wang, W. Wu, Q. Yang, Y. Li, C.-H. Noh, *J. Alloys Compd*. 486 **2009** 706.

[275] J.R. Retama, D. Mecerreyes, B. Lopez-Ruiz, E. Lopez-Cabarcos, *Colloids and Surfaces A: Physicochem. Eng. Asp.*. 270 **2005** 239.

[276] M. Baibarac, P. Gómez-Romero, M. Lira-Cantú, N. Casañ-Pastor, N. Mestres, S. Lefrant, *Eur. Polym. Journal*. 42(10) **2006** 2302.

[277] J. Lee, J.Y. Jho, *Sol. Energy Mater. Sol. Cells* 95(11) **2011** 3152.

[278] W. Ge, *Solid-State Physics II*, Spring **2009**.

[279] G. Kalita, M. Masahiro, W. Koichi, M. Umeno, *Solid-State Electronics* 54 **2010** 447.

[280] S.K. Jang, S.C. Gong, H.J. Chang, *Synthetic Met.* 162 **2012** 426.

[281] J. Schafferhans, A. Baumann, A. Wagenpfahl, C. Deibel, V. Dyakonov, *Org. Electron.* 11 **2010** 1693.

[282] Y. Liang, D. Feng, Y. Wu, S.-T. Tsai, G. Li, C. Ray, L. Yu, *J. Am. Chem. Soc.* 131 **2009** 22.

[283] W. Ma, C. Yang, X. Gong, K. Lee, A. J. Heeger, *Adv. Funct. Mater*. 15 **2005** 1617.

[284] Y. Lu, Y. Hou, Y. Wang, Z. Feng, X. Liu, Y. Lu, *Synthetic. Met.* 161 **2011** 906.

[285] M. Nam, S. Kim, M. Kang, S.-W. Kim, K.-K. Lee, *Org. Electr*. 13 **2012** 1546.

[286] C.W. Lin, D.Y. Wang, Y.T. Wang, C.C. Chen, Y.J. Yang, Y.F. Chen, *Sol. Energy Mater. Sol. Cells* 95 **2011** 1107.

[287] K. Lee, J.Y. Kim, S.H. Park, S.H. Kim, S. Cho, A.J. Heeger, *Adv. Mater.* 19 **2007** 2445.

[288] L. Qian, J. Yang, R. Zhou, S. Tang, Y. Zheng, T.-K. Tseng, D. Bera, J. Xue, P.H. Holloway, *J. Mater. Chem.* 21 **2011** 3814.

[289] Z. Pei, S. Thiyagu, M.-S. Jhong, W.-S. Hsieh, S.-J. Cheng, M.-W. Ho, Y.-H. Chen, J.-C. Liu, C.-M.Yeh, *Sol. Energy Mater. Sol. Cells* 95 **2011** 2431.

[290] C. Domingo, V. Resta, S. Sánchez-Cortés, J.V. García-Ramos, J. Gonzalo, *J. Phys. Chem. C* 111 **2007** 8149.

[291] D.H. Wang, D.Y. Kim, K.W. Choi, J.H. Seo, S.H. Im, J.H. Park, O.O. Park, A.J. Heeger, *Angew. Chem. Int.* 50 **2011** 5519.

[292] Y. Zhou, F.S. Riehle, Y. Yuan, H.-F. Schleiermacher, M. Niggermann, G.A. Urban, M. Kruger, *Appl. Phys. Lett.* 96 **2010** 013304.

[293] F.C. Krebs, T.D. Nielsen, J. Fyenbo, M. Wadstrom, M.S. Pedersen, *Energ. Environ. Sci.* 3 **2010** 512.

[294] D. Chen, Y. Wang, M. Hong, *Nano Energy* 1 **2012** 73.

[295] H. Hafez, M. Saif, M.S.A. Abdel-Mottaleb, *Journal of Power Sources* 196 **2011** 5792.

[296] H. Hoppe, N.S. Sariciftci, *J. Mater. Res.* 19 **2004** 1924.

[297] N.J. Alley, K.-S. Liao, E. Andreoli, S. Dias, E.P. Dillon, A.W. Orbaek, A.R. Barron, H.J. Byrne, S.A. Curran, *Synthetic Metals* 162 **2012** 95.

[298] D. Gupta, M. Bag, K.S. Narayan, *Appl. Phys. Lett.* 92 **2008** 093301.

[299] J. Guo, Y.Y. Liang, *J. Phys. Chem. B* 114 **2010** 742.